Evaluation of the performances of scaled CBRAM devices to optimize technological solutions and integration flows

Jeremy Guy

UNIVERSITÉ GRENOBLE ALPES

THÈSE

Pour obtenir le grade de

DOCTEUR DE L'UNIVERSITÉ GRENOBLE ALPES

Spécialité : **Nano Electronique et Nano Technologie**

Arrêté ministériel : 7 août 2006

Présentée par

Jérémy Guy

Thèse dirigée par **Fabien Clermidy**

préparée au sein du **CEA – Leti**

Evaluation des performances des mémoires CBRAM (Conductive Bridge Memory) afin d'optimiser les empilements technologiques et les solutions d'intégration.

Thèse soutenue publiquement le **18 décembre 2015,**
devant le jury composé de :

Gérard Ghibaudo
Professeur à l'INPG, Président
Abdelkader Souifi
Professeur à l'INL, Rapporteur
Jean-Michel Portal
Professeur à l'IM2NP, Rapporteur
Faiz Dahmani
Ingénieur chercheur chez ALTIS, Examinateur
Gabriel Molas
Ingénieur chercheur CEA - LETI, Encadrant
Fabien Clermidy
Ingénieur chercheur CEA - LETI, Directeur de thèse
Barbara De Salvo
Ingénieur chercheur CEA - LETI, Invitée

Abstract

The constant evolution of the data storage needs over the last decades have led the technological landscape to completely change and reinvent itself. From the early stage of magnetic storage to the most recent solid state devices, the bit density keeps increasing toward what seems from a consumer point of view infinite storage capacity and performances. However, behind each storage technology transition stand density and performances limitations that required strong research work to overcome. This manuscript revolves around one of the promising emerging technology aiming to revolutionize data storage landscape: the Conductive Bridge Random Access Memory (CBRAM). This technology based on the reversible formation and dissolution of a conductive path in a solid electrolyte matrix offers great advantages in term of power consumption, performances, density and the possibility to be integrated in the back end of line. However, for this technology to be competitive some roadblocks still have to be overcome especially regarding the technology variability, reliability and thermal stability. This manuscript proposes a comprehensive understanding of the CBRAM operations based on experimental results and a specially developed Kinetic Monte Carlo model. This understanding creates bridges between the physical properties of the materials involved in the devices and the devices performances (Forming, SET and RESET time and voltage, retention, endurance, variability). A strong emphasis is placed on the current limitations of the technology previously stated and how to overcome these limitations. Improvement of the thermal stability and device reliability are demonstrated with optimized operating conditions and proper devices engineering.

Outline

The manuscript developed here is a part of the requirements for obtaining the degree of Doctor of Philosophy of the Grenoble Institute of Technology (Grenoble INP). This Ph.D. thesis was focused on an emerging non – volatile memory technology: the Conductive Bridge Random Access Memory (CBRAM) which is offering great advantages in term of power consumption, performances, density and the possibility to be integrated in the back end of line.

This manuscript aims to cover all the aspects of the CBRAM technology from experimental results to technological optimization based on physical simulation of the devices.

Chapter I of this manuscript will depict the current state of the art of the CBRAM technology and more globally of the data storage landscape. As an introduction to the rest of the manuscript, this chapter will offer an overview of the electrical performances and CBRAM simulations at which will be confronted this Ph.D. work. A strong focus will be placed on the current limitations affecting the technology and especially the lack of comprehensive physical understanding of the CBRAM operations.

Chapter II will be focused on describing the studied samples and the characterization methods that will be used to address the CBRAM behavior. This chapter, will serve as basis to all devices tested and experimental results presented in the following of the manuscript.

Chapter III, similarly to chapter II, will serve as a reference for the following of the manuscript regarding the Kinetic Monte Carlo model developed to enhance the global understanding of the CBRAM. It will describe the model in term of involved physics and resolution progression. The several evolutions and updates of the model will also be presented to reflect to progressive changes in the global understanding.

Chapter IV will treat the basic operations that are Forming, SET and RESET with an intensive study of the technological and physical factors involved in the CBRAM behavior. Based on the joint study of electrical characterizations and simulation results, bonds between electrical

characteristics and materials physical properties will be proposed. Performances way of optimization will also be discussed.

Chapter V will be focus on one of the current limitation of the CBRAM technology: the states variability and devices reliability. A comprehensive understanding of the intrinsic and cell to cell variability of LRS and HRS will be discussed. The great importance of the operating conditions on endurance and reliability will be addressed and endurance optimizations presented.

Chapter VI will analyze the data retention behavior which is driving the CBRAM studies for the last past years. Based on the filament morphology, a physical understanding of the retention behavior will be presented. Optimizations of the data retention behavior correlated to the operating conditions will be proposed.

Chapter VII will serve as a comprehensive synthesis of the work presented in this manuscript. The great importance of the conductive filament morphology will be discussed through all the experimental and theoretical results obtained during this research work.

Table of contents

French extended abstract – Résumé étendu en Français

Ces dernières décennies, la constante évolution des besoins de stockage de données a mené à un bouleversement du paysage technologique qui s'est complètement métamorphosé et réinventé. Depuis les débuts du stockage magnétique jusqu'aux plus récents dispositifs fondés sur l'électronique dite d'état solide, la densité de bits stockés continue d'augmenter vers ce qui semble du point de vue du consommateur comme des capacités de stockage et des performances infinies. Cependant, derrière chaque transition et évolution des technologies de stockage se cachent des limitations en termes de densité et performances qui nécessitent de lourds travaux de recherche afin d'être surmontées et repoussées. Ce manuscrit s'articule autour d'une technologie émergeante prometteuse ayant pour vocation de révolutionner le paysage du stockage de données : la mémoire à pont conducteur ou Conductive Bridge Random Access Memory (CBRAM). Cette technologie est fondée sur la formation et dissolution réversible d'un chemin électriquement conducteur dans un électrolyte solide. Elle offre de nombreux avantages face aux technologies actuelles tels qu'une faible consommation électrique, de très bonnes performances de programmation et de lecture ainsi que la capacité d'être intégrée aux seins des interconnexions métalliques d'une puce afin d'augmenter la densité de stockage. Malgré tout, pour que cette technologie soit compétitive certaines limitations ont besoin d'être surmontées et particulièrement sa variabilité et sa stabilité thermique qui posent encore problème. Ce manuscrit propose une compréhension physique globale du fonctionnement de la technologie CBRAM fondée sur une étude expérimentale approfondie couplée à un modèle Monte Carlo cinétique spécialement développé. Cette compréhension fait le lien entre les propriétés physiques des matériaux composant la mémoire CBRAM et ses performances (tension et temps de programmation, rétention de données, endurance et variabilité). Un fort accent est mis la compréhension des limites actuelles de la technologie et comment les repousser. Grâce à une optimisation des conditions d'opérations ainsi qu'à un travail d'ingénierie des dispositifs mémoire, il est démontré dans ce manuscrit une forte amélioration de la stabilité thermique ainsi que de la variabilité des états écrits et effacés.

1. Présentation de la technologie CBRAM

1.1 Fonctionnement de la technologie

La technologie CBRAM appartient à la famille des mémoires résistives dont le stockage de données se fonde sur la coexistence de plusieurs niveaux de résistance électrique. Une des forces de la technologie CBRAM est la simplicité de sa structure, à savoir une structure Métal Isolant Métal (MIM) comme représentée Figure 1. La mémoire CBRAM repose sur la formation d'un pont conducteur reliant les deux électrodes métalliques au travers de la couche isolante. La particularité de la technologie CBRAM en comparaison aux autres technologies RRAM est le caractère métallique du filament conducteur formé à partir des atomes composant une des électrodes. Cette spécificité impose le choix d'une des électrodes à base d'un métal dit actif tel que le cuivre ou l'argent. La seconde électrode doit être faite d'un métal inerte tel que le tungstène. La formation et dissolution réversible du filament permet une modification de la résistance électrique de la cellule et le stockage de l'information. Le filament reste formé dans l'isolant sans maintien de tension, offrant à cette technologie un caractère non volatile.

L'utilisation standard de la CBRAM se fonde sur trois états différents :

- Un état de très forte résistance, correspondant à l'état vierge de la cellule avant toute étape d'écriture.
- Un état de faible résistance (LRS) aussi appelé état écrit, obtenu après formation du filament. La commutation de la cellule dans cet état nécessite une opération appelée Forming depuis l'état vierge ou une opération appelée SET depuis un état effacé.
- Un état de haute résistance (HRS) aussi appelé état effacé, obtenu après la dissolution du filament. La commutation de la cellule dans cet état depuis l'état écrit nécessite une opération appelée RESET.

Afin de permettre la commutation de la cellule d'un état à un autre, des conditions spécifiques de tension et courant sont à appliquer. Les opérations de Forming, SET et RESET correspondent à l'application d'une rampe ou d'un pulse de tension contrôlé en courant. La tension ainsi que le temps nécessaire à la commutation dépendent grandement de l'architecture, des dimensions ainsi que des matériaux constituant la CBRAM.

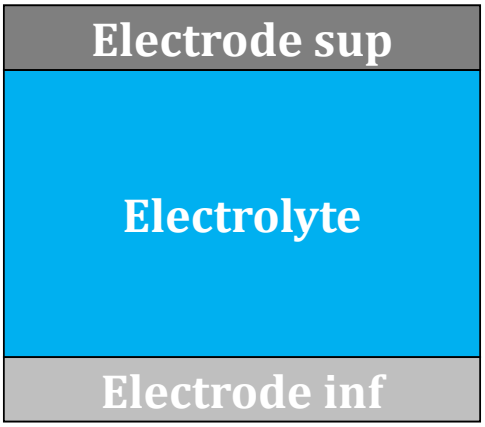

Figure 1. Représentation schématique de la structure MIM d'une CBRAM

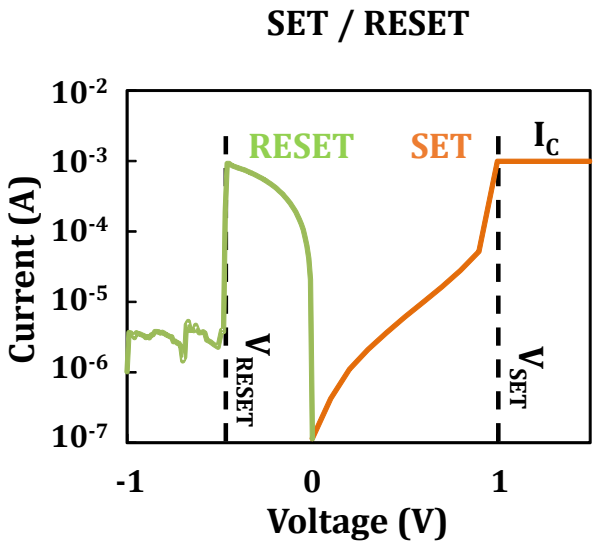

Figure 2. Courbe I(V) des opérations d'écriture et d'effacement

Les étapes de Forming et de SET correspondent à l'application d'une tension positive sur l'électrode active alors que l'étape de RESET correspond à l'application d'une tension négative sur cette électrode. Ces étapes sont visibles sur la mesure courant tension représentée Figure 2. On y distingue les tensions de commutation (V_{SET} et V_{RESET}) ainsi que le courant limitant l'écriture (I_C) et permettant d'éviter la dégradation de la cellule mémoire.

1.2 Fondements physique de la technologie

La formation et dissolution du filament sur lesquels repose le fonctionnement de la CBRAM sont possibles grâce à des réactions électrochimiques entre les électrodes et l'isolant. Dans un premier temps l'oxydation de l'électrode active induite par l'application de la tension positive permet la création d'ions métalliques chargés. Cette réaction explique la nécessité d'avoir une électrode active comme précédemment exposé. La réaction d'oxydoréduction a été reliée par plusieurs études aux équations de Buttler Volmer [AChen 1, Valov 1]. Une fois les ions formés, ils migrent à travers l'isolant et en direction de l'électrode opposée sous l'effet du champ. Cette migration, a été à plusieurs reprises décrite par l'approche de Mott Gurney. Afin de permettre la bonne migration des ions et donc la commutation de la cellule, un choix judicieux de l'isolant en accord avec les espèces migrante est à faire (exemple : GeS_2 pour Ag [Jameson 1] ou Al_2O_3 for Cu [Belmonte 1]). Une fois que les ions ont atteints l'électrode opposée, ils sont réduits et perdent leur charge. A mesure que le nombre d'ions atteignant l'électrode inerte augmente, le filament se forme

et sa hauteur augmente réduisant progressivement la dimension de la zone isolante. Lorsque le filament atteint l'électrode opposée, le chemin conducteur est formé et la résistance électrique s'en retrouve grandement diminuée.

L'enchainement d'étapes précédemment décrit correspond à l'opération d'écriture. L'opération d'effacement correspond quant à elle à l'enchainement inverse, à savoir l'oxydation des atomes composant le filament et la migration des ions en direction de l'électrode active suite à l'application d'une tension positive sur l'électrode inerte. L'opération d'effacement est également accélérée par le fort dégagement thermique résultant de la haute densité de courant circulant dans le filament.

Il a également été récemment démontré [Molas 1], l'implication de lacunes d'oxygène dans le fonctionnement de la technologie CBRAM. Ces lacunes, chargées positivement migrent également sous l'effet du champ facilitant la migration des ions métalliques et la formation du pont conducteur. La Figure 3 schématise le fonctionnement de la CBRAM en comparaison des RRAM fondées uniquement sur les lacunes d'oxygènes (OxRAM) ou l'électro-migration.

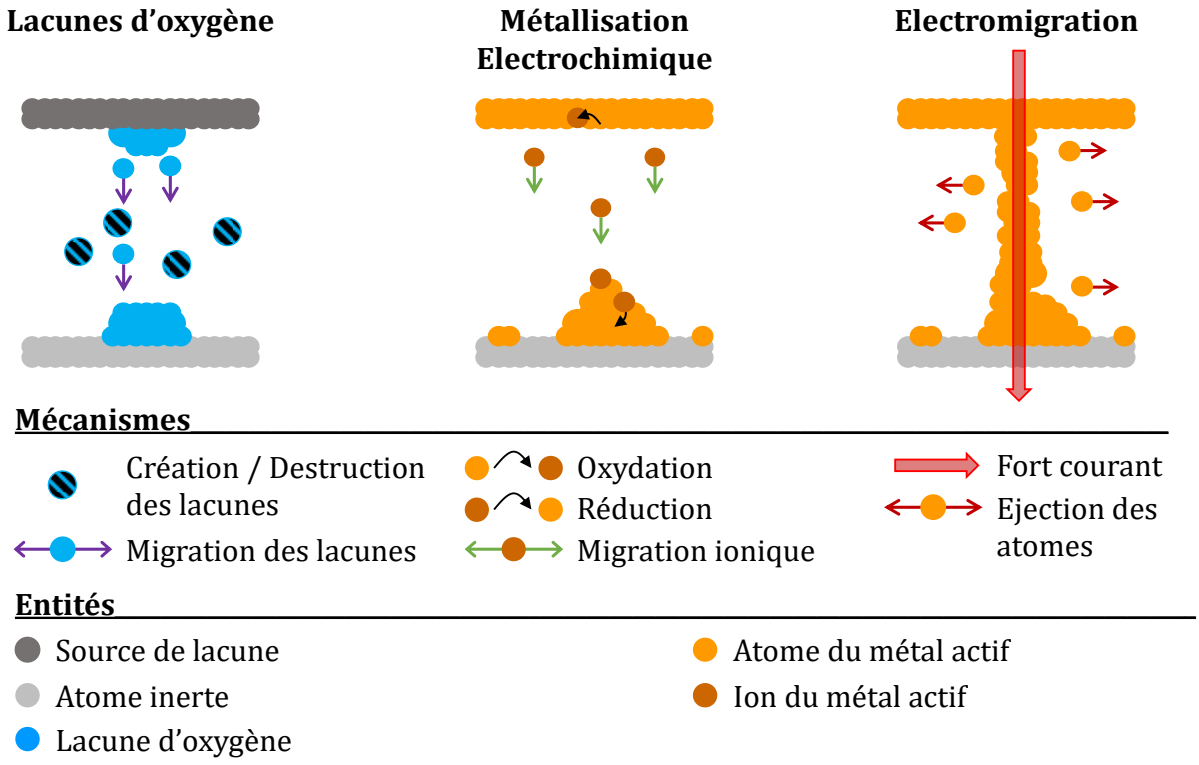

Figure 3. Comparaison des mécanismes de commutation de la CBRAM à ceux d'autres technologies

2. Modèle Monte Carlo cinétique

Afin d'apporter une compréhension générale au fonctionnement des CBRAM, un modèle Monte Carlo cinétique a été développé. Ce modèle se fonde sur la simulation de la migration atomique et des réactions d'oxydoréduction au niveau atomique et électronique. Le modèle a été réalisé de sorte à proposer une résolution en 2 dimensions et ainsi obtenir des performances permettant la simulation statistique d'un grand nombre de cycle et/ou dispositifs. L'environnement de simulation ainsi que les mécanismes simulés sont représentés Figure 4. La progression de la résolution est présentée Figure 5, cette résolution se décompose en une succession d'itérations durant lesquels les mécanismes peuvent se produire.

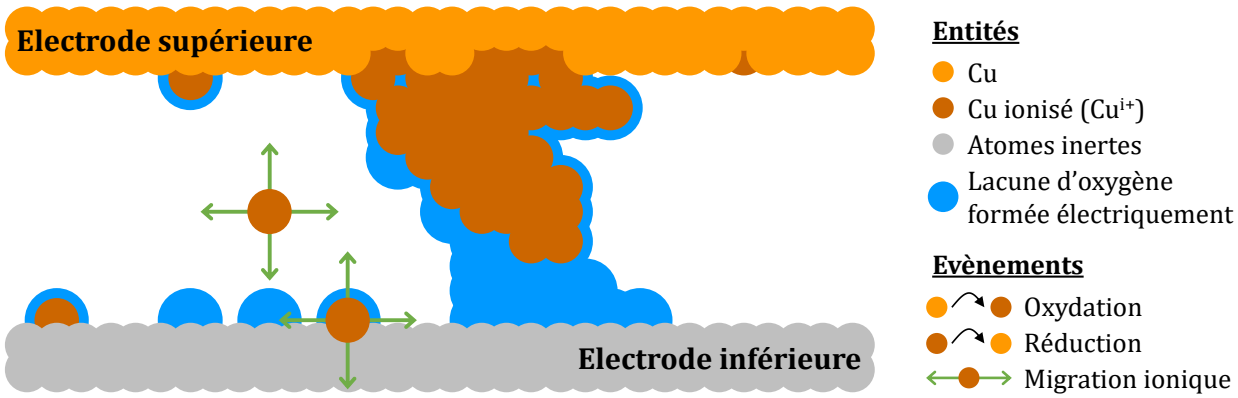

Figure 4. Environnement de la simulation Monte Carlo cinétique ainsi que les mécanismes simulés

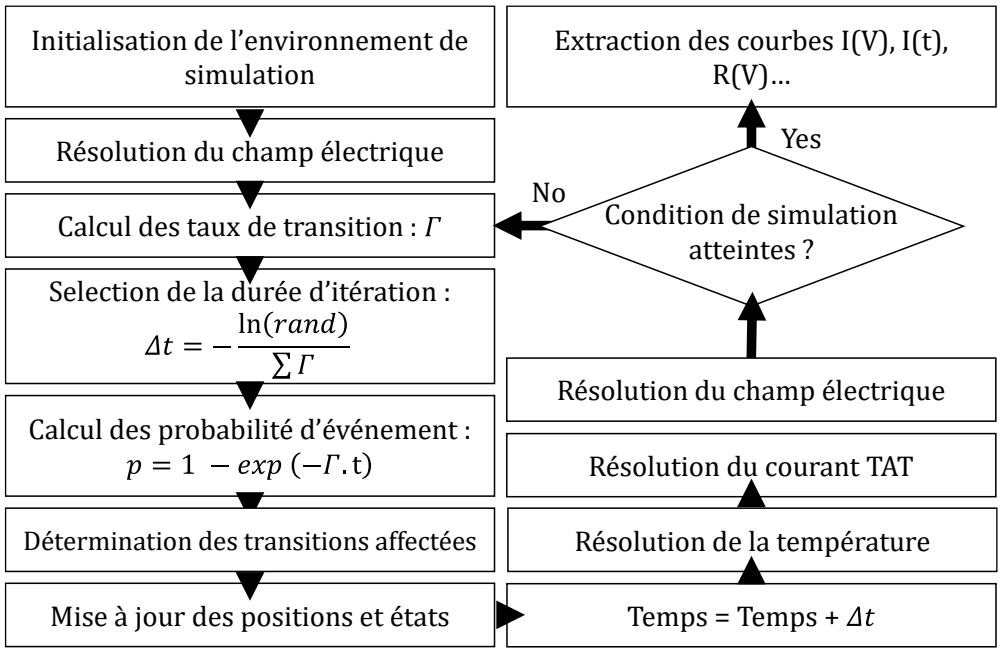

Figure 5. Déroulement de la resolution de la simulation

La résolution physique des mécanismes repose sur l'utilisation de la théorie des transitions d'état [Laidler 1, Larentis 1, Russo 1] qui consiste à considérer les mécanismes (migration, réactions) comme le passage d'une particule d'un niveau d'énergie à un autre niveau plus favorable. Cette transition de niveaux d'énergie se fait en passant une barrière énergétique dont la hauteur dépend du mécanisme et des particules en jeu. La Figure 6 représente cette théorie des transitions d'état appliquée à différents mécanismes. La barrière d'énergie peut être modulée par la température, le champ électrique…

Afin de quantifier cette transition d'état, le modèle calcule le taux de transition dont l'équation de base est :

$$\vec{\Gamma} = \nu . exp\left(-\frac{E_A}{k_B T}\right)(\vec{x},\vec{y})$$

Avec $\vec{\Gamma}$ le taux de transition, ν la fréquence de vibration (environ égale à 10^{-13} s^{-1}), E_A la barrière d'énergie entre les deux états, k_B la constante de Boltzmann et T la température. Ce taux de transition correspond au temps moyen nécessaire à la transition d'une particule au-dessus d'une barrière d'énergie E_A. A partir de cette équation de base et en tenant compte de tous les facteurs modifiant la transition de particules, une équation plus complète du taux de transition est utilisée :

$$\vec{\Gamma} = \nu . \exp\left(-\frac{E_A - \frac{1}{2}(\,Q\,d\,(\,1 + L\,\chi)\;\vec{\varepsilon}_{Global} + \phi_{final} - \phi_{initial}\,)}{k_B T}\right)(\vec{x},\vec{y})$$

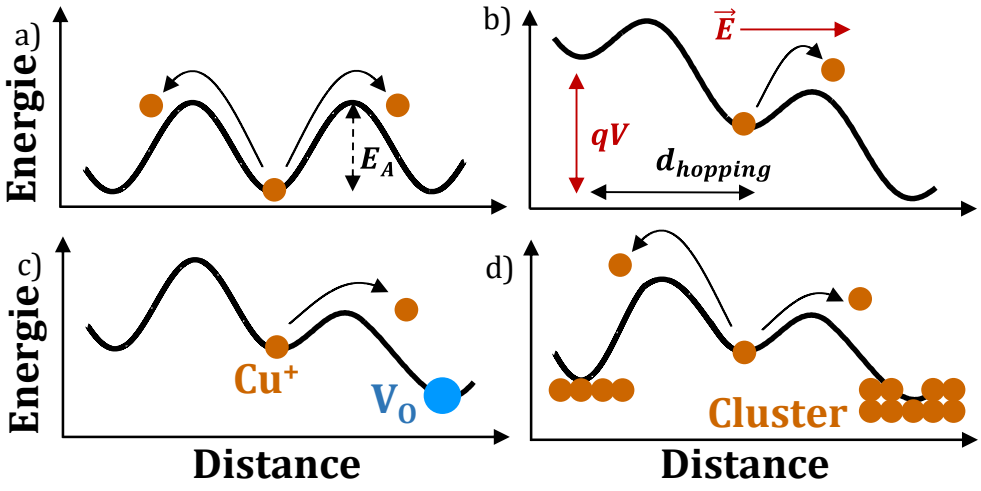

Figure 6. Représentation des profile énergétiques pour les différents mécanismes simulés et fondés sur la transition d'état (a). (b) L'application du champ électrique, (c) la présence de lacunes d'oxygène et (d) l'agrégation de Cu réduisent la barrière d'énergie.

Avec Q la charge de la particule, d la distance de saut, $\vec{\varepsilon}_{Global}$ le champ électrique global, L le facteur de Lorentz, ϵ_0 la permittivité du vide, χ la susceptibilité électrique, ϕ_{initial} et ϕ_{final} les niveaux d'énergie respectifs de l'état initial et final de la transition. Cette équation est utilisée pour l'intégralité des mécanismes décrits précédemment avec pour seule modification l'énergie d'activation et les niveaux d'énergie initiaux et finaux.

Les taux de transitions sont ensuite traduits en probabilités d'apparition en se fondant sur une indépendance des transitions les unes des autres [Voter 1] :

$$P = 1 - \exp\left(-\Gamma * t_{\text{iteration}} \right)$$

Avec Γ le taux de transition précédemment décrit et $t_{\text{iteration}}$ la durée de l'itération. La probabilité pour une transition de se produire est donc directement reliée à la durée de l'itération du modèle. Afin d'optimiser à la fois la précision de la résolution sans pour autant sacrifier les performances du modèle la durée de l'itération n'est pas fixée globalement mais varie d'une itération à l'autre et plus particulièrement en fonction des transitions pouvant se produire durant l'itération en cours :

$$t_{\text{iteration}} = -\frac{\ln(P_{\text{None}})}{\sum_{\text{atoms \& ions}} \Gamma}$$

Avec P_{None} la probabilité qu'aucune transition ne se produise. Cette probabilité contrôle à la fois la précision et les performances du modèle, une valeur trop faible entraine une perte de précision vis-à-vis des transitions rapides mais une valeur trop haute entraine une perte de performance. Il a été fait le choix, après calibration, d'utiliser une probabilité de l'ordre de 50% offrant le meilleur compromis.

Une fois les probabilités de toutes les transitions possibles calculées, le modèle détermine aléatoirement (mais pondéré par leur probabilité) les transitions se produisant et met à jours la position et l'état des particules. Le modèle calcule ensuite les grandeurs clefs (temps, tension, courant résistance…) et relance une itération tant que les grandeurs cibles ne sont pas atteintes.

Comme préciser précédemment, les taux de transitions sur lesquels repose l'intégralité du modèle dépend de nombreux paramètres et notamment de deux grandeurs physiques : la tension et la température. Afin de pouvoir calculer ces taux de transition la création de modèles physique est nécessaire. Ces modèles, au nombre de deux : thermique et électrique, ont été développés avec le même effort d'optimisation que le reste du modèle afin d'offrir un temps de simulation réduit.

Ainsi, l'utilisation d'éléments finis bien que très précise s'est révélée trop lourde pour pouvoir offrir l'aspect statistique rechercher dans la simulation des CBRAM.

La résolution des modèles physiques repose sur une approche par réseaux de résistances aussi bien pour la partie électrique que thermique. Le modèle électrique propose une approche simplifier de la conduction tunnel assistée par pièges avec une variation exponentielle de la résistance en fonction de la distance entre les atomes conducteurs :

$$R_{at-at} = R_{Quantum}\, exp\left(2\frac{\sqrt{2m^* E_C}}{\hbar}\,(d-a)\right)$$

Avec $R_{Quantum}$ le quantum de résistance (12.9 kΩ), m^* la masse effective des électrons spécifique à l'isolant, E_C la barrier d'énergie tunnel des électrons, d la distance entre deux atomes, a la distance de contact entre deux atomes et $\hbar$ la constante de Planck. A partir des valeurs de résistance entre atomes, un maillage de résistances est créé comme représenté Figure 7. La résolution des lois d'Ohm et Kirchhoff permet d'obtenir le courant circulant dans la cellule ainsi que la tension en chaque point. A partir de cette tension, le champ électrique est calculé et utilisé dans le calcul des taux de transition :

$$\vec{E} = -\overrightarrow{grad}(V)$$

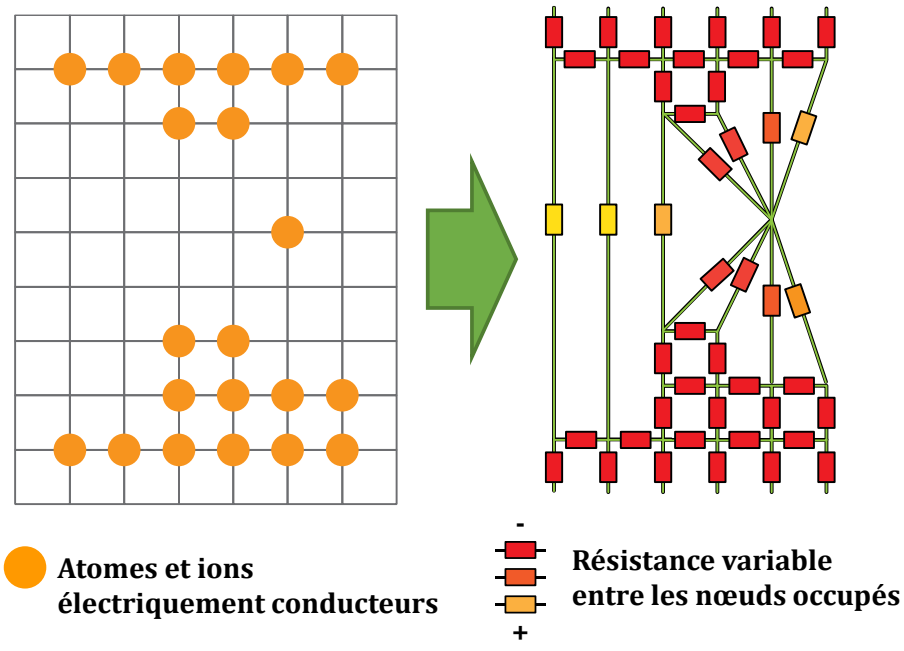

Figure 7. Représentation schématique du passage de la position des atomes au maillage de résistances à partir du modèle de conduction tunnel assistée par pièges.

Avec V la tension en chaque point et $\vec{E}$ le champ électrique.

Le modèle thermique repose sur une génération thermique par effet Joule induite par le passage du courant puis sur une dissipation de la chaleur dans les matériaux constituant la CBRAM. En fonction des matériaux, un réseau de résistances thermiques est créé puis résolue afin d'avoir la température en chaque point grâce à l'analogie tension température :

$$\Delta T = P * R_{th}$$

Avec ΔT l'augmentation de température, P la puissance générée par effet Joule et R_{th} la résistance thermique dépendant des matériaux. Enfin, afin de pallier l'aspect dynamique manquant de ce type de résolution, une correction exponentielle a été ajoutée pour le faible nombre d'itérations dont le temps est trop court pour que le système soit en régime stationnaire. Cette correction a été calibrée grâce à une étude par éléments finis réalisée sous COMSOL Multiphysics.

L'enchainement des étapes décrites précédemment couplé à la résolution de ces modèles physiques permet la simulation de l'intégralité des opérations de base de la CBRAM : Forming, SET, RESET, endurance et rétention (Figure 8 et 9)

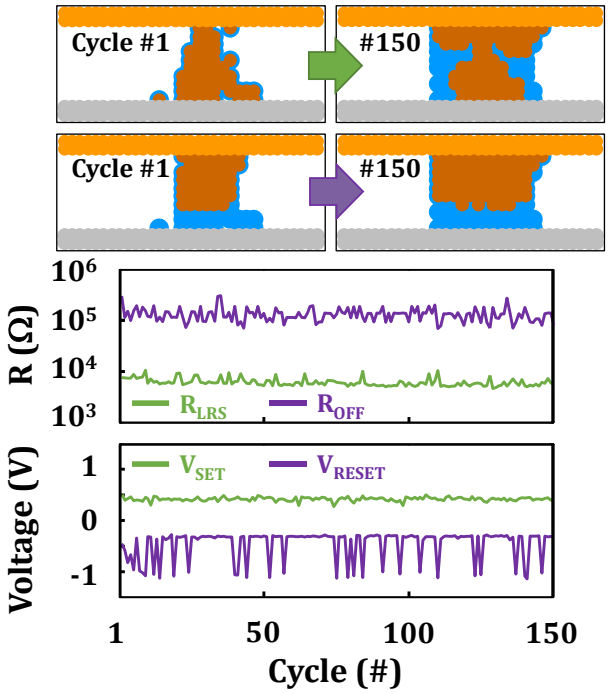

Figure 8. Simulation d'une étape d'écriture et d'effacement standard

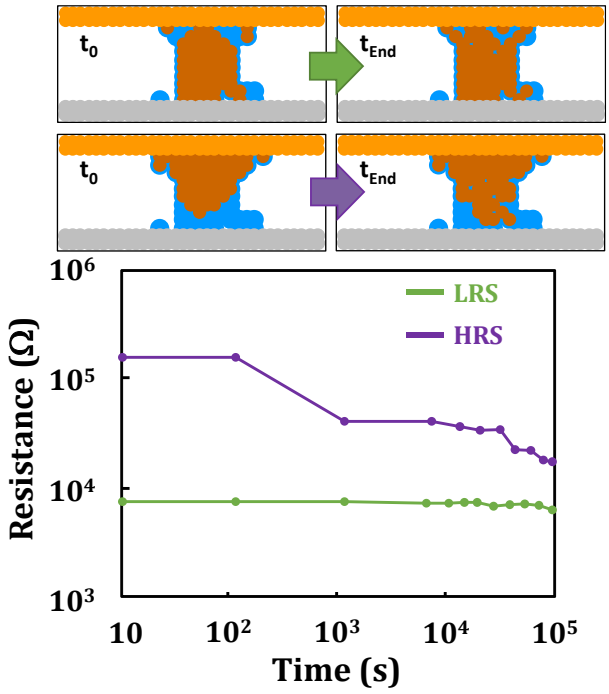

Figure 9. Simulation d'une succession de cycle d'écritures et d'effacements.

3. Forming, SET et RESET

Cette partie s'attache à montrer l'importance des dimensions et des propriétés des matériaux dans les performances des CBRAM. Ainsi, à l'aide de la structure Nano – Trench (Figure 10), une architecture novatrice fondée sur le confinement de la zone active (électrode inférieure et isolant), l'impact du confinement est étudié. Le confinement se fait à travers la réduction de deux dimensions critiques : l'épaisseur du « Liner » pour l'électrode inférieure et la largeur de la « Trench » pour l'isolant. De plus, grâce à une large sélection d'échantillons et de combinaisons de matériaux, le rôle de chaque niveau de la CBRAM est discuté. Enfin, il est proposé une compréhension générale des opérations de commutation de la technologie CBRAM.

Les points clefs mis en avant par cette étude de cellules confinées peuvent être divisés en deux catégories, ceux portant sur la performance de la CBRAM et ceux apportant une compréhension phénoménologique de la technologie, l'échantillon de base faisant référence ici est une cellule nano – Trench composée de l'empilement suivant : CuTeGe/Al_2O_3/TiN (électrode supérieure / isolant / électrode inférieure).

3.1 Confinement et réduction des dimensions

Dans un premier temps, la réduction des dimensions montre une diminution de la résistance des cellules vierges. Cette observation Figure 11 est en accord avec la conduction volumique de l'état vierge dépourvue de toute trace de filament. L'augmentation de la résistance à mesure que le

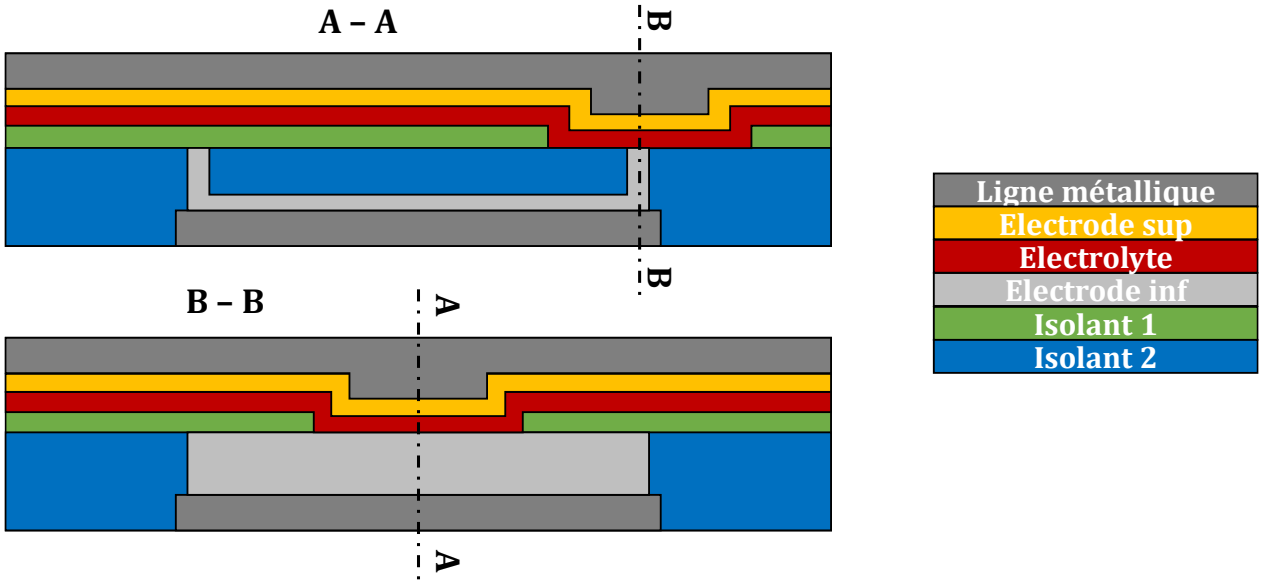

Figure 10. Représentation schématique d'une architecture Nano-Trench

confinement croit, suit une loi en 1/surface, confirmant cette hypothèse de conduction volumique. En opposition à cette première observation, l'évolution de la résistance des états écrits et effacés ne suit pas la même loi de décroissance comme le montre la figure 12. Cette stabilité de la résistance de l'état écrit peu importe la taille du dispositif est explicable par le caractère filamentaire de la conduction de cet état. La dimension du filament ne dépend pas du confinement de la cellule. Ce filament a en effet été observé par une équipe de l'IMEC [Celano 1] avec des dimensions inférieures à 10 nm. Il n'est donc pas limitépar le confinement actuel de la cellule (50x10nm² ici). En revanche la stabilité de l'état effacé apporte plus de questions. En effet, si la conduction de l'état effacé est volumique, une variation similaire à celle de l'état vierge devrait être observée. La stabilité ici présente montre donc une conduction électrique dictée par un comportement filamentaire. Cependant, la résistance étant supérieur au quantum de résistance [Sune 1] le filament n'est pas intégralement maintenu après effacement. La conduction électrique de l'état effacé est donc contrôlée par un filament résiduel dans l'isolant. Cette observation est valable pour l'empilement technologique de référence ici mais également extensible à une majorité de CBRAM à base d'oxyde.

D'un point de vu des performances, la réduction des dimensions apporte une accélération des vitesses de commutation comme représenté Figure 13. Ainsi, le passage d'un « Liner » de 40 nm à 10 nm permet de réduire le temps d'écriture de 5 décades à 0.8 V et d'offrir un temps d'écriture de l'ordre de 70 ns. Cette nette amélioration des performances peut être expliquée par un effet de

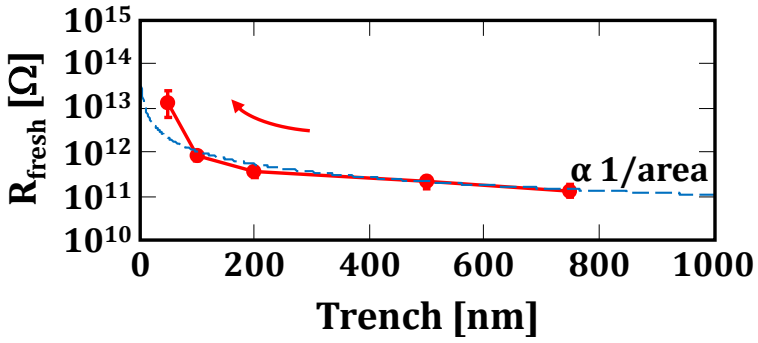

Figure 11. Evolution de la résistance de cellules vierges en fonction de la dimension du « Trench ».

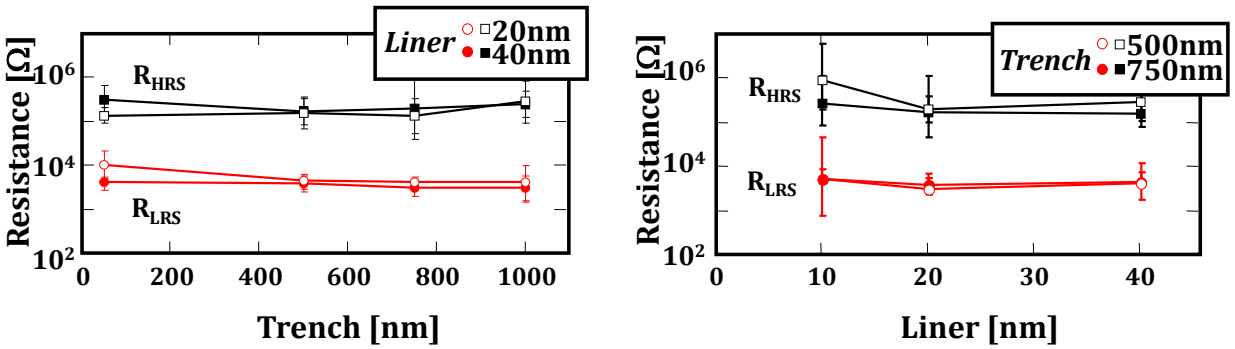

Figure 12. Evolution des niveaux de résistance en fonction des dimensions de la cellule

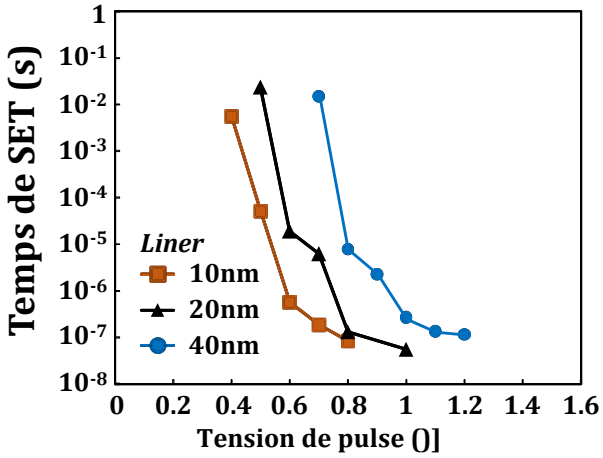

Figure 13. Temps de commutation dynamique en fonction de la tension de pulse appliquée

pointe de plus en plus marqué à mesure que le confinement s'accentue. Cet effet de pointe induit une augmentation locale du champ électrique qui, moteur des mécanismes de commutation, accélère les vitesses d'écriture. Cette courbe du temps de commutation en fonction de la tension appliquée est une caractéristique majeure de la technologie CBRAM sur laquelle nous reviendrons par la suite.

3.2 Compréhension globale des mécanismes de commutation

3.2.1 Etude du Forming et SET

L'écriture d'une cellule CBRAM peut se faire soit à partir d'un état effacée : le SET ou à partir d'un état vierge : le Forming. Cette étape de Forming est liée à l'utilisation d'oxyde comme couche isolante. Dans le cas de l'utilisation de chalcogénures, la cellule CBRAM n'a pas besoin de cycle de Forming à haute tension. La compréhension des mécanismes de commutation s'appuie principalement sur une étude du Forming afin de limiter au maximum dans un premier temps tout

impact de phénomènes parasites tels que par exemple la dégradation de l'isolant ou la présence d'un filament résiduel.

En modifiant la composition de la CBRAM il est possible de fortement modifier son comportement et ses performances d'écriture. Ces performances, que traduisent les courbes temps de commutation en fonction de la tension appliquée, sont modifiables de deux façons comme le récapitule la Figure 14. Ainsi, dans un premier temps, il est possible de décaler les courbes temps-tension en modifiant les niveaux d'énergies des matériaux employés. Ces niveaux d'énergies viennent directement modifier les vitesses de transition d'état de la migration et des réactions. En effet comme décrit dans l'équation précédemment détaillée :

$$\vec{\Gamma} = \nu . \exp\left(- \frac{E_A - \frac{1}{2}(Q\, d\, (1 + L\, \chi)\ \vec{\varepsilon}_{Global} + \phi_{final} - \phi_{initial})}{k_B T} \right) (\vec{x}, \vec{y})$$

Les niveaux d'énergies (ϕ_{final} et $\phi_{initial}$) modifient linéairement la hauteur de barrière de la transition d'état. Cette modification linéaire induit le décalage des courbes temps de commutation tension et permet d'accélérer les vitesses de commutation.

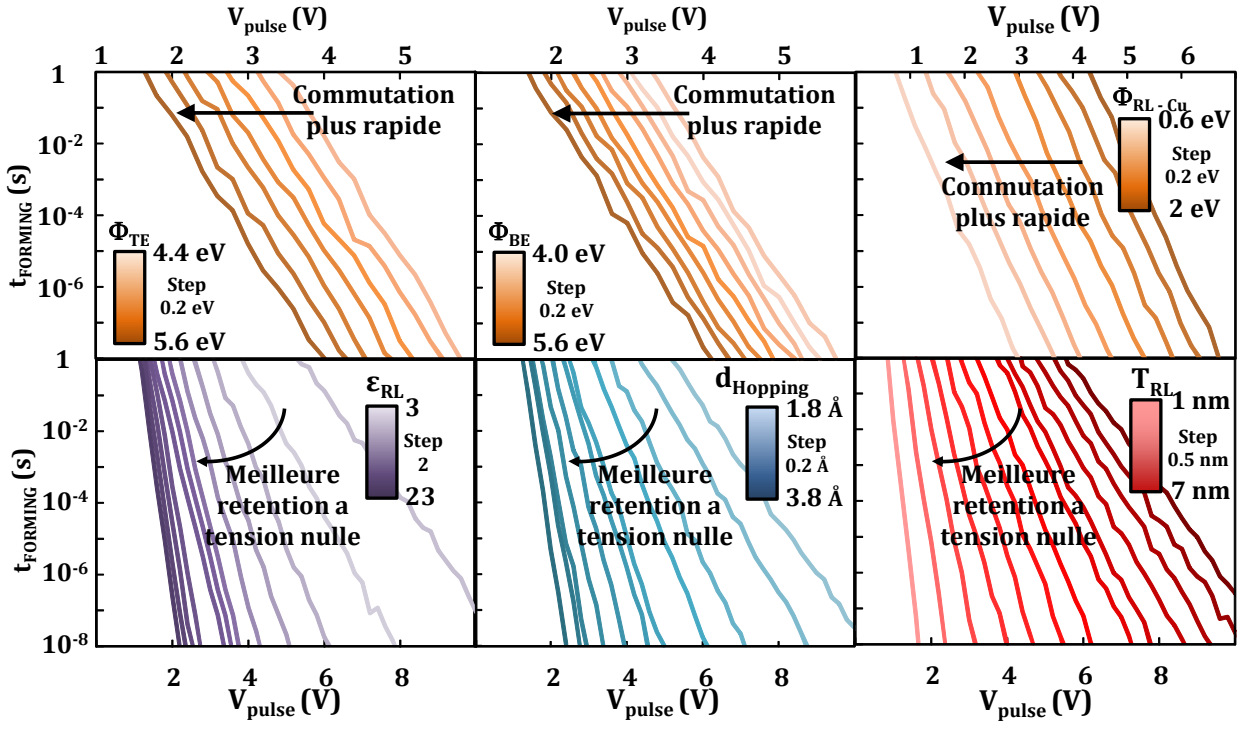

Figure 14. Synthèse des liens entre les propriétés matériaux et les performances de programmation la technologie CBRAM

Dans un deuxième temps, il est également possible de modifier la pente de ces courbes, ce qui signifie qu'il est possible de modifier l'efficacité de la tension à accélérer la commutation. En revenant à l'équation précédente, on voit cette fois-ci que la distance de transition ainsi que la susceptibilité électrique de l'isolant modifient l'efficacité du champ à réduire la barrière de transition. La distance de transition correspond à la distance entre les deux niveaux d'énergie, cette distance peut être modifiée par la densité du matériau. La susceptibilité électrique est-elle liée à la permittivité électrique de l'isolant et dépend de sa composition ainsi que de sa densité. Enfin, le champ électrique est directement lié à la tension appliquée et l'épaisseur de l'isolant. Ainsi en modifiant l'épaisseur de l'isolant, il est également possible de modifier l'efficacité de la tension à réduire la barrière de transition et donc de modifier la pente de la caractéristique de commutation. Tous ces paramètres permettent donc, au même titre que les précédents, d'accélérer les mécanismes de commutation et donc l'écriture et l'effacement mais ils permettent également de modifier la sensibilité de la cellule aux faibles tensions. En effet, plus la pente sera faible plus le temps de commutation à tension nulle ou très faible sera court. De ce fait, la rétention de la donnée (tension nulle) ou la lecture (faible tension) sont dans ce cas amenées à poser des problèmes plus rapidement que dans le cas d'une pente forte. Il est ainsi possible de relier les performances de la cellule CBRAM aux propriétés physiques des matériaux la composant.

La température a également un rôle prépondérant dans le fonctionnement de la CBRAM. Ce rôle, déjà mis en avant par d'autres études dans les mécanismes du RESET [Tada 1], est également important dans la compréhension des mécanismes du SET. En effet, il est possible à partir du model Monte Carlo d'observer l'opération d'écriture et de la décomposer en deux étapes (Figure 15). Dans un premier temps un filament initial se crée jusqu'à ce que le courant limite d'écriture soit atteint. A ce niveau de courant un fort dégagement thermique se produit, introduisant une grande quantité d'énergie supplémentaire dans le système. Cette énergie (thermique et électrique) entraine la surcroissance du filament. Durant la surcroissance, le filament s'élargit, diminuant ainsi la résistance et donc la température et la tension vu par la cellule jusqu'à atteindre un état stable dans

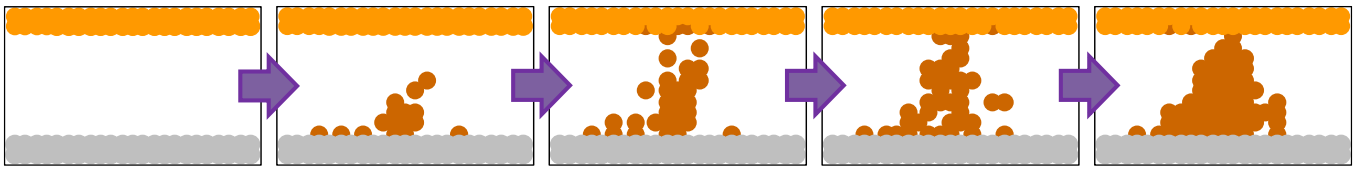

Figure 15. Formation et stabilisation du filament

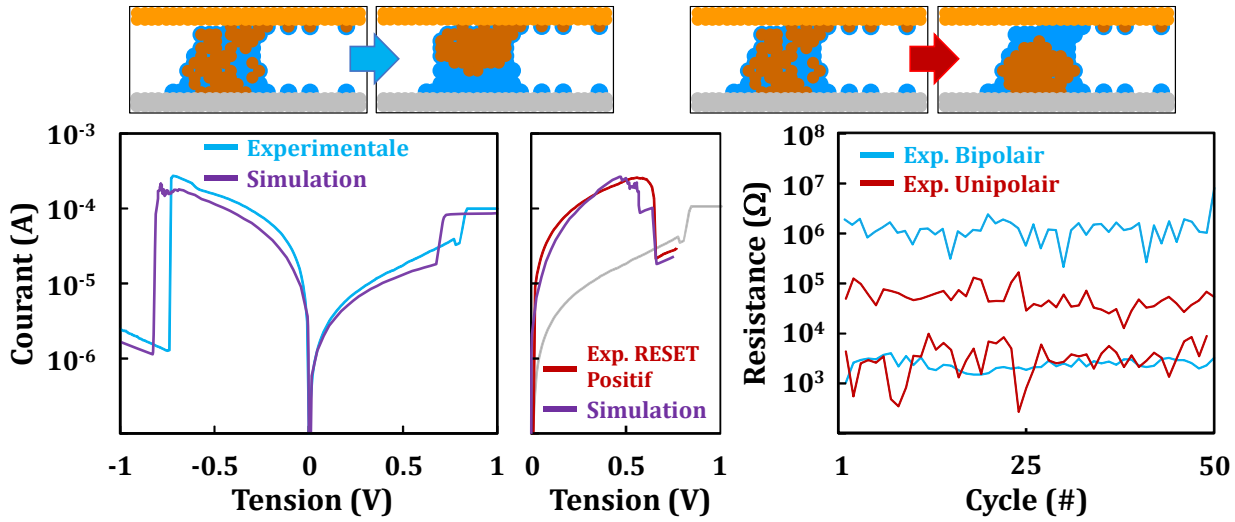

Figure 16. Comparaison de fonctionnement unipolaire et bipolaire mesurés et simulés

lequel l'énergie du système ne permet plus aux transitions d'état de se réaliser. L'apport thermique engendré par le fort courant circulant dans le filament peut également être mis à profit afin de réaliser un effacement unipolaire. En effet, en supprimant la limitation de courant il est possible d'effacer la cellule CBRAM grâce à la déstabilisation induite par le fort dégagement thermique comme représenté Figure 16. Ce type de cyclage unipolaire n'a pas pour vocation de remplacer le cyclage bipolaire notamment à cause de sa mauvaise endurant, fenêtre et stabilité. Il a simplement été mis en avant dans le but de comprendre l'impact du dégagement thermique pendant le SET.

3.2.2 Etude du RESET

Comme brièvement énoncé précédemment, le RESET est fortement lié à la température. La température joue un double rôle sur l'opération de RESET en modifiant la tension nécessaire à l'effacement ainsi que la valeur de la résistance après effacement. Pour comprendre l'implication de la température dans le RESET, deux échantillons ont été comparés : cellules nano – Trench CuTeGe/Al_2O_3/TiN et CuTeGe/Al_2O_3/WSi. Ces échantillons diffèrent au niveau de leur électrode inférieure qui possèdent deux conductivités thermiques très différentes (κ_{TiN} = 30 W.m^{-1}.K^{-1} ; κ_{WSi} = 170 W.m^{-1}.K^{-1}). La Figure 17 représente l'impact du changement d'électrode inférieure sur les caractéristiques du RESET. Le passage d'une électrode TiN à WSi induit une augmentation de la résistance de l'état effacé mais également une augmentation de la tension nécessaire à l'effacement.

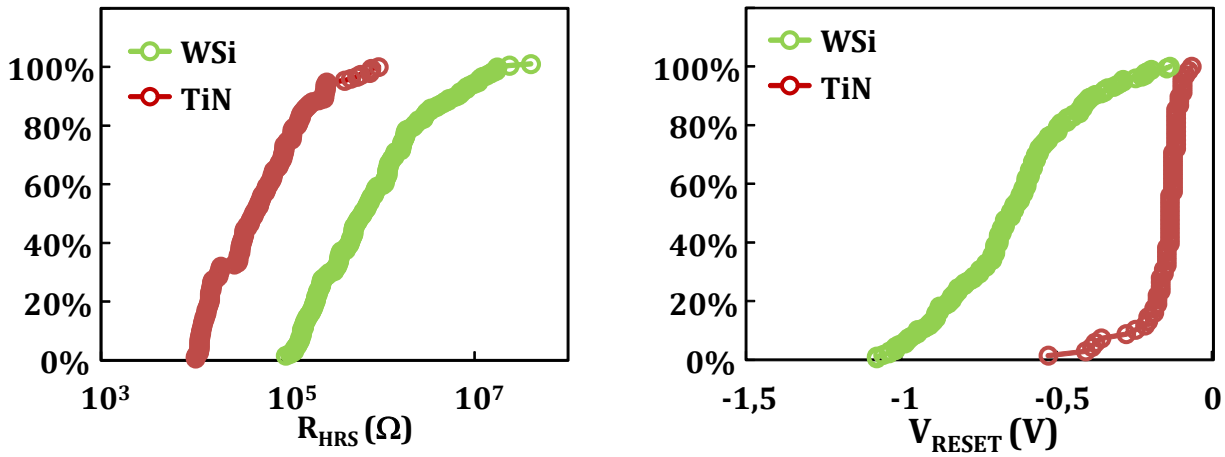

Figure 17. Impact de l'électrode inférieure sur l'opération d'effacement et la résistance post effacement

Afin de comprendre l'impact de l'électrode inférieure sur la tension d'effacement, une étude théorique a été menée grâce au logiciel de résolution par élément finis COMSOL multiphysics. Cette étude thermique calcule l'évolution de la température dans les deux échantillons en fonction de la tension appliquée. Ces résultats, regroupés Figure 18, montrent une nette différence entre les deux échantillons avec une augmentation de la température plus rapide pour l'échantillon à base de TiN. Cet accroissement de la température est dû à la mauvaise conduction thermique du TiN qui dégrade la thermalisation de l'échantillon. La température plus élevée à tension identique pour l'échantillon à base de TiN induit accroissement plus rapide de l'énergie disponible au RESET. L'atteinte de l'énergie (thermique et électrique) nécessaire à l'effacement se fait donc plus

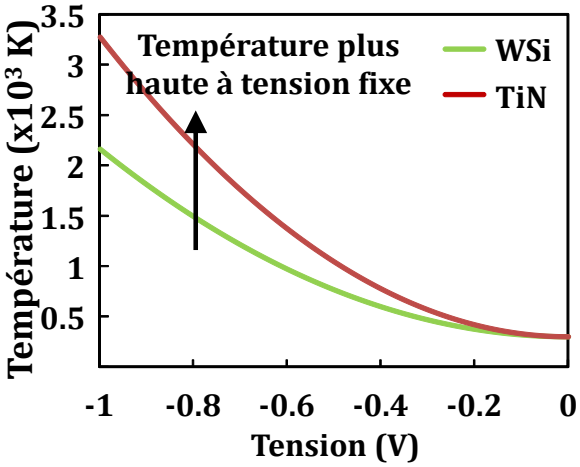

Figure 18. Evolution de la température dans l'échantillon en fonction de l'électrode inférieure

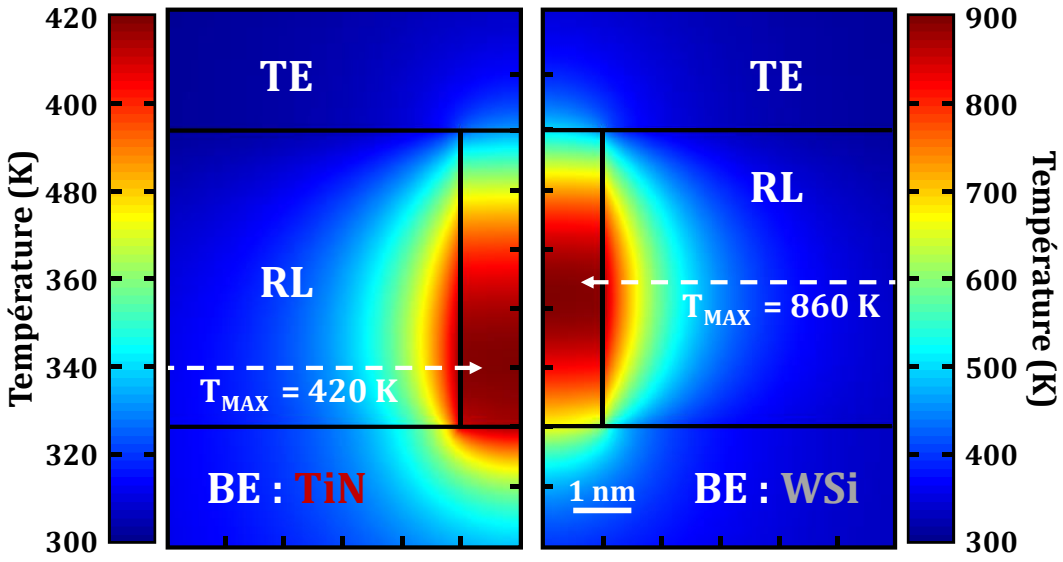

Figure 19. Répartition de la température à V_{RESET} dans la cellule CBRAM pour les deux échantillons avec des électrodes inférieures différentes

rapidement pour l'échantillon à base de TiN, expliquant la tension d'effacement plus faible que pour l'échantillon à base de WSi.

En se penchant cette ensuite sur la répartition de la température et non plus sur sa valeur nominale Figure 19, on voit que la position du point de plus haute température est décalée avec la conduction thermique de l'électrode inférieure. Pour l'échantillon à base de TiN et donc à faible conduction thermique, le point chaud est proche de l'électrode inerte alors que pour l'échantillon à base de WSi, le point chaud est plus haut dans l'isolant. Or, ce point chaud correspond à la zone où l'énergie est maximum pendant l'effacement et donc à la zone où l'effacement a la plus forte probabilité de démarrer. Ainsi, durant l'effacement, le filament va débuter sa dissolution au niveau du point chaud et par effet du champ électrique, le résidu de filament se trouvant entre le point chaud et l'électrode inerte va se dissoudre également. La Figure 20 schématise l'étape d'effacement pour les deux échantillons. Pour l'échantillon à base de TiN, l'effacement intervient plus tôt mais avec un point chaud plus bas et une zone de dissolution petite. En revanche, pour l'échantillon à base de WSi, l'effacement se fait plus tard mais de par la position du point chaud plus haute, la zone effacée est plus grande. Cette zone effacée correspond à une région de l'isolant dépourvue d'atomes conducteur, plus sa dimension est étendue plus sa résistance électrique est forte. Ainsi, la plus grande zone effacée de l'échantillon à base de WSi explique la plus forte résistance électrique de l'état effacé. La bonne conduction thermique de l'électrode inférieure a donc un rôle double, elle améliore la résistance post effacement en modifiant la zone de plus forte énergie mais elle retarde

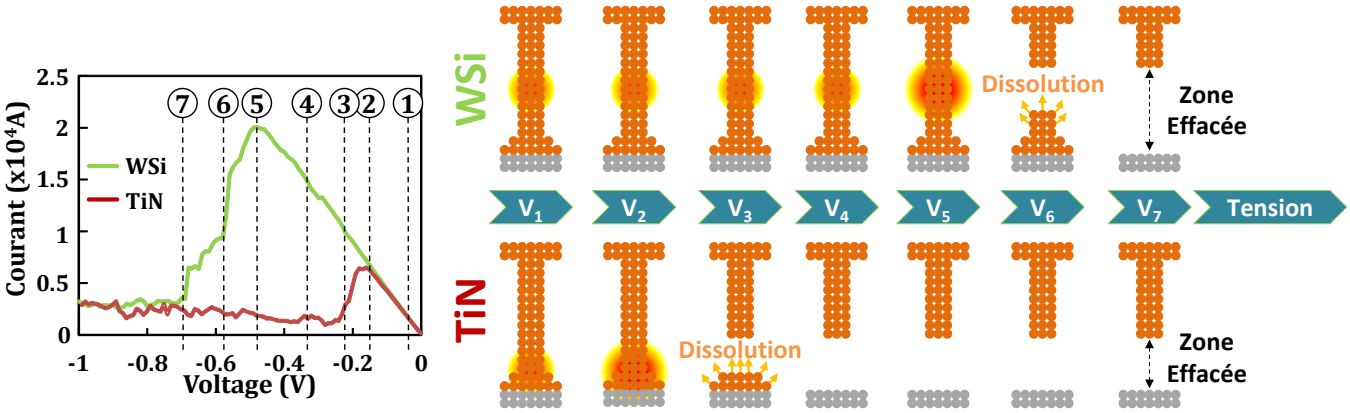

Figure 20. Représentation schématique de l'opération d'effacement pour les deux échantillons et les positions correspondantes sur la courbe I(V)

également l'effacement en augmentant les déperditions thermiques. Les performances d'effacement sont donc touchées par un compromis entre vitesse et efficacité.

3.2.3 Optimisations technologiques

Les performances des dispositifs CBRAM ont été optimisées en se fondant sur les observations et la compréhension des mécanismes de commutation précédemment exposés. Ainsi, en jouant sur les paramètres physiques des matériaux constituant les cellules tels que la densité, la permittivité électrique, la conductivité thermique… il a été possible d'obtenir des cellules aux

Tableau 1.Caractéristiques électrique d'une sélection d'échantillons testés R_{HRS} Max correspond à la plus haute valeur atteignable pour la résistance de l'état effacé en appliquant une rampe de tension jusqu'à $V_{RESET\ Stop}$ Max

Empilement mémoire (TE/RL/BE)	Epaisseur d'isolant	QS $V_{Forming}$	PS $V_{forming}$ (t_{Pulse} = 10 µs)	Pente du forming	R_{HRS} Max	$V_{RESET\ Stop}$ Max
Cu/Al_2O_3/WSi	3.5 nm (ALD)	3.1 V	4.5 V	3.5 Decades / V	10^6 Ω	-1.5 V
	5 nm (ALD)	4.4 V	6.5 V	2.0 Decades / V	10^6 Ω	-1.5 V
$CuTe_X$/Al_2O_3/WSi	3.5 nm (ALD)	3 V	4.75 V	3.5 Decades / V	10^6 Ω	-1.5 V
	5 nm (ALD)	4.5 V	7 V	2.0 Decades / V	10^6 Ω	-1.5 V
Cu/Al_2O_3/TiN	3.5 nm (ALD)	2.6 V	3.75 V	3.5 Decades / V	$5x10^4$ Ω	-1 V
	5 nm (ALD)	3.8 V	4.75 V	2.0 Decades / V	$5x10^4$ Ω	-1 V
$CuTe_X$/Al_2O_3/TiN	3.5 nm (ALD)	2.8 V	4 V	3.5 Decades / V	$5x10^4$ Ω	-1 V
	5 nm (ALD)	4.3 V	6.25 V	2.0 Decades / V	$5x10^4$ Ω	-1 V
$CuTe_X$/HfO_2/Ta	5.5 nm (ALD)	2.2 V	2.75 V	8.0 Decades / V	$5x10^5$ Ω	-1 V
$CuTe_X$/MO_x/Ta	5 nm (PVD)	2 V	2.4 V	8.0 Decades / V	10^4 Ω	-1 V
$CuTe_X$/HfO_2 + MO_x/Ta	5.5 + 1 nm	2 V	2.4 V	8.0 Decades / V	$5x10^5$ Ω	-1 V

performances de commutations améliorées. Le tableau 1 regroupe une sélection des différentes cellules CBRAM testées.

4. Etude de l'endurance et de la fiabilité

Dans la continuité de la compréhension des mécanismes de commutation, cette partie s'attache à exposer et comprendre une des limitations actuelle de la technologie : la variabilité et la fiabilité des CBRAM. Cette variabilité s'exprime doublement, d'une cellule à l'autre dans un premier temps mais également lors d'un cycle à l'autre. La compréhension de la variabilité et des mécanismes de défaillance repose sur la capacité du modèle Monte Carlo cinétique à proposer une résolution statistique fondée sur une succession de tirages aléatoires. Ainsi, chaque commutation simulée est unique, au même titre que la commutation de cellules réelles. Cette étude théorique s'appuie également sur une étude électrique de dispositifs organisés en matrices de 64 cellules afin de faciliter l'étude statistique. Ces structures correspondent à l'empilement de matériaux suivant : $CuTe_X/Al_2O_3/TaN$.

4.1 Variabilité de l'état de basse résistance

La variabilité de l'état de basse résistance est mise en avant Figure 21. On y voit la distribution de résistance de l'état écrit obtenue après écriture de deux distributions d'état effacés. Une écriture à partir d'un état effacée standard en rouge mène à une distribution identique à celle obtenue après une écriture à partir d'un état effacé faiblement dispersé en bleu. Cette quasi-

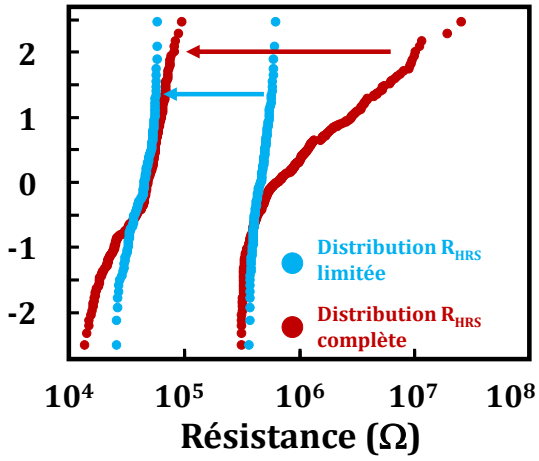

Figure 21. Distribution expérimentale de R_{LRS} après écriture depuis une distribution HRS standard (Rouge) ou une distribution restreinte (Bleu)

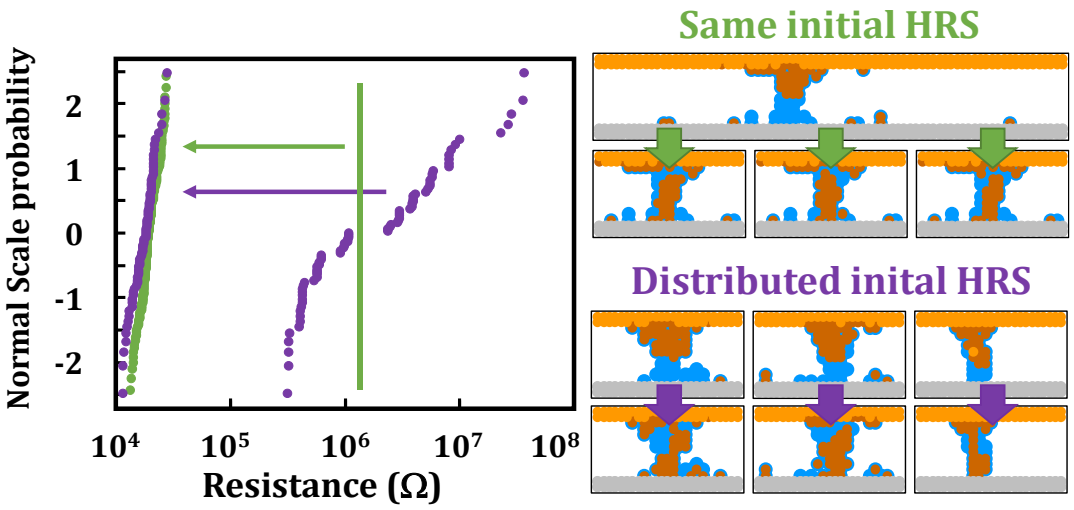

Figure 22. Distribution simulée de R_{LRS} après écriture depuis une distribution HRS standard (Violet) ou un filament unique (Vert)

superposition des états écrits montre l'existence d'une variabilité intrinsèque de l'écriture des CBRAM puisque l'état initial ne semble pas avoir d'influence directe sur l'état post écriture. Cette étude a été approfondie en utilisant le modèle Monte Carlo. La Figure 22 représente une étude similaire mais simulée. Les distributions de départ correspondent ici à une distribution HRS standard en violet et à une distribution à dispersion nulle vert (filament résiduel unique pour toutes les étapes de SET). Cette figure montre que la dispersion finale après écriture est quasi-identique peu importe la dispersion initiale et confirme donc l'hypothèse de variabilité intrinsèque de l'opération d'écriture. Cette variabilité intrinsèque peut en revanche être reliée au courant limite pendant l'écriture. En effet, comme montré Figure 23, la dispersion du LRS varie en fonction du courant de programmation. Plus fort est ce courant, plus la variabilité et donc la dispersion sont réduites. Cette figure montre en outre la bonne corrélation entre la modélisation et la caractérisation électrique, donnant ainsi plus de poids aux observations. Afin de comprendre l'impact du courant de programmation sur la dispersion de l'état écrit, il faut se pencher plus en détail sur la stabilisation du filament se produisant pendant l'étape d'écriture. Cette étape, énoncée plus haut est schématisée en détail Figure 24. On y voit que l'énergie maximum (tension et température) est atteinte en même temps que le courant limite de programmation. L'énergie disponible est responsable de l'introduction d'ions supplémentaires et de leur diffusion. L'augmentation du nombre d'ions induit une augmentation du diamètre du filament et donc moins de chaleur dégagée et une tension vue

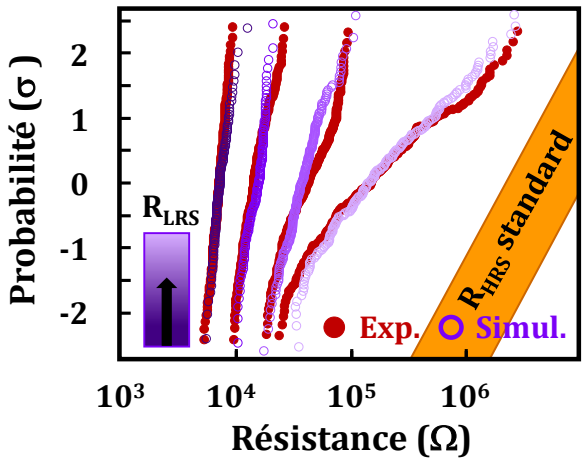

Figure 23. Dispersion simulée et mesurée de l'état écrit en fonction du courant limite de programmation

par la cellule réduite également. L'insertion d'ions induite par l'énergie mène donc à la réduction de l'énergie et tant qu'elle sera suffisante, des ions seront introduits et continueront à la réduire. Ainsi plus la quantité d'énergie est importante et plus la stabilisation du filament sera longue et complète. La Figure 25 (a), montre la différence de dispersion (simulée) de résistances avant l'étape de stabilisation et en fin de stabilisation. On y voit une dispersion réduite et une valeur moyenne plus faible. L'énergie responsable de la stabilisation est directement liée au courant limite de programmation (Figure 25 (b)), un fort courant entrainant un fort dégagement thermique et donc une grande quantité d'énergie à dissiper. Figure 25 (b) montre également que la dispersion de l'énergie disponible au système évolue et se réduit à mesure que le courant de programmation augmente. Cette modification de la dispersion est liée a là modification du nombre d'atomes intervenant dans la formation du filament lorsque le courant est modifié comme montré

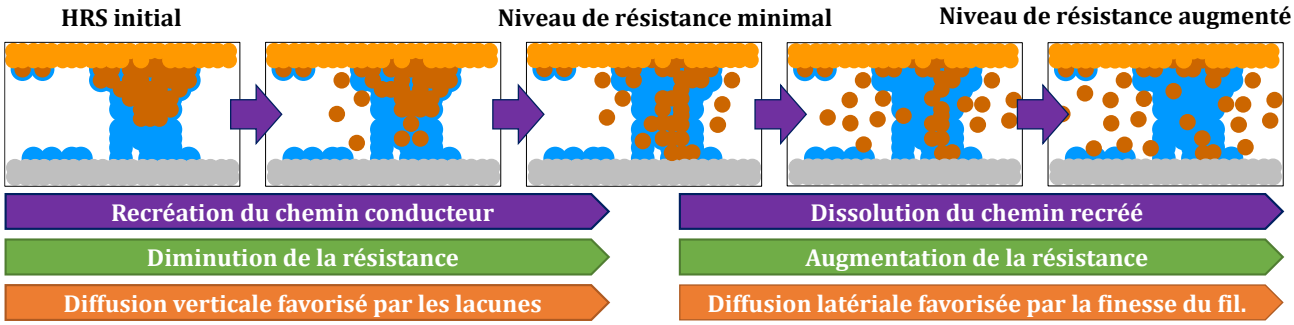

Figure 24. Représentation schématique des différents stades de formation et de stabilisation du filament pendant l'opération d'écriture.

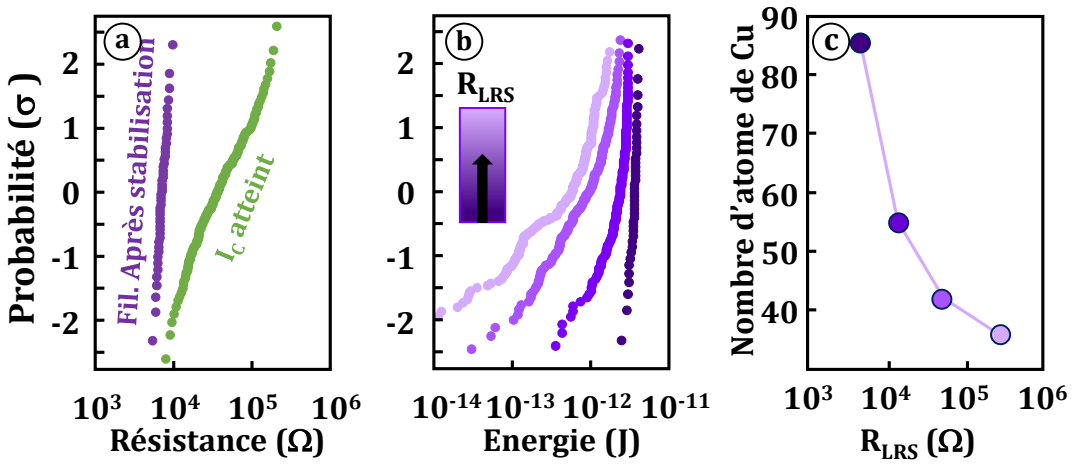

Figure 25. (a) Modification de la résistance pendant l'état de stabilisation (b) Energie disponible pendant l'écriture en fonction du courant d'écriture (c) Nombre d'atomes dans le filament en fonction du courant d'écriture. Toutes ces valeurs sont extraites de la simulation Monte Carlo

Figure 25 (c). Un faible courant ne nécessite qu'un faible nombre d'atomes pour être atteint. Dans ce cas de figure, le déplacement de seul atome à un fort impact sur le courant et l'énergie du système, en comparaison au cas où le filament est composé de nombreux atomes. Cette différence d'impact des mouvements atomiques explique la forte dispersion de l'énergie à faible courant. Cette réduction de l'énergie de stabilisation ainsi que l'augmentation de sa dispersion à mesure que le courant diminue induit une stabilisation plus variable et globalement moins poussée du filament à faible courant. Ainsi, le courant de programmation peut être relié à l'augmentation de la dispersion de la résistance LRS à travers le degré de stabilisation, l'énergie disponible et nombre d'atomes induits

4.2 Variabilité de l'état de haute résistance

Similairement à l'étude précédente, la variabilité de l'état effacé a été étudiée afin de déterminer le caractère intrinsèque ou cycle à cycle de cette variabilité. Dans un premier temps, la distribution de l'état effacé a été comparée à partir de deux distributions écrites différentes. On peut voir Figure 26 que peu importe la distribution initiale, l'état effacé est dispersé. En revanche, en partant d'une distribution à dispersion nulle de l'état écrit, la dispersion de l'état effacé s'en retrouve réduite. Cette première observation indique donc la coexistence d'une variabilité intrinsèque mais également d'une variabilité cycle à cycle mise en avant par la différence de distribution des deux courbes HRS. Afin d'approfondir l'étude de la variabilité cycle à cycle, les

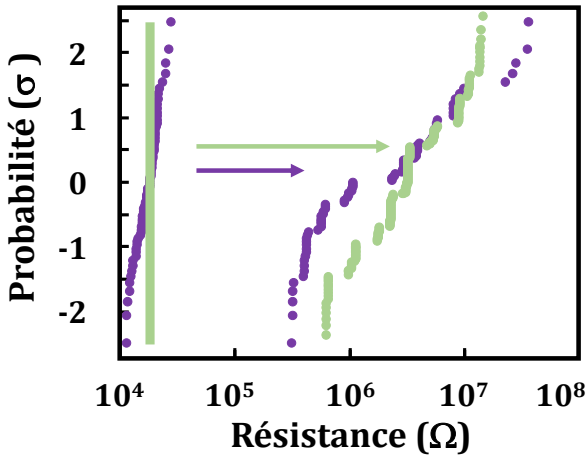

Figure 26. Distribution R_{LHS} simulée après effacement d'un filament unique correspondant au filament moyen (Vert) ou d'une distribution standard d'état écrit (Violet)

distributions des états effacés obtenus après effacement de trois états écrits à différents niveaux de courant sont comparées Figure 27. Les distributions des trois états effacés sont similaires avec uniquement un décalage de la valeur moyenne. Cette valeur moyenne de R_{HRS} augmente avec R_{LRS}, signe d'une variabilité cycle à cycle. Enfin, l'origine de cette variabilité cycle à cycle a été reliée à la morphologie du filament. La distribution de l'état effacé standard a été comparée à celle obtenues après effacement de deux états écrits différents : un filament fin et un filament large. On voit

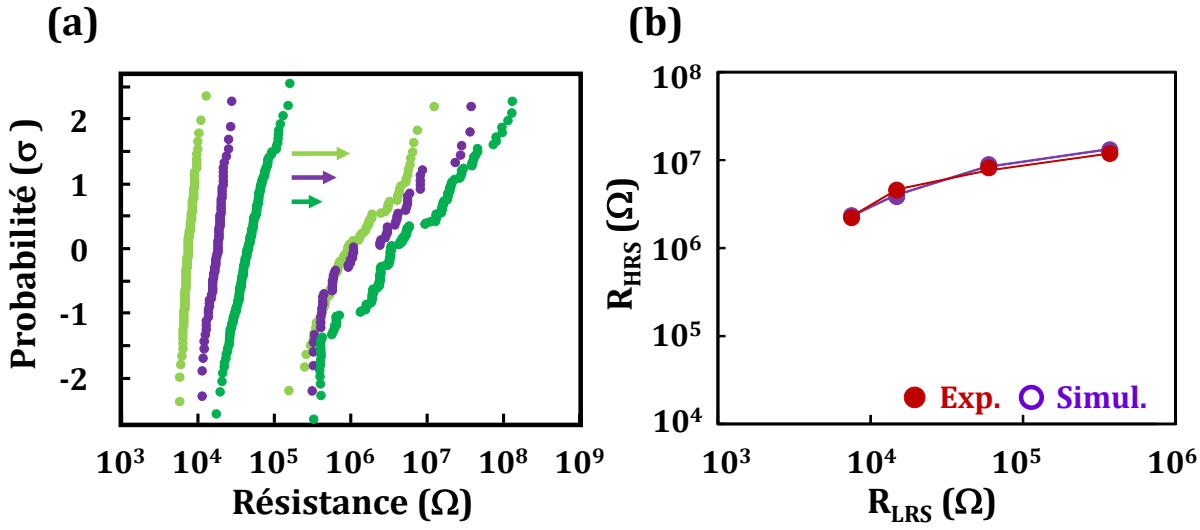

Figure 27. (a) Impact de la distribution initiale LRS sur la distribution HRS après effacement. (b) relation entre la valeur moyenne de résistance de l'état écrit sur la résistance moyenne de l'état effacé

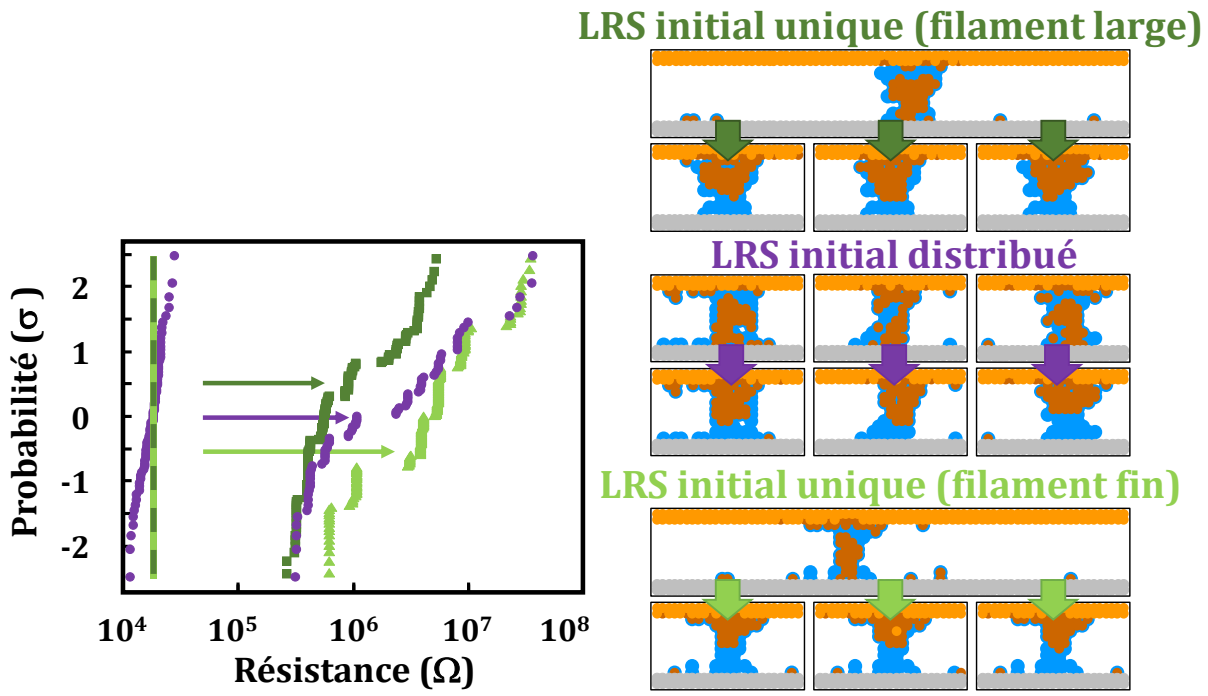

Figure 28. Distribution R_{LHS} simulée après écriture depuis deux LRS fixé (Vert: même R_{LRS} mais différentes morphologies de filament) et un LRS distribué (Violet)

Figure 28 qu'en accord avec les observations précédentes, les distributions des états effacés obtenus à partir des filaments uniques ont des dispersions réduites. De plus la valeur moyenne de ces distributions est liée à l'épaisseur du filament. Plus le filament est fin, plus la résistance après effacement est faible. Ceci peut être expliqué par la facilité à dissoudre un filament fin composé de peu d'atomes comparé à un filament large.

La dispersion intrinsèque est quant à elle liée au phénomène d'effacement lui-même. Comme exposé plus tôt, la dissolution du filament pendant le RESET démarre dans une zone favorable énergétiquement. La dissolution du filament peut statistiquement démarrer depuis n'importe quel atome dans cette zone et induire une progression de l'effacement et un état final foncièrement différent d'une dissolution qui aurait commencé à partir d'un autre atome.

4.3 Fiabilité et mécanismes de dégradation de l'endurance

L'endurance d'une technologie de stockage correspond au nombre de cycles d'écriture et d'effacement que la technologie peut endurer avant son disfonctionnement. L'endurance de la technologie CBRAM est une de ces limitations actuelles et les mécanismes aboutissant à sa dégradation sont encore méconnus. A l'aide du modèle et de la caractérisation électrique des

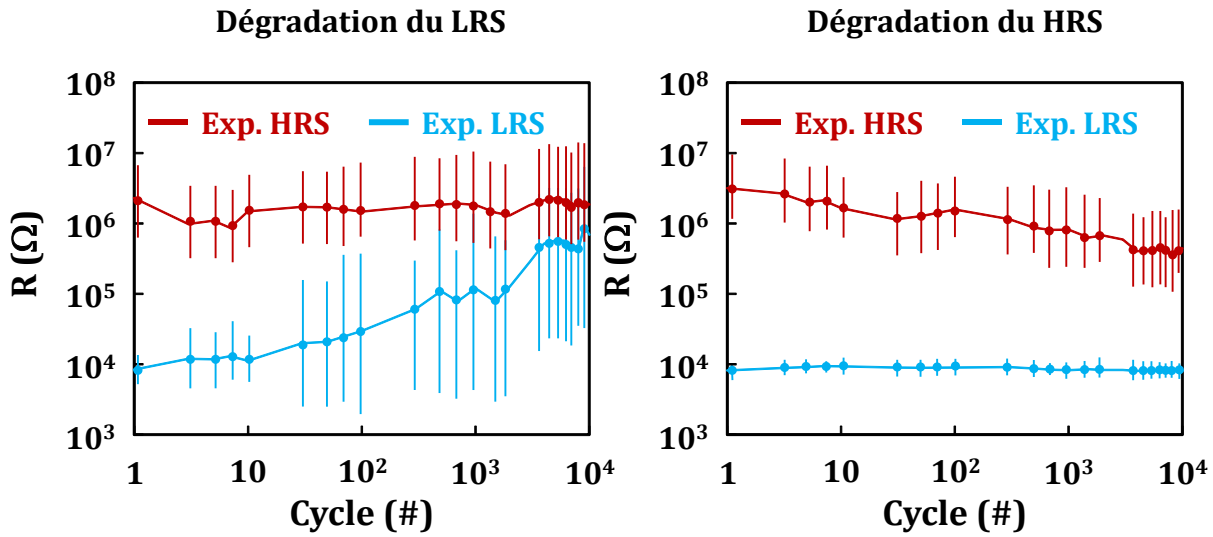

Figure 29. Dispersion de résistance et valeur moyenne pour deux matrices de 64 bit montrant la dégradation de l'état LRS (gauche) et HRS (droite)

matrices de cellules précédemment étudiées, cette partie s'attache à comprendre deux types de dégradation. Ces deux types de dégradation sont représentés Figure 29. On peut y observer la dégradation alternative d'un état de résistance vers l'état opposé à mesure que le nombre de cycles augmente. Bien que ces deux types de dégradation semblent globalement similaires, ils diffèrent fondamentalement comme le montre la Figure 30. En effet, la dégradation de l'état écrit correspond à une augmentation du nombre de cellules impossibles à écrire à mesure que le cyclage avance. En revanche, la dégradation de l'état effacée repose sur un décalage progressif du niveau de résistance.

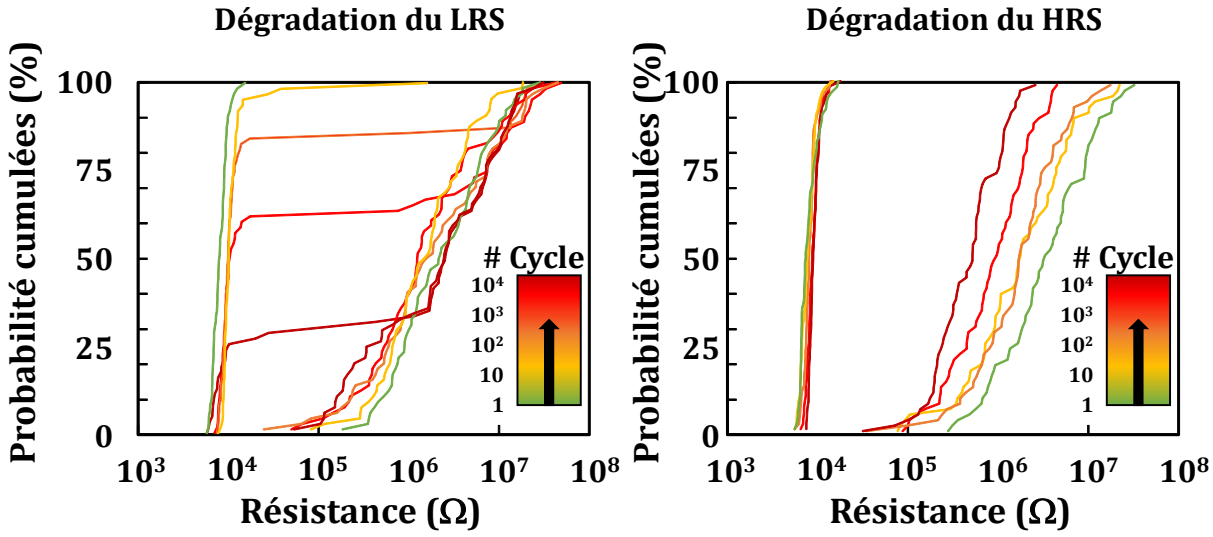

Figure 30. Probabilités cumulées des résistances LRS et HRS pour les deux mécanismes de dégradation

La dégradation de l'état écrit est observée pour des conditions d'écriture faibles (faible tension et temps court). A mesure que le cyclage avance, la hauteur du filament résiduel diminue et la distance à combler augmente. Cette diminution progressive est due au manque d'énergie pendant le SET qui limite la reformation du filament de plus en plus dissout par les effacements successifs. Cette augmentation progressive de la zone effacée en visible Figure 29 sur laquelle on peut voir la légère augmentation continue de la résistance de l'état effacé à partir du dixième cycle. L'augmentation progressive de cette zone effacée a pour conséquence la réduction du nombre de chemins possibles pour la recréation du filament conducteur. A mesure que ce nombre de chemins diminue, la probabilité d'arriver à former le filament diminue également, menant ainsi à la dégradation aléatoire de l'état écrit. Cette dégradation aléatoire est en accord avec la variabilité intrinsèque touchant l'état de faible résistance. En effet, aucune variation de résistance de l'état écrit n'est visible avant l'impossibilité stochastique à écrire la cellule. Ce type de dégradation peut être corrigé par l'application d'une SET plus agressif lors de la perte de l'état écrit.

La dégradation de l'état effacé est observée pour des conditions de programmation forte (tension forte et temps long). A mesure que le cyclage avance, la largeur du filament augmente due à une forte sur-écriture et insertion continue d'atomes conducteurs dans l'isolant durant le SET. De plus, le fort effacement nécessaire à la dissolution de ce large filament induit également une dégradation progressive de l'isolant avec la création ou l'insertion de lacunes d'oxygène. Cette augmentation du nombre d'atomes conducteurs et de lacune d'oxygène a pour conséquence une diminution progressive de la résistance de l'état effacé. Ce mécanisme de dégradation est en accord avec la variabilité cycles à cycles propre à l'effacement précédemment exposée. En effet, l'augmentation progressive de la largeur du filament et du nombre d'atomes rend plus difficile son effacement et induit une diminution de la résistance. Contrairement à la perte de l'état écrit, il est impossible de corriger cette perte de l'état effacée du fait de la dégradation irréversible de l'isolant.

Afin d'améliorer la fiabilité et l'endurance de la technologie CBRAM il est donc important d'appliquer des conditions de programmation optimisées. Ces conditions visent à limiter au maximum l'énergie apportée à la cellule durant le cyclage. En effet, une cellule CBRAM semble être capable d'endurer une certaine quantité d'énergie totale (électrique et thermique) avant d'être dégradée. Il est donc primordial de limiter cette énergie en utilisant par exemple des routines de programmation dite intelligentes. Ainsi la programmation intelligente du SET correspond à une succession d'opérations de SET à énergie croissante (temps ou tension) entrecoupées d'opérations

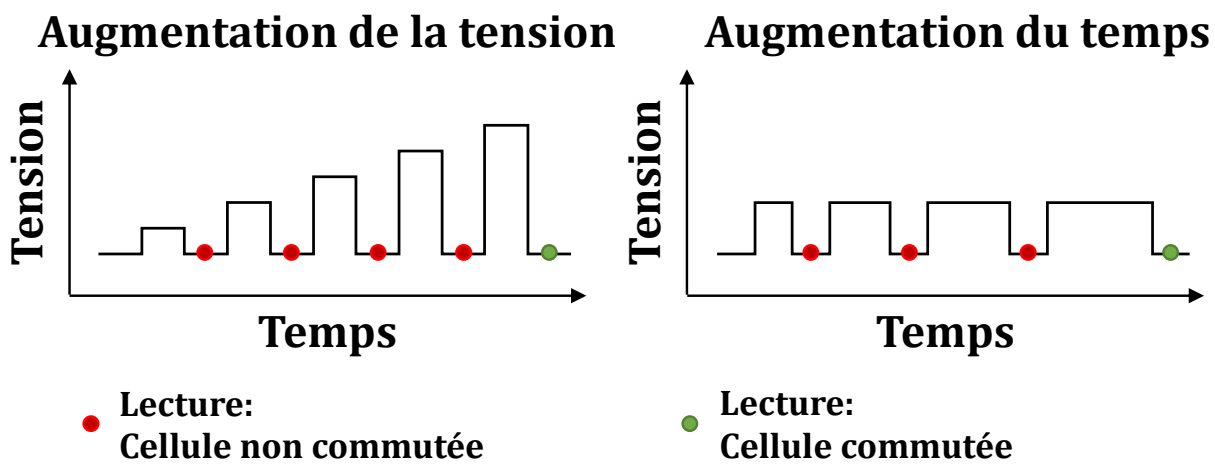

Figure 31. Deux types de routine de programmation intelligente visant à limiter l'énergie endurée par la cellule

de lecture. Des lors que la cellule est écrite la routine cesse, de sorte à ce que l'écriture se fasse au niveau d'énergie le plus bas possible. Le protocole d'effacement suit le même raisonnement avec l'arret des RESET successif des lors que la résistance cible est atteinte. La Figure 31 schématise deux types de programmations intelligentes.

5. Etude de la rétention de données et comportement à haute température

La rétention de données est un critère primordial dans l'utilisation d'une technologie mémoire. Elle correspond à la capacité d'une mémoire à conserver l'information dans le temps. La durée de rétention visée étant généralement de plusieurs années, son étude doit donc être accélérée et deux types d'accélération sont communément utilisés. Il est ainsi possible d'accélérer l'étude de rétention en tension [Longnos 1, Vianello 1, Hsieh 1] en appliquant une tension faible et en étudiant la variation de la résistance au court du temps. La deuxième méthode d'accélération de l'étude est une accélération en température. Ce type d'accélération que nous développerons ici, repose sur des séjours prolongés à haute température et une étude de la variation de la résistance en fonction du temps passé à haute température. La Figure 32 représente une étude standard de la rétention de donné de l'état écrit ainsi que l'impact de la température, montrant la perte rapide de l'information lorsque la température augmente. Les résultats électrique détaillés dans cette partie reposent sur des échantillons nano-Trench $CuTe_X/Al_2O_3/TiN$ et seront analysés grâce à la dernière brique du modèle Monte Carlo capable de simuler la rétention de données.

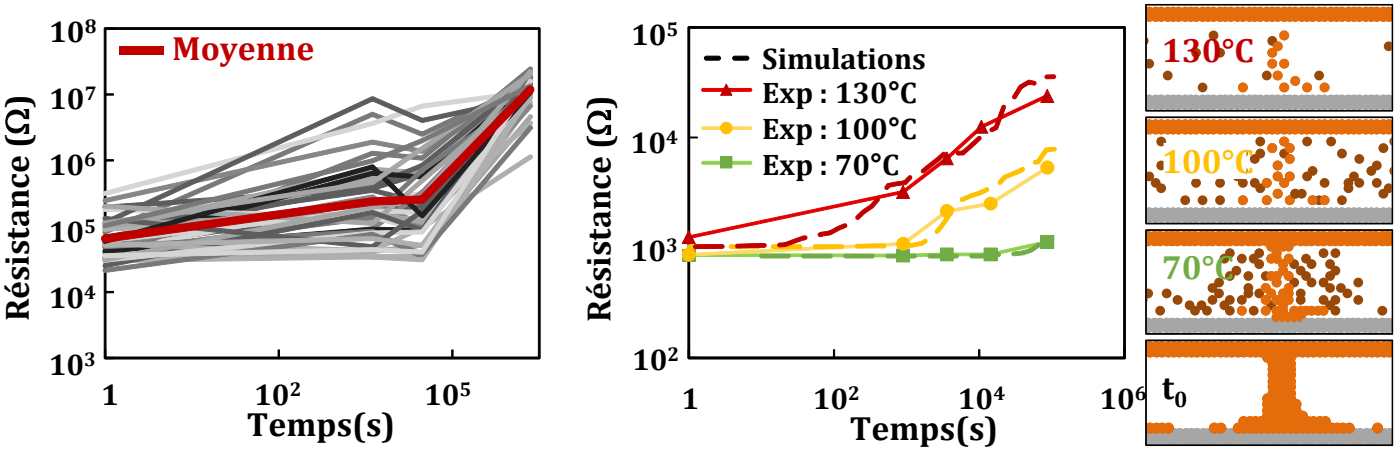

Figure 32. Rétention mesurée de l'état écrit à haute température (200°C) et simulation de l'impact de la température sur le comportement en rétention

5.1 Mécanismes de dégradation de la rétention de données

Le stockage de l'information de la technologie CBRAM repose sur le maintien d'un filament complet dans l'isolant pour l'état écrit ou d'une zone sans filament pour l'état effacé. Le maintien de ces deux configurations de l'isolant assure la rétention de la donnée. Concernant l'état écrit, la perte de l'information dans le temps est liée à la dissolution progressive et spontanée du filament dans l'isolant. Cette dissolution explique l'augmentation de la résistance au court du temps visible Figure 32 et peut être divisée en deux phases. Dans un premier temps, les atomes composant le filament se détachent de celui-ci et migrent dans l'isolant où la concentration en atomes conducteur est bien plus faible, en accord avec les principes de Fick. Cette diminution du nombre d'atomes du filament entraine une réduction progressive de son rayon et une augmentation de sa résistance électrique. Cette première phase de rétention s'achève lorsque le cœur du filament est rompu et qu'il n'existe plus de chemin conducteur continu entre les deux électrodes. L'augmentation de la résistance de cette première phase est donc due à la diminution progressive du rayon du filament conducteur. Dans une seconde phase, les atomes composant initialement le filament se répartissent uniformément dans l'isolant. La résistance initiale de cette phase est bien plus haute mais son augmentation est également plus lente. Cette dernière est due à l'augmentation de la distance moyenne entre les atomes participant à la conduction tunnel assistée par pièges.

La dégradation de la rétention de l'état effacé est plus complexe. Elle s'apparente à une perte de l'état effacé avec un décalage de la résistance haute vers une valeur plus faible voir même l'atteinte

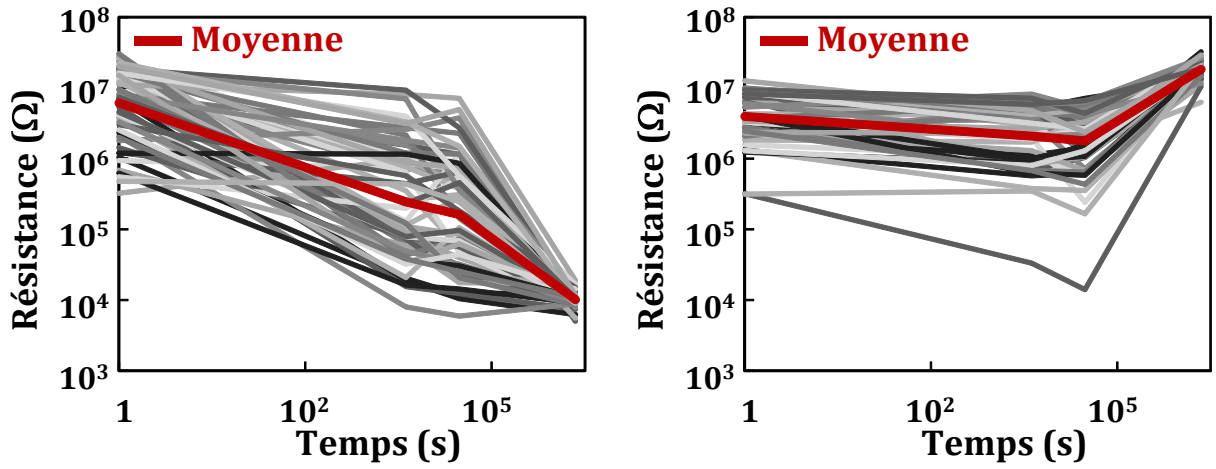

Figure 33. Comportement en rétention de l'état effacé généralement présenté (gauche) et comportement complet (droite) si la température et le temps sont suffisant pour visualiser la double pente. Ces deux résultats ont été obtenus à 200°C sur des échantillons différents

d'un état pseudo écrit. Ce comportement de l'état effacé au court de temps est généralement connu et représenté comme sur la Figure 33 (gauche). Cependant, si la durée de la rétention et la température sont suffisantes, il est possible d'observer une double pente. La première pente correspond donc à la diminution progressive de la résistance de l'état effacé. Cette diminution est liée à la recréation du chemin conducteur à partir des atomes du filament résiduel. Par effet thermique, les atomes migrent dans l'isolant et viennent recréer un chemin conducteur entre les deux électrodes, menant ainsi à une forte diminution de la résistance. Dans un deuxième temps, lorsque le filament est recrée, les atomes le constituant vont continuer leur migration dans le reste de l'isolant et mener par un mécanisme similaire à la rétention de l'état écrit à une augmentation de la résistance. Cette double pente de la rétention de l'état effacé est donc la succession d'une étape de recréation du chemin conducteur suivit de sa dissolution comme schématisé Figure 34. Il

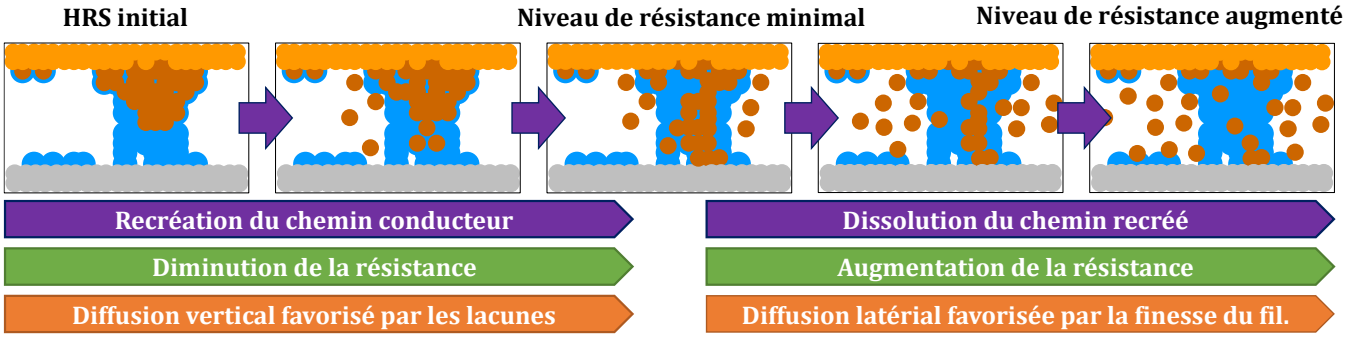

Figure 34. Représentation schématique de la recréation du chemin conducteur puis de sa dissolution expliquant la double pente de la rétention de l'état effacé

est également important de noter que cette double pente est souvent apparue comme un artefact de mesure. En effet, de par l'échelle des temps logarithmique les mesures sont très espacées dans le temps et peuvent manquer de précision dans le discernement de ces deux phases. Il est cependant primordial de tenir compte de ce comportement puisque la simple considération de l'état de résistance en fin d'étude de rétention pourrait occulter une défaillance en court d'étude et ne pas rendre compte de la réelle capacité de rétention.

5.2 Optimisation de la rétention de données

Comme décrit précédemment, la dégradation de la rétention est liée à la dissolution du filament où à sa reformation. Les conditions de programmation ont un fort impact sur les capacités de rétention. En effet, comme le montre la Figure 35, la rétention de l'état écrit peut être directement reliée au niveau d'écriture. Plus le courant d'écriture et fort et donc plus la résistance initiale est faible, meilleure est la rétention de données. Ceci se traduit par une réduction de l'accroissement de la résistance par an à mesure que la résistance initiale diminue. Cette observation peut être expliquée grâce à la compréhension du mécanisme de dégradation de la rétention. En effet, comme exposé précédemment, la perte de l'état écrit repose sur la dissolution du filament. Or, plus la résistance initiale est faible plus large est le filament. Cette largeur accrue du filament lui permet de rester stable plus longtemps et donc de maintenant un niveau de résistance faible. En revanche, si le filament est trop fin et donc la résistance initiale trop forte, il plus

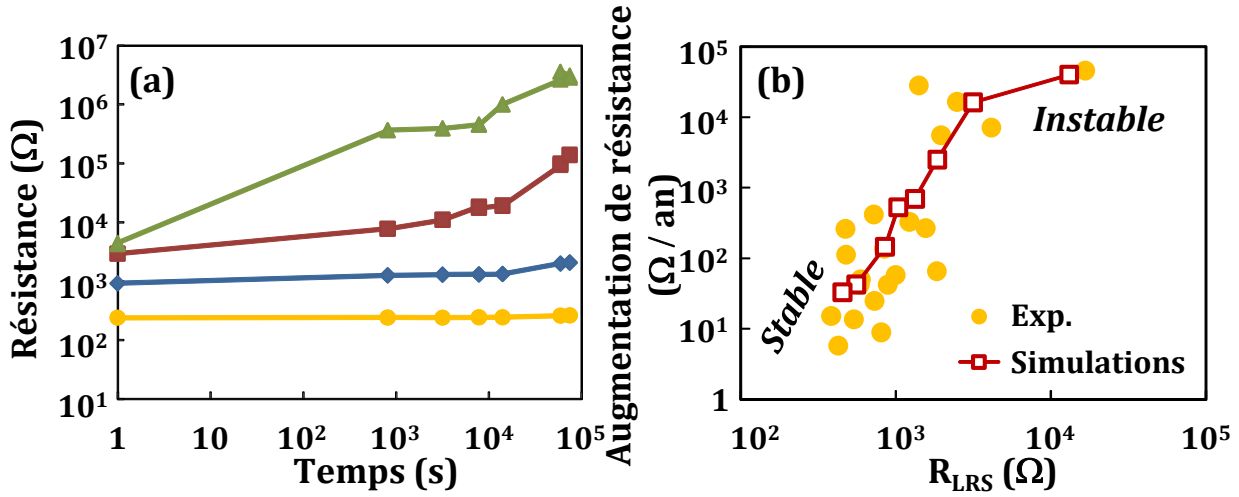

Figure 35. (a) Dégradation du LRS au cours du temps en fonction du niveau de résistance initial à 100°C (b) accroissement mesuré et simulé de la résistance par an en fonction de la résistance LRS initiale.

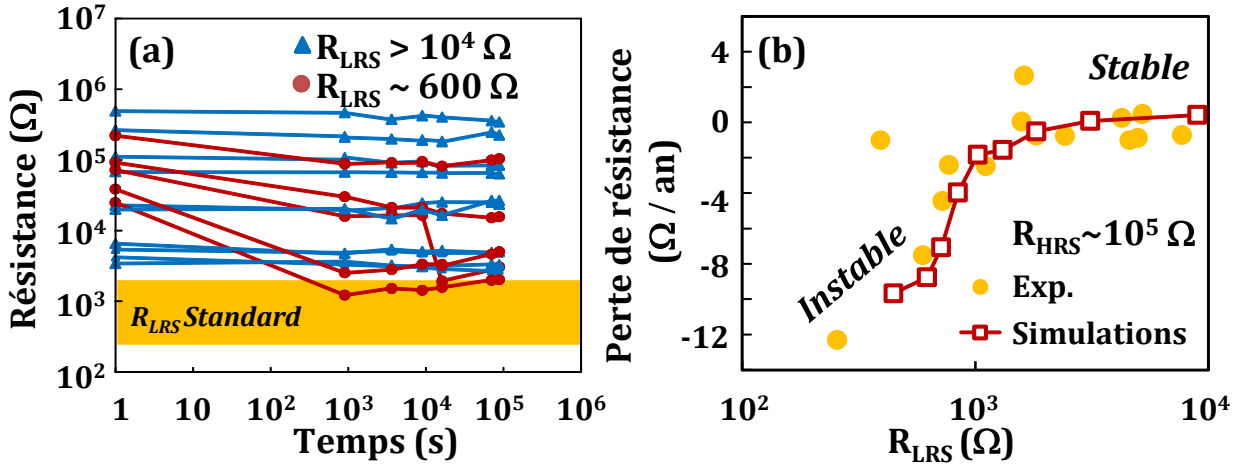

Figure 36. (a) Mesures expérimentales de la rétention du HRS montrant deux comportements différents en fonction du R_{LRS} antérieur. (b) Perte de résistance de l'état effacé en fonction de la résistance de l'état écrit antérieur.

facilement rompu. La morphologie du filament est donc encore une fois directement liée à une caractéristique macroscopique de la cellule.

L'impact de la résistance initiale dans la rétention de l'état effacée n'est cette fois-ci pas aussi direct que pour l'état écrit. En effet, comme le montre la Figure 36 (a), les comportements stables et instables ne sont pas immédiatement discernables à partir de leur résistance initiale. Cependant, il est possible de discerner les deux comportements à partir de la résistance de l'état écrit précédent l'effacement. Ainsi une cellule écrite fortement (faible résistance) engendre potentiellement une rétention de l'état effacé dégradée en comparaison à une cellule écrite faiblement. Cette observation est également visible Figure 36 (b), montrant qu'à parité d'effacement (R_{HRS} fixe) la perte de résistance de l'état effacé est directement reliée à la valeur de la résistance de l'état écrit antérieur. Dans un deuxième temps, en fixant cette fois-ci la valeur de la résistance de l'état écrit antérieur, on peut voir Figure 37 qu'il est possible de regagner en stabilité grâce à une augmentation de la résistance initiale de l'état effacé. Comme expliqué précédemment, la dégradation de la rétention de l'état effacé est liée à la reformation du filament conducteur. Cette reformation se fait à partir du filament résiduel et est ainsi directement liée à sa morphologie. En effet, plus le filament résiduel est grand et large, plus le réservoir d'atomes est important et la distance isolante à combler faible. Une telle morphologie de filament résiduel est donc défavorable à la rétention car elle facilite la reformation du filament. La largeur du filament résiduel peut être corrélée à la largeur du filament écrit initialement : plus le courant de programmation est fort, plus le filament résiduel est large. La

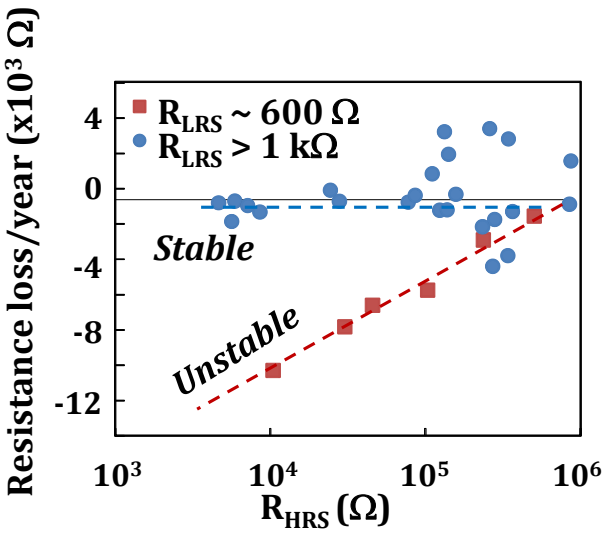

Figure 37. Perte de résistance par an de l'état effacé pour deux populations de résistances LRS et en fonction de l'effacement subit et de la résistance HRS initiale

hauteur du filament résiduel est quant à elle liée à l'effacement : plus l'effacement est fort, plus petit est le filament résiduel. Ainsi, en réduisant le courant de programmation, on réduit la largeur filament et on améliore le comportement en rétention de l'état effacé. Il est également possible, en partant d'un niveau d'écriture plus fort de stabiliser la rétention de l'état effacé en appliquant des conditions d'effacement plus forte comme le montre la Figure 37.

La capacité de la CBRAM à maintenir son état de résistance dans le temps se fait donc au prix d'un compromis entre l'état écrit et l'état effacé. La stabilité de l'état écrit requiert une forte écriture et un filament large qui a pour conséquence de dégrader la stabilité dans le temps de l'état effacé, à moins d'appliquer également des conditions d'effacement fortes. La Figure 38 regroupe les différentes configurations possibles avec notamment deux situations stables : des conditions de programmation contenues pour les SET et le RESET mais une fenêtre stable réduite ou des conditions de programmation agressives et une fenêtre stable plus importante.

Il est également possible d'optimiser technologiquement la rétention de données. En effet, les mécanismes de dégradation reposent sur la diffusion spontanée des atomes formant le filament et filament résiduel. En stabilisant ses atomes, et donc en rendant leur migration plus couteuse énergétiquement, il est théoriquement possible d'améliorer le comportement en rétention. Cette hypothèse a été vérifiée en utilisant le dopage antimoine de l'isolant d'une technologie CBRAM chalcogénures (en opposition avec la technologie oxyde). Cette optimisation a permis de stabiliser

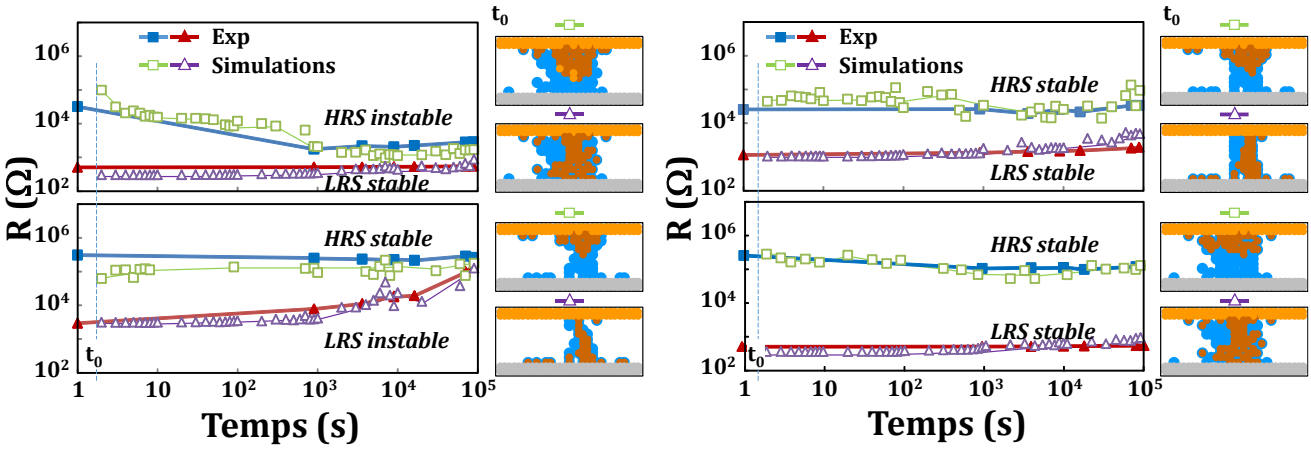

Figure 38. Rétention simulée et mesurée à 100°C du LRS et HRS pour des conditions de programmation non optimisée (gauche) et optimisées (droite). Les formes de filament initiales et finales sont représentées pour chaque condition. Condition optimisées : $V_{RESET} \approx$ - 0.5 V ; $V_{SET} \approx$ 0.5 V ; $E_{SET} \approx$ 5 pJ (haut) ; $V_{RESET} \approx$ -1 V ; $V_{SET} \approx$ 0.9 V ; $E_{SET} \approx$ 50 pJ (bas).

l'état écrit tout en réduisant les courants de programmation et donc d'offrir une double amélioration de la stabilité de l'état écrit.

6. Conclusion

La compréhension physique de la technologie CBRAM ne cesse de s'améliorer mais accuse encore en retard vis-à-vis de la très forte progression industrielle et au développement de circuits émergents. Le travail de recherche présenté dans ce manuscrit offre une première compréhension complète du fonctionnement de la technologie CBRAM. Cette théorie fait le pont entre les propriétés physiques des matériaux composant la CBRAM et son comportement durant chaque opération de son cycle de vie. De plus, le rôle crucial de la forme du filament sur de nombreux aspects du fonctionnement de la CBRAM a été mis en avant et des moyens de contrôler cette morphologie ont été proposés. Ainsi la largeur du filament induit une bonne rétention de l'état écrit mais dégrade celle de l'état effacé. Elle complique également l'étape d'effacement en réduisant la résistance atteignable mais améliore la distribution de l'état écrit…

A partir de la compréhension générale du fonctionnement de la CBRAM, des optimisations technologiques et électriques ont été développées avec notamment des programmations intelligentes, des dispositifs à forte conduction thermique ou double électrolyte, le dopage de l'isolant… Ces optimisations, initialement purement théoriques ont montré de bons résultats expérimentaux sur des cellules d'étude réalisées spécifiquement pour ce travail. Il a ainsi été

possible d'améliorer la rétention des deux états de résistance ainsi que l'endurance qui sont à l'heure actuelle deux paramètres limitant de la technologie. La variabilité a également et traitée grâce à la spécificité du modèle Monte Carlo permettant de la simuler. Les variabilités intrinsèques et cycle à cycle ont ainsi pu être mise en avant et différenciées pour les deux niveaux de résistance. Ce travail de recherche a également mis en avant les compromis récurrents touchant cette technologie. Il semble ainsi à l'heure actuelle ne pas exister de dispositif CBRAM parfait offrant à la fois une grande fenêtre de programmation, une bonne stabilité thermique et une bonne endurance. Certains de des points ont été mis en avant dans ce manuscrit avec notamment l'impact de l'état écrit sur la variabilité de l'état effacé mais également la rétention de l'état effacé dégradé par l'opération d'écriture… L'ensemble des caractéristiques de la technologie CBRAM semblent être reliées entre elles, notamment par l'intermédiaire de la morphologie du filament. Modifier une de ces caractéristiques modifie également les autres, signe de l'équilibre complexe de cette technologie. Ceci pourrait ainsi apparaitre comme une limitation de la technologie mais ce pourrait également être une de ces forces. Il est en effet possible optimiser des points clefs de la technologie en fonction des applications visées par le biais de solutions technologiques mais aussi simplement opératoires et post production.

La technologie CBRAM offre encore plusieurs axes d'amélioration et pas uniquement en termes de réduction des dimensions. En effet, un travail d'optimisation des matériaux et conditions d'utilisation est encore à faire. De plus, la compréhension générale, dont celle proposée ici, doit encore évoluer et être confrontée aux évolutions industrielles de cette technologie. De grandes innovations technologiques semblent approcher et le développement de circuits de programmations intelligentes apparait comme une solution viable aux limitations intrinsèques mise en avant dans ce manuscrit. L'intégration de CBRAM à haute densité à récemment été présentée et annonce une évolution particulièrement intéressante de la technologie dans les années à venir.

Réferences de résumé étendue

[AChen 1] An Chen, James Hutchby, Victor Zhirnov, George Bourianoff, John Wiley & Sons, “Emerging Nanoelectronic Devices”, 2015. Web. 2 Oct. 2015.

[Belmonte 1] Belmonte, A.; Kim, W.; Chan, B.; Heylen, N.; Fantini, A.; Houssa, M.; Jurczak, M.; Goux, L., "90nm WAl2O3TiWCu 1T1R CBRAM cell showing low-power, fast and disturb-free operation," in Memory Workshop (IMW), 2013 5th IEEE International , vol., no., pp.26-29, 26-29 May 2013

[Celano 1] Celano, U.; Goux, L.; Belmonte, A.; Schulze, A.; Opsomer, K.; Detavernier, C.; Richard, O.; Bender, H.; Jurczak, M.; Vandervorst, W., "Conductive-AFM tomography for 3D filament observation in resistive switching devices," in Electron Devices Meeting (IEDM), 2013 IEEE International , vol., no., pp.21.6.1-21.6.4, 9-11 Dec. 2013

[Hsieh 1] Min-Che Hsieh, Yung-Wen Chin, Yu-Cheng Lin, Yu-Der Chih, Kan-Hsueh Tsai, Ming-Jinn Tsai,Ya-Chin King and Chrong Jung Lin, “A new laterally conductive bridge random access memory by fully CMOS logic compatible process,” Japanese Journal of Applied Physics, Vol. 53, Num. 4S, Mar. 2014.

[Jameson 1] Jameson, J.R.; Gilbert, N.; Koushan, F.; Saenz, J.; Wang, J.; Hollmer, S.; Kozicki, M.; Derhacobian, N., "Quantized Conductance in Ag/GeS_2/W Conductive-Bridge Memory Cells," in Electron Device Letters, IEEE , vol.33, no.2, pp.257-259, Feb. 2012

[Larentis 1] Larentis, S.; Nardi, F.; Balatti, S.; Ielmini, D.; Gilmer, D.C., "Bipolar-Switching Model of RRAM by Field- and Temperature-Activated Ion Migration," in *Memory Workshop (IMW), 2012 4th IEEE International* , vol., no., pp.1-4, 20-23 May 2012

[Laidler 1] K.J. Laidler and M.C. King, “Development of transition-state theory,” The Journal of physical chemistry, vol.87, pp.2657-2664, 1983

[Longnos 1] Longnos, F.; Vianello, E.; Molas, G.; Palma, G.; Souchier, E.; Carabasse, C.; Bernard, M.; De Salvo, B.; Bretegnier, D.; Liebault, J., "On disturb immunity and P/E kinetics of Sb-doped GeS2/Ag conductive bridge memories," in Memory Workshop (IMW), 2013 5th IEEE International , vol., no., pp.96-99, 26-29 May 2013

[Molas 1] Molas, G.; Vianello, E.; Dahmani, F.; Barci, M.; Blaise, P.; Guy, J.; Toffoli, A.; Bernard, M.; Roule, A.; Pierre, F.; Licitra, C.; De Salvo, B.; Perniola, L., "Controlling oxygen vacancies in doped oxide based CBRAM for improved memory performances," in Electron Devices Meeting (IEDM), 2014 IEEE International , vol., no., pp.6.1.1-6.1.4, 15-17 Dec. 2014

[Russo 1] Russo, U.; Kamalanathan, D.; Ielmini, D.; Lacaita, A.L.; Kozicki, M.N., "Study of Multilevel Programming in Programmable Metallization Cell (PMC) Memory," in Electron Devices, IEEE Transactions on , vol.56, no.5, pp.1040-1047, May 2009

[Sune 1] Sune, J.; Long, S.; Cagli, C.; Perniola, L.; Lian, X.; Cartoixa, X.; Rurali, R.; Miranda, E.; Jimenez, D.; Liu, M., "Electrical evidence of atomic-size effects in the conduction filament of RRAM," in Solid-State and Integrated Circuit Technology (ICSICT), 2012 IEEE 11th International Conference on , vol., no., pp.1-4, Oct. 29 2012-Nov. 1 2012

[Tada 1] M. Tada, T. Sakamoto, Y. Tsuji, N. Banno, Y. Saito, Y. Yabe, S. Ishida, M. Terai, S. Kotsuji, N. Iguchi, M. Aono*, H. Hada, and N. Kasai, “Highly Scalable Nonvolatile TiOx/TaSiOy Solid-electrolyte Crossbar Switch Integrated in Local Interconnect for Low Power Reconfigurable Logic”, IEEE IEDM Tech. Dig. 2009, pp.943-946.

[Valov 1] I. Valov, R. Waser, J. R. Jameson, and M. N. Kozicki, “Electrochemical metallization memories—fundamentals, applications, prospects,” Nanotechnology, vol. 22, no. 28, p. 289502, Jul. 2011.

[Vianello 1] Vianello, E.; Molas, G.; Longnos, F.; Blaise, P.; Souchier, E.; Cagli, C.; Palma, G.; Guy, J.; Bernard, M.; Reyboz, M.; Rodriguez, G.; Roule, A.; Carabasse, C.; Delaye, V.; Jousseaume, V.; Maitrejean, S.; Reimbold, G.; De Salvo, B.; Dahmani, F.; Verrier, P.; Bretegnier, D.; Liebault, J., "Sb-doped GeS2 as performance and reliability booster in Conductive Bridge RAM," in Electron Devices Meeting (IEDM), 2012 IEEE International, pp.31.5.1-31.5.4, 10-13 Dec. 2012

[Voter 1] A. F. Voter, “Introduction to the Kinetic Monte Carlo Method,” Radiation Effects in Solids, K. E. Sickafus and E.A. Kotomin, eds., Springer, 2005.

Chapter I. State of the art of the CBRAM technology

7. Context

Ever since its emergence, the electronic market importance kept growing to reach last year a revenue of more than 330 billions of dollars. This quasi constant increase of revenue presented Figure 1 is tied to the market expansion and segmentation related to the electronic product. The diversification and segmentation of the electronic market explains this great success and development. Figure 2 shows the segmentation of the semiconductor market in Germany as an example of the electronic devises large scope of application. The most important point of the figure are not the numbers which are proper to the German industry (known for it strongly developed automotive industry) but the detailed segments that all rely on data storage (or transmission). The data storage has a key role in today's electronics and the amount of data created and required to be stored keeps increasing every seconds. Figure 3 shows the data quantity evolution since the early stage of the electronic to 2007. This constant growth is tied to a complete revolution of the electronic utilization. Starting from the beginning, the greatest ancestor to the electronic and modern computing is the Turing machine, which allowed the Enigma decryption and introduced the world to the use of a machine making calculations and encryption. The early stages of electronics followed the same path and aimed to compute and solve mathematical problem. However, with the increase of market benefits shown in Figure 1 came a global reduction of price and a popularization of the electronic use. This popularization started with the commercialization

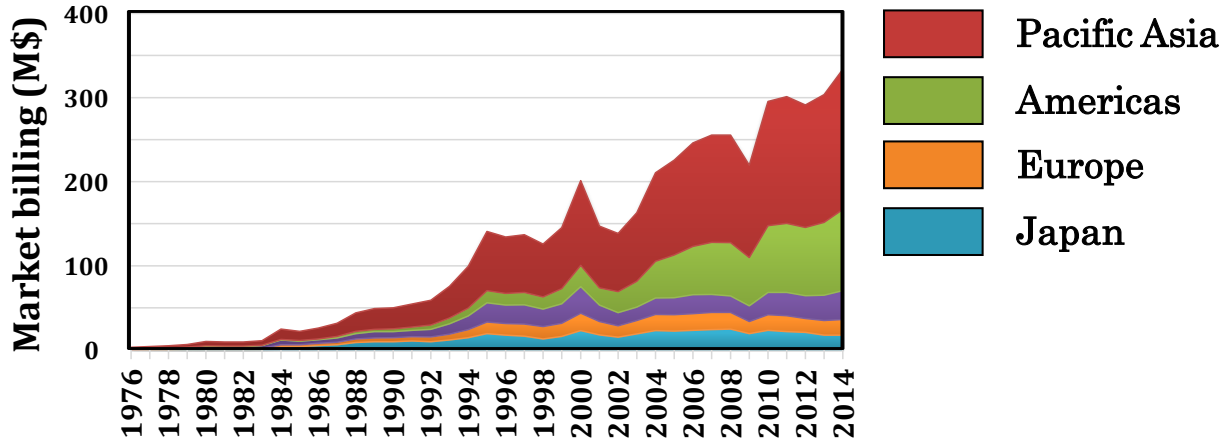

Figure 1. Electronic annual market billing since 1976 [Web 1]

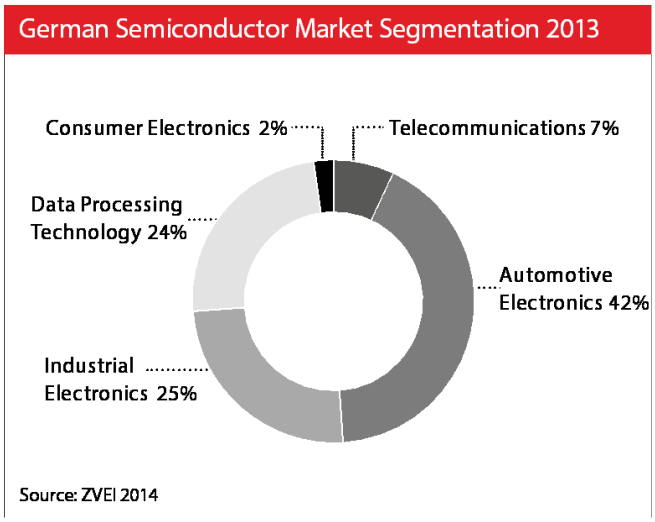

Figure 2. Semiconductor market segmentation in Germany [Web 2]

of the personal computer and keeps evolving today with the smartphone, tablet and wearable market increase. The increase of created data is not only due to the growth of user base but also to a strong change in mentality regarding the "Connected Life [Web 3]" and great rise in cloud

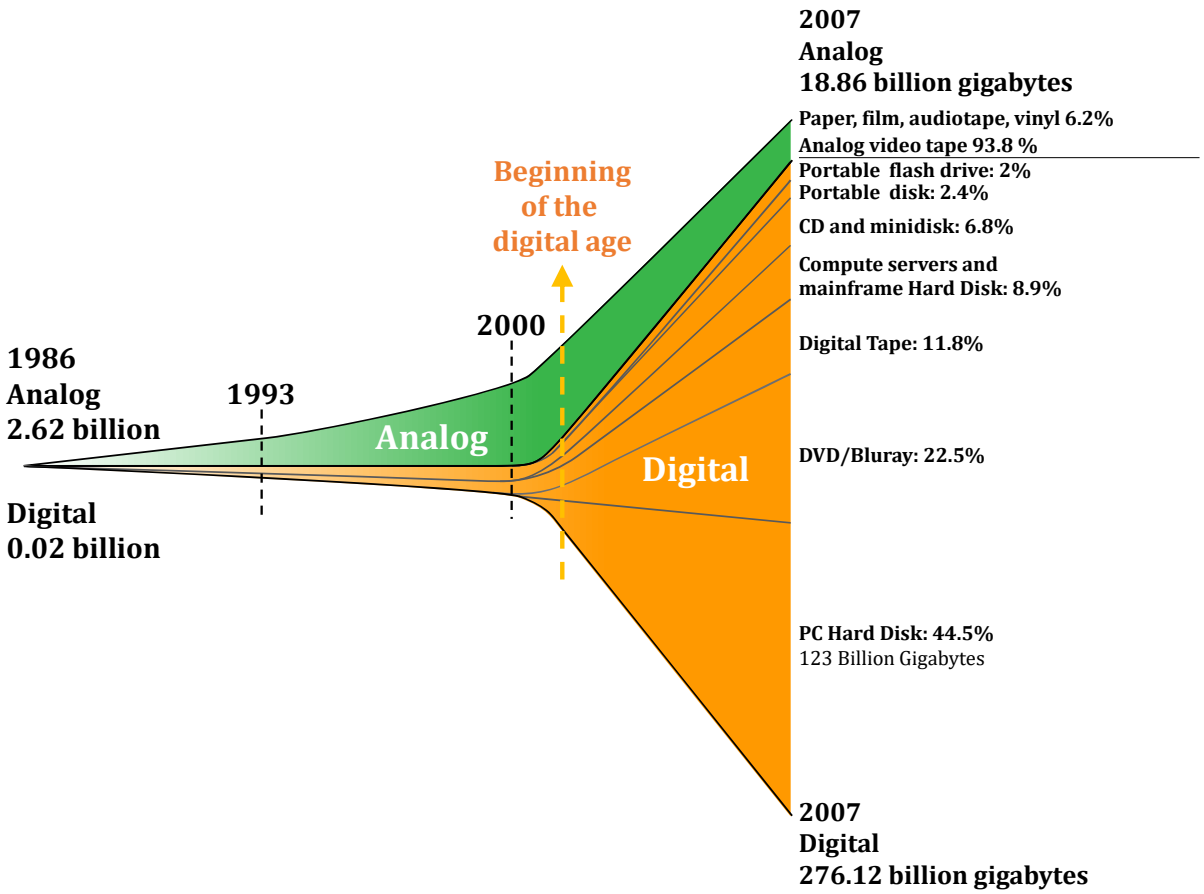

Figure 3. Evolution of the data stored quantity on analog and digital supports [Hilbert 1, Web 4]

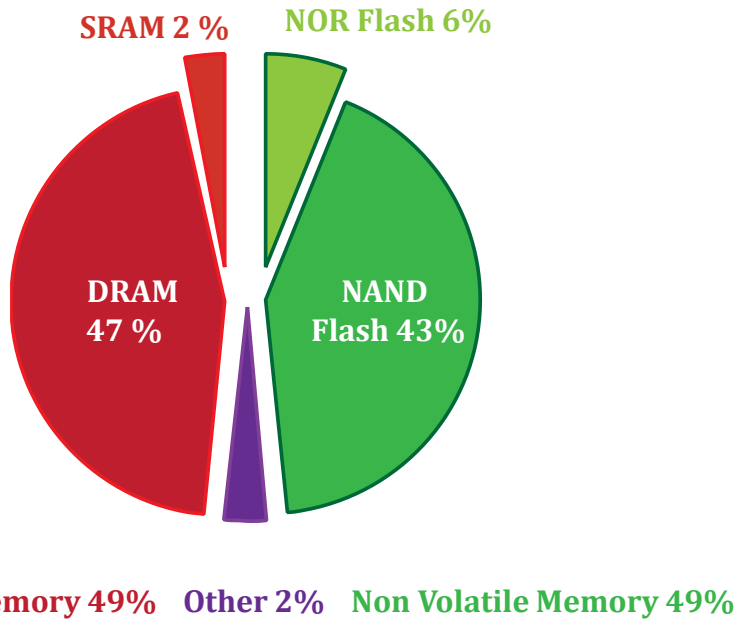

Figure 4. Worldwide repartition of the memory technology market [Charentenay 1]

computing [Ambrust 1], which ultimately leads to an increase of data per user. All this evolution explains the constant increase of stored data and especially digital storage in comparison to 1980 where the majority of data where stored under analog form. (Figure 3).

The vast majority of storage is thus digital, including magnetic hard drives, optical disc (CD, DVD, Blu-Ray…). Among these storage technologies, rises the non-volatile semiconductor technology. Semiconductor memory technologies are originally used for volatile memory unit such as Dynamic Random Access Memory (DRAM) or Static Random Access Memory (SRAM). However the Floating Gate Flash memory has progressively emerged as a dominant non-volatile memory technology since 2000's, from its introduction in the small form factor USB – keys to its current high speed, high density Solid State Drive (SSD) in computers, tablet and smartphones. Nowadays, the memory market of the semiconductor technology is balanced between non-volatile and volatile memory as shown in Figure 4. The cost reduction of Flash memory due to high density integration coupled to its great performances makes it a competitive alternative to the traditional mechanical hard disk drives (HDD). Figure 5 shows the great cost reduction of the Flash technology price compared to the HDD whose cost have been impacted by the Thailand inundations in 2011.

This technology has heavily relied on the physical scaling of the Floating Gate (similarly to the CMOS process) to achieve higher bits density, increasing the capacity and reducing the cost/bit. The figure 6 reports the evolution of the floating gate length with the corresponding average

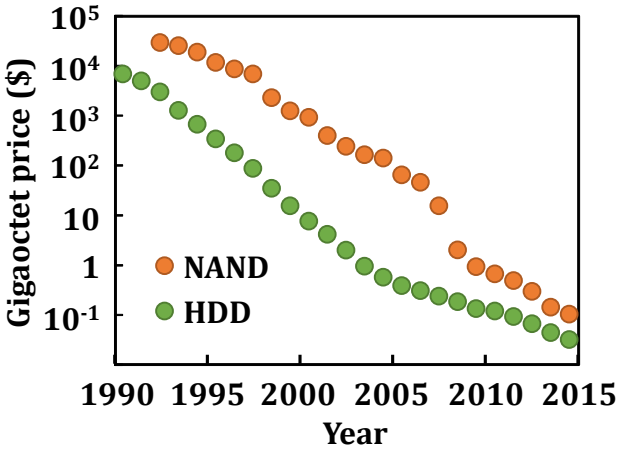

Figure 5. Price reduction of both Flash NAND memory and mechanical Hard Disk Drive (HDD) [Chu 1]

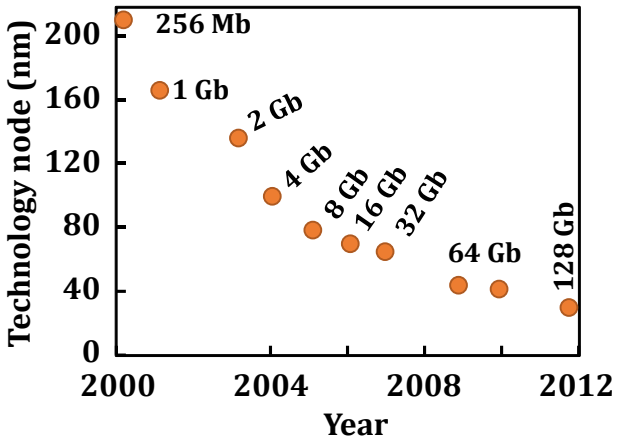

Figure 6. Progressive scaling down of the Flash technology node and corresponding storage capacity

capacity on the market and shows a decreasing trend similar to the price shown in Figure 5. However, the constant size reduction of the Flash memory cells faces key technological and physical issues including lithography limitations, tunnel oxide thickness reduction, reduction of the space between cells and diminution of the number of stored electrons [Shig 1]. Voltage scaling is also limited due to these issues, leading to high voltage requirement operations. These high voltages cause long term reliability problems like disturbs and dielectric wear-out in the devices. Reduction in tunnel oxide thickness is not possible without compromising the long term reliability of the cell caused, due to Stress Induced Leakage Current (SILC), related defects generation and pinhole defects formation in the tunnel oxide.

While all these limitations seem to be unexpectedly [ITRS 1] overcome at each new scaling node, the amount of money involved keeps growing and leads to an increase of interest toward alternative technologies. Figure 7 summarizes the current state of memory technologies divided between volatile and non-volatile storage.

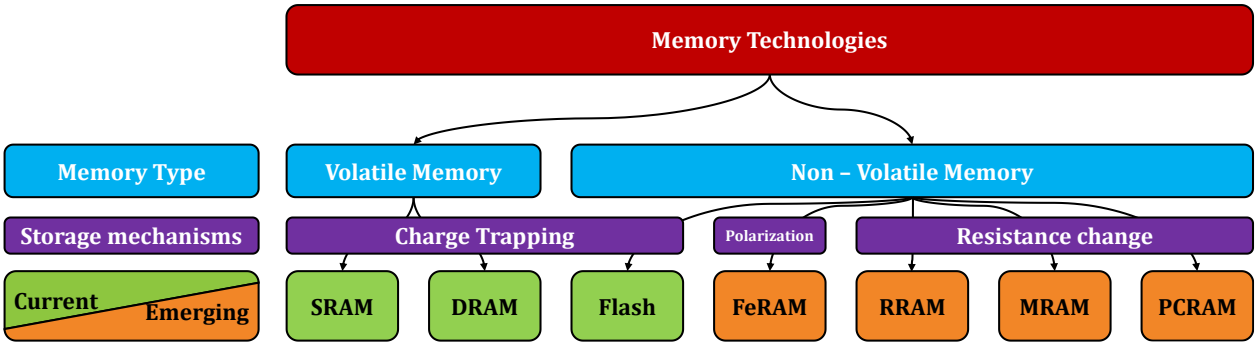

Figure 7. Current state of the memory technology. [ITRS 1]

The CBRAM technology belongs to these emerging memories, which show a large variability of maturity. Among these emerging technologies, the oldest one is the Ferroelectric RAM (FeRAM), which is produced by Fujitsu [Fujitsu 1] and Texas Instrument [TexIn 1] and already on the market. These FeRAM memory cells rely on two stable polarization states proper to perovskite structures [Muller 1], (for example $Pb(Zr, Ti)O_3$). This technology relies on the same architecture as DRAM adding the non-volatility behavior with a ferroelectric layer acting as a capacitor. The Magnetoresistive memory (MRAM) is another emerging technology whose data storage is based this time on the magnetization change of a material layer [Jullière 1]. The change of magnetization induces a variation of resistance allowing an easy determination of the state of the cell. The Phase Change memory (PCRAM) also relies on a resistance modification induced by a phase change of a material composing the cell. This technology uses the chalcogenides offering two different stable phase [Wuttin 1]. Finally, the Oxide RAM (OxRAM) and Conductive Bridge RAM (CBRAM) also share the ability to store data with a variation of resistance. They both rely on the formation and dissolution of a conductive path in a resistive matrix. They belong to the Resistive RAM (RRAM) group and show great similarities. The CBRAM being the core of this manuscript, these technologies will be described in the following of the chapter.

The market segmentation stated Figure 2 brings a large variation of specifications depending on the targeted applications, from low end to high end electronics, allowing a progressive introduction of the emerging technologies. Table 1 summarizes and compares the performances of all the previous emerging technologies versus the Flash memory. It can be seen that the RRAM and thus CBRAM offer already great performances but also a great potential in the future. Figure 8 shows the improving maturity of the emerging technologies compared to Flash. A more precise state of the art of the current CBRAM performances and devices will be given in the following of the chapter.

Table 2. 2013 and 2026 projection of the memory performances [ITRS 1]

		Flash	FeRAM	PCRAM	MRAM	RRAM
Integration F (nm)	2013	16	180	45	65	5
	Projected	<10	65	8	16	<5
Cell surface (F^2)	2013	4	22	4	20	4
	Projected	4	12	4	8	4
Programing voltages (V)	2013	15 – 20	1.3 – 3.3	3	1.8	0.6
	Projected	15	0.7 – 1.5	<3	<1	<0.5
Programing/Erasing time	2013	1 / 0.1 ms	65 ns	100 ns	35 ns	< 1 ns
	Projected	1 / 0.1 ms	< 10 ns	< 50 ns	< 1 ns	< 1 ns
Programming power (J/bit)	2013	$4x10^{-16}$	$3x10^{-14}$	$6x10^{-12}$	$2.5x10^{-12}$	$1x10^{-12}$
	Projected	$1x10^{-16}$	$7x10^{-15}$	$1x10^{-15}$	$1.5x10^{-13}$	$1x10^{-16}$
Read voltage	2013	4.5	1.3 – 3.3	1.2	1.8	0.2
	Projected	4.5	0.7 – 1.5	<1	<1	0.1
Read time (nm)	2013	0.1 ms	40 ns	12 ns	35 ns	50 ns
	Projected	0.1 ms	< 20 ns	< 10 ns	< 20 ns	< 10 ns
Data retention (year)	2013	10	10	> 10	> 10	< 10
	Projected	10	10	> 10	> 10	> 10
Endurance (Cycle)	2013	10^5	10^{14}	10^9	10^{12}	10^{12}
	Projected	10^5	$> 10^{15}$	10^9	$>10^{15}$	$> 10^{12}$

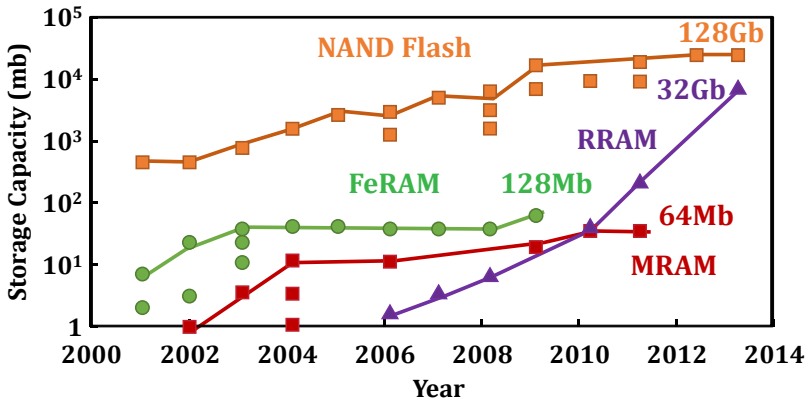

Figure 8. Storage capacity evolution for various non – volatile technologies [ISSCC 2013].

8. Resistive Memory

8.1 Generalities

RRAM devises are based on the reversible formation and dissolution of a conductive path in a resistive layer (RL). This conductive path connects both electrodes of the Metal Insulator Metal (MIM) structure composing the RRAM and reduces the global electrical resistance of the cell. Figure 9 shows a simplified view of a RRAM structure. This technology relies on a resistance variation of the RL to store the data and depending on the presence of the conductive path, the global resistance is modified leading to the ability to store one bit per cell. Both states, with and without conductive path, remain intact once the power supply is shut down giving this technology a Non – Volatile behavior. Depending on the stability and reliability of the technology, it is possible to store more bits per cell [Aratani 1, Dimin 1, Cong 1] leading to a great scaling of the surface occupied per bit. This ability will be discussed further but to simplify the RRAM understanding the following description will firstly be focused on a standard one bit per cell approach.

The standard operating behavior of a RRAM cell is composed by three different states:

- A highly resistive initial state: the pristine sate which corresponds to the RRAM resistance state after processing.
- A Low Resistance State (LRS) or written state occurring once the conductive path is created. Switching the cell to this state requires a Forming operation at high voltage from the pristine state or a SET operation from the erased state.
- A High Resistance State (HRS) or erased state occurring once the conductive path is dissolved. Switching the cell to this state requires a RESET operation.

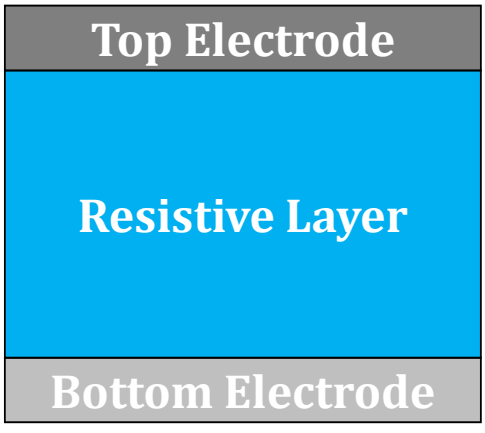

Figure 9. Schematic view of the Metal Insulator Metal structure of RRAM

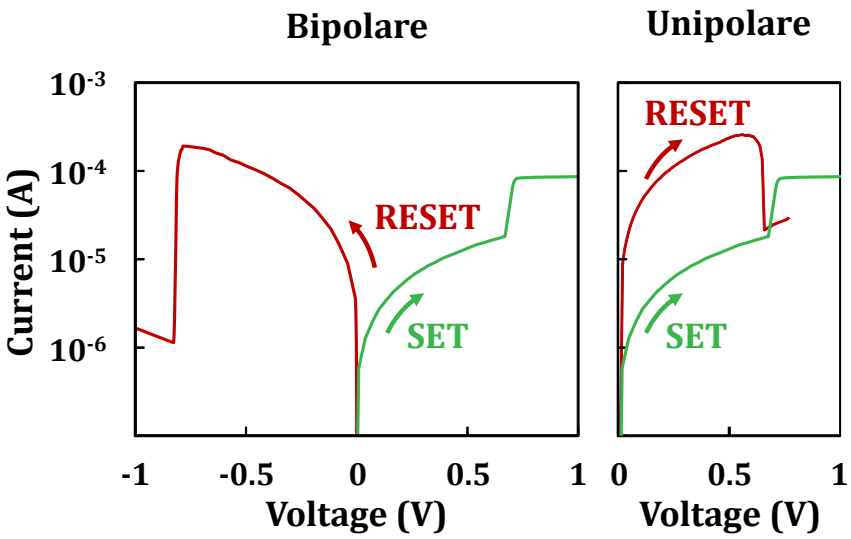

Figure 10. Bipolar and unipolar behavior of the RRAM

In order to switch from one state to the other, voltage and current routines have to be applied. The Forming, SET and RESET operations correspond to the application of a voltage ramp or pulse inducing the switching mechanisms. The voltage or time required to switch the cell depends on the technology. RRAM cells can be divided in two groups depending on the voltage routine they require to switch, either unipolar or bipolar. Figure 10 exposes the difference between both behaviors. Unipolar behavior requires the same polarity for both SET and RESET. During SET, the current is limited but the voltage is higher than during RESET. The bipolar behavior requires the SET and RESET operations to be performed at opposite voltages. The current limitation is required during SET (unipolar and bipolar) to avoid the degradation of the resistive layer and its definitive breakdown. Bipolar and unipolar behaviors are tied to the technology, OxRAM shares both unipolar and bipolar behavior in function of the materials involved whereas the CBRAM devices are considered bipolar only.

8.2 Advanced RRAM understanding

The basis of the RRAM technology is the ability to electrically control switching mechanisms with precise current and voltages. While all the switching mechanisms revolve around the modification of a resistance state, the resistance modification is based on different physical phenomena. These phenomena [Waser 1] regroup various mechanisms and associated technologies: from electro – mechanical effect at nanometric scale for Carbon nanotubes memory [Kianian 1] to MRAM using the resistance change of a magnetic junction [EChen 1] or PCRAM

relying on the resistance difference between crystalline or amorphous states [Wutting 1]. The RRAM family relies on a group of physical phenomena regrouping thermochemical effects, valence change, electrostatic effects and electrochemical metallization. The first three physical phenomena are used in OxRAM technology whereas the electrochemical metallization is the core of the CBRAM giving to this technology its other usual name: Programmable Metallization Cell (PMC). The difference of physical phenomena leads to a separation of RRAM into two groups depending on nature of the conductive path modifying the resistance state: Filamentary and independent of the cell dimensions or Non – Filamentary and dependent of the surface. In the following of this section, OxRAM and CBRAM will be described and compared to point out the differences but also great similitudes of these technologies. The physical mechanisms involved in each technology described in the following are mainly theoretical and subject to modification as a complete physical understanding is still missing.

8.2.1 Switching mechanisms

8.2.1.1 Oxygen vacancies, creation, migration and destruction

The oxygen vacancies displacement is at origin of the OxRAM technology and relies on oxide microstructure and valence changes. OxRAM cells are based on transition metal oxide (HfO_2, Ta_2O_5, NiO [Govoreanu 1, Lee 1, Courtade 1]) surrounded by two electrodes. The cells require defect rich zones playing the role of oxygen vacancies supplier. These zones can be obtained with particular oxidizable electrodes (Hf , Ta, Ti) or using a resistive layer depleted in oxygen [Fang 1, YChen 1, Lee 1].

A first approach of OxRAM behavior consists in the redistribution of the oxygen vacancies in the resistive layer. The oxygen vacancies are considered already present in the oxide or created during the first writing operation: Forming. These vacancies are positively charged and migrate under the electric field induced by the applied voltage. Their migration allows the formation and destruction of a conductive path depending on the voltage which modifies the resistance level. The current flowing through this path also generates heat enhancing the vacancies migration and filament destruction. In this approach, the oxygen vacancies are responsible for the electrical conduction and their migration induced by the electric field explain the bipolar switching.

Another approach to understand to OxRAM behavior is based on the creation and destruction of oxygen vacancies [Bocquet 1] at each cycle and not only during Forming. Local redox reactions of

the resistive layer can modify the vacancies concentration during SET or RESET. Thus, this metal oxide is reduced at its metal state during SET creating a conductive path rich in metal. During RESET, the same atoms are oxidized decreasing the metal concentration. Both these processes are accelerated by the thermal heating induced by the high current density. In This approach, the conductive path is formed by a decrease of oxygen concentration and increase of metal content. The bipolarity of the switching mechanism is explained by the difference of voltage favoring either the oxide reduction or metal oxidation. A unipolar switching is also possible if the RESET operation is only thermally driven. Figure 11 shows a schematic representation of these two switching mechanisms compared to the following one.

8.2.1.2 Electrochemical metallization

As stated previously, this switching mechanism is at the core of the CBRAM technology. This commutation process is composed by three consecutive steps as describe in [Waser 1, Valov 1]: Oxidation, Migration and Reduction.

First, the oxidation corresponds to the creation of free ions from atoms at the electrode (top electrode for clarity) interface. To achieve such oxidation reaction, the metal composing the top electrode has be electrochemically active (Silver [Rahaman 1], Copper [Maikap 1]). These reaction have been tied by several study to Buttler – Volmer equations [AChen 1, Valov 2].

Once the ions created they start migrating through the resistive layer toward the second electrode (bottom electrode). This migration is driven by the electric field, in agreement with the Mott Gurney approach. To allow the ions migration, proper resistive layer medium has to be chosen and strongly depends on the nature of migrating ions (example: GeS_2 for Ag [Jameson 1] or Al_2O_3 for Cu [Belmonte 1]).

Once the ions reach the interface of the bottom electrode they get reduced. As the number of incoming ions increases a filament start to form between the two electrodes progressively reducing the insulative gap with the top electrode. This leads in the end to the creation of a filamentary conductive path between the two electrodes greatly reducing the resistance level.

The process previously described addresses the SET operation or writing process. Depending on the technology choice the first SET might require a higher voltage than the followings. This operation called Forming is proper to oxide based CBRAM and can be assimilated to an initial required breakdown of the oxide.

The RESET operation or erase process consists in the reversed operation with the oxidation of the metal atoms at the bottom electrode interface and the ions migration toward the top electrode. It is thus essential for the bottom electrode to be composed of electrochemically inert material to avoid its dissolution during RESET which would lead to the impossibility to properly erase the cell. The RESET operation is also enhanced by an increase of temperature induced by the high density of current flowing in the filament [Govoreanu 2].

To summarize, this switching mechanisms required some technological specificities to be properly used: an electrode composed by an electrochemically active material, another one composed by an electrochemically inert material and a resistive layer allowing the proper migration of the corresponding ions.

Oxygen vacancies have also been demonstrated to be part of the switching mechanisms, enabling the ion migration in certain resistive layers [Molas 1]. These oxygen vacancies positively charged migrate through the electrolyte as exposed in the previous section for the OxRAM. Figure 11 shows a comparison of the switching mechanisms.

8.2.1.3 Electromigration

Following a similar behavior, the formation and dissolution of the conductive filament is also possible using the electromigration phenomenon but without ionizing the metal atoms. The commutation process is based on a momentum transfer between the electrons and the diffusing metal atoms [Suga 1, Bellisario 1]. This phenomenon requires sufficient amount of current to be impactful which makes it more reliable for the RESET operations. However, it has been proved [Takahashi 1] the feasibility of a nonvolatile memory relying on such switching mechanism. Figure 11 shows a comparison of the switching mechanisms.

8.2.2 Electrical conduction mechanisms

The role of RRAM cells is based on the change of resistance which is tied to the electrical conduction. Various hypotheses have been proposed to explain the OxRAM and CBRAM electrical conduction. Depending on the resistance state the conduction mechanisms differ, in accord with the evolution of the conductive path. In the case of a conductive path being a complete metallic filament (typical LRS), the standard Ohm conduction is generally employed [Bocquet 1, Larentis 1]. This conduction form is also used to simplify the HRS electrical conduction but with a strongly reduced conductivity. It is important to note that it exists a continuum [Goux 1] of states

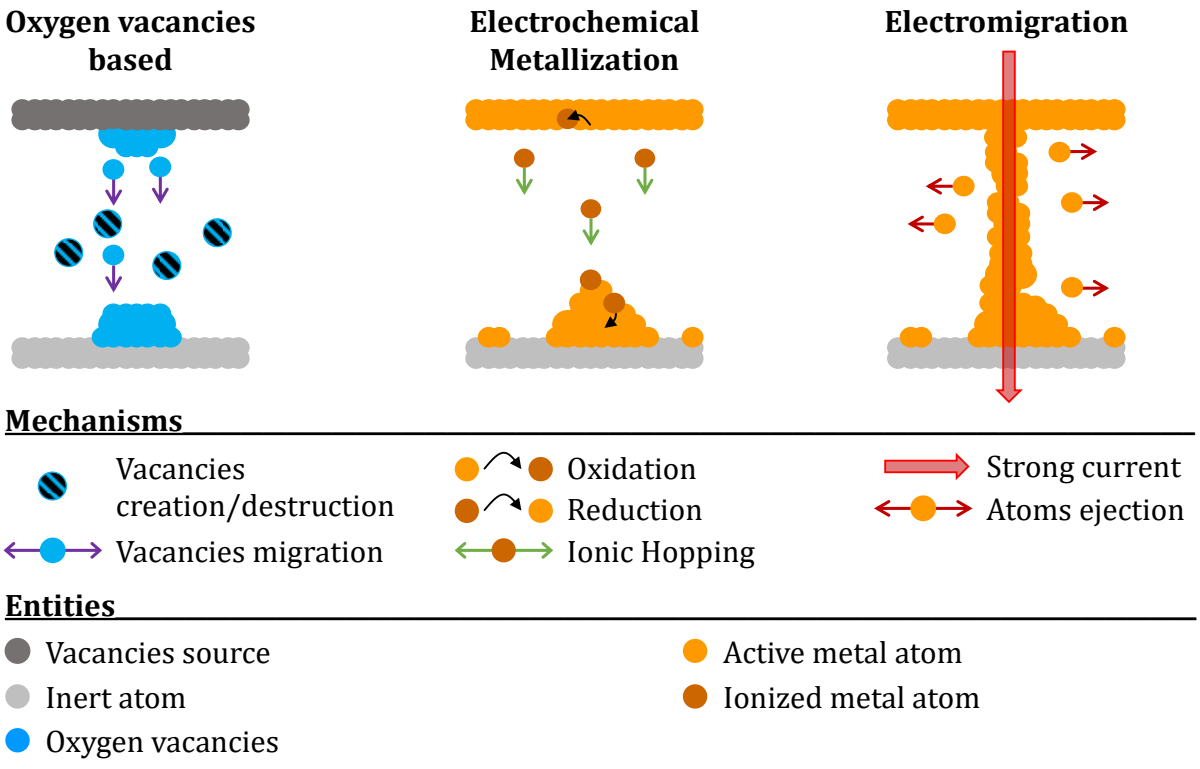

Figure 11. Comparison of the different switching mechanisms

between a fully formed filament in LRS and a fully dissolved on in HRS. Depending of the conductive state, the electrical conduction can be attributed to various physical mechanisms. During the early stages of RESET, the filament thickness is greatly reduced at a constriction point. Once the constriction is small enough (few atoms), the electrical conduction can be tied to a Quantum Point Contact conduction [Sune 1, Degraeve 1, Long 1]. This conduction is attributed to the very low amount of atoms allowing the current to flow, resulting in a quantum conduction in one dimension. Following the filament dissolution, shortly after it breaks and a gap appears between both top and bottom side of the filament, in this case the conduction can be explained by Fowler–Nordheim tunneling [Benoist 1, Kamiya 1]. With the RESET progression, the gap increases and charge trap might appear in the gap during the process. The last conduction model, bonded to theses traps relies on Trap Assisted Tunneling (TAT) [Larcher 1, Gao 1, Guan 1].

8.2.3 Advanced understanding synthesis

As exposed in this section both OxRAM and CBRAM have a lot in common: they share similar switching mechanisms, electrical conduction and global architecture. These technologies

resemblances are intensified by the lack of a comprehensive physical understanding of the RRAM technologies. The physical hypotheses exposed in this section are continuously put to the test, updated or modified and the research work conducted and reported in this manuscript aims to enhance the global understanding of the RRAM and more specifically CBRAM. To differentiate CBRAM and OxRAM, only RRAM using an electrochemically active metal electrode will be referred as CBRAM in this manuscript. The conductive path must be made from the atoms coming from this top electrode. Moreover, oxygen vacancies are not restricted to OxRAM and are now considered as part of the CBRAM switching mechanisms [Molas 1]. In the present state, OxRAM technology offers a better thermal stability favoring the soldering and data retention. However, with the transition to oxide based CBRAM the thermal stability of CBRAM cell keeps increasing.

9. CBRAM technological evolution

The CBRAM research landscape regroups a lot of actors either academic or industrial, both jointly working on the CBRAM since its invention in 1996 by Michael Kozicki, professor of electrical engineering at Arizona State University [Kozicki 1]. Figure 12 shows how far the CBRAM evolution has come since the early stage of horizontally processed CBRAM to one of the most advanced patent to scale down the CBRAM active area. The CBRAM understanding has been greatly improved since 1996: from early proof of concept, attached to demonstrate the feasibility of materials or architecture combinations, to technology optimization and most recently industrial demonstrators and high density chips.

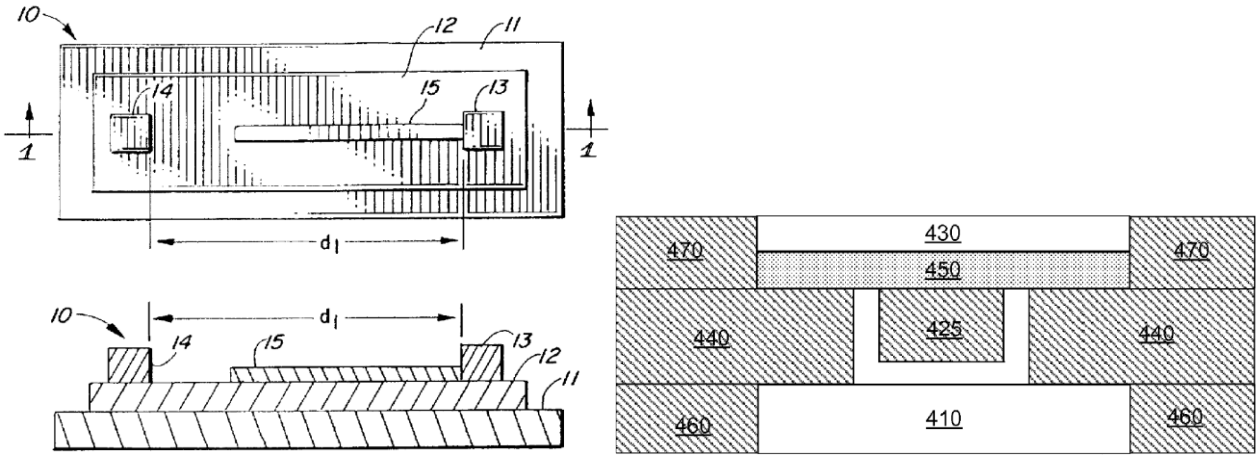

Figure 12. (Left) Initial CBRAM concept patent by M. Kozicki [Kozicki 1] (13 and 14 are the electrode and 15 the filament), (Right) One of the most advanced patent on the CBRAM confinement (450 and 410 are the electrodes and 450 the resistive layer) [Vaithyanathan 1].

9.1.1 Early stages of the technology

The early stage of the CBRAM development could be assimilated to a succession of proof of concept studies aimed to propose a large screening of the material combinations offering the awaited switching mechanisms. Following the CBRAM invention, a great interest on the use of chalcogenide as resistive layer has grown and a lot of researches were presented on various resistive layers and electrodes combinations. Among others, the Ge_xS_y and Ge_xSe_y were the two most studied components mainly coupled with silver top electrode but various bottom electrodes such as Tungsten, Platine or Nickel. M. Kozicki et al. played a great role in proving the feasibility of such technology with a lot of publications on the subject ever since its invention. A lot of other research team also proposed work on chalcogenide materials such as GeTe [CJKim 1], GST [Pandian 1], $Zn_xCd_{1-x}S$ [ZWang 1, Van der Sluis 1] or Cu_2S [SWKim 1, Sakamoto 1, Banno 1]. As the technology started growing interest, the performances improved but limitations appeared, especially concerning the thermal stability. This thermal stability is indeed a major concern as it can limit the CBRAM integration in CMOS integrated circuits due to the high temperatures used in standard back-end-of-line processing. To address the thermal stability different chalcogenide stoichiometries have been proposed as well as resistive layer doping [Vianello 1]. Both showed improvements in the thermal stability but the real improvement came from the use of oxide as resistive layer. Oxides used as resistive layer offers more stability at high temperature but are also already used in the CMOS technology, which is a great advantage to enhance the CBRAM integration. The materials screening researches has thus been conducted on oxides mainly coupled with copper top electrode. Among these oxides the most frequently used are Al_2O_3, Ta_2O_5 or GdO_x and offer a much better thermal stability. The vast majority of the CBRAM technologies being currently developed and presented relies on an oxide resistive layer, except for a recent CBRAM based on chalcogenide materials and made by Adesto technologies [Jameson 2]. With no need to prove the feasibility of the CBRAM technology anymore, the main research efforts have been focus on improving the devices performances and dimensions.

9.1.2 Technology optimization

In order compete against Flash memory and other emerging memory technologies, the CBRAM technology optimization follows two trends: improving the global performances (speed,

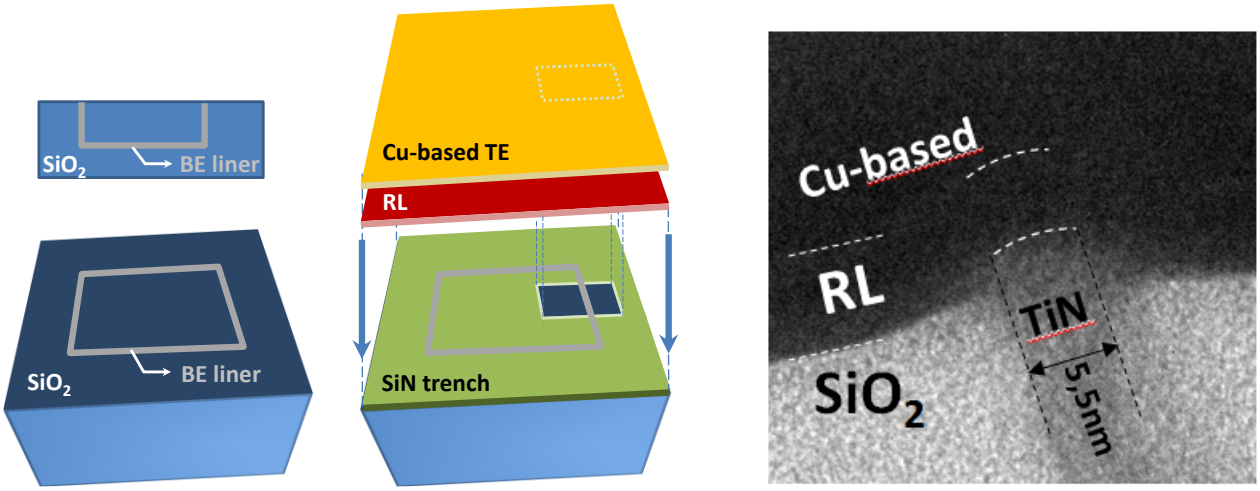

Figure 13. Schematic view and TEM observation of one of the most confined CBRAM architecture (processed in CEA Leti).

power consumption, thermal stability and retention) and scaling down the cells dimensions to offer higher density.

The cell dimensions are governed by the technological limits of etching and lithography processes (close to 10 nm at this time). The critical dimension of the CBRAM cell in term of switching capabilities is the electrodes surfaces in contact with the resistive layer and can corresponds to the active zone. A strong confinement of this active zone has been presented in 2005, with a CBRAM confined in a 20 nm plug [Kund 1]. It has also been shown the possibility to artificially create a strong active zone confinement with architectures specificities such as the µ-Trench [Vaithyanathan 1] or characterization trick using an AFM tip as electrode [Deleruyelle 1]. This was made to study the CBRAM operations under extreme scaling conditions and showed good results with dimension scaled down to 10x10 nm^2 [Govoreanu 1] or 5x50 nm^2 [Guy 1] as shown Figure 13. The confinement is also a factor impacting the performance and might, if well mastered, improve the cell characteristics such has the memory window [Choi 1].

Chalcogenide based CBRAM devices offer great overall performances and more precisely in term of operating voltages, memory window and endurance. In comparison with oxide based CBRAM they offer strong RESET capabilities, allowing the devices to almost recover their pristine state after RESET operation. The main downside of the technology, as previously stated, is the poor temperature stability and data retention. To address these concerns, a transition from chalcogenides toward oxide based CBRAM has been pursued. However, with the great increase of thermal stability came an increase in programming voltages and the requirement of a high energy first

writing step, the Forming operation. The memory window is also impacted and seems to be tied to the endurance of the devices. Indeed, while chalcogenide CBRAM were offering high endurance and wide memory window, oxide CBRAM don't offer the same characteristics. Several studies have been carried [Liu 1] [Goux 2] to solve this concern but it seems to be impossible to find the materials and architecture combination to match the chalcogenide CBRAM's endurance and memory windows. Oxide CBRAM technology even appears to suffer from a tradeoff between both characteristics: a wide memory window being achievable only for a low number of cycle ($<10^5$ cycles). Figure 14 exposes the two typical behaviors of oxide based CBRAM, either high endurance or high memory window. As shown Figure 15, a high endurance is then achievable but with a limited memory window which brings the last limitation of the CBRAM technology. A small memory window is not a problem if the states (LRS and HRS) are stable and repeatable. However, while LRS generally shows only small variability, HRS is much more prone to state dispersion leading to a superposition of LRS and HRS during high cycle number. To offer high endurance reliability, this last technological lock needs to be broken. Finally, if both wide memory margin and variability concerns are solved for a high number of cycles, the CBRAM technology will be able to offer great multi-level memory allowing the storage of multiple bits per cell.

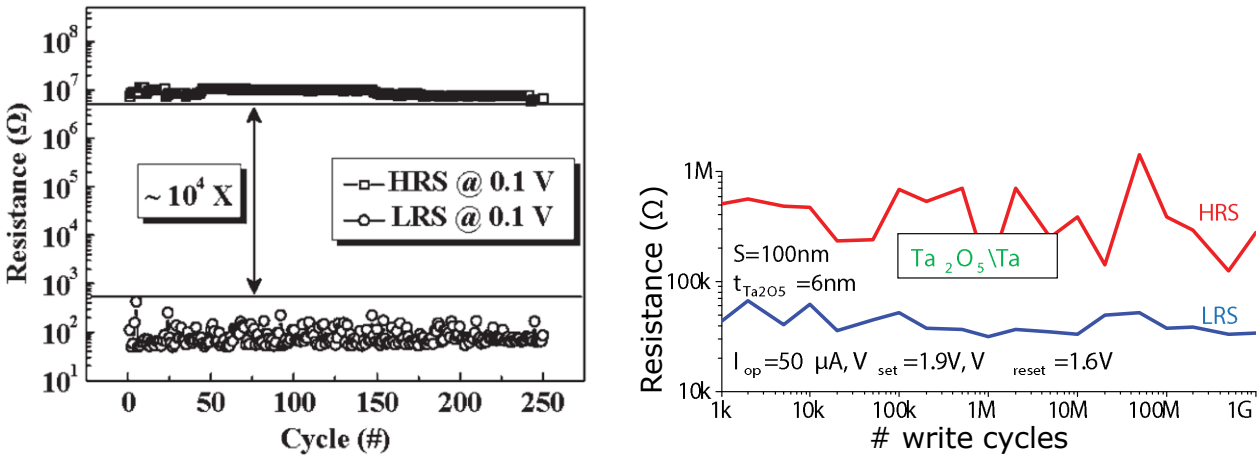

Figure 14. Two extreme CBRAM behaviors showing either a great memory window but limited endurance [Liu 1] (left) or narrow memory window but great endurance [Goux 2] (right).

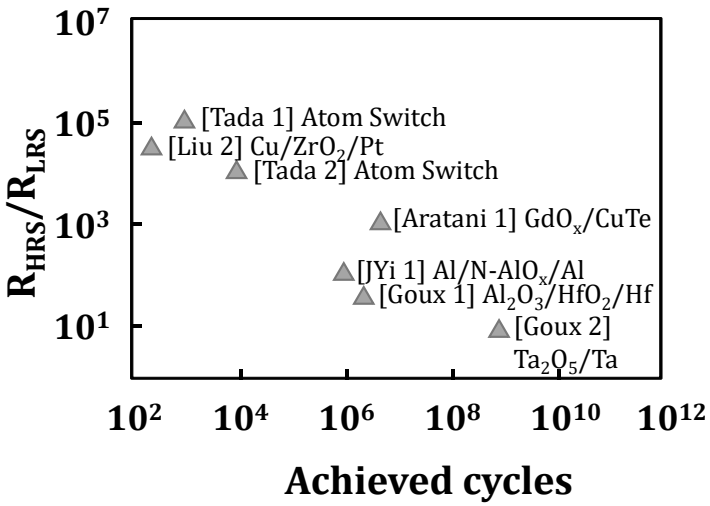

Figure 15. Memory versus endurance trade off reported on various materials stack (OxRAM and CBRAM) [Vianello 2]

9.1.3 CBRAM technology toward industrialization

As previously stated, the CBRAM still suffers from critical limitations before being able to replace the flash memory as a storage class memory. However, taking advantages of the current state of the CBRAM technologies, device integration has shown great evolution. The early stage of the CBRAM technology was mainly developed around single cells (1R structure) or coupled with one transistor (1T – 1 R structures). In the following years, first bit arrays were developed using selection transistor. In 2007 Qimonda and ALTIS presented a 2Mbit CBRAM array based on chalcogenide [Dietrich 1] showing fast switching (< 50 ns), competitive endurance (10^6 cycles) and good retention. In 2011 Sony [Watatu 1] proposed a 4Mbit also based on 1T – 1R architecture offering great performances (read at 2.3 GB/s and write at 216 MB/s). The major breakthrough happened in 2013 with the presentation at IEDM of 16GB CBRAM by Micron [Zahurak 1]. This demonstrator shown Figure 16 offers great performances (read at 900 MB/s and write at 180 MB/s) but with an endurance of 10^5 cycles still limiting the technology as mentioned before. Crossbar [Hyun 1] also proposed a very promising integrated CBRAM technology, 3D stackable, highly scalable and offering good performances as shown in Figure 17.

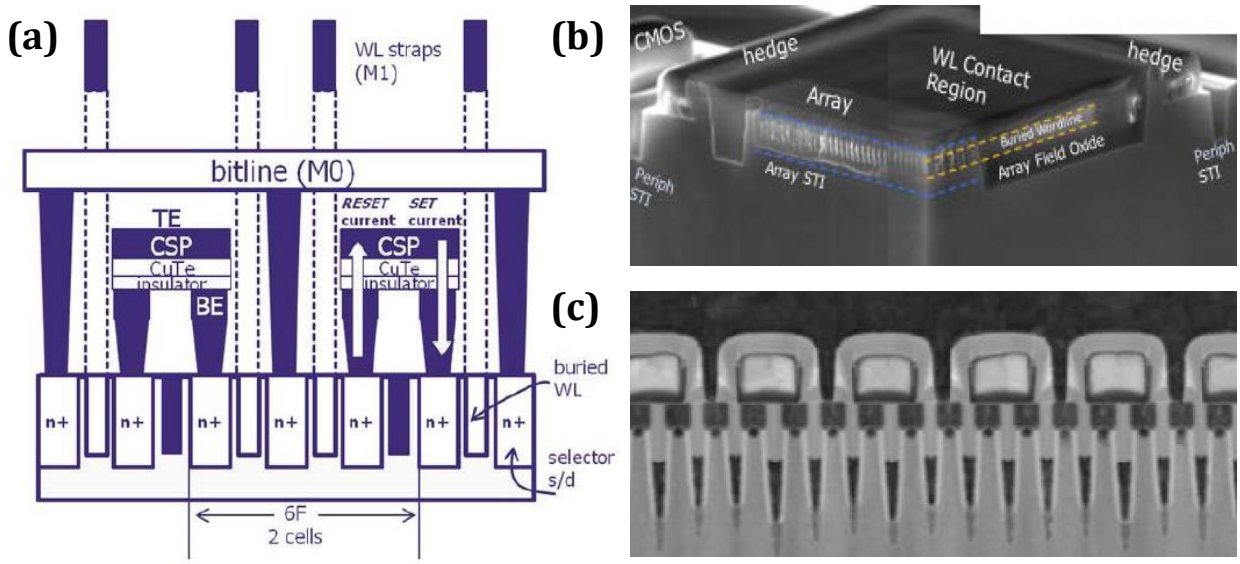

Figure 16. (a) Schematic of Cu-ReRAM 6F2 Architecture. (b) 3D Perspective showing Epi Array used for planarity. (c) Completed 27 nm array showing A-FET, silicide, metal plugs, Damascene cell and SAC DL [Zahurak 1]

One of the limitation of the 1T – 1R structure is the requirement of a transistor (or any other selector device) for each CBRAM, greatly reducing the integration density. Another approach to increase the storage density is to develop CBRAM devices with self-limiting current during SET thus avoiding the necessity of a selector. Various studies have been carried out to achieve such technology with mixed results [Goux 3, Hsu 1]. This technology could be of great use for the last possibility to increase the CBRAM density: the 3D integration, already studied at design state [YWang 1].

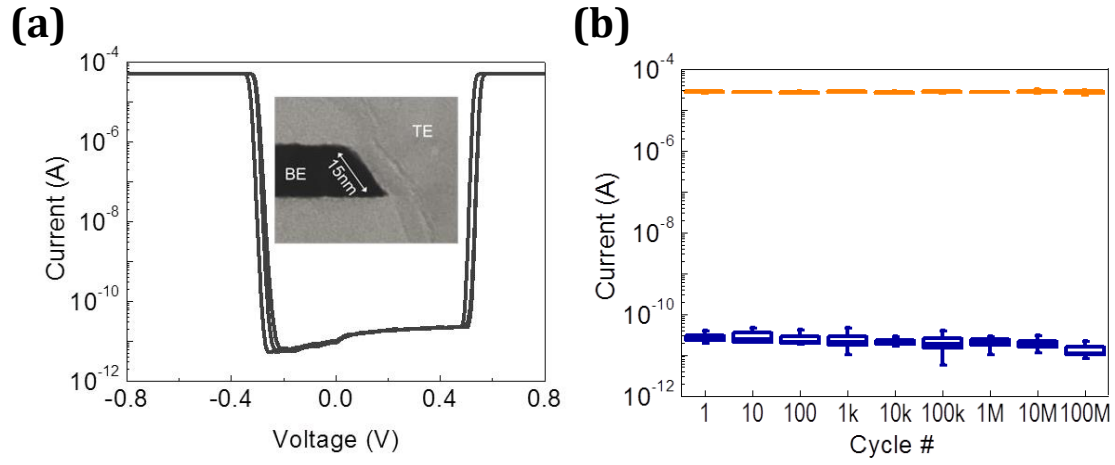

Figure 17. (a) Scalability of the Crossbar technology (b) High memory margin and endurance capabilities [Hyun 1]

10.CBRAM modelling

The CBRAM simulation is of great importance to enhance the global understanding of this technology. It allows the validation of essential theories at various level of understanding, from fundamental physical mechanisms to integrated devices global behavior. The CBRAM simulation is closely tied to the experimental results and the technology evolution, as it offers insights regarding possible evolutions or optimizations from inputs of the current state. The current section will be organized around the level of understanding focused by the simulation from pure physical modeling to single device and integrated device simulation.

10.1 Physical modeling

As previously stated in the advanced RRAM understanding, the CBRAM technology is still lacking a comprehensive understanding and a lot of simulation work is carried out to solve this crucial need. Among these researches, a lot of effort are put into ab-initio calculation which allows the computation of various properties (electronic, mechanical, energetic…) of a material from first principles calculations. Ab-initio calculation is very beneficial to the CBRAM technology understanding as it offers insights on the resistive layer behavior in function of the metal atom

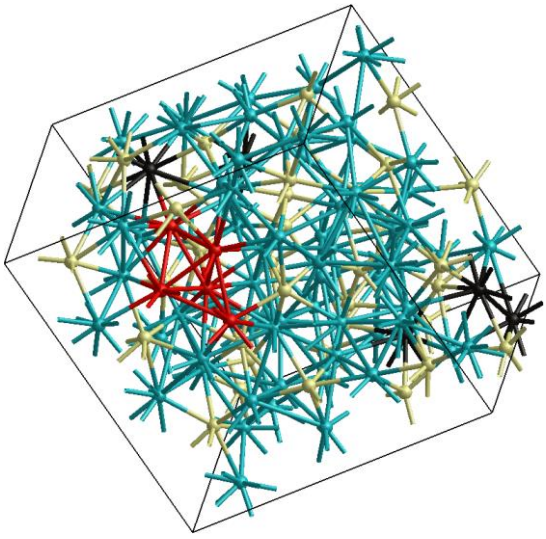

Figure 18. Bulk model for silver doped argentite Ag_2S with silver in Ag in blue, S in yellow, Ag dopant in black and Ag_5 cluster in red. [Todorova 1]

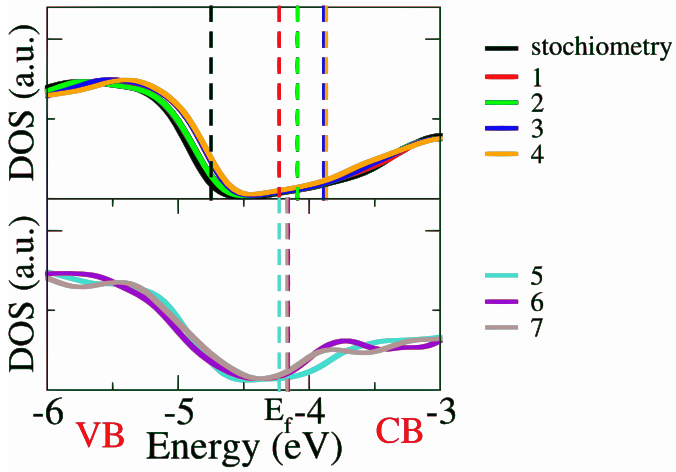

Figure 19. Calculated total DOS for silver doped argentite showing the displacement of the Fermi level (dashed lines) toward the toward the conduction band (CB) with the increase of dopants (1-5). For dopant number higher than 5 the system becomes metallic. [Todorova 1]

composing the conductive path. The atomic rearrangement can be obtained from ab-initio calculations, as well as the energy required for each atomic displacement, two very beneficial information regarding the atomic migration during switching operations [Sankaran 1]. Ab-initio calculations also offer the possibility to study the conduction mechanisms in various resistive layer (chalcogenide [Todorova 1] or oxide matrix [Sakamoto 2]). Figure 18 shows the simulated atom matrix obtained through ab – initio calculations. It is possible to see the position of the dopants and the formation or Ag aggregates. Figure 19 shows the evolution of the electrical conduction behavior in function of the number of dopants: from insulator to metallic. However, ab – initio calculations is strongly limited by the number of atom it can simulate, as can be seen on these figures. Only few atoms or few mesh units at best can be simulated in a relative short time duration (few days to weeks), which makes it impossible to simulate a whole RRAM cell.

Based on these ab-initio calculations and experimental inputs, electrical conduction models have been developed following various conduction hypothesis such as Ohmic current through highly resistive layer [Bocquet 1, Larentis 1], Fowler-Nordheim tunneling [Benoist 1, Kamiya 1], Trap Assisted Tunneling [Larcher 1, Gao 1, Guan 1] or Quantum-Point-Contact [Sune 1, Degraeve 1, Long 1]. These electrical conduction models are essential to the global simulation of CBRAM devices. Figure 20 shows an example of electrical conduction model relying on an electrical conductivity modification in function of the doping concentration. This conduction model is integrated into a device simulation rendering the SET operation [Larentis 1].

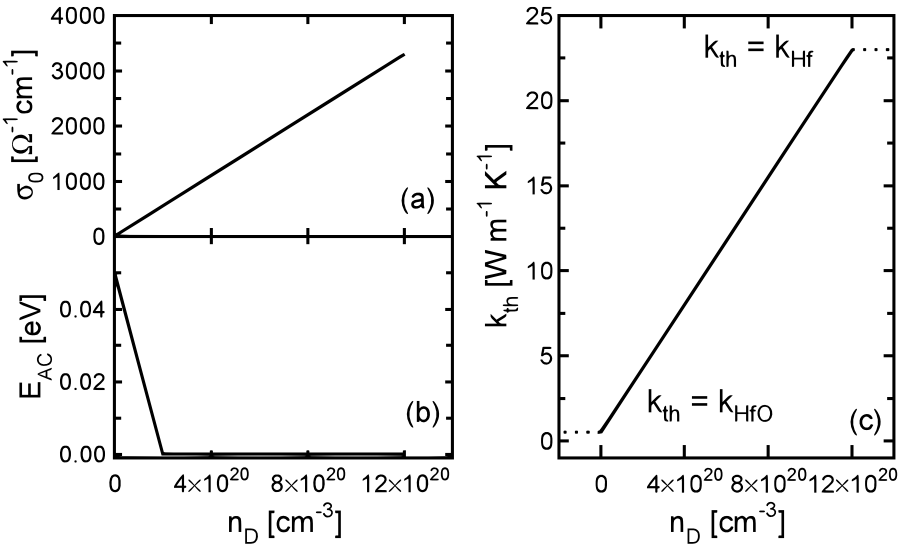

Figure 20. (a) Electrical conductivity pre-exponential factor σ_0, (b) activation energy for conduction E_{AC}, and (c) thermal conductivity kth as a function of local doping density n_D. [Larentis 1]

Insight of the ion migration and redox reaction have been observed with ab-initio calculations. These mechanisms, basis of the CBRAM switching, have also been simulated using Butler-Volmer equations for redox reactions and Mott-Gurney laws for ion migration [AChen 1, Valov 2].
All these physical models can be seen as blocks precisely describing small aspects of the CBRAM operation and which can be combined to describe the global behavior of the device.

10.2 Device simulation

Several simulation protocols have been studied in order to simulate the CBRAM switching mechanisms with various degrees of accuracy. The large majority of the CBRAM simulations relies on continuous modelling, computing Butler-Volmer, Mott Gurney and Poole-Frenkel equations. These simulations compute the filament growth from the incoming flux of oxidized and migrating ions. Depending on the growth speed and coupled to an electrical conduction model they offer a good modeling of Forming and SET operations [Valov 2, Shaoli 1, SLin 1]. Figure 21 exposes one of these models. The physical mechanisms that are redox reaction and ions migration have also been computed using the Transition State Theory (TST) [Larentis 1, Russo 1] or diffusion coefficient method similar to Fick laws [Qin]. From the calculation of the migration, the filament growth is computed and Forming/SET obtained as previously stated. Mathematical variations of the solving procedures have been developed to simulate the CBRAM writing process with TCAD and level set method [Dorion 1].
In opposition to continuous models, discrete models based on Kinetic Monte Carlo (KMC) simulation have also been developed to compute the writing process. The first one-dimensional approach have been proposed by Adesto Technologies [Jameson 3] and relies on the individual

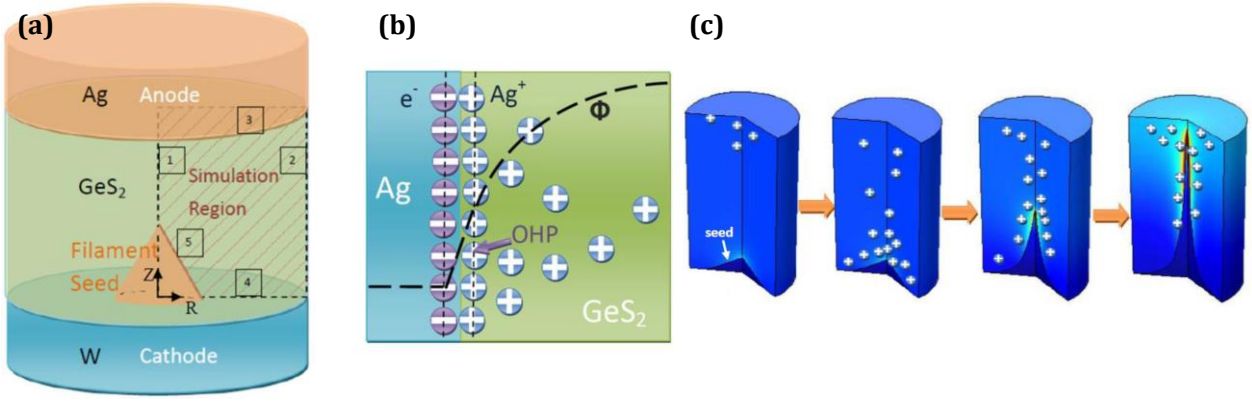

Figure 21. (a) Schematic view of the simulated CBRAM cell. (b) Electrostatic potential Φ across the electric double layer and charge accumulation. (c) Filament growth during the simulated forming process. [SLin 1]

treatment of each migrating ions on their way to form the conductive filament. This approach offered interesting result and linked material properties to the device behavior. Following a similar KMC method, a two dimensional model have been proposed to compute the filament growth considering more physical mechanisms [Pan 1]. Figure 22 shows the evolution between the two models.

The CBRAM modeling is greatly developed, however only the SET operation have been widely treated and the RESET, cycling and data retention are still lacking comprehensive models.

Only a few studies regarding the RESET operation have been proposed as it requires an advanced understanding of the physical mechanisms involved. RESET operations have been simulated using the same approach than SET with limited accuracy [YLin 1, Palma 1]. However, by adding a thermal component to the continuous models, improved RESET operation simulations have been presented [Menzel 1, SLin 1]. Table 2 summarizes the most notable publications regarding device simulations. It clearly shows the lack of endurance and retention modeling and the strong dominance of continuous model over statistical approach. The physical properties included in the models are also still limited.

The device simulation first goal is to improve the understanding of the technology. However, from the simulation of a single device behavior is it possible to extend the simulation to a large number of devices and study the potential integration of CBRAM cells.

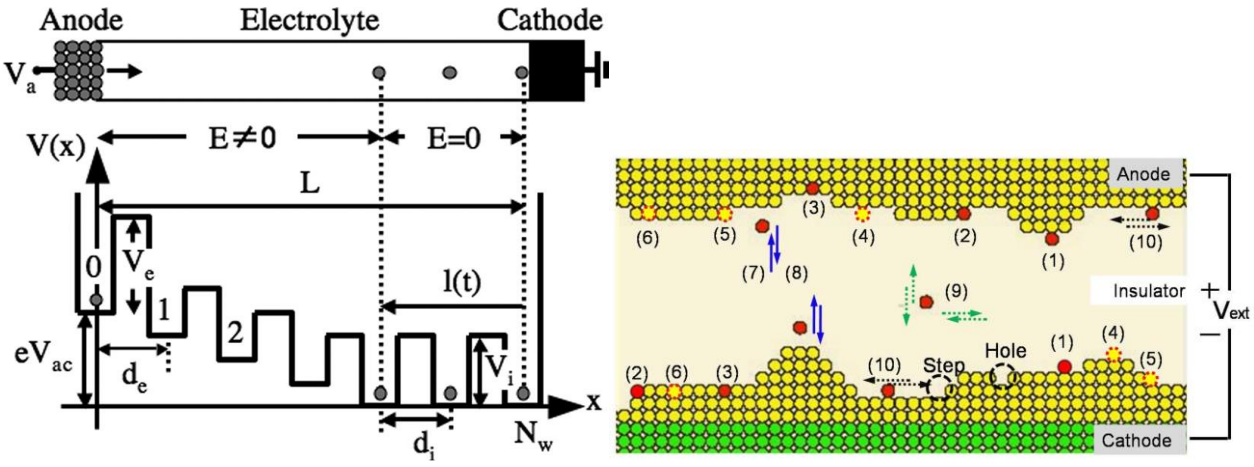

Figure 22. Schematic representation of both KMC approach of the Forming operation either in one dimension [Jameson 1] (left) or two dimensions [Pan 1] (right). More physical mechanisms are also considered in the 2 dimensions KMC.

Table 3. Developed CBRAM models with the simulated operations, and the physical phenomena and properties integrated.

Reference	Switching equations	Model type	Simulated operation	Electrical Conduction mechanisms	Thermal effects	Physical properties links
[Shaoli 1]	Butler Volmer Mott Gurney	Continuous	Forming/SET	None	None	None
[Jameson 3]	TST	Statistical	SET	None	None	Electrodes work functions
[Dorion 1]	Butler Volmer Mott Gurney	Continuous	SET	Electrical conductivity	None	None
[Russo 1]	TST	Continuous	SET	Electrical conductivity	Joule Heating	None
[Pan 1]	TST Butler Volmer	Statistical	SET	N/A	None	None
[Menzel 1]	Butler Volmer	Continuous	RESET	Electrical conductivity	Joule Heating	Thermal conduction Electrical conductivity
[Ylin 1]	Current summation	Continuous	RESET	Tunneling current Ohmic current	None	None
[Slin 1]	Butler Volmer Pool Frenkel	Continuous	SET / RESET	None	None	None
[Palma 1]	Butler Volmer Mott Gurney	Continuous	SET / RESET	Electrical conductivity	None	None
[Larentis 1]	TST Pool Frenkel	Continuous	SET / RESET	Electrical conductivity	Joule Heating Wiedemann–Franz	Thermal conduction Electrical conductivity

10.3 Circuit simulation

The CBRAM simulation can also be seen as a way to mathematically reproduce the electrical behavior of the cell without attaching importance to the physical exactitude of the model. These kind of model, called compact models, uses strongly simplified approaches of the device simulation previously exposed. The goal of these models is no longer to enhance the understanding of the CBRAM technology but rather to offer the simplest approach in order to get incorporated in circuit simulators. Several compact models have been developed, each offering different accuracy and simplicity level [Yu 1, Reyboz 1, Reyboz 2].

Circuit simulation aims to prove the feasibility of certain circuit with the available technology or to extract the CBRAM electrical characteristics required for the circuit to work. The feasibility aspect of the simulation can concern the integration of a large number of cells and extract the expected performances [Zahurak 1] or the introduction of a new circuit allowing 3D stacking [YWang 1]. Another aspect of the feasibility resides in taking advantage of the strength of the CBRAM to invent or reinvent new circuits. Several new circuit designs such as reconfigurable logic [Palma 2], FPGA [Vianello 2] or non-volatile Flip-Flop [Onkaraiah 1] have been presented and benefits from the CBRAM specificities: non-volatility, high memory margin and fast

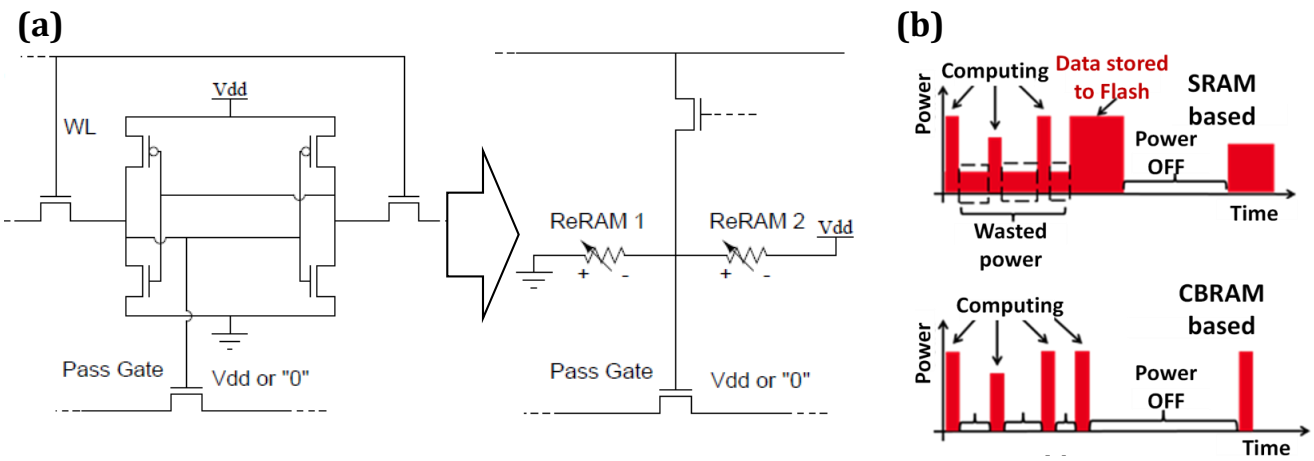

Figure 23. (a) Circuit integrating CBRAM devices in reprogrammable cell to replace CMOS transistor. (b) power consumption reduction induced by this transition [Palma 2].

switching. Figure 23 shows an example of non-volatile flip flop circuit integrating CBRAM devices to reduce the power consumption and occupied surface. This circuit integration replaces 5 CMOS transistors by 2 CBRAM devices in order to store the state of the reprogrammable cell. (Figure 23 (a)). The power consumption reduction is carried in two stages, firstly by integrating non-volatile memory no power is required to refresh the reprogrammable cell state and secondly once the power is turned off, there is no need to store the reprogrammable cell state on flash memory (Figure 23 (b)).

The unique traits of the CBRAM and RRAM globally have also led to the great increase in neuromorphic computation. Using the CBRAM low power consumption and multi-level storage, circuit simulations have been proposed as an alternative approach to neuromorphic systems [Suri 1, Suri 2].

In its current state the CBRAM technology has still to be improved in certain areas to compete with the Flash memory. The circuit simulation offers a wide array of present applications and future possibilities one step ahead of the technology state. This field of simulation pull the technology characteristics toward precise target in function of the applications and offers new ways to exploit the CBRAM strengths.

11.Chapter I synthesis

The RRAM technology offers great advantages in terms of performances, density, and integration in the back end of logic process to compete against the Flash technology. The RRAM

technology founds the data storage on the resistance modification of a solid electrolyte. Various physical mechanisms can explain the resistance modifications but the CBRAM technology relies on the formation and dissolution of a metallic conductive filament whereas oxygen vacancies are creating the conductive path in the OxRAM technology. OxRAM and CBRAM devices have grown apart during the early stage of development with CBRAM based on chalcogenides and OxRAM on oxides. However, the CBRAM technology has then gradually transitioned toward oxides reducing the differences between both technologies. This transition occurred recently as three years ago at the beginning of this research work, the main CBRAM researches were focus on chalcogenide based CBRAM. The transition to oxide based CBRAM was made to offer strong stability at high temperature, great data retention and better compatibility with CMOS process. Nevertheless, this transition also came with a degradation of performances: higher voltages, reduced endurance and requirement of a high energetic Forming step. A long work of optimization and has since then been carried out by various research teams all around the globe to solve the last technical limitations of this technology. At the same time, the physical mechanisms ruling the CBRAM switching process and electrical conduction are still misunderstood and requires deep analyses. To solve these physical questions lots of simulation works have been published at various levels of understanding, from deep physics with ab-initio calculations to switching behavior at device scale. However, while the current state of understanding have been greatly enhanced, a comprehensive understanding is still missing.

In an attempt to clarify the CBRAM behavior at both device and deep physics scale, a strongly correlated study have been carried out on electrical/physical characterization and model development. Taking advantage of the CEA-Leti processing and characterization capabilities, this research work aims to propose a comprehensive understanding of CBRAM based on experimental results. As summarized in Table 1, the CBRAM modeling has been mainly focused on the SET and slightly on the RESET operation. In this manuscript, a comprehensive model of SET, RESET, Endurance and Data Retention will be presented. Taking advantage of a statistical approach, the model also offers the simulation of the device variability and reliability. This model aims to create a bond between material properties, physical parameters and devices behavior, which coupled to experimental results allows to understand the complete behavior of the CBRAM technology. All

the concerns of the CBRAM technology developed in this chapter will be addressed, and theoretical and experimental optimizations will be proposed.

For the sake of clarity each step of the CBRAM life-cycle will be describe in a proper chapter. First, the second chapter will focus on describing the studied samples and the characterization method that will be used to address the CBRAM behavior. This chapter will serve as basis to all devices tested and experimental results presented in the following of the manuscript.

Then, in the third chapter, the unified model developed will be fully described in term of involved physics and resolution progression. The several evolutions and updates of the model will be presented and will serve similarly to the second chapter as reference for the following of the manuscript. The rest of the manuscript will be strictly focused on addressing the different operations relative to the CBRAM.

The fourth chapter will treat the basics operation Forming, SET and RESET with an intensive study of the technological and physical factors involved in the CBRAM behavior.

The fifth chapter will be focused on cycling and reliability, one of the last limitation to the CBRAM industrialization. A comprehensive understanding of the intrinsic and cell to cell variability of LRS and HRS will be discussed, and endurance optimization ways will be presented.

The sixth chapter will analyze the data retention behavior which has been driving the CBRAM studies during the last past years. This chapter will propose an understanding and optimizations of the data retention behavior correlated to the operating conditions.

Finally, the seventh and last chapter will serve a comprehensive synthesis of the work presented in this manuscript. The great importance of the conductive filament morphology will be discussed through all the experimental and theoretical results obtained during this research work.

Chapter I references

[AChen 1] An Chen, James Hutchby, Victor Zhirnov, George Bourianoff, John Wiley & Sons, “Emerging Nanoelectronic Devices”, 2015. Web. 2 Oct. 2015.

[Ambrust 1] Michael Armbrust, Armando Fox, Rean Griffith, Anthony D. Joseph, Randy Katz, Andy Konwinski, Gunho Lee, David Patterson, Ariel Rabkin, Ion Stoica, And Matei Zaharia, “A View of Cloud Computing”, Communications Of The Acm, Vol. 53, No. 4, April 2010

[Aratani 1] Aratani, K.; Ohba, K.; Mizuguchi, T.; Yasuda, S.; Shiimoto, T.; Tsushima, T.; Sone, T.; Endo, K.; Kouchiyama, A.; Sasaki, S.; Maesaka, A.; Yamada, N.; Narisawa, H., "A Novel Resistance Memory with High Scalability and Nanosecond Switching," in Electron Devices Meeting, 2007. IEDM 2007. IEEE International , vol., no., pp.783-786, 10-12 Dec. 2007

[Bellisario 1] D. O. Bellisario, Z. Ulissi, and M. S. Strano, “A quantitative and predictive model of electromigrationinduced breakdown of metal nanowires,” The Journal of Physical Chemistry C, vol. 117, no. 23, pp. 12373– 12378, Jun. 2013.

[Belmonte 1] Belmonte, A.; Kim, W.; Chan, B.; Heylen, N.; Fantini, A.; Houssa, M.; Jurczak, M.; Goux, L., "90nm WAl2O3TiWCu 1T1R CBRAM cell showing low-power, fast and disturb-free operation," in Memory Workshop (IMW), 2013 5th IEEE International , vol., no., pp.26-29, 26-29 May 2013

[Benoist 1] A. Benoist, S. Blonkowski, S. Jeannot, S. Denorme, J. Damiens, J. Berger, P. Candelier, E. Vianello, H. Grampeix, J. Nodin, E. Jalaguier, L. Perniola, and B. Allard, “28nm advanced CMOS resistive RAM solution as embedded non-volatile memory,” IEEE International Reliability Physics Symposium, 2014.

[Bocquet 1] M. Bocquet, D. Deleruyelle, H. Aziza, C. Muller, J.-M. Portal, T. Cabout, and E. Jalaguier, “Robust compact model for bipolar oxide-based resistive switching memories,” IEEE Transactions on Electron Devices, vol. 61, no. 3, pp. 674–681, Mar. 2014

[Charentenay 1] Y. De Charentenay, “Emerging NVM enter niche memory markets; expected to reach 2B by 2018. Will NVM eventually replace DRAM and NAND?”, LETI Memory Workshop, 2013

[Choi 1] Sang-Jun Choi; Lee, Jung-Hyun; Hyung-Jin Bae; Woo-Young Yang; Tae-Wan Kim; Ki-Hong Kim, "Improvement of CBRAM Resistance Window by Scaling Down Electrode Size in Pure-GeTe Film," in Electron Device Letters, IEEE , vol.30, no.2, pp.120-122, Feb. 2009.

[Chung 1] L. Chung, “Chart courtesy of Dr. Chung Lam”, IBM Research updated version of plot from IBM Journal R&D article, 2010

[CJKim 1] Kim C-J, Yoon S-G, Choi K-J, Ryu S-O, Yoon S-M, Lee N-Y and Yu B-G 2006 Characterization of silver-saturated Ge–Te chalcogenide thin films for nonvolatile random access memory J. Vac. Sci. Technol. B 24 721

[Cong 1] Cong Xu; Niu, D.; Muralimanohar, N.; Jouppi, N.P.; Yuan Xie, "Understanding the trade-offs in multi-level cell ReRAM memory design," in Design Automation Conference (DAC), 2013 50th ACM/EDAC/IEEE , vol., no., pp.1-6, May 29 2013-June 7 2013

[Courtade 1]L. Courtade, C. Turquat, C. Muller, J. Lisoni, L. Goux, D. Wouters, D. Goguenheim, P. Roussel, and L. Ortega, “Oxidation kinetics of Ni metallic films: Formation of NiO-based resistive switching structures,” Thin Solid Films, vol. 516, no. 12, pp. 4083–4092, Apr. 2008

[Degraeve 1] R. Degraeve, A. Fantini, S. Clima, B. Govoreanu, L. Goux, Y. Y. Chen, D. Wouters, P. Roussel, G. Kar, G. Pourtois, S. Cosemans, J. Kittl, G. Groeseneken, M. Jurczak, and L. Altimime, “Dynamic ‘hour glass’ model for SET and RESET in HfO_2 RRAM,” IEEE Symposium on VLSI Technology, pp. 75–76, Jun. 2012.

[Deleruyelle 1] D. Deleruyelle, Magalie Putero, T. Ouled-Khachroum, Marc Bocquet, M.V. Coulet, et al., “Ge2Sb2Te5 layer used as solid electrolyte in conductive-bridge memory devices fabricated on flexible substrate”, Solid-State Electronics, Elsevier, 2012.

[Dietrich 1] Dietrich, S.; Angerbauer, M.; Ivanov, M.; Gogl, D.; Hoenigschmid, H.; Kund, M.; Liaw, C.; Markert, M.; Symanczyk, R.; Altimime, L.; Bournat, S.; Mueller, G., "A Nonvolatile 2-Mbit CBRAM Memory Core Featuring Advanced Read and Program Control," in Solid-State Circuits, IEEE Journal of , vol.42, no.4, pp.839-845, April 2007

[Dimin 1] Dimin Niu; Qiaosha Zou; Cong Xu; Yuan Xie, "Low power multi-level-cell resistive memory design with incomplete data mapping," in Computer Design (ICCD), 2013 IEEE 31st International Conference on , vol., no., pp.131-137, 6-9 Oct. 2013

[Dorion 1] Dorion, P.; Cueto, O.; Reyboz, M.; Vianello, E.; Barbe, J.C.; Grigoriu, A.; Maday, Y., "Simulation of CBRAM devices with the level set method," in Simulation of Semiconductor Processes and Devices (SISPAD), 2013 International Conference on , vol., no., pp.340-343, 3-5 Sept. 2013

[EChen 1] E. Chen, D. Apalkov, Z. Diao, A. Driskill-Smith, D. Druist, D. Lottis, V. Nikitin, X. Tang, S. Watts, S. Wang, S. a. Wolf, a. W. Ghosh, J. W. Lu, S. J. Poon, M. Stan, W. H. Butler, S. Gupta, C. K. a. Mewes, T. Mewes, and P. B. Visscher, “Advances and future prospects of spin-transfer torque random access memory,” IEEE Transactions on Magnetics, vol. 46, no. 6, pp. 1873–1878, Jun. 2010

[Fang 1] Z. Fang, X. Wang, J. Sohn, B. Weng, Z. Zhang, Z. Chen, Y. Tang, G.-Q. Lo, J. Provine, S. Wong, H.-. Wong, and D.-L. Kwong, “The role of Ti capping layer in HfO_x-based RRAM devices,” IEEE Electron Device Letters, pp. 1–3, 2014

[Fujitsu 1] Fujitsu, “8/2/2006 Fujitsu Press Release”, http://www.fujitsu.com/us/about/resources/news/press-releases/2006/fma-20060802.html

[Gao 1] B. Gao, B. Sun, H. Zhang, L. Liu, X. Liu, R. Han, J. Kang, and B. Yu, “Unified physical model of bipolar oxidebased resistive switching memory,” IEEE Electron Device Letters, vol. 30, no. 12, pp. 1326–1328, Dec. 2009.

[Goux 1] Goux, L.; Sankaran, K.; Kar, G.; Jossart, N.; Opsomer, K.; Degraeve, R.; Pourtois, G.; Rignanese, G.-M.; Detavernier, C.; Clima, S.; Chen, Y.-Y.; Fantini, A.; Govoreanu, B.; Wouters, D.J.; Jurczak, M.; Altimime, L.; Kittl, J.A., "Field-driven ultrafast sub-ns programming in WAl2O3TiCuTe-based 1T1R CBRAM system," in VLSI Technology (VLSIT), 2012 Symposium on , vol., no., pp.69-70, 12-14 June 2012

[Goux 2] Goux, L.; Fantini, A.; Redolfi, A.; Chen, C.Y.; Shi, F.F.; Degraeve, R.; Chen, Y.Y.; Witters, T.; Groeseneken, G.; Jurczak, M., "Role of the Ta scavenger electrode in the excellent switching control and reliability of a scalable low-current operated TiN\Ta_2O_5\Ta RRAM device," in VLSI Technology (VLSI-Technology): Digest of Technical Papers, 2014 Symposium on , vol., no., pp.1-2, 9-12 June 2014

[Goux 3] Goux, L.; Opsomer, K.; Schuitema, R.; Degraeve, R.; Muller, R.; Detavernier, C.; Wouters, D.J.; Jurczak, M.; Altimime, L.; Kittl, J.A., "Self-Limited Filament Formation and Low-Power Resistive Switching in $CuxTe_{1-x}/Al_2O_3$/Si CBRAM Cell," in Memory Workshop (IMW), 2011 3rd IEEE International , vol., no., pp.1-4, 22-25 May 2011.

[Govoreanu 1] B. Govoreanu, G. Kar, Y. Chen, V. Paraschiv, S. Kubicek, A. Fantini, I. P. Radu, L. Goux, S. Clima, R. Degraeve, N. Jossart, O. Richard, T. Vandeweyer, K. Seo, P. Hendrickx, G. Pourtois, H. Bender, L. Altimime, D. Wouters, J. Kittl, and M. Jurczak, “$10\times10nm^2$ Hf/HfO_x crossbar resistive RAM with excellent performance, reliability and low-energy operation,” IEEE International Electron Devices Meeting Technical Digest, pp. 729–732, 2011

[Govoreanu 2] B. Govoreanu, S. Clima, I. Radu, Y.-Y. Chen, D. Wouters, and M. Jurczak, “Complementary role of field and temperature in triggering ON/OFF switching mechanisms in Hf/HfO_2 resistive RAM cells,” IEEE Transactions on Electron Devices, vol. 60, no. 8, pp. 2471–2478, 2013.

[Guan 1] X. Guan, Y. Shimeng, and H.-S. Philip Wong, “On the witching parameter variation of metal-oxide RRAM—Part I: physical modeling and simulation methodology,” IEEE Transactions on Electron Devices, vol. 59, no. 4, pp. 1172–1182, 2012.

[Guy 1] Guy, J.; Molas, G.; Blaise, P.; Carabasse, C.; Bernard, M.; Roule, A.; Le Carval, G.; Sousa, V.; Grampeix, H.; Delaye, V.; Toffoli, A.; Cluzel, J.; Brianceau, P.; Pollet, O.; Balan, V.; Barraud, S.; Cueto, O.; Ghibaudo, G.; Clermidy, F.; De Salvo, B.; Perniola, L., "Experimental and theoretical understanding of Forming, SET and RESET operations in Conductive Bridge RAM (CBRAM) for memory stack optimization," in Electron Devices Meeting (IEDM), 2014 IEEE International , vol., no., pp.6.5.1-6.5.4, 15-17 Dec. 2014.

[Hilbert 1] M. Hilbert and P. López, “The world’s technological capacity to store, communicate, and compute information.” Science (New York, N.Y.), vol. 332, no. 6025, pp. 60–5, Apr. 2011

[Hsu 1] Chung-Wei Hsu; Chia-Chen Wan; I-Ting Wang; Mei-Chin Chen; Chun-Li Lo; Yao-Jen Lee; Wen-Yueh Jang; Chen-Hsi Lin; Tuo-Hung Hou, "3D vertical TaOx/TiO2 RRAM with over 10^3 self-rectifying ratio and sub-μA operating current," in Electron Devices Meeting (IEDM), 2013 IEEE International , vol., no., pp.10.4.1-10.4.4, 9-11 Dec. 2013.

[Hyun 1] Sung Hyun Jo; Kumar, T.; Narayanan, S.; Lu, W.D.; Nazarian, H., "3D-stackable crossbar resistive memory based on Field Assisted Superlinear Threshold (FAST) selector," in Electron Devices Meeting (IEDM), 2014 IEEE International , vol., no., pp.6.7.1-6.7.4, 15-17 Dec. 2014

[ISSCC 1] ISSCC, “MEMORY – 2013 Trends”, International Solid-State Circuits Conference, February 2013

[ITRS 1] International Technology Roadmap for Semiconductors (ITRS), “Emerging research devices,” 2013

[Jameson 1] Jameson, J.R.; Gilbert, N.; Koushan, F.; Saenz, J.; Wang, J.; Hollmer, S.; Kozicki, M.; Derhacobian, N., "Quantized Conductance in Ag/GeS_2/W Conductive-Bridge Memory Cells," in Electron Device Letters, IEEE , vol.33, no.2, pp.257-259, Feb. 2012

[Jameson 2] Jameson, J.R.; Blanchard, P.; Cheng, C.; Dinh, J.; Gallo, A.; Gopalakrishnan, V.; Gopalan, C.; Guichet, B.; Hsu, S.; Kamalanathan, D.; Kim, D.; Koushan, F.; Kwan, M.; Law, K.; Lewis, D.; Ma, Y.; McCaffrey, V.; Park, S.; Puthenthermadam, S.; Runnion, E.; Sanchez, J.; Shields, J.; Tsai, K.; Tysdal, A.; Wang, D.; Williams, R.; Kozicki, M.N.; Wang, J.; Gopinath, V.; Hollmer, S.; Van Buskirk, M., "Conductive-bridge memory (CBRAM) with excellent high-temperature retention," in Electron Devices Meeting (IEDM), 2013 IEEE International , vol., no., pp.30.1.1-30.1.4, 9-11 Dec. 2013

[Jameson 3] Jameson, J., Gilbert, N., Koushan, F., Saenz, J., Wang, J., Hollmer, S. and Kozicki, M., “One-dimensional model of the programming kinetics of conductive-bridge memory cells”, Appl. Phys. Lett., 99(6), p.063506.

[Jullière 1] M. Jullière, "Tunneling between ferromagnetic films," Phys. Lett. A., vol. 54, pp. 225-226, 1975

[JYi 1] Jaeyun Yi; Hyejung Choi; Seunghwan Lee; Jaeyeon Lee; Donghee Son; Sangkeum Lee; Sangmin Hwang; Seokpyo Song; Park, Jinwon; Sookjoo Kim; Wangee Kim; Ja-Yong Kim; Sunghoon Lee; Jiwon Moon; Jinju You; Moonsig Joo; JaeSung Roh; SungKi Park; Chung, Sung-Woong; Junghoon Lee; Hong, Sung-Joo, "Highly reliable and fast nonvolatile hybrid switching ReRAM memory using thin Al2O3 demonstrated at 54nm memory array," in VLSI Technology (VLSIT), 2011 Symposium on , vol., no., pp.48-49, 14-16 June 2011

[Kamiya 1]Kamiya, K., Young Yang, M., Park, S., Magyari-Köpe, B., Nishi, Y., Niwa, M. and Shiraishi, K., “ON-OFF Switching Mechanism Of Resistive–Random–Access–Memories Based On The Formation And Disruption Of Oxygen Vacancy Conducting Channels”, Appl. Phys. Lett. 100.7 (2012): 073502. Web. 2 Oct. 2015.

[Kianian 1] S. Kianian, G. Rosendale, M. Manning, D. Hamilton, X. Huang, K. Robinson, Y. Kim, and T. Rueckes, “A 3D stackable carbon nanotube-based nonvolatile memory (NRAM),” IEEE European Solid State Device Research Conference, pp. 404–407, 2010

[Kozicki 1] Michael N. Kozicki, William C. West, “PROGRAMMABLE METALLIZATION CELL STRUCTURE AND METHOD OF MAKING SAME”, US Patent 5 761 115, June 2, 1998.

[Kund 1] Kund, M.; Beitel, G.; Pinnow, C.-U.; Rohr, T.; Schumann, J.; Symanczyk, R.; Ufert, K.-D.; Muller, G., "Conductive bridging RAM (CBRAM): an emerging non-volatile memory technology scalable to sub 20nm," in Electron Devices Meeting, 2005. IEDM Technical Digest. IEEE International , vol., no., pp.754-757, 5-5 Dec. 2005

[Larcher 1] L. Larcher, A. Padovani, O. Pirrotta, L. Vandelli, and G. Bersuker, “Microscopic understanding and modeling of HfO_2 RRAM device physics,” IEEE International Electron Devices Meeting Technical Digest, p. 20.1.1, 20.1.4, 2012.

[Larentis 1] S. Larentis, F. Nardi, S. Balatti, D. C. Gilmer, and D. Ielmini, “Resistive switching by voltage-driven ion migration in bipolar RRAM — Part II : modeling,” IEEE Transactions on Electron Devices, vol. 59, no. 9, pp. 2468–2475, 2012.

[Lee 1] M.-J. Lee, C. B. Lee, D. Lee, S. R. Lee, M. Chang, J. H. Hur, Y.-B. Kim, C.-J. Kim, D. H. Seo, S. Seo, U.-I. Chung, I.-K. Yoo, and K. Kim, “A fast, high-endurance and scalable non-volatile memory device made from asymmetric $Ta2O_{(5-x)}/TaO_{(2-x)}$ bilayer structures,” Nature materials, vol. 10, no. 8, pp. 625–30, Aug. 2011

[Liu 1] Liu, Qi; Long, Shibing; Wang, Wei; Qingyun Zuo; Sen Zhang; Junning Chen; Liu, Ming, "Improvement of Resistive Switching Properties in ZrO_2-Based ReRAM With Implanted Ti Ions," in Electron Device Letters, IEEE , vol.30, no.12, pp.1335-1337, Dec. 2009

[Liu 2] Liu, Qi; Liu, Ming; Long, Shibing; Wang, Wei; Manhong Zhang; Qin Wang; Junning Chen, "Improvement of resistive switching properties in ZrO2- based ReRAM with implanted metal ions," in Solid State Device Research Conference, 2009. ESSDERC '09. Proceedings of the European**,** vol., no., pp.221-224, 14-18 Sept. 2009.

[Long 1] S. Long, X. Lian, C. Cagli, X. Cartoixà, R. Rurali, E. Miranda, D. Jiménez, L. Perniola, M. Liu, and J. Suñé, “Quantum-size effects in hafnium-oxide resistive switching,” Applied Physics Letters, vol. 102, no. 18, p. 183505, 2013.

[Maikap 1] Maikap, S.; Rahaman, S.Z.; Wu, T.Y.; Chen, F.; Kao, M.J.; Tsai, M.J., "Low current (5 pA) resistive switching memory using high-κ Ta2O5 solid electrolyte," in Solid State Device Research Conference, 2009. ESSDERC '09. Proceedings of the European, vol., no., pp.217-220, 14-18 Sept. 2009

[Menzel 1] Menzel, S.; Valov, I.; Waser, R.; Adler, N.; van den Hurk, J.; Tappertzhofen, S., "Simulation of polarity independent RESET in electrochemical metallization memory cells," in Memory Workshop (IMW), 2013 5th IEEE International , vol., no., pp.92-95, 26-29 May 2013

[Molas 1] Molas, G.; Vianello, E.; Dahmani, F.; Barci, M.; Blaise, P.; Guy, J.; Toffoli, A.; Bernard, M.; Roule, A.; Pierre, F.; Licitra, C.; De Salvo, B.; Perniola, L., "Controlling oxygen vacancies in doped oxide based CBRAM for improved memory performances," in Electron Devices Meeting (IEDM), 2014 IEEE International , vol., no., pp.6.1.1-6.1.4, 15-17 Dec. 2014

[Muller 1] C. Muller, "Mémoires ferroélectriques FRAM : principe, limitations, innovations, applications." in Diélectriques ferroélectriques intégrés sur silicium, Hermès science, 2011, pp. 425-451

[Onkaraiah 1] S. Onkaraiah, O. Turkylmaz, M. Reyboz, F. Clermidy, J. Portal, and C. Muller, “An hybrid cbram/cmos look-up-table structure for improving performance effi- ciency of field programmable gate array,” in To be published in Proceedings of Symposium on Circuits and Systems (ISCAS), 2013 IEEE International, 2013.

[Palma 1] Palma, G.; Vianello, E.; Cagli, C.; Molas, G.; Reyboz, M.; Blaise, P.; De Salvo, B.; Longnos, F.; Dahmani, F., "Experimental Investigation and Empirical Modeling of the Set and Reset Kinetics of Ag-GeS2 Conductive Bridging Memories," in Memory Workshop (IMW), 2012 4th IEEE International , vol., no., pp.1-4, 20-23 May 2012.

[Palma 2] Palma, G.; Vianello, E.; Thomas, O.; Suri, M.; Onkaraiah, S.; Toffoli, A.; Carabasse, C.; Bernard, M.; Roule, A.; Pirrotta, O.; Molas, G.; De Salvo, B., "Interface Engineering of Ag-GeS_2-Based Conductive Bridge RAM for Reconfigurable Logic Applications," in Electron Devices, IEEE Transactions on , vol.61, no.3, pp.793-800, March 2014.

[Pan 1] Feng Pan; Shong Yin; Subramanian, Vivek, "A Comprehensive Simulation Study on Metal Conducting Filament Formation in Resistive Switching Memories," in Memory Workshop (IMW), 2011 3rd IEEE International , vol., no., pp.1-4, 22-25 May 2011.

[Pandian 1] Pandian R, Kooi B J, Palasantzas G, De Hosson J T M and Pauza A 2007 Polarity-dependent reversible resistance switching in Ge–Sb–Te phase-change thin films Appl. Phys. Lett. 91 152103

[Qin 1] Shengjun Qin; Jinyu Zhang; Zhiping Yu, "A unified model of metallic filament growth dynamics for conductive-bridge random access memory (CBRAM)," in Simulation of Semiconductor Processes and Devices (SISPAD), 2013 International Conference on , vol., no., pp.344-347, 3-5 Sept. 2013

[Rahaman 1] Rahaman, S. Z. and Maikap, S. and Chen, W. S. and Lee, H. Y. and Chen, F. T. and Tien, T. C. and Tsai, M. J., “Impact of TaOx nanolayer at the GeSex/W interface on resistive switching memory performance and investigation of Cu nanofilament”, Journal of Applied Physics, 111, 063710 (2012),

[Reyboz 1] Reyboz, M.; Onkaraiah, S.; Palma, G.; Vianello, E.; Perniola, L., "Compact model of a CBRAM cell in Verilog-A," in Non-Volatile Memory Technology Symposium (NVMTS), 2012 12th Annual**,** vol., no., pp.94-97, Oct. 31 2012-Nov. 2 2012

[Reyboz 2] Reyboz, M.; Jovanovic, N.; Longnos, F.; Vianello, E.; Thomas, O.; Clermidy, F.; Molas, G.; Onkaraiah, S.; Portal, J.-M.; Muller, C., "From compact model to innovative circuit design of Ag-GeS_2 conductive bridge memories," in Memory Workshop (IMW), 2014 IEEE 6th International , vol., no., pp.1-4, 18-21 May 2014

[Russo 1] Russo, U.; Kamalanathan, D.; Ielmini, D.; Lacaita, A.L.; Kozicki, M.N., "Study of Multilevel Programming in Programmable Metallization Cell (PMC) Memory," in Electron Devices, IEEE Transactions on , vol.56, no.5, pp.1040-1047, May 2009

[Sakamoto 1] Sakamoto T, Banno N, Iguchi N, Kawaura H, Sunamura H, Fujieda S, Terabe K, Hasegawa T and Aono M 2007 A Ta2O5 solid-electrolyte switch with improved reliability Symp. on VLSI Technology Dig. of Tech. Papers p 38

[Sakamoto 2] Sakamoto, T., Lister, K., Banno, N., Hasegawa, T., Terabe, K. and Aono, M., “Electronic transport in Ta_2O_5 resistive switch”,. Appl. Phys. Lett., 91(9), p.092110.

[Sankaran 1] Sankaran, K., Goux, L., Clima, S., Mees, M., Kittl, J., Jurczak, M., Altimime, L., Rignanese, G. and Pourtois, G., “Modeling of Copper Diffusion in Amorphous Aluminum Oxide in CBRAM Memory Stack”, ECS Transactions, 45(3), pp.317-330.

[Shaoli 1] Shaoli Lv; Jun Liu; Lingling Sun; He Wang; Jinyu Zhang; Zhiping Yu, "An analytical model for predicting forming/switching time in conductive-bridge resistive random-access memory (CBRAM)," in Simulation of Semiconductor Processes and Devices (SISPAD), 2013 International Conference on , vol., no., pp.364-367, 3-5 Sept. 2013

[Shih 1] Y.-H. Shih, "3D charge trapping (CT) NAND Flash," Sematech symposium, 2011.

[SLin 1] Sen Lin; Liang Zhao; Jinyu Zhang; Huaqiang Wu; Yan Wang; He Qian; Zhiping Yu, "Electrochemical simulation of filament growth and dissolution in conductive-bridging RAM (CBRAM) with cylindrical coordinates," in Electron Devices Meeting (IEDM), 2012 IEEE International , vol., no., pp.26.3.1-26.3.4, 10-13 Dec. 2012

[Suga 1] H. Suga, T. Sumiya, M. Horikawa, S. Kumaragurubaran, T. Shimizu, and Y. Naitoh, "Threshold Current Density of the Resistance Switching in Pt Nanogap Electrode," Japanese Journal of Applied Physics, vol. 50, no. 6, p. 06GF11, Jun. 2011.

[Sune 1] Sune, J.; Long, S.; Cagli, C.; Perniola, L.; Lian, X.; Cartoixa, X.; Rurali, R.; Miranda, E.; Jimenez, D.; Liu, M., "Electrical evidence of atomic-size effects in the conduction filament of RRAM," in Solid-State and Integrated Circuit Technology (ICSICT), 2012 IEEE 11th International Conference on , vol., no., pp.1-4, Oct. 29 2012-Nov. 1 2012

[Suri 1] Suri, M.; Bichler, O.; Querlioz, D.; Palma, G.; Vianello, E.; Vuillaume, D.; Gamrat, C.; DeSalvo, B., "CBRAM devices as binary synapses for low-power stochastic neuromorphic systems: Auditory (Cochlea) and visual (Retina) cognitive processing applications," in Electron Devices Meeting (IEDM), 2012 IEEE International , vol., no., pp.10.3.1-10.3.4, 10-13 Dec. 2012

[Suri 2] Suri, M.; Querlioz, D.; Bichler, O.; Palma, G.; Vianello, E.; Vuillaume, D.; Gamrat, C.; DeSalvo, B., "Bio-Inspired Stochastic Computing Using Binary CBRAM Synapses," in Electron Devices, IEEE Transactions on , vol.60, no.7, pp.2402-2409, July 2013

[SWKim 1] Kim S-W and Nishi Y 2007 Copper sulfide-based resistance change memory Proc. Non-Volatile Memory Symp. (NVMTS) p 75

[Tada 1] Tada, M.; Sakamoto, T.; Okamoto, K.; Miyamura, M.; Banno, N.; Katoh, Y.; Ishida, S.; Iguchi, N.; Sakimura, N.; Hada, H., "Polymer solid-electrolyte (PSE) switch embedded in 90nm CMOS with forming-free and 10nsec programming for low power, nonvolatile programmable logic (NPL)," inElectron Devices Meeting (IEDM), 2010 IEEE International , vol., no., pp.16.5.1-16.5.4, 6-8 Dec. 2010

[Tada 2] Tada, M.; Sakamoto, T.; Banno, N.; Okamoto, K.; Miyamura, M.; Iguchi, N.; Hada, H., "Improved reliability and switching performance of atom switch by using ternary Cu-alloy and RuTa electrodes," in Electron Devices Meeting (IEDM), 2012 IEEE International , vol., no., pp.29.8.1-29.8.4, 10-13 Dec. 2012

[Takahashi 1] T. Takahashi, S. Furuta, Y. Masuda, S. Kumaragurubaran, T. Sumiya, M. Ono, Y. Hayashi, T. Shimizu, H. Suga, M. Horikawa, and Y. Naitoh, "4kb nonvolatile nanogap memory (NGpM) with 1 ns programming capability," IEEE Silicon Nanoelectronics Workshop (SNW), p. 1, 2, 2012.

[TexIn 1] Texas Intrument, "FRAM – New Generation of Non-Volatile Memory", http://www.ti.com/lit/ml/szzt014a/szzt014a.pdf

[Todorova 1] Todorova, T.Z.; Blaise, P.; Vianello, E.; Fonseca, L.R.C., "Understanding the conduction mechanism of the chalcogenide Ag2S silver-doped through ab initio simulation," in Solid-State Device Research Conference (ESSDERC), 2013 Proceedings of the European , vol., no., pp.342-345, 16-20 Sept. 2013

[Vaithyanathan 1] V. Vaithyanathan et al., “NON-VOLATILE MEMORY CELL INCLUDING SMALL VOLUME ELECTRICAL CONTACT REGIONS”, US Patent 8 022 547 B2, Sep. 20, 2011.

[Valov 1] I. Valov, R. Waser, J. R. Jameson, and M. N. Kozicki, “Electrochemical metallization memories—fundamentals, applications, prospects,” Nanotechnology, vol. 22, no. 28, p. 289502, Jul. 2011.

[Valov 2] Ilia Valov, Ina Sapezanskaia, Alpana Nayak, Tohru Tsuruoka, Thomas Bredow, Tsuyoshi Hasegaw, Georgi Staikov, Masakazu Aono and Rainer Waser, “Atomically controlled electrochemical nucleation at superionic solid electrolyte surfaces”, Nature Materials, April 29th 2012

[Van der Sluis 1] Van der Sluis P 2003 Non-volatile memory cells based on $ZnxCd_{1-x}S$ ferroelectric Schottky diodes Appl. Phys. Lett. 82 4089

[Vianello 1] Vianello, E.; Molas, G.; Longnos, F.; Blaise, P.; Souchier, E.; Cagli, C.; Palma, G.; Guy, J.; Bernard, M.; Reyboz, M.; Rodriguez, G.; Roule, A.; Carabasse, C.; Delaye, V.; Jousseaume, V.; Maitrejean, S.; Reimbold, G.; De Salvo, B.; Dahmani, F.; Verrier, P.; Bretegnier, D.; Liebault, J., "Sb-doped GeS2 as performance and reliability booster in Conductive Bridge RAM," in Electron Devices Meeting (IEDM), 2012 IEEE International , vol., no., pp.31.5.1-31.5.4, 10-13 Dec. 2012

[Vianello 2] Vianello, E.; Thomas, O.; Molas, G.; Turkyilmaz, O.; Jovanovic, N.; Garbin, D.; Palma, G.; Alayan, M.; Nguyen, C.; Coignus, J.; Giraud, B.; Benoist, T.; Reyboz, M.; Toffoli, A.; Charpin, C.; Clermidy, F.; Perniola, L., "Resistive Memories for Ultra-Low-Power embedded computing design," inElectron Devices Meeting (IEDM), 2014 IEEE International , vol., no., pp.6.3.1-6.3.4, 15-17 Dec. 2014.

[Waser 1] R. Waser, R. Dittmann, G. Staikov, and K. Szot, “Redox-based resistive switching memories – Nanoionic mechanisms, prospects, and challenges,” Advanced Materials, vol. 21, no. 25-26, pp. 2632–2663, Jul. 2009

[Watatu 1] Otsuka, Wataru; Miyata, K.; Kitagawa, M.; Tsutsui, K.; Tsushima, T.; Yoshihara, H.; Namise, T.; Terao, Y.; Ogata, K., "A 4Mb conductive-bridge resistive memory with 2.3GB/s read-throughput and 216MB/s program-throughput," in Solid-State Circuits Conference Digest of Technical Papers (ISSCC), 2011 IEEE International , vol., no., pp.210-211, 20-24 Feb. 2011

[Web 1] Semiconductor Industry Association, “Historical Billing Reports,” http://www.semiconductors.org/industry_statistics/historical_billing_reports/

[Web 2] Germany Trade and Invest, “INDUSTRY OVERVIEW The Electronics and Microtechnology Industry in Germany”, http://www.gtai.de/

[Web 3] TNS Global, “Connected Life”, http://connectedlife.tnsglobal.com/

[Web 4] M. Hilbert, “The world’s technological capacity to handle information”, http://www.martinhilbert.net/WorldInfoCapacity.html

[Wutting 1] M. Wuttig and N. Yamada, "Phase-change materials for rewriteable data storage," Nature Materials, vol. 6, pp. 824-832, 2007

[YChen 1] Y. Chen, L. Goux, S. Clima, B. Govoreanu, R. Degraeve, G. Kar, A. Fantini, G. Groeseneken, D. Wouters, and M. Jurczak, “Endurance/Retention trade-off on HfO_2/Metal cap 1T1R bipolar RRAM,” IEEE Transactions on Electron Devices, vol. 60, no. 3, pp. 1114–1121, 2013

[YLin 1] Yu-Yu Lin; Feng-Ming Lee; Wei-Chih Chien; Yi-Chou Chen; Kuang-Yeu Hsieh; Chih-Yuan Lu, "A model for the RESET operation of electrochemical conducting bridge resistive memory (CB-ReRAM)," in Electron Devices Meeting (IEDM), 2010 IEEE International , vol., no., pp.22.2.1-22.2.4, 6-8 Dec. 2010

[Yu 1]Shimeng Yu; Wong, H.-S.P., "Compact Modeling of Conducting-Bridge Random-Access Memory (CBRAM)," in Electron Devices, IEEE Transactions on , vol.58, no.5, pp.1352-1360, May 2011

[YWang 1] Yuhao Wang; Chun Zhang; Nadipalli, R.; Hao Yu; Weerasekera, R., "Design exploration of 3D stacked non-volatile memory by conductive bridge based crossbar," in 3D Systems Integration Conference (3DIC), 2011 IEEE International , vol., no., pp.1-6, Jan. 31 2012-Feb. 2 2012.

[Zahurak 1] Zahurak, J.; Miyata, K.; Fischer, M.; Balakrishnan, M.; Chhajed, S.; Wells, D.; Hong Li; Torsi, A.; Lim, J.; Korber, M.; Nakazawa, K.; Mayuzumi, S.; Honda, M.; Sills, S.; Yasuda, S.; Calderoni, A.; Cook, B.; Damarla, G.; Tran, H.; Bei Wang; Cardon, C.; Karda, K.; Okuno, J.; Johnson, A.; Kunihiro, T.; Sumino, J.; Tsukamoto, M.; Aratani, K.; Ramaswamy, N.; Otsuka, W.; Prall, K., "Process integration of a 27nm, 16Gb Cu ReRAM," in Electron Devices Meeting (IEDM), 2014 IEEE International , vol., no., pp.6.2.1-6.2.4, 15-17 Dec. 2014.

[ZWang 1] Wang Z, Griffin P B, McVittie J, Wong S, McIntyre P C and Nishi Y 2007 Resistive switching mechanism in ZnxCd1−xS nonvolatile memory devices IEEE Electron Device Lett. 28 14

Chapter II. Studied structures and Electrical Characterization setup

1. Objectives

Throughout the thesis various CBRAM samples have been studied from simple single resistor (1R) full sheet devices to more complex one transistor - one selector (1T – 1R) or µ - Trench devices. This second chapter is focused on giving an overview of the studied devices (integration flow, deposited materials…) but also of the electrical and thermal measurements carried on the devices. Each device studied presents specific characteristics in terms of architecture, dimension, material composition or circuit used to understand the behavior of the CBRAM. Some devices have been used in several studies whereas others have been briefly studied to clarify specific points of the CBRAM behavior. Therefore, for the sake of clarity and coherence, this chapter will be used as a reference of all the devices and measurement methods for the following of the manuscript.

2. Studied CBRAM devices

The studied devices differ in terms of architecture, integrated layers and electric circuit built around the CBRAM itself but they all share the same core which is, as stated in the previous chapter, a solid electrolyte or resistive layer (RL) between two metallic electrodes: an active electrode, source of ions and an inert electrode.

2.1 Devices architectures

Following the fast evolution trend proper to the microelectronic market, the CBRAM technology has drastically changed during these past three years. The CEA – Leti has been able to offer a great improvement in term of architectures, from large non-confined study samples to the smallest CBRAM devices [GUY 1].

2.1.1 VIA devices

In this structure, the electrolyte and top electrodes are deposited on a metal VIA, connected to a bottom metal line. The electrolyte is not patterned, meaning that it is common to all devices

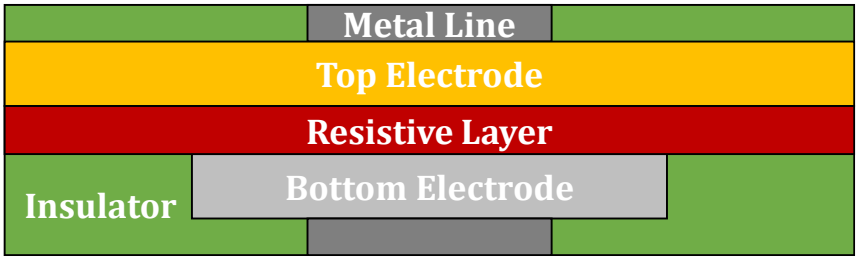

Figure 1. Schematic view of a VIA device

on the wafer die. This simple architecture, far from being industrially viable, is primarily used to study the materials impact on the CBRAM behavior, with abstraction of the modification that could bring scaling, confinement, etching... The main advantage of this technology resides in it fast and ease of production due to the lack of complex patterning/etching and low number of process steps. This architecture also allows to test the feasibility of a material stack, including surface engineering between layers, before integrating the stack in more complex architectures.

Figure 1 shows the final VIA CBRAM stack. The fabrication process starts by etching and depositing the inferior metal line over which an electrical insulator layer is deposited. Vias are etched over the metal line and filled with the metal bottom electrode. Once the bottom electrode created, starts the full sheet deposition giving its name to the architecture. This step consists in the successive deposition on the whole wafer of the solid electrolyte, top electrode and superior metal line. The process ends with the contact opening on the inferior metal line. In the end, all the cells of the wafer share a common top metal line and top electrode with small openings to reach the individual bottom lines.

2.1.2 MESA devices

This architecture corresponds to the industrially viable counterpart of the VIA architecture. These two architectures diverge after the full sheet deposition of the solid electrolyte, top electrode

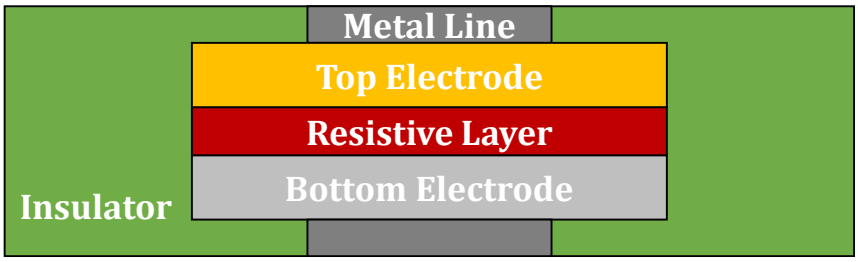

Figure 2. Schematic view of a MESA device

and superior metal line. Regarding MESA architecture, the devices are separated from each other by etching wells around the cells. The wells are then filled with insulator. Figure 2 shows typical MESA devices. The dimension of the cell is controlled during the wells etching and can be as low as the lithography technology allows it to be [Liebmann 1]. In our case the dimension are relaxed (> 1µm) to avoid the behavior alterations that could bring electrolyte confinement and etched surfaces.

2.1.3 Nano - Trench devices

Not only to pursue the Moore's Law and find a viable position on the memory market but also to reduce some inherent variability troubles of this technology [Belmonte 1], the scaling of the CBRAM cells is of great importance. This is why cell architectures aiming to reduce the critical dimension of the CBRAM active zone have been introduced by various research facilities and industry [Karg 1, Choi 1, Lee 1] The CEA – Leti proposed as scaling solution the µ - Trench (or nano – Trench) structure shown Figure 3 and inspired by a Seagate Technology patent [Vaithyanathan 1]. The bottom electrode is defined by a metallic liner deposited by CVD in an etched via. The thickness of the layer, down to 5nm, controls the length of the BE. The via is then filled with SiO_2 and the BE contact is opened by chemical mechanical planarization to create a ring. The second critical dimension is defined by a nano - trench, etched in a SiN capping layer

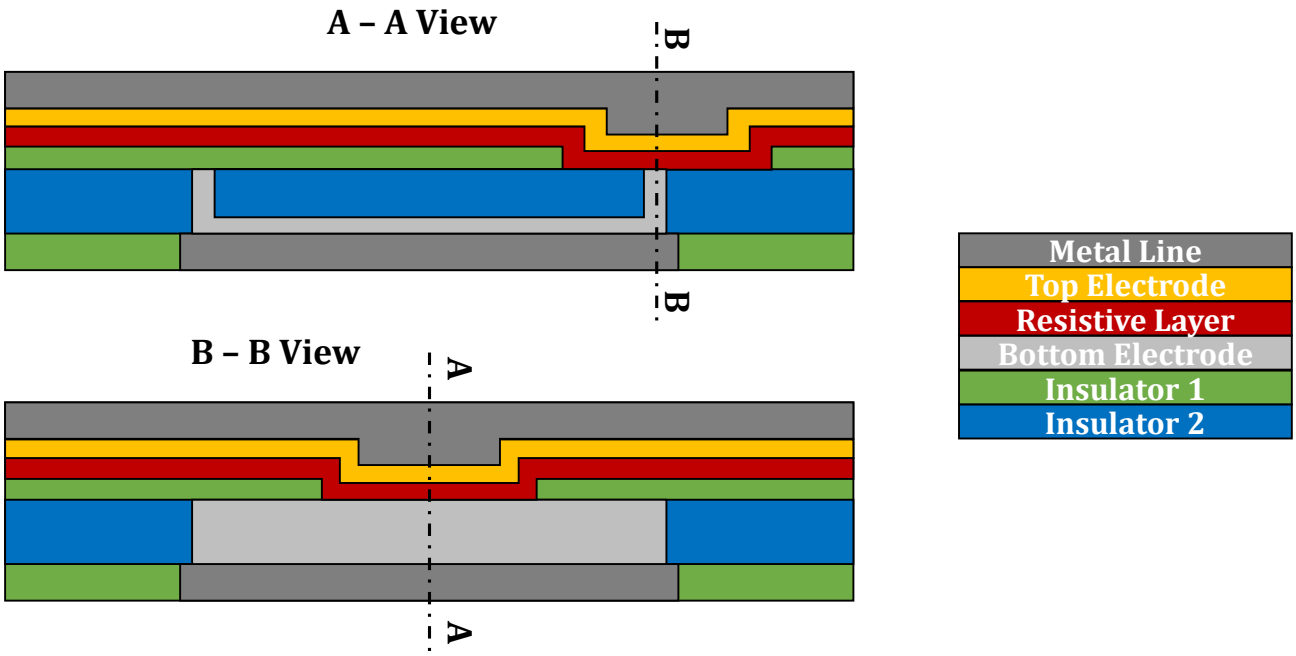

Figure 3. Schematic view of a nano-Trench device

deposited over the planarized BE. This trench is defined by e-Beam lithography down to 50nm and leads to the reduction of the active part of the CBRAM to 5x50nm^2. The solid electrolyte is then deposited in the µ - trench and capped by a top electrode metal deposition.

2.2 Materials stacks

As stated in Chapter I, the choice of materials integrated in the CBRAM stack is of great importance to guarantee an operational memory cell. The studied samples revolve around two different technologies: the first based on chalcogenide electrolytes and the second based on oxides electrolytes. The chalcogenide electrolytes have to be coupled to a top electrode based on silver whereas oxides electrolytes can be coupled with various top electrodes (see Chapter 1) but generally copper based. A vast panel of materials has been studied regarding both electrolyte and electrodes among other: silver or copper based (Cu, CuTeGe, $CuTe_2Ge$) top electrode, GeS_2 or GdO_x electrolyte and TiN or WSi bottom electrodes. This large selection of materials offered the opportunity to carry a deep analysis of the materials properties impact on the CBRAM behavior.

2.3 Device integration

Depending on the targeted application, the CBRAM devices can be integrated in sophisticated circuitry [Palma 1, Vianello 1, Onkaraiah 1]. The interests attached to the CBRAM in this study are various, from the physical understanding of the mechanisms involved in its operating to their impact on industrial cells. This is why the panel of studied CBRAM is large and covers simple study sample as well as complex devices close to industrialization state.

2.3.1 One Resistor cell

The simplest form of CBRAM that has been studied is the one resistor (1R) sample which corresponds to single CBRAM cells without any selectors. This simple structure offers a fast integration process and the ability to test the CBRAM itself without the interference of any other devices (diodes, transistors…). However some limitations are induced by the lack of selector. Indeed, the metal lines being directly connected to the test bench, current overshoots can appear and lead to the degradation of the cell. This current overshoot corresponds to the lack of proper limitation current during the SET operation and more noticeably Forming operation. While still being studied [Tirano 1], the overshoot is considered to be caused by an uncontrolled electrical capacitance discharge of the bench test cables in the CBRAM, during a brief period of time.

Moreover, the cable capacitance and series resistance limiting the current induce a RC time constant between 10 and 100 ns which is limiting fast switching measurements. This time constant induce a charging time of cables such as the voltage seen by the CBRAM during this charging time is reduced. The charging time doesn't affect the global behavior of the CBRAM when the applied voltage is low and switching time is long. However, when the voltage is high and the switching time close to the charging time, the loss of voltage seen by the CBRAM greatly affect its switching time. This means that the switching times measured under 10 to 100 ns are over evaluated, limiting the study of very fast switching cells.

2.3.2 One Transistor – One Resistor

The second type of tested CBRAM is the One Transistor – One Resistor (1T – 1R) and corresponds to one of the possible approach to add a selector to the CBRAM cell. This selector offers a better control of the current flowing through the cell and greatly reduces the overshoot current. It also enables the use of large matrix of CBRAM by cancelling the leakage current between the cells. Using 1T – 1R matrix technology offered the capacity to study 64 bit arrays, particularly interesting for variability and data analyses. Finally, the transistor speed allows to study shorter switching time than the standard 1R structure. However, the use of a transistor induces a few drawbacks. Indeed, it is hard to extract the electrical response of the CBRAM from the 1T – 1R couple, which is complicating the study of precise mechanisms occurring during the CBRAM switching process. Moreover, the current range achievable depends of the transistor and generally leads to a reduced current windows.

3. Measurement Method

The characterizations and physical measurements had the essential role to control the correct CBRAM operation, to prove the viability of a material stack and to study all the possible conditions (electrical and thermal) that could experience a CBRAM throughout its life time. But most of all, it offers inputs from real devices with known material composition, architectures and dimensions to the second great component of this research work: the physical simulation of a CBRAM.

3.1 Quasi – Static programming

The first and essential programming method is the Quasi – Static (QS) programming. This method consists in applying a positive or negative voltage ramp between the top and bottom electrode depending on the operation. During the ramp, the current flowing through the cell is measured with a Parameter Analyzer (Agilent 4156 or B1500) and can be internally limited. The limiting current is called compliance (I_C) and is used during SET to control the resistance value and to avoid irreversible cell degradation. During the QS programming it is possible to monitor the current evolution in function of the applied voltage and to then obtain the switching voltage V_{SET} and V_{RESET} as seen in the Figure 4. It is also possible to obtain the cell resistance value and thus its state (written or erased) with the READ operation. For this operation, a much smaller voltage ramp is applied (a tenth of mV versus a few V for switching) and a linear regression on the measured current is performed. The resistance value is then extrapolated using a simple Ohm law. During READ operations, the applied voltage ramp is reduced in order to keep the state of the cell from changing, which would result in a disturbance of state (READ disturb) [Longnos 1]. The QS programming is generally employed as a standard test to verify the correct operation and main characteristics of the cell as it allows to perform all the standard operations (Forming, SET, RESET and READ). However, QS programming lacks a good temporal control especially regarding fast speed and short duration. This is why QS programming is limited in term of dynamic and temporal characteristics study.

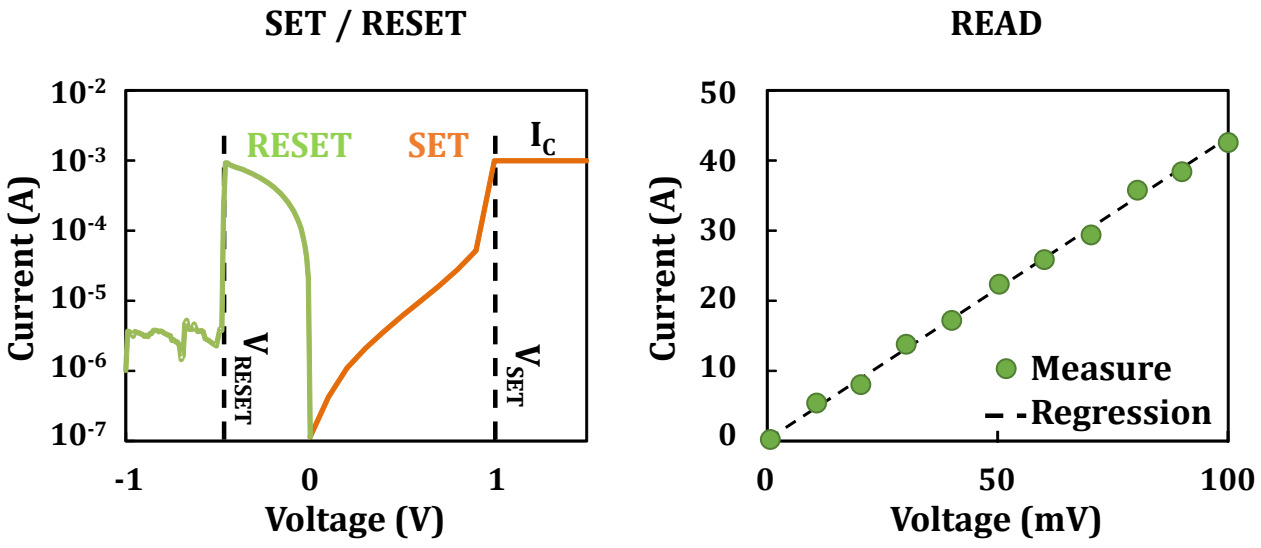

Figure 4. Quasi Static Programming: SET, RESET and READ operation

3.2 Pulsed programming

To overcome the lack of high speed dynamic and temporal information resulting of the QS programming, the Pulsed method (PS) is used. This method consists in applying a positive or negative voltage pulse between the top and bottom electrode depending on the operation, for a given duration of time. The voltage pulse can be controlled in terms of shape, height, ascending/descending slope and duration. Using an oscilloscope it is possible to monitor the voltage in function of the time and extract the switching time t_{SET} and t_{RESET}. Figure 5 shows the typical SET and t_{SET} extraction. It is also possible to monitor the current level flowing through the cell by joining an external resistance to the CBRAM and measuring its voltage. The resistance value can be obtained by applying low voltage pulse and measuring the current in the cell, then using a standard Ohm law the resistance value can be extracted. For the sake of accuracy the resistance value is taken as the average value after 5 to 10 READ pulses. A great advantage of PS programming is the reduced stress caused to the cells in oppositions to QS programming. The cell degradation is then much slower. PS programming corresponds to the standard programming conditions for industrial CBRAM.

3.3 Cycling

To study the life – time of a CBRAM, it is essential to monitor its ability to handle a high number of cycles. A cycle consists in consecutives SET, READ, RESET and finally READ again.

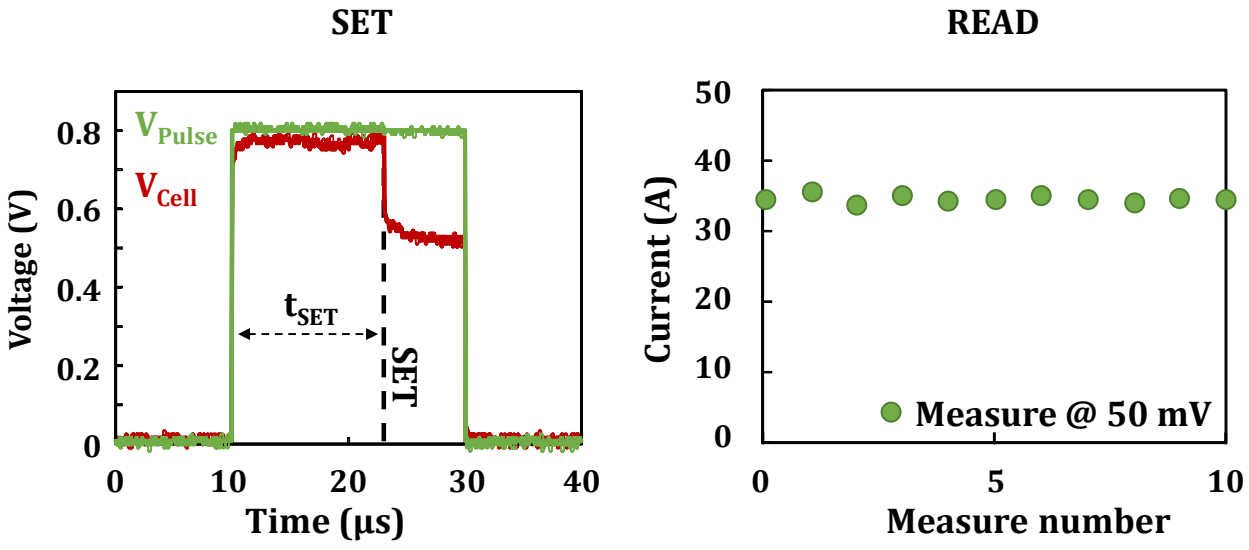

Figure 5. Pulsed Programming: SET and READ operation

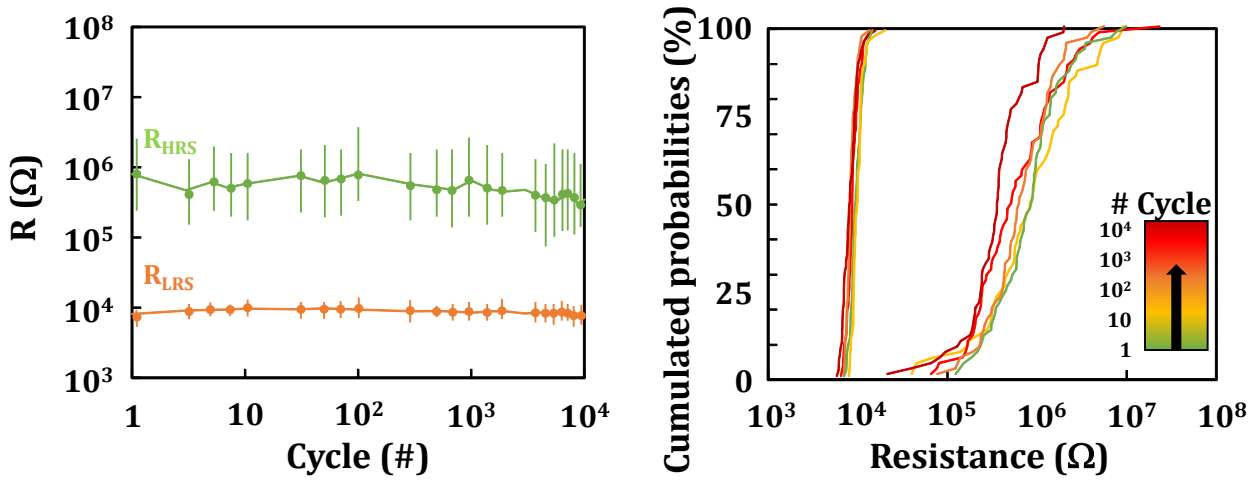

Figure 6. PS cycling and resistance distribution in function of the cycle number

Depending on the application, as seen in the first chapter, the required number of cycles a cell has to handle might differ. To study the cycling ability of a cell and especially for high number of cycles (higher than 10^3 cycles) PS programming is generally used as it offers a faster cycling speed and reduces the stress on the cell. Figure 6 shows an example of PS cycling and the benefit it offers over QS cycling with resistance distributions easier to obtain. It is also possible to skip the READ operation after each cycles and only periodically read the cells state following a logarithmic scale on the cycle number. This allows to reach very high number of cycles (higher than 10^7 cycles) in less than 20 minutes. However, to monitor the evolution of V_{SET} or V_{RESET} in function of the cycle number, QS programming is still required. Figure 7 shows an example of QS cycling with the resistances and switching voltages extracted.

3.4 Data retention

Data retention stands as the ability of a CBRAM cell to keep its state over time. It can also be seen as the capability of the cell to maintain its resistance value the as close as possible to its original value. Depending on the targeted application (see chapter I) the required retention time could differ. However, the targeted time being generally too long to be studied in standard conditions (ex. 10 years at room temperature), the retention study needs to be accelerated. There is two common ways to accelerate the retention studies, the first is by applying a voltage bias on the cell [Longnos 1] and the second is by applying a high temperature. Only the second one will be presented and used in this manuscript. The data retention study consists in putting the cell in the

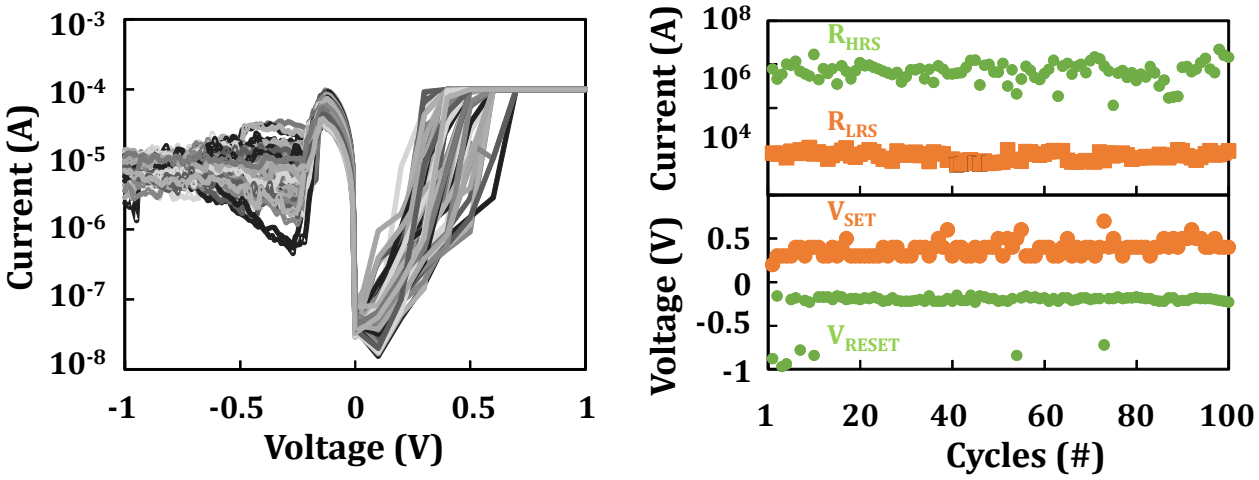

Figure 7. QS cycling I(V) curves offering resistance levels but also switching voltages.

desired stat (written or erase), using either QS or PS programming, and then putting the sample in an oven at high temperature (50 to 300 °C). Following a logarithmic scale of the time spend at high temperature, the samples are periodically taking out of the oven, thermalized at room temperature and their resistance value extracted through READ operations. Figure 8 shows the typical loss of information over time at high temperature encountered during retention study. The progressive degradation of resistance values and loss of both HRS and LRS states can be seen. Arrhenius plots are commonly used to study the retention characteristics [Muller 1, Symanczyk 1, Vianello 2] and get insight about the retention capability. They consist in extracting the retention time for a chosen failure parameter (percentage of failing cells) at any temperature from three data retention study at

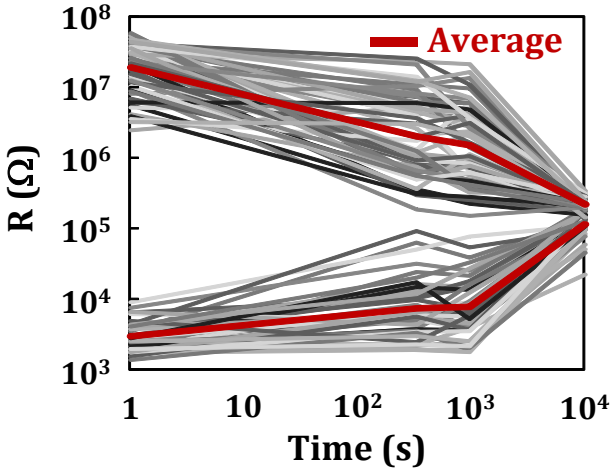

Figure 8. Typical Data Retention characteristics showing the progressive loss of both LRS and HRS

different temperatures. However, Arrhenius plots study are based on extrapolations and more in depth studies are generally required in order to achieve precise retention characteristics.

4. Chapter II synthesis

This chapter introduced the required notions to apprehend the following of the manuscript. Indeed, for the sake of clarity every studied architectures and characterization technics are referenced here. Thanks to the CEA – Leti a very large panel of devices has been characterized, offering various materials and architectures combinations. As will be seen in the following of the manuscript, this great diversity of samples has been taken advantage of. Indeed, this diversity of samples combined to the variety of characterization technics offers many research fronts, including the impact on the CBRAM of the material stack, the scaling impact, the temperature… Finally this variety of samples and characterizations technics also played a great role in the development and improvement of a Kinetic Monte Carlo simulation owing to the large amount of easily accessible data. This Kinetic Monte Carlo simulation is the object of the following Chapter.

Chapter II references

[Belmonte 1]Belmonte, A.; Degraeve, R.; Fantini, A.; Kim, W.; Houssa, M.; Jurczak, M.; Goux, L., "Origin of the deep reset and low variability of pulse-programmed WAl2O3TiWCu CBRAM device," in Memory Workshop (IMW), 2014 IEEE 6th International , vol., no., pp.1-4, 18-21 May 2014

[Choi 1] Sang-Jun Choi; Lee, Jung-Hyun; Hyung-Jin Bae; Woo-Young Yang; Tae-Wan Kim; Ki-Hong Kim, "Improvement of CBRAM Resistance Window by Scaling Down Electrode Size in Pure-GeTe Film," in Electron Device Letters, IEEE , vol.30, no.2, pp.120-122, Feb. 2009

[Karg 1] Siegfried Friedrich Karg, Gerhard Ingmar Meijer, "MEMORY CELL AND SELECT ELEMENT", US 8 279 665 B2, Oct. 2, 2012

[Lee 1] Tzyh-Cheang Lee, Ming-Yi Yang, Fu-Liand Yang, Duan-Iee Tang, "PHASE CHANGE MEMORY", US 7 989 920 B2, Aug. 2, 2011.

[Liebmann 1] Liebmann, L.; Torres, J.A., "A Designer's Guide to Subresolution Lithography: Enabling the Impossible to Get to the 14-nm Node [Tutorial]," in Design & Test, IEEE , vol.30, no.3, pp.70-92, June 2013

[Longnos 1] Longnos, F.; Vianello, E.; Molas, G.; Palma, G.; Souchier, E.; Carabasse, C.; Bernard, M.; De Salvo, B.; Bretegnier, D.; Liebault, J., "On disturb immunity and P/E kinetics of Sb-doped GeS2/Ag conductive bridge memories," in Memory Workshop (IMW), 2013 5th IEEE International , vol., no., pp.96-99, 26-29 May 2013

[Muller 1] Muller, G.; Happ, T.; Kund, M.; Gill Yong Lee; Nagel, N.; Sezi, R., "Status and outlook of emerging nonvolatile memory technologies," in Electron Devices Meeting, 2004. IEDM Technical Digest. IEEE International , vol., no., pp.567-570, 13-15 Dec. 2004

[Onkaraiah 1] S. Onkaraiah, O. Turkylmaz, M. Reyboz, F. Clermidy, J. Portal, and C. Muller, "An hybrid cbram/cmos look-up-table structure for improving performance effi- ciency of field programmable gate array," in To be published in Proceedings of Symposium on Circuits and Systems (ISCAS), 2013 IEEE International, 2013.

[Palma 1] Palma, G.; Vianello, E.; Thomas, O.; Suri, M.; Onkaraiah, S.; Toffoli, A.; Carabasse, C.; Bernard, M.; Roule, A.; Pirrotta, O.; Molas, G.; De Salvo, B., "Interface Engineering of Ag-GeS2-Based Conductive Bridge RAM for Reconfigurable Logic Applications," in Electron Devices, Transactions on , vol.61, no.3, pp.793-800, March 2014.

[Tirano 1] S. Tirano, L. Perniola, J. Buckley, J. Cluzel, V. Jousseaume, C. Muller, D. Deleruyelle, B. De Salvo, and G. Reimbold, "Accurate analysis of parasitic current overshoot during forming operation in RRAMs," Microelectronic Engineering, vol. 88, no. 7, pp. 1129–1132, Jul. 2011.

[Symanczyk 1] Symanczyk, R.; Bruchhaus, R.; Dittrich, R.; Kund, M., "Investigation of the Reliability Behavior of Conductive-Bridging Memory Cells," in Electron Device Letters, IEEE , vol.30, no.8, pp.876-878, Aug. 2009

[Vaithyanathan 1] V. Vaithyanathan et al., "NON-VOLATILE MEMORY CELL INCLUDING SMALL VOLUME ELECTRICAL CONTACT REGIONS", US Patent 8 022 547 B2, Sep. 20, 2011.

[Vianello 1] Vianello, E.; Thomas, O.; Molas, G.; Turkyilmaz, O.; Jovanovic, N.; Garbin, D.; Palma, G.; Alayan, M.; Nguyen, C.; Coignus, J.; Giraud, B.; Benoist, T.; Reyboz, M.; Toffoli, A.; Charpin, C.; Clermidy, F.; Perniola, L., "Resistive Memories for Ultra-Low-Power embedded computing design," inElectron Devices Meeting (IEDM), 2014 IEEE International , vol., no., pp.6.3.1-6.3.4, 15-17 Dec. 2014.

[Vianello 2]Vianello, E.; Molas, G.; Longnos, F.; Blaise, P.; Souchier, E.; Cagli, C.; Palma, G.; Guy, J.; Bernard, M.; Reyboz, M.; Rodriguez, G.; Roule, A.; Carabasse, C.; Delaye, V.; Jousseaume, V.; Maitrejean, S.; Reimbold, G.; De Salvo, B.; Dahmani, F.; Verrier, P.; Bretegnier, D.; Liebault, J., "Sb-doped GeS2 as performance and reliability booster in Conductive Bridge RAM," in Electron Devices Meeting (IEDM), 2012 IEEE International , vol., no., pp.31.5.1-31.5.4, 10-13 Dec. 2012

Chapter III. Kinetic Monte Carlo Simulation

1. Objectives

The model that will be described in this chapter has been developed with the goal to determine and understand the physical mechanisms involved in the life cycle of a CBRAM. The CBRAM technology being known as suffering from high variability and stochasticity [Belmonte 1,Goux 2], it has been chosen to use a Kinetic Monte Carlo (KMC) approach to benefit from the randomness factor involved in its solving. Historically, the KMC method takes its name from a famous neighborhood of Monaco known for its Casino and gambling.

As previously stated, the KMC simulation developed here aims to describe and model the complete life cycle of a CBRAM, which means simulating Forming, SET, RESET, Endurance and Data Retention characteristics. The strength of the model stands in is ability to simulate all these CBRAM operation in the same framework and using the same physical properties and parameters, allowing for example a cell to be formed, cycled and its retention capability to be tested. The physical properties involved in the model resolutions are inputs from ab – initio calculations, properties of materials reported in the literature or obtained from physical and chemical characterization. The physical interpretation of the mechanisms implicated in the CBRAM

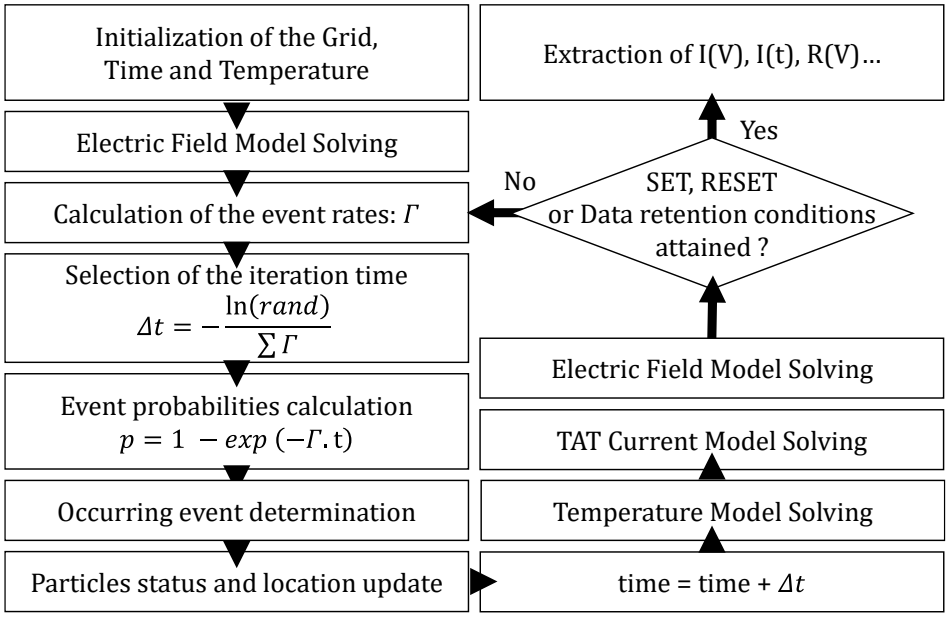

Figure 1. KMC simulation Flowchart

operation are based on the Transition State Theory (TST) and are driven by the electric field and temperature in the device.

This Chapter will be organized around the model flowchart detailed in Figure 1 by first describing the outline of the KMC model and its computation and then focusing on the physical appendix required to solve the model. In the same manner as Chapter II, this chapter will be used as reference for the following of the manuscript regarding the use of the model.

2. KMC Model outline and operating

2.1 System Initialization

The KMC model is based on atomic migration and oxidation/reduction reactions treated at the atomic and electronic level. Each and every atom is treated individually, according to their electrical and thermal environment. To simulate the CBRAM operation, the KMC model relies on a 2 dimensional (2D) grid (Figure 2) corresponding to every possible atomic and ionic positions inside the resistive layer. The choice of a 2D resolution had been made for the sake of computation time as the model aim to assess the CBRAM variability, which requires a large amount of simulated data. The grid parameter (hopping distance between two adjacent points) is defined in our case by the atomic Cu-Cu distance in the electrolyte. Some insights of this latter can be obtained by ab-initio calculation [Sankaran 1, Goux 1] and depends on the electrolyte nature and density.

The KMC environment involves an inert bottom electrode considered as composed by unmovable atoms and an active top electrode, source of the ions used to form the conductive bridge. This top electrode can be finite or infinite, but both cases showed the same CBRAM behavior and results

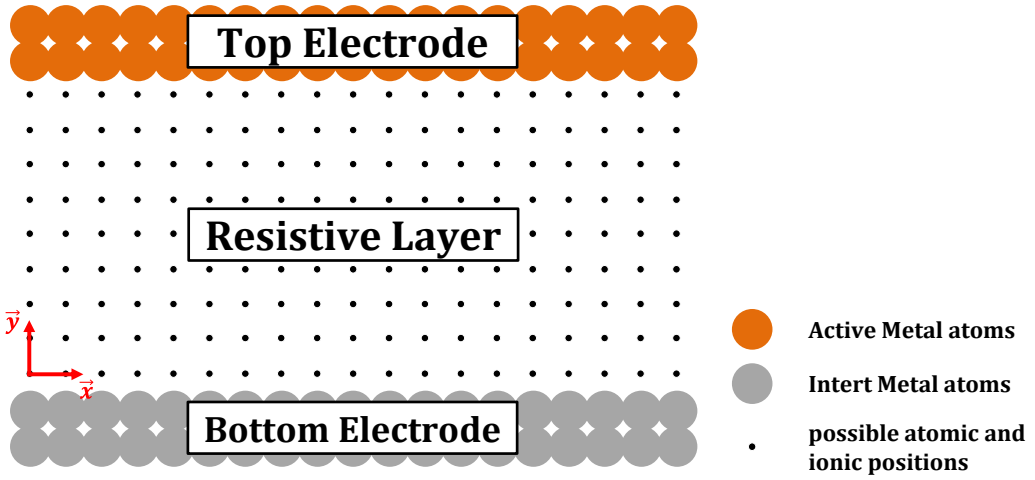

Figure 2. Simulation framework

with only a longer resolution time for the finite top electrode. Thus, to carry on with the optimization of the resolution time, the top electrode has been taken infinite. This assumption seems suitable for our studied samples considering the thinness of electrolyte (few nm for oxides based CBRAM) compared to the top electrode thickness (tens of nm). For each point of the grid the temperature is initialized at a precise value depending on the simulated operation ($T_{Retention}$ for data retention at high temperature or T_{Room} for endurance). Finally, the KMC resolution is built around quantified jumps in time to iteratively compute the progression of the CBRAM operation. Consequently the time has to be initialized at 0 s. Each iteration of time corresponds to a certain probability for an event to happen.

At the end of this initialization, corresponding to the first three flowchart steps, the geometrical space in which the model will be solved has been generated. This space is based on physical input from the device (electrolyte deposited thickness and Cu – Cu distance). The notion of temperature, electric potential and time have been established, initialized and will be incremented further in the model. The KMC model, is then ready to start its first iteration. The typical progress of an iteration will be describe throughout the following part of this outline.

2.2 Physical mechanisms involved in the CBRAM operation and modeled in the KMC

2.2.1 Mechanisms description

The physical mechanisms involved during the switching or data retention and taken into account in the KMC are represented Figure 3. For the sake of simplicity, Cu top electrode and Al_2O_3 electrolyte will be used to illustrate the model physical theories. The physical mechanisms

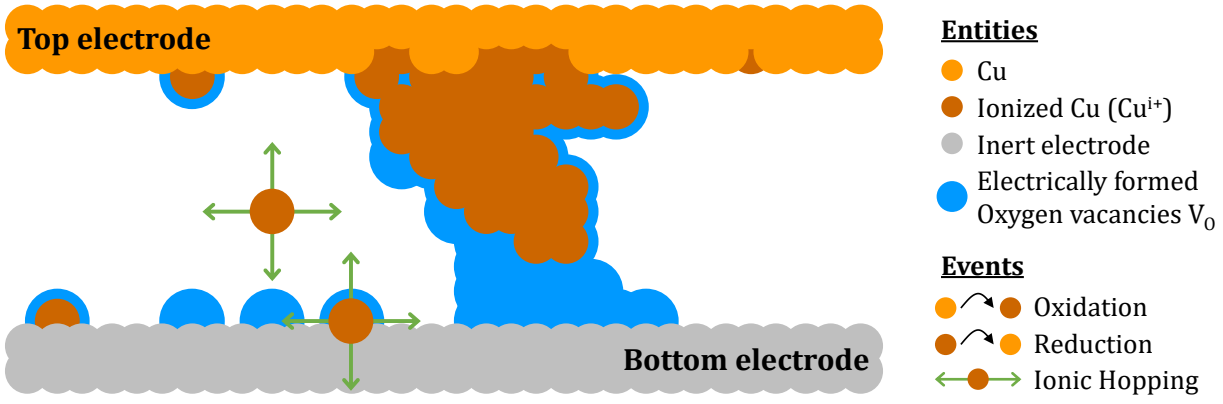

Figure 3. Physical mechanisms taken into account in the Kinetic Monte Carlo simulations used in this work.

occurring during the CBRAM operation can be divided in two types: the reactions and the displacements. The reactions correspond to oxidations or reductions of atoms or ions coming from the top electrode. Once the ions are generated from the reaction, they can move through the electrolyte following ionic hopping behavior. It has been chosen to simulate these two types of physical mechanisms with the same physical theory: the Transition State Theory (TST) [Laidler 1, Larentis 1, Russo 1]. This theory relies on the transition of a particle from a starting energy state to a more favorable one separated by an energy barrier. However, depending on the modeled mechanism, the involved particle differs. Indeed, regarding displacements, the considered particles are the ions whereas, concerning the reactions, the particles are electrons. The TST is schematized in Figure 4, the particle hopping rates depends on the barrier energy height and the difference of energy between the starting and finishing state. The barrier energy height can also be modulated by the electrical field seen by the particle. The latest version of the KMC model also integrates aggregation mechanisms and oxygen vacancies generation, both translating into a reduction of the energy level pulling ions toward them. The oxygen vacancies are tied to the resistive layer degradation progressively occurring during cycling. Their consideration in the KMC simulation where a necessity to address the endurance concern of the cells. Ab – initio calculations have been carried and prove much higher required energy for an atom to move in an electrolyte in comparison to an ion. This is why, only ions are considered as moving particles in the KMC resolution. Aggregates and oxygen vacancies act as favored location for migrating ions. This behavior is

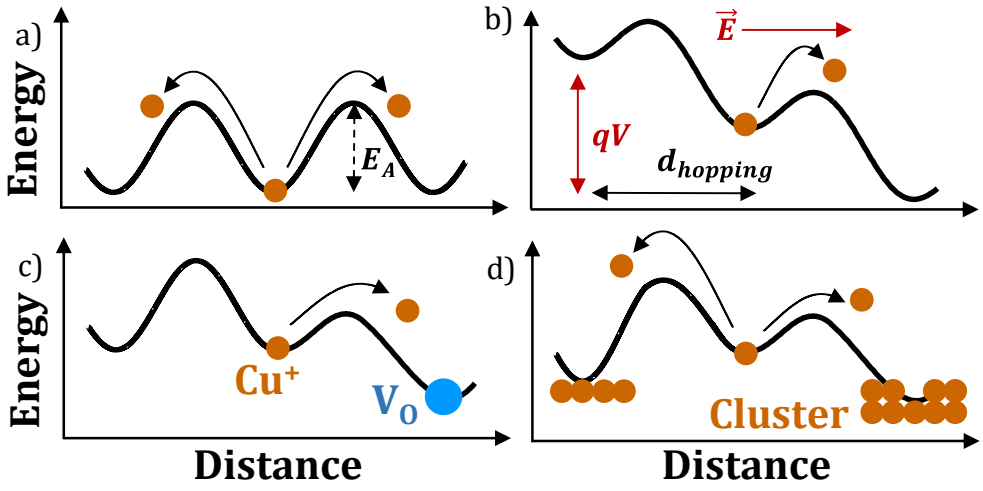

Figure 4. Schematics of the energy profiles for different simulated mechanisms, assuming transition state theory (a). (b) Applied electric field, (c) V_O presence and (d) Cu aggregation reduce the energy barrier.

simulated by a reduction of the energy level at these location which is represented Figure 4. The use of an energy level mapping allows to distinguish volume diffusion from surface diffusion, adsorption or desorption. It is possible to have insight from ab – initio calculations of the energy barrier height and the impact of the aggregation and oxygen vacancies on energy levels. However those parameters are generally taken as fitting parameters around physically suitable values.

The introduction of oxygen vacancies into the electrolyte is only at a preliminary state and would require deep modifications of the KMC model to perform completely as expected. Indeed, the vacancies are not considered as movable entities in the current state of the model. They are created at the locations of copper atoms and left behind after the copper migration. Finally, they don't participate to the electrical conduction mechanisms. This corresponds to one of the current limitation of the model and it might be beneficial to consider the vacancies as proper migrating entities modifying the global electrical conduction similarly to the migrating ions.

The chemical reactions (oxidation and reduction) treatment is based on a transition of electron states over an energy barrier. This energy barrier is considered the same for both reactions and can be extracted from ab – initio calculations. The chemical reactions are happening in interface area between the electrolyte and metal atoms or ions. The atoms and ions closest to the interface are

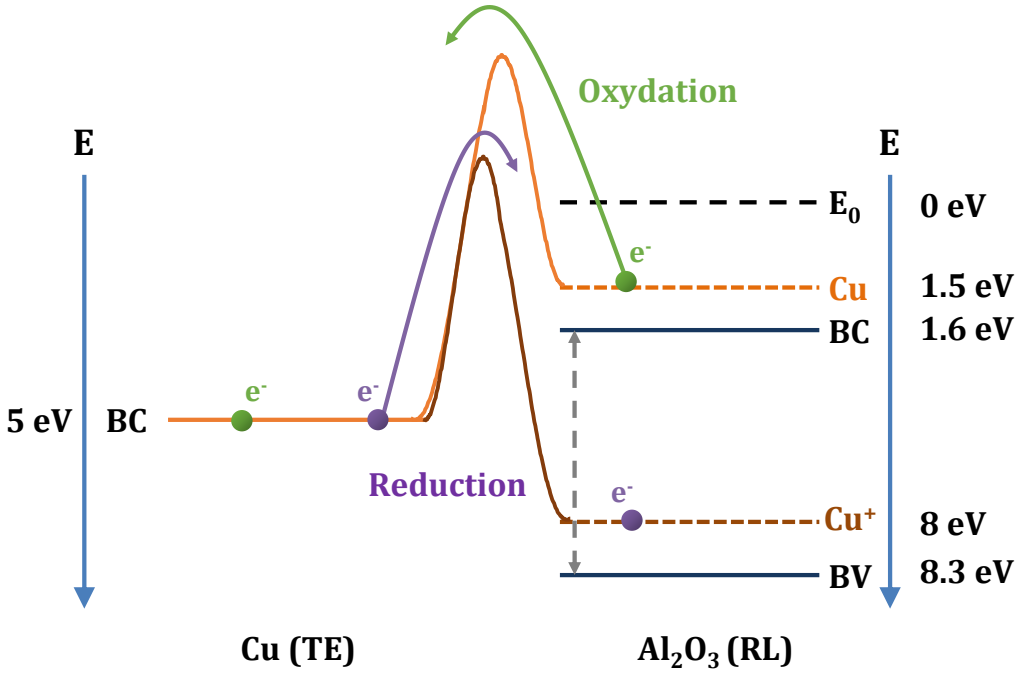

Figure 5. Energetic path of electrons during either oxidation or reduction of an active atom inside the resistive layer. Example given for the Cu/Al_2O_3 couple.

considered as traps in the electrolyte, meaning that the electrons energy levels correspond to the energy levels of these traps extracted from ab initio calculations. The electronic path responsible for the oxidation of an atoms or reduction of an ion is schematized Figure 5.

The oxidation reaction is simulated as the transition of electrons from the trap energy level of copper atoms (inside the electrolyte) toward the conduction band of a surrounding metal (top electrode metal, here). To allow this reaction, the energy available for the electrons (under the form of temperature and electrical field) has to be sufficiently high to overcome the energy barrier between the two energy states. If the energy is sufficient, the copper atom loses electrons and becomes an ion that can migrate through the electrolyte. The reduction reaction is simulated as the transition of electrons from a conduction band of a surrounding metal to the trap energy level of a copper ion. Similarly to the oxidation reaction, in the case of a sufficient energy available to the electrons, the copper ion gains electrons a return to its unmovable atom state.

It is important to note that only the case of electrons exchange with the top electrode is schematized here. However, it is possible for electrons to transit toward (for oxidation) or from (for reduction) copper atoms in the electrolyte or metal atoms of the bottom electrode. In these cases, the corresponding initial or final energy levels are modified accordingly.

This representation of the redox mechanisms aims to create a bond between electronic energy level and chemical reaction. It is possible to use a different approaches based on the reaction potential [Nieminen 1] following the same general equation but different physical values. Insights of an electro-chemist might be of great help to improve the current vision of the redox model.

2.2.2 Mechanisms computation

The calculation of the transition rates of all the mechanisms requires the temperature and electric field at every point of the framework grid as will be seen in this part. The physical models computing the temperature and electric field must be solved before computing the mechanisms. For the sake of clarity these models will be described in depth in the third part of the chapter but the electric field and temperature are considered known at this stage of the iteration.

The Transition State Theory, chosen to describe the physical mechanisms involved in the CBRAM operation, revolves around the computation of transition rates. A transition rate can be seen as the average time required for a transition to occur and is expressed in s^{-1}. The computation of all involved mechanisms relies on the simplest form of transition rate:

$$\vec{\Gamma} = \nu . exp\left(-\frac{E_A}{k_B T}\right)(\vec{x}, \vec{y})$$

Where $\vec{\Gamma}$ is the transition rate, ν the vibration frequency (approximately equal to 10^{-13} s^{-1}), E_A the energy barrier height between the two states, k_B the Boltzmann constant and T the absolute temperature. This first expression only shows the thermal effect on the transaction speed, however, as state before the physical mechanisms are also affected by other factors. The first one being the electric field:

$$\vec{\Gamma} = \nu . exp\left(-\frac{E_A - \alpha\ Q\ d\ \vec{\varepsilon}}{k_B T}\right)(\vec{x}, \vec{y})$$

Where α is the symmetry factor of the state transition and corresponds to the location of the energy barrier between initial and final states (taken as placed in the middle here, so equal to 0.5). Q is the number of involved electric charges, d the distance between the two locations (equal to the framework grid parameter) and $\vec{\varepsilon}$ the electric field. It has been demonstrated that an atomic bond experiences an electric field different from the global electric field seen by the electrolyte. Due to the polarization of the atomic bonds in solid electrolyte the electric field seen by the bonds is:

$$\vec{\varepsilon}_{Bond} = \vec{\varepsilon}_{Global} + \mathrm{L}\left(\frac{\mathrm{P}}{\epsilon_0}\right) = (1 + L\ \chi)\ \vec{\varepsilon}_{Global}$$

Where $\vec{\varepsilon}_{Bond}$ is the electric field seen by the atomic bonds, $\vec{\varepsilon}_{Global}$ the electric field seen by the electrolyte, L the Lorentz factor, P the polarization, ϵ_0 the vacuum permittivity and χ the electric susceptibility. This local electric field is referred as the Lorentz relation or Mossotti field and the Lorentz factor depends of the atomic organization [McPherson 1, Kittle 1]

Moreover, the energy difference between the initial state and final state of the transition also affects the energy barrier height:

$$\vec{\Gamma} = \nu . \exp\left(-\frac{\mathrm{E_A} - \frac{1}{2}(\mathrm{Q\ d\ (1 + L\ \chi)\ \vec{\varepsilon}_{Global}} + \phi_{\mathrm{final}} - \phi_{\mathrm{initial}})}{\mathrm{k_B T}}\right)(\vec{\mathrm{x}}, \vec{\mathrm{y}})$$

Where ϕ_{initial} and ϕ_{final} are respectively the energy level of the initial and final state of the transition. This equation is valid for all the mechanisms described previously, with the only differences being the Activation energy, initial and final state energy values.

A KMC model being built around the computation of event probabilities the transition rates have to be transformed into probabilities.

2.3 Probabilities determination

The transition rate of every physical mechanisms being known, it has now to be linked to the mechanisms probably to occur. The system is considered as memoryless similarly to atomic exponential decay, meaning that once the state of an atom or ion changes it does not remember the state it came from. In other words, each state transition is independent of the previous transition occurring or not [Voter 1]. This is possible as each transition duration is considered much shorter than the waiting time it takes for the transition to occur. This allows us to express the probability P of each action for a time duration t as:

$$P = 1 - \exp\left(-\Gamma * t_{iteration} \right)$$

Where Γ is the transition rate previously described and $t_{iteration}$ the iteration time. This equation links the transition probability to the iteration time, the longer the time the closer to 1 is the transition probability. Finally, the determination of the iteration time can seem trivia but is of great importance in the KMC solving in term of precision and speed as will be described in the following.

2.4 Iteration duration determination

As previously stated, the duration of each transition is considered much shorter than the waiting time it takes for the transition to occur. In the KMC framework, the transition duration is neglected and considered as instantaneous. Considering the vibration constant around 10^{-13} s [Meekhof 1], the previous assumption can be considered correct. This allows to simplify the KMC solving by separating each iteration from the others. The iteration duration is tied to the transition probabilities and the choice of this duration is of great importance regarding the convergence speed and precision.

Figure 6 shows the impact of the iteration duration on the transition probabilities for three arbitrary transition rates. As expected, the probabilities increase with the increase of iteration duration until it reaches a saturation close to 1.

If the iteration duration is too long, the transitions have almost the same probabilities (close to 1) with no regard to their transition rate. This cause a loss of precision in the determination of the

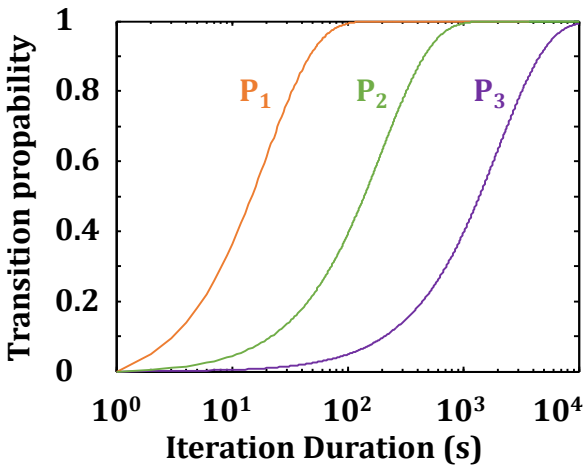

Figure 6. Transition probabilities evolution in function of the iteration time for three arbitrary transition rates

occurring transitions. In contrary, if the iteration duration is too short the probabilities for the transitions to occur are very low. This means that a high number of iterations is required for a transition to occur, slowing down the KMC convergence. In order to achieve in the same time high precision and fast convergence speed, the iteration duration is set depending on all the transition rate of the current iteration. Thus, the iteration duration changes at each iteration in function of the transitions rates. Going back to the probability for a transition to occur:

$$P = 1 - \exp(-\Gamma * t_{iteration})$$

Where P is the probability, Γ is the transition rate and $t_{iteration}$ is the iteration duration. From this equation, the probability for the same transition not to occur is:

$$P^{-} = 1 - P = \exp(-\Gamma * t_{iteration})$$

Where P^{-} is the probability for the transition not to occur. The probability for no transition at all to occur is then:

$$P_{None} = \prod_{atoms\ \&\ ions} P^{-} = \prod_{atomes\ \&\ ions} \exp(-\Gamma * t_{iteration})$$

Or:

$$P_{None} = \exp\left(- t_{iteration} * \sum_{atoms\ \&\ ions} \Gamma \right)$$

Where P_{None} is the probability for no transition to occur. Finally from this equation it is possible to extract the iteration duration corresponding to no transition to occur:

$$t_{iteration} = -\frac{\ln(P_{None})}{\sum_{atoms\ \&\ ions} \Gamma}$$

Figure 7 shows the transition probabilities for the three previous transitions, completed by the probability for no transition to occur. P_{None} has to be chosen high enough to respect the transition rate impact on the transition probabilities but not too high to increase the computation speed. P_{None} has then been set to 50% which shows the best tradeoff between computation speed and precision. To summarize, the iteration duration has a double role on the KMC computation and impacts both precision and performances. In order to optimize these two parameters, the iteration duration varies for each iteration in function of all the transition rates. In the end, the iteration duration is set to the time corresponding to the probability of no transition occurring equals to 50%.

2.5 Occurring transitions determination

Once the iteration duration is set, it is possible to compute the transition probabilities of all transitions. Each particle, atom or ion, can only be affected by one transition or none, meaning for

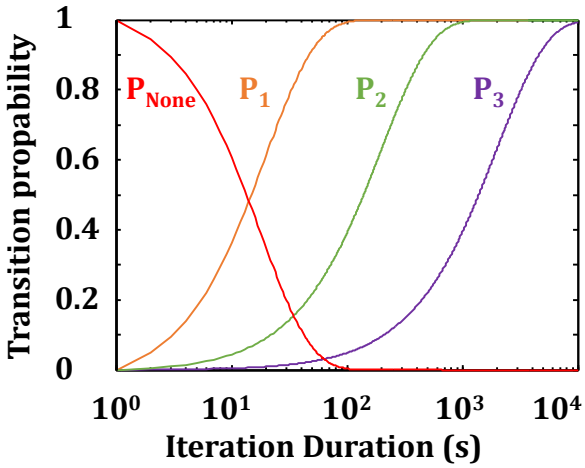

Figure 7. Transition probabilities for the three arbitrary transition rates and the probability for none to occur

example, that an ion cannot migrate and being reduced during the same iteration. To prevent the model from the double transition possibility, the transition probabilities of each particles are normalized between 0 and 1. Then a randomly generated number is picked in the same range for each particle. Then, the transition corresponding to this random number is fixed as occurring transition for the particles and the others are discarded. This selection process is schematized Figure 8.

For the first ion, the randomly generated number is 0.3 which falls in the "Left Hopping" probability range. From this random selection the "Left Hopping" is set. In the same way, the random generated number for the second ion is 0.8, leading to no transition occurring during this iteration. The same pattern is used for atoms but with only one possible transition.

2.6 System update and end of the iteration

The iteration comes to an end, the transition rates have been extracted from the driven forces (temperature and electric field). The probabilities of transition have been computed from the rates and the optimized iteration duration determined from the transition rates. The occurring transitions have been randomly chosen and depending on these transitions the state and locations of all the particles have to be updated. The global time is also incremented with the iteration duration. Then the time, current, voltage… are compared to the targeted operating values. Finally, depending on

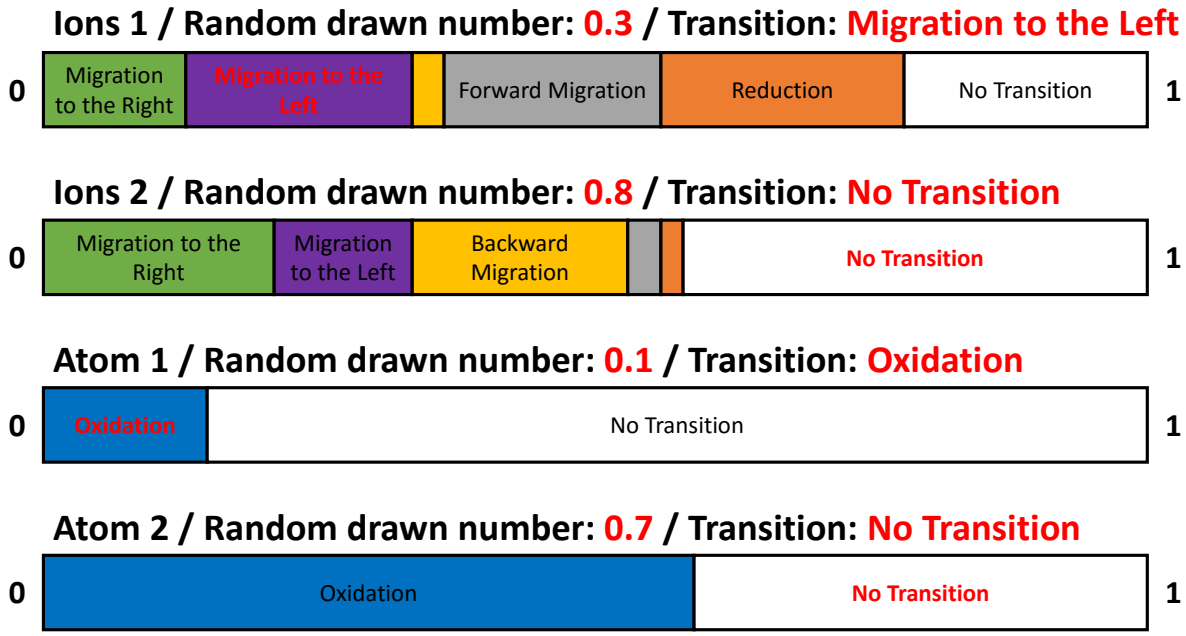

Figure 8. Selection process of the occurring transitions during the iteration.

the attainment of this targeted value or not (Ex: voltage for QS SET, time for data retention), the simulation stops or starts another iteration. With this succession of steps, the KMC simulation is able to simulate all the CBRAM operations with the great advantage of statistical behavior tied to the random factor involved in the model resolution.

3. Physical model required to computed the KMC

As can be seen in the model flowchart Figure 1, major blocks of the resolution are missing in the previous description of the model progression. These blocks correspond to the physical models computing the temperature, voltage, electric field and current flowing through the cell. All these models have been developed with the goal to combine fast computation time and result precision, in order to offer the possibility to simulate high volume of data and study the CBRAM variability.

3.1 Electrical Conduction Model

The current flowing through the cell is of great importance during experimental characterization as it serves to monitor the CBRAM state transition. In the case of the KMC model, the current offers the same information but also creates a bond between the simulation and the experimental characterization. The electrical current has known three major version, developed and updated to cover the various aspect of the CBRAM behavior and all these version will be described. All the versions revolve around the copper (or doping entities) as conductive medium inside the resistive layer but differ in term of conduction mechanisms.

3.1.1 Version 1: Area Concentration Model

This first version initially developed to study the data retention behavior, relies on the electrolyte being considered as semiconductor doped with metal atoms coming from the top electrode.

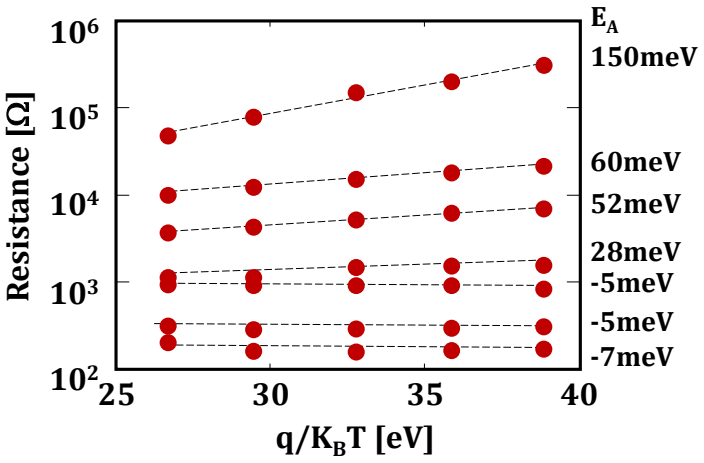

Figure 9. Resistance as a function of temperature for various LRS and HRS levels. Activation energy EA is indicated.

This assumption was motivated by the experimental evolution of a CBRAM resistance in function of the temperature at which the READ operation was performed. This study, illustrated Figure 9 shows an electrical behavior similar to the one of a doped semiconductor. This behavior, which is the decrease of resistance with the increase of temperature, can be attributed to a higher quantity of free carrier in the electrolyte reducing its resistivity. For low resistance value (typically under $10^3\ \Omega$) the temperature shows little to no impact on the resistance value, which can be due to a behavior in between metal and semiconductor. Finally, to insure the reliability of these measurements, the resistance of each cell was measured before and after the temperature ramp and only the unchanged ones were kept in order to avoid the possible impact of thermally activated modification of the conductive bridge.

This theory concerning the semiconductor behavior of the electrolyte has been backed up by ab – initio calculations as seen in Figure 10. This figure represents the Density of State (DOS) for γ-Al2O3 with an increase of Cu inclusions. Cu generates defect levels in the inter-band. These defects become wider when the Cu concentration increases, in agreement with the Cu dependence of the Al_2O_3 conductivity. This can translate into the transition from an insulator state to a semiconductor or quasi metallic one.

Considering the semiconductor state of the doped electrolyte it is possible to use the following law [Larentis 1]:

$$\rho = \frac{1}{\sigma} = \frac{1}{q.n.\mu}$$

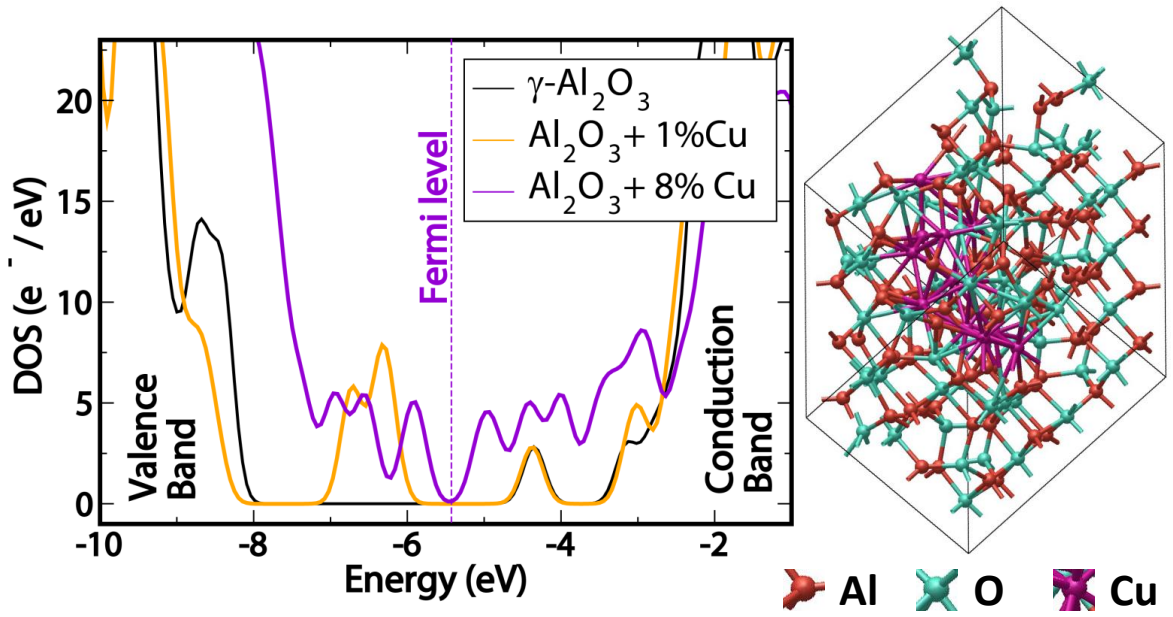

Figure 10. Density of States of stoichiometric Al2O3 (γ-phase) with and without Cu inclusion in the matrix (~2Å of Cu interatomic distance). Increasing the Cu content reduces the bandgap up to a conductor behavior of the system.

Where σ is the Local conductivity, n the Local Cu concentration and μ the Carrier mobility. From the grid used as simulation framework it is possible to know the exact position of every Cu atoms/ions. Making the hypothesis that a Cu dopant does not only affect the conductivity of a unique point of the grid but also of the environing points. For each point of this grid a surrounding area is created (Figure 11 a)) and the numbers of atoms it comprehends are counted. This number of atoms is then divided by the number of points in the area to normalize the atoms weight. This normalization is required as the areas are overlapped around the nearby points. The concentrations around each point of the grid are then computed from the normalized number of atom and the corresponding resistivity calculated (Figure 11 b)). Using the electrical resistivity and the distance between the centers of each area (distance between each point of the grid) a resistance grid is created, bonding each point of the grid to its first neighbors (Figure 11 c)). Finally, from this resistance network it is possible to resolve the Kirchhoff and Ohm laws and get the global resistance of the cell and the current flowing through it. Moreover, the resolution of the resistance mesh also gives the electric potential in each point of the grid.

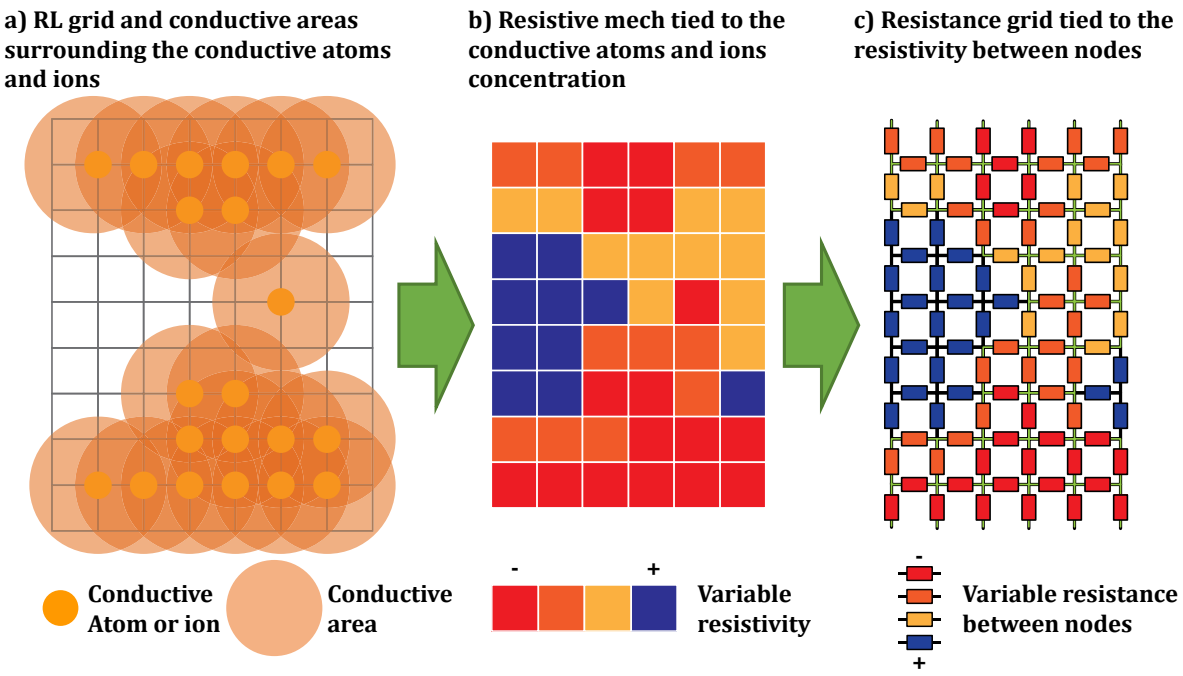

Figure 11. Schematic representation of the model step to compute the global resistance of the cell from the atoms and ions location in the resistive layer.

This first version of the conduction model was developed to respond to a crucial need to complete the analyses of the CBRAM data retention behavior. Its offers a fast solving and comportment in agreement with the literature, ab – initio and electrical characterization.

However this version shows some limitations, especially concerning the choice of the surface area surrounding the grid point and involved in the concentration calculation. The decision of using this surface has been pushed to overcome the binary behavior of a contact model (atoms in contact: current, space between atoms: no current) but ends up showing the same behavior in extreme conditions (at the end of the surfaces for few atoms) as shown in Figure 12. The size of the surfaces are thus of great importance in the model convergence and was taken as fitting parameter in a physically suitable range.

3.1.2 Version 2: Contact Model

This version has been developed to study the Forming and SET operations of the CBRAM and aim to get closer to the physical mechanisms involved in the CBRAM operations. Thus, it relies on the point contact theory Contact [Sune 1, Degraeve 1, Long 1] and the quantification of resistance, two theories accepted in the CBRAM understanding and still in agreement with the previous ab – initio calculations.

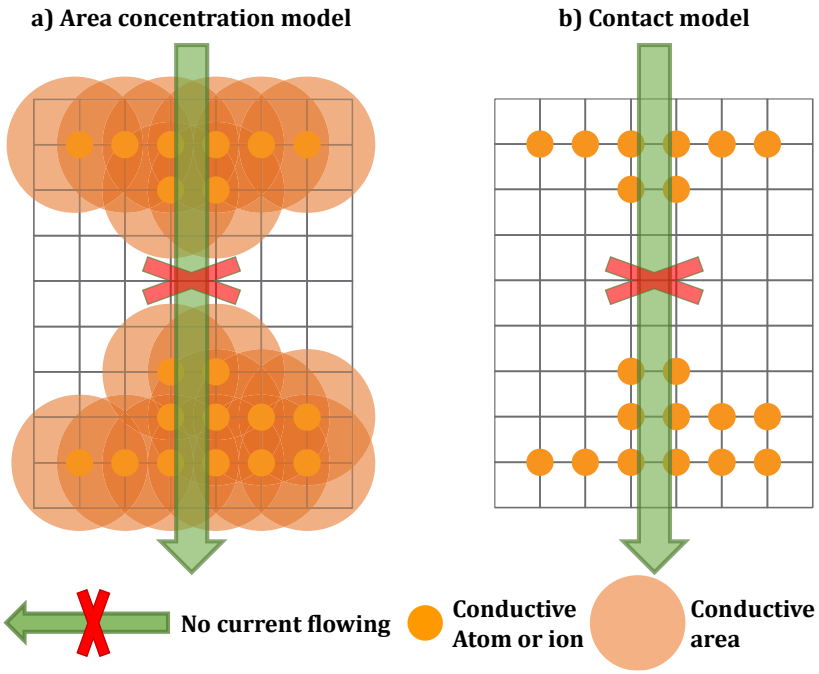

Figure 12. Limit behavior of the area concentration model acting as a contact model if the distance is too large between atoms

In this case, and in opposition to the previous version, there is no surrounding surface taken into account around the points of the grid. Each point of the grid depending on the presence of a dopant is conductive or not. This means that for a current to flow between the top and bottom electrode, a continuous path of dopants must exist. Figure 13 shows a schematic representation of this conduction model. It follows the same resolution pattern as the version 1: the creation of a resistance network between the points of the grid in function of the presence of dopant or not. Kirchhoff and Ohm laws are then solved and the global resistance of the cell, the current flowing through and the electric potential at every points of the grid are obtained. The resistance value between two adjacent atoms is equal to 12.9 kΩ [Sune 1] and corresponds to the quantum of resistance.

The simulation of Forming and SET is much more demanding in term of iterations (iteration number and complexity) than the retention simulation. The contact model shows a faster resolution time than the previous one due to the deletion of the concentrations calculation and normalization which slightly compensates complexification of global solving. Moreover, this model greatly simplifies the electric field calculation as will be shown later. However, due to its binary behavior (contact or not) this version shows an important drawback in its impossibility to correctly compute

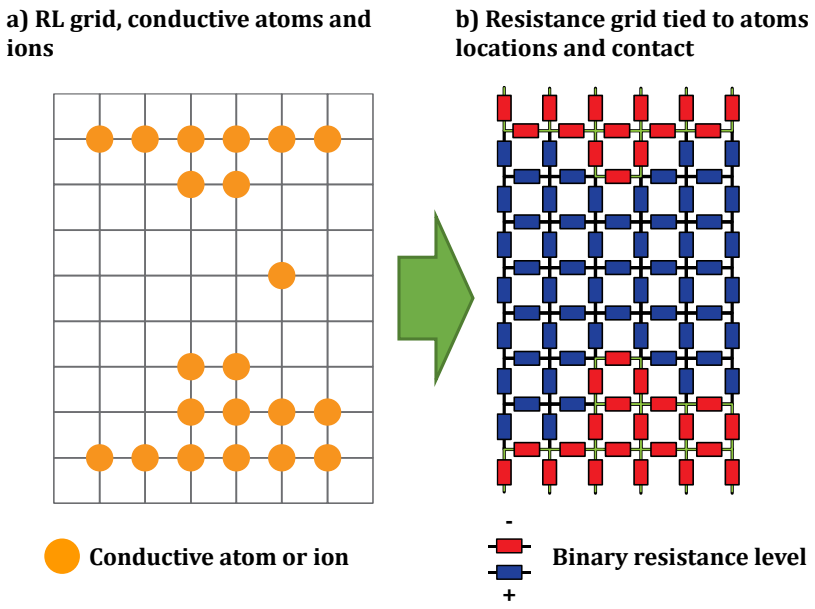

Figure 13. Schematic representation of the model step to compute the global resistance of the cell from the atoms and ions location in the resistive layer

the resistance of HRS. Indeed, a single atom missing in the conductive path leads to a complete loss of electrical conduction.

3.1.3 Version 3: Point Contact & Simplified Tunneling Model

This version of the model has been developed to overcome the impossibility of the previous version to correctly compute the R_{HRS}. Indeed, in order to completely simulate the CBRAM life – time, it is crucial to simulate both LRS and HRS resistances. This is why a model coupling point contact and simplified electron tunneling has been introduced. Once again this model relies on the creation and resolution of a resistance network through Kirchhoff and Ohm laws. However, this time, the resistance network is not a strict overlay of the framework grid but varies with the position of the atoms/ions as seen in Figure 14. Each node of the resistance network corresponds to an atom/ion and the resistance connecting the nodes is tied to the distance between them:

$$R_{Cu-Cu} = R_{Quantum}\, exp\left(2\frac{\sqrt{2m^{*}E_C}}{\hbar}\,(d-a)\right)$$

Where $R_{Quantum}$ is the Quantum of resistance (12.9 kΩ), m^* the effective mass of electron for a specific electrolyte, E_C the energy barrier for electron tunneling, d the distance between two atoms, a the contact distance between two atoms and $\hbar$ the Planck constant. For atoms/ions in contact the

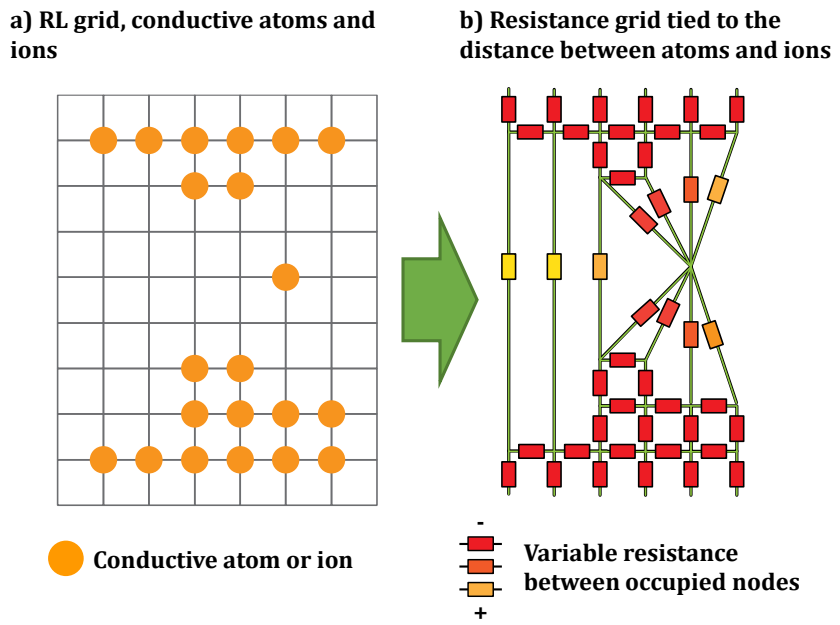

Figure 14. Schematic representation of the model step to compute the global resistance of the cell from the atoms and ions location in the resistive layer

exponential term is null and only stands the quantum of resistance. When the atoms/ions aren't in contact the resistance value exponentially varies with the distance between them. This conduction model offers a continuous resolution in opposition to the two previous binary versions in term of distance between atoms/ions. This model update allows to correctly compute both resistances of LRS and HRS and then study the Forming, SET, RESET, Data Retention and Cycling operations. However, as expected, this version if much more CPU – time consuming, and required an advanced optimization of the whole KMC model to achieve reasonable computation time and allow statistical simulations. Finally, as the previous model versions, the Kirchhoff and Ohm laws resolution also gives the electric potential at each point of the resistance network. This time the resistive network being built around the atom positions, finite difference method is required to translate the electric potential at the atoms position to every point of the framework grid. This conduction model is based on the metal atom and ions location in the electrolyte but does not include other traps that might modify the cell resistance especially in pristine state. This induce a limitation in the calculation of the pristine resistance value.

3.1.4 Electrical conduction model synthesis

No matter the version of the model, the final result of this step is the global calculation of the cell resistance value. Mathematically, all these versions relies on the same fundaments: the

resolution of a resistance network. However the conduction mechanisms behind this resolution differ. From area concentration and semiconductor behavior to quantum conductance and tunnel conduction, the model has evolved in accordance to the requirements imposed by the physical mechanisms and CBRAM operations studied. Figure 15 summarizes the difference between the conductions models. It can be seen that the simplified tunnel model offers the best of the two previous version with only limitations regarding the pristine resistance. It also greatly reduces the computation time by decreasing the number of nodes in the resistance computation, each node being an occupied point of the grid instead of all the grid points. Finally, from this resolution it is also possible to extract the voltage at each point of the grid, which will come in handy as will be shown in the next part.

3.2 Electric Field Model

As seen in the description of the physical mechanisms involved in the CBRAM operations, the electric field is one of the two driving forces considered in this KMC model, along with the temperature. It is then crucial to be able to rapidly compute the electric field value at each point of the grid and for every iterations. The most accurate procedure to compute the electric field would be to solve the Poisson equation using finite elements method [Dörfler 1]. However, this method is very slow and CPU – time consuming, making it difficult to integrate it in a switching simulation which requires a high number of iterations. To overcome this concern, it has been chosen to use

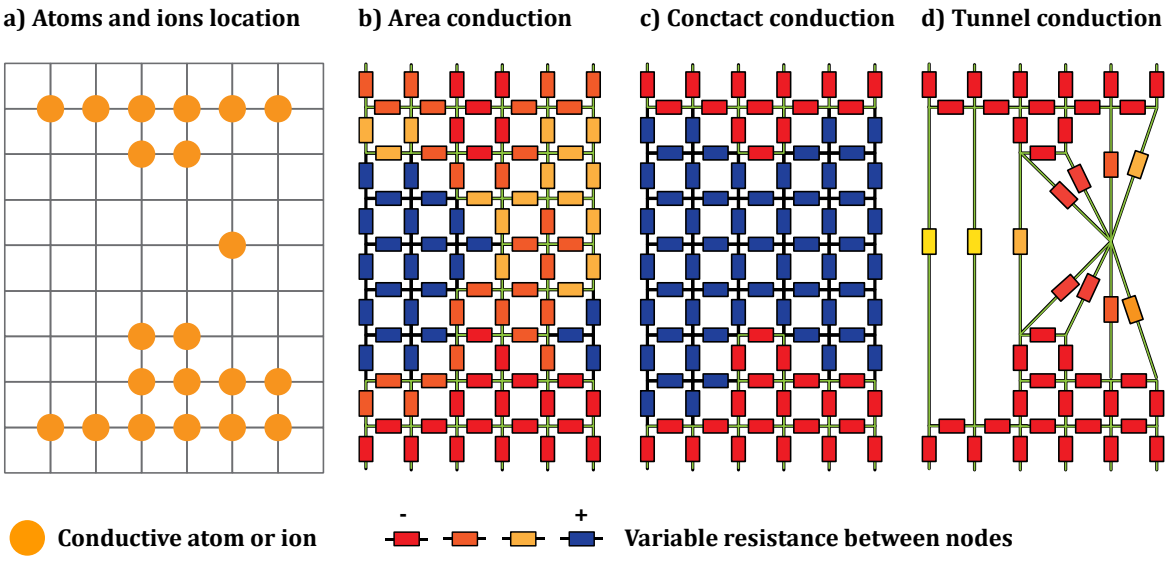

Figure 15. Comparaison of the conduction models

the voltage values at every points of the grid obtain though the current solving and to calculate the electric field from it, using the equation from Maxwell analyses:

$$\vec{E} = -\overrightarrow{grad}(V)$$

Where V is the voltage at each point of the grid and $\vec{E}$ the corresponding electric field. This method takes advantage of the conduction model solving to extract, at very low computation cost, the electric field value. It shows great performances considering that the electric potential has to be calculated to solve the conduction model, but it also offers great accuracy comparable to finite elements. However, this model neglect the charge of the migrating entities in regard to the high voltage on the electrodes. This might appear as a limitation in the case of a strong accumulation of charged particles during SET or RESET, as the field modification induced by this accumulation would not be correctly computed.

3.3 Thermal Model

The temperature is the second driving force considered in the KMC model. The temperature not only plays a role during the thermally accelerated data retention but also during the Forming, SET and RESET operations [Govoreanu 2].This thermal model has actually been developed to accurately compute the SET and RESET operations. The tunnel current model and thermal model were jointly developed and every references to the current or electric potential in this section refer to values obtained from the tunnel current model. The temperature in the CBRAM cell comes from two sources, the ambient temperature (ex: room temperature or oven temperature) and the energy dissipated by Joule Heating. The ambient temperature is stable throughout the simulation but the temperature induced by Joule Heating evolves over time in function of the current and the filament morphology. The model is built around the calculation of the generated energy by Joule Heating and the energy loss by conduction in the surrounding medium.

3.3.1 Joule Heating energy generation

As seen in the tunnel current model, the location (point of the grid) of every conductive atoms and ions are bonded to each other by a resistance value exponentially dependent of the distance between them. However, the thermal generation is based on Joule Effect which requires an ohmic contact to occur. This is why only the touching atoms are considered for the thermal generation. Thus, considering the Joule Effect, the generated power can be written as:

$$P = R.I^2$$

Where R is the resistance between the two atoms and I the current flowing through. It is possible to express the power in function of the electrical potential:

$$P = \frac{U^2}{R}$$

Where U is the electrical potential between the locations of the two atoms. We consider the power generated by a Cu – Cu bond, coming half from the first atom and half from the second:

$$P_{atom_1} = P_{atom_1} = \frac{1}{2} \frac{(V_1 - V_2)^2}{R_{1,2}}$$

Where P_{atom_1} and P_{atom_2} are the power generated at each atom 1 and 2 location, V_1 and V_2 the electric potential of the two atoms and $R_{1,2}$ the resistance between them. Finally, considering for each atom, its bonds to every other atoms, the total generated power is:

$$P_{atom_i} = \frac{1}{2} \sum_{n_{atoms}(\neq i)} \frac{(V_i - V_n)^2}{R_{i,n}}$$

Where P_{atom_i} is the power generated at the i^{th} atom, V_i and V_n are the electric potential of the two atoms i^{th}, n^{th} and $R_{i,n}$ the resistance between them. It is then possible to calculate the generated power by Joule Effect at each atom location from the output of the tunnel current model. However, once the power is generated it is dissipated by the surrounding elements of the CBRAM: electrodes, electrolyte and filament and this dissipation also has to be computed.

3.3.2 Thermal conduction

Similarly to solving the electric field in the CBRAM, the most accurate method to solve the thermal conduction would require to compute the Poisson equation with finite elements. However, as stated before, this choice is too CPU demanding and wouldn't allow any statistical study. This is why, it has been chosen to follow the same computation path as for the electric field, using a thermal resistances network to solve the thermal conduction. The analogy between electricity and temperature is of great help here, indeed to the Ohm law attached to the thermal conduction follows the equation:

$$\Delta T = P * R_{th}$$

Where ΔT is the increase of temperature, P the power generated and R_{th} the thermal resistance depending on the material. The thermal resistance can be obtained from the thermal conductivity and the geometry of the involved element. From this equation and using the previously calculated power generated a resistance network is created following the framework grid. Using Kirchhoff and Ohm laws, it is possible to rapidly compute the temperature in the cell considering ambient temperature on the edges. The filament and Cu atoms/ions are not only generating heat but also participating in the conduction and dissipation of this heat. The morphology of the filament as therefore a great importance on the thermal profile of the cell.

It is important to note, that using the Ohm law thermal analogy involve a stable thermal state of the CBRAM and a stationary system. As mentioned before, the global KMC model is computed iteration by iteration, and each iteration duration has to be sufficiently long to be considered in a stationary state and in agreement with the previous statement. Moreover, the mechanisms speed and iteration time depend on the available energy to the system, in term of temperature and voltage. In those conditions, if the generated energy becomes too high the iteration time might become too short to consider the system in a stationary state. Using a finite elements computation software (COMSOL Multiphysics) as can be seen in Figure 16, it was possible to extract the thermalization time of a CBRAM system around the nanosecond, depending on the architecture and materials. Iteration times under the nanosecond have been encountered during the simulation of RESET, with high current and temperature. Computing a transient state thermal simulation on top of the rest of the model would have taken too long to develop and to solve in this work. This is why a simplified

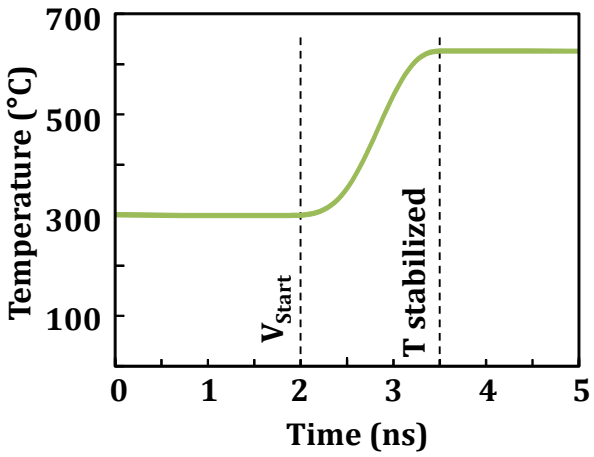

Figure 16. Temperature dynamic resolution showing the thermal stabilization 1.5 ns after the voltage pulse application.

approach, using exponential decay of the temperature has been introduced. Using a time constant around the nanosecond allows to obtain correct RESET characteristics with limited computation time. A more precise temperature solving should be used for future work. However, the present version offered enough accuracy to understand crucial behavior of the cell and compare different materials.

3.3.3 Thermal model synthesis

The thermal model relies on the same approach as the conduction model, the resolution of Kirchhoff and Ohm law on a resistance network. This approach offers great performances and relatively good precision overall. Indeed, the main limitation of the model stands in the lack of proper dynamic simulation which is really only occurring briefly during the CBRAM RESET operation. The temperature is considered as generated by Joule Heating and the thermalization occurring by conduction. A simplification of transient state has been integrated to overcome the very short iteration time induce by the simulation of high current operations. Finally, from this resolution it is possible to extract the temperature at each point of the grid depending of the current, the materials thermal conductivity and the filament morphology.

4. Chapter III synthesis

This chapter presented the evolution and final state of the KMC model used to understand the global functioning of the CBRAM. The KMC computation relies on the transition state theory which corresponds to the particles transition from an energy state to a more favorable one. The whole KMC model is built around the use of real physical constants and material properties, extracted from physical characterization, from ab – initio calculations or from the literature. The mechanisms involved in the CBRAM operation and computed in the KMC can be divided in two types: the ion displacement and atoms/ions oxidation reduction reactions, both kinds following the Transition State Theory. These mechanisms are assisted by the introduction of oxygen vacancies and the formation of copper aggregates into the electrolyte. The temperature and electric field are the two driving forces of the physical mechanisms and require proper physical models solving along with the electrical conduction model. The computation of transition probabilities, base of the KMC model, relies on the transitions rates and an optimized choice of iteration duration. This optimization aims to greatly reduce the convergence time of the model without sacrificing its

precision. This was made possible by adapting the iteration duration in function of the system state in opposition to taking a fixed iteration duration all the way through the KMC computation.

The physical models developed to solve the electrical conduction, temperature, voltage and electric field are based on the resolution of resistances networks to reduce the computation time in opposition to finite elements method.

Using the various optimization presented in this chapter and the improvement brought by the progressive understanding of the CBRAM operation, the KMC model is able to compute the complete life cycle of a CBRAM: Forming, SET, RESET, cycling and data retention (Figure 17 - 20). However, the KMC model still shows ways of improvement, especially in a proper and complete Poisson resolution regarding electric field and temperature. An integration of the oxygen vacancies as migrating entities modifying the electrical conduction might also offer a better representation of the CBRAM.

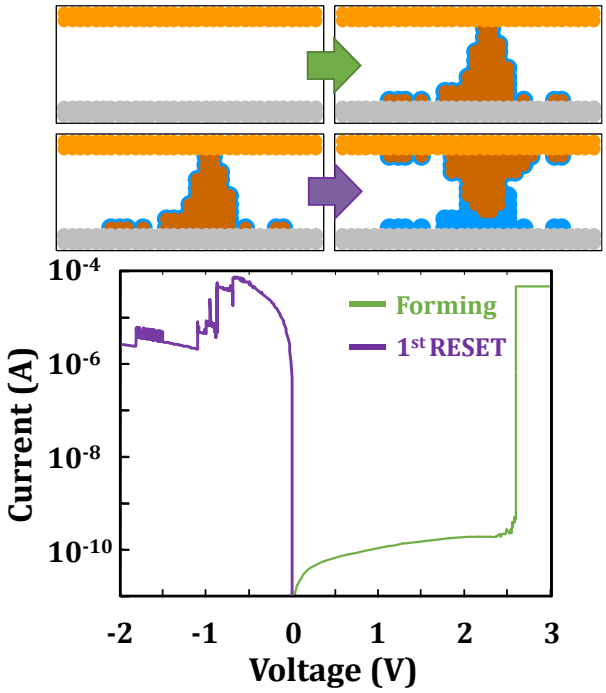

Figure 17. Typical simulated forming and 1st RESET IV characteristics.

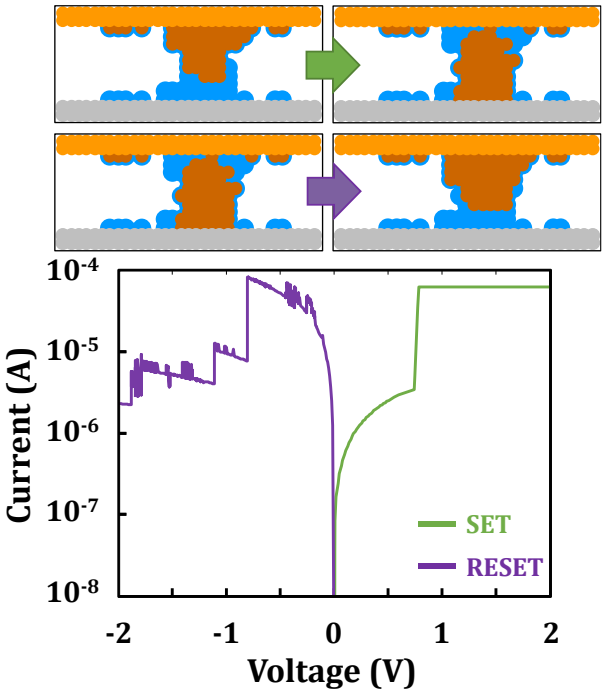

Figure 18. Typical simulated SET and RESET IV characteristics.

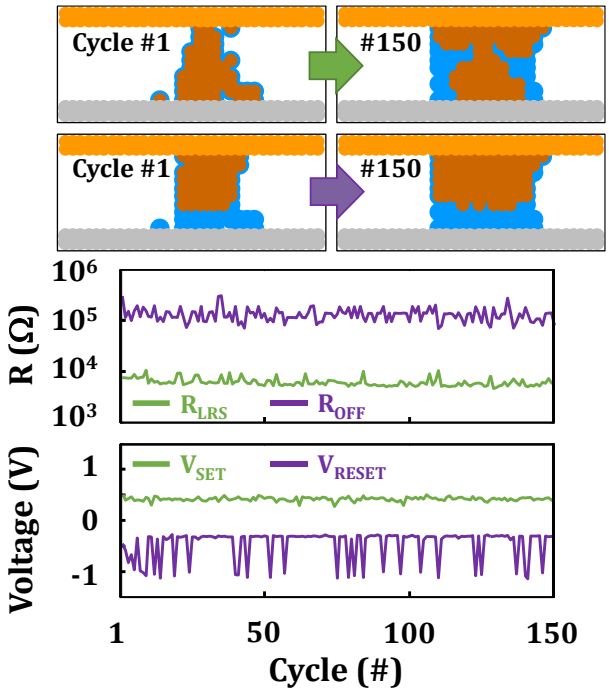

Figure 19. Typical simulated endurance characteristics with resistance and switching voltages evolution.

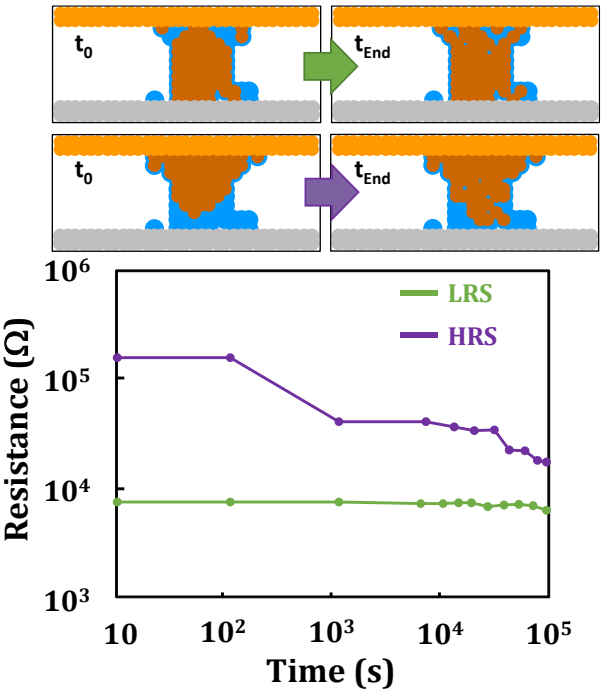

Figure 20. Typical simulated LRS and HRS retention characteristics illustrating window margin reduction.

Chapter III references

[Belmonte 1] Belmonte, A.; Degraeve, R.; Fantini, A.; Kim, W.; Houssa, M.; Jurczak, M.; Goux, L., "Origin of the deep reset and low variability of pulse-programmed WAl2O3TiWCu CBRAM device," in *Memory Workshop (IMW), 2014 IEEE 6th International* , vol., no., pp.1-4, 18-21 May 2014

[Degraeve 1] R. Degraeve, A. Fantini, S. Clima, B. Govoreanu, L. Goux, Y. Y. Chen, D. Wouters, P. Roussel, G. Kar, G. Pourtois, S. Cosemans, J. Kittl, G. Groeseneken, M. Jurczak, and L. Altimime, "Dynamic 'hour glass' model for SET and RESET in HfO_2 RRAM," IEEE Symposium on VLSI Technology, pp. 75–76, Jun. 2012.

[Govoreanu 1] B. Govoreanu, G. Kar, Y. Chen, V. Paraschiv, S. Kubicek, A. Fantini, I. P. Radu, L. Goux, S. Clima, R. Degraeve, N. Jossart, O. Richard, T. Vandeweyer, K. Seo, P. Hendrickx, G. Pourtois, H. Bender, L. Altimime, D. Wouters, J. Kittl, and M. Jurczak, "$10\times10nm^2$ Hf/HfO_x crossbar resistive RAM with excellent performance, reliability and low-energy operation," IEEE International Electron Devices Meeting Technical Digest, pp. 729–732, 2011.

[Goux 1] L. Goux, K. Sankaran, G. Kar1, N. Jossart1, K. Opsomer1, R. Degraeve1, G. Pourtois, G.-M. Rignanese, C. Detavernier, S. Clima , Y.-Y. Chen, A. Fantini, B. Govoreanu , D.J. Wouters, M. Jurczak , L. Altimime, J.A. Kittl, "Field-driven ultrafast sub-ns programming in $W\backslash Al_2O_3\backslash Ti\backslash CuTe$-based 1T1R CBRAM system," VLSI Tech Dig 2012, pp.69-70.

[Goux 2] Goux, L.; Fantini, A.; Degraeve, R.; Raghavan, N.; Nigon, R.; Strangio, S.; Kar, G.; Wouters, D.J.; Chen, Y.Y.; Komura, M.; De Stefano, F.; Afanas'ev, V.V.; Jurczak, M., "Understanding of the intrinsic characteristics and memory trade-offs of sub-μA filamentary RRAM operation," in *VLSI Technology (VLSIT), 2013 Symposium on* , vol., no., pp.T162-T163, 11-13 June 2013

[Kittle 1] C. Kittel, Introduction to Solid State Physics, Fourth Edition~Wiley, NewYork, 1971, pp. 457–459.

[Larentis 1] Larentis, S.; Nardi, F.; Balatti, S.; Ielmini, D.; Gilmer, D.C., "Bipolar-Switching Model of RRAM by Field- and Temperature-Activated Ion Migration," in *Memory Workshop (IMW), 2012 4th IEEE International* , vol., no., pp.1-4, 20-23 May 2012

[Laidler 1] K.J. Laidler and M.C. King, "Development of transition-state theory," The Journal of physical chemistry, vol.87, pp.2657-2664, 1983.

[Long 1] S. Long, X. Lian, C. Cagli, X. Cartoixà, R. Rurali, E. Miranda, D. Jiménez, L. Perniola, M. Liu, and J. Suñé, "Quantum-size effects in hafnium-oxide resistive switching," Applied Physics Letters, vol. 102, no. 18, p. 183505, 2013.

[McPherson 1] J.W. McPherson, R.B. Khamankar and A. Shanware, "Complementary model for intrinsic time-dependent dielectric breakdown in SiO 2 dielectrics," Journal of Applied Physics, vol.88, pp.5351-5359, Mar. 2003.

[Meekhof 1] D. M. Meekhof, C. Monroe, B. E. King, W. M. Itano, and D. J. Wineland, "Generation of Nonclassical Motional States of a Trapped Atom", Phys. Rev. Lett. 76, 1796.

[Nieminen 1] R.M. Nieminen, A.P.J. Jansen, "Monte Carlo simulations of surface reactions", Applied Catalysis A: General, Volume 160, Issue 1, Pages 99-123, 14 October 1997,

[Sankaran 1] Sankaran, K., Goux, L., Clima, S., Mees, M., Kittl, J., Jurczak, M., Altimime, L., Rignanese, G. and Pourtois, G., "Modeling of Copper Diffusion in Amorphous Aluminum Oxide in CBRAM Memory Stack", ECS Transactions, 45(3), pp.317-330.

[Sune 1] Sune, J.; Long, S.; Cagli, C.; Perniola, L.; Lian, X.; Cartoixa, X.; Rurali, R.; Miranda, E.; Jimenez, D.; Liu, M., "Electrical evidence of atomic-size effects in the conduction filament of RRAM," in Solid-State and Integrated

Circuit Technology (ICSICT), 2012 IEEE 11th International Conference on , vol., no., pp.1-4, Oct. 29 2012-Nov. 1 2012

[Voter 1] A. F. Voter, “Introduction to the Kinetic Monte Carlo Method,” Radiation Effects in Solids, K. E. Sickafus and E.A. Kotomin, eds., Springer, 2005.

[DÖRFLER 1] WILLY DÖRFLER, “A CONVERGENT ADAPTIVE ALGORITHM FOR POISSON’S EQUATION”, SIAM JOURNAL ON NUMERICAL ANALYSIS 1996 33:3, 1106-1124

Chapter IV. Forming, SET and RESET operations

1. Objectives

This chapter is the first of the three chapters combining electrical characterization and KMC simulation to understand the global behavior of the CBRAM. References will be made to chapters II and III regarding the description of the characterization protocols, studied samples and KMC simulations. As it is the case for the global electronic market, scaling is an important factor in the viability of the CBRAM technology. This is why, the impact of scaling the critical dimensions of a CBRAM cell on its electrical properties will be firstly addressed. Then, by putting aside the impact of scaling and focusing the study on devices of same dimension and architecture, this chapter will propose a comprehensive understanding of the CBRAM physical behavior during cycling, including the role of the material physical properties and the filament morphology.

The chapter will thus be organized firstly around the scaling impact. Then, focus will be put alternatively on the Forming/SET then RESET to address to physical behavior of the cell. Finally, by knowing the different factors impacting the CBRAM operation, optimization ways to obtain the proper CBRAM behavior for the targeted applications will be discussed.

2. CBRAM scaling impact on the electrical characteristics of the cell

The scaling study is based on nano-Trench (see chapter II) devices whose critical

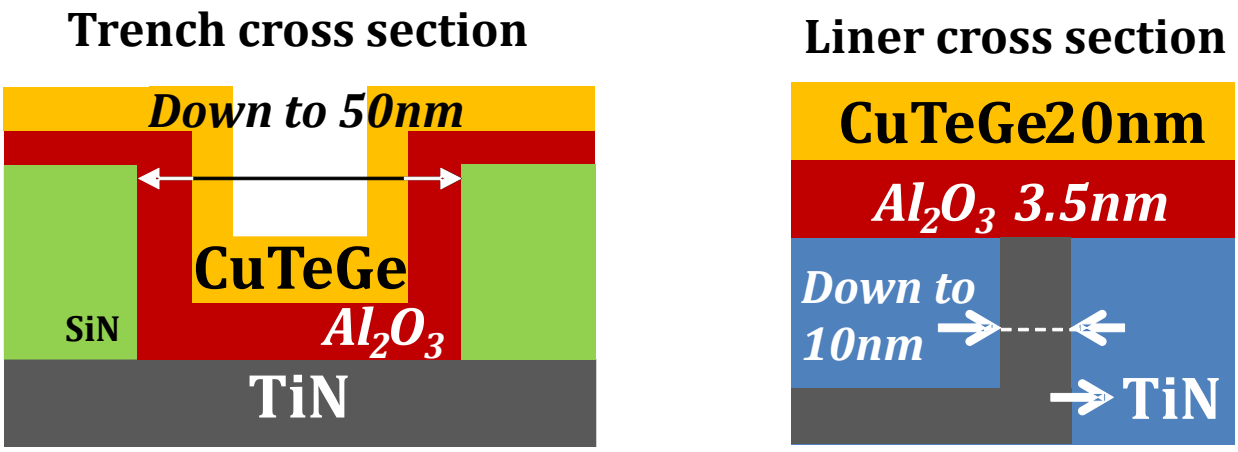

Figure 1. Schematics representation of the studied nano-Trench samples and the critical dimensions.

dimensions are controlled by the liner thickness used as bottom electrode, and the nano-Trench

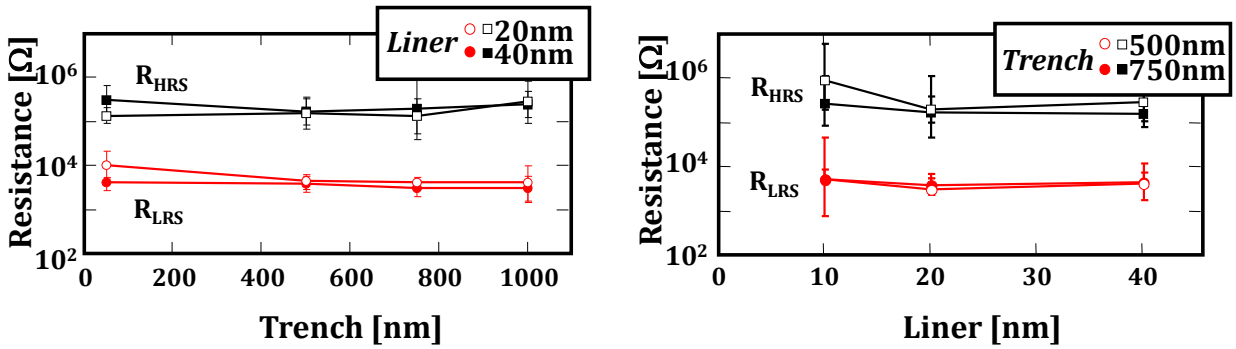

Figure 2. Size dependency of the LRS and HRS resistance level for both Trench and Liner scaling.

etching filled with the electrolyte and top electrode. The nano-Trench devices studied here were oxide based CBRAM with a CuTeGe/Al_2O_3/TiN material stack. Figure 1 shows a schematic representation of the studied samples with an insight of the critical dimension locations.

The resistance value of both HRS and LRS in function of the cell size is represented in Figure 2. There is little to no dependency of the resistance values regarding the cell dimension. The lack of dependency regarding LRS could have been foreseen as the electrical conduction of this state relies on a conductive filament smaller [Celano 1] (less than 10 nm) than the critical dimension studied there. However, the lack of dependency regarding HRS is unexpected and raises questions. Indeed, if the conduction mechanisms were based on volume electrical conduction through the electrolyte, the greater the dimension, the stronger the current should have been. Such a small correlation between size and resistance value of the HRS shows that there might be a residual conductive filament still in the HRS mainly responsible for the electrical conduction. Figure 3 schematizes this assumption by comparing the area responsible for the electrical conduction depending on

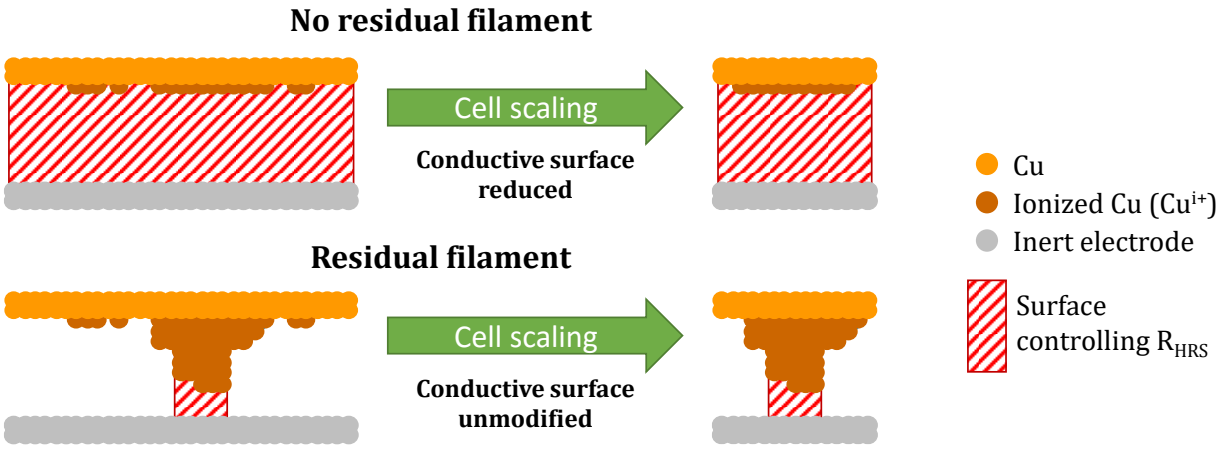

Figure 3. Comparison of the scaling impact on the conductive area with and with residual filament.

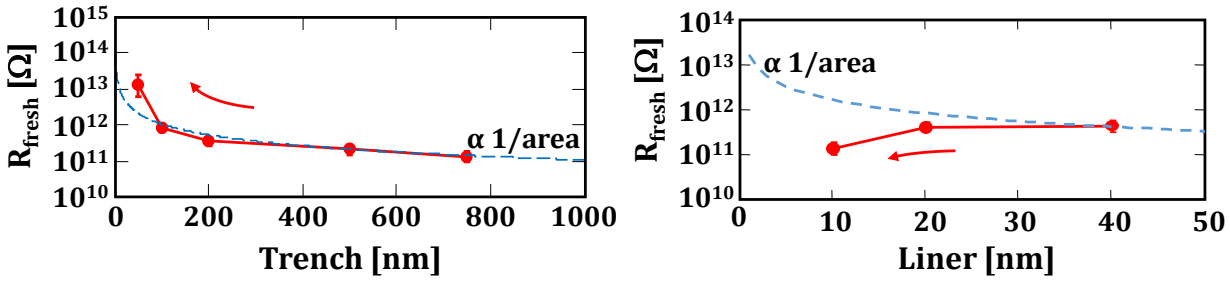

Figure 4. Size dependency of the fresh resistance level for both Trench and Liner scaling.

electrolyte state. This corresponds to the first hint of the presence of a residual filament in HRS, and this hypothesis will be completed while studying the physical mechanisms involved during RESET.

The fresh cells (or pristine cells) resistance has also been studied in function of the device size Figure 4. Regarding the trench size, the resistance value follows the inverse of the device area: the smaller the device size, the bigger the resistance. This correlation is proper to a volume conduction as expected in the pristine state. However, the impact of the liner dimension is not as clear and shows an inverted behavior with an increase of resistance when the liner dimension increases, the 1/area law being no more verified. This observation might be due to side effects becoming stronger as the liner dimension is reduced. Such effects could be surface defects, pending bonds or be related to the deposition technic involving loss of deposition uniformity for very small dimensions.

Figure 5 shows the impact of the scaling on the Forming voltage. Interestingly, the Forming voltage follows the same trends as the resistance versus Trench size. A clear increase of $V_{Forming}$ is measured for the 50nm trench devices and can be explained by both the increase of pristine resistance and a lower defects probability initiating the filament formation. On the other hand $V_{Forming}$ remains roughly constant (~ 2.8V) as the liner is scaled. Similarly to the Trench impact,

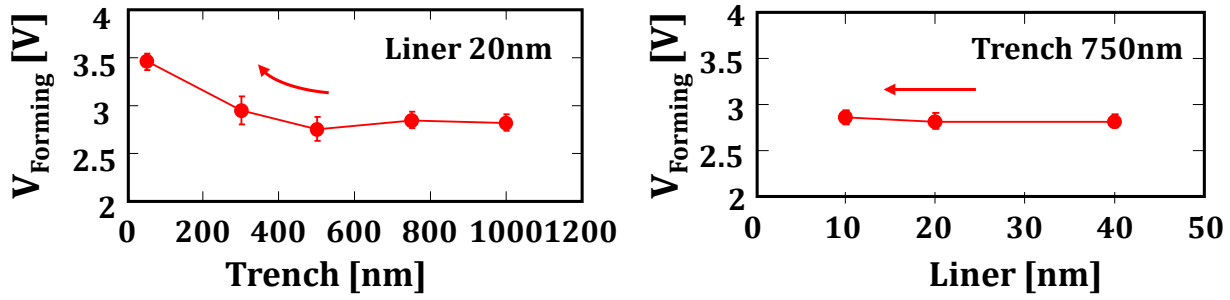

Figure 5. Size dependency of the Forming Voltages for both Trench and Liner scaling.

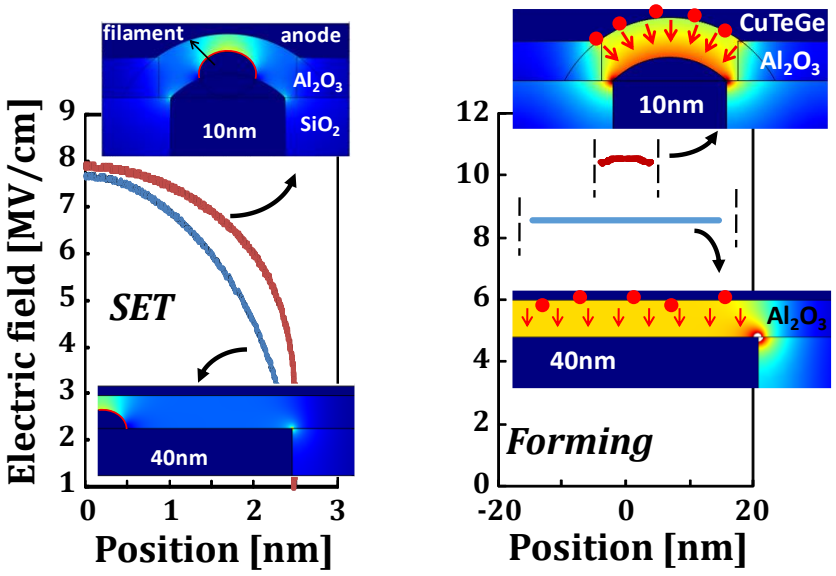

Figure 6. Simulations (COMSOL) of the electric field at the surface of the filament during SET (1V) and on the cathode during forming (3V) for 10 and 40nm devices

both pristine resistance and defect probability play a role. However, the size reduction toward such small dimensions leads to a non-negligible lightning rod effect involving an increase of electric field with the size reduction as simulated and shown in Figure 6. This is why, the pristine resistance reduction as well as the increase of electric field with the liner thinness should induce a reduction of $V_{Forming}$. However, the lower defect probability has an opposite effect and should increase $V_{Forming}$. These antagonist effects might stabilize the Forming voltage with the liner size variation and explain the experimental results.

Interestingly, the impact of scaling on the SET voltage shows an opposite trend to the Forming voltage on Figure 7. The SET voltage is roughly constant as the trench is scaled down but decrease with the liner dimension. During forming, a deteriorated path is created in the electrolyte to

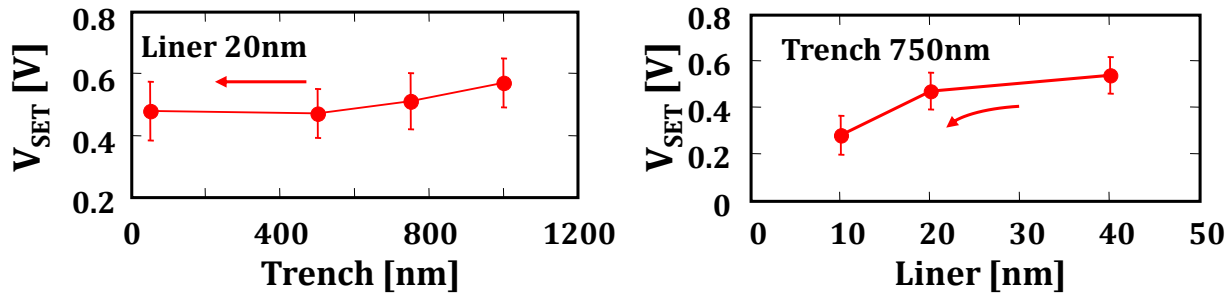

Figure 7. Size dependency of the SET Voltages for both Trench and Liner scaling

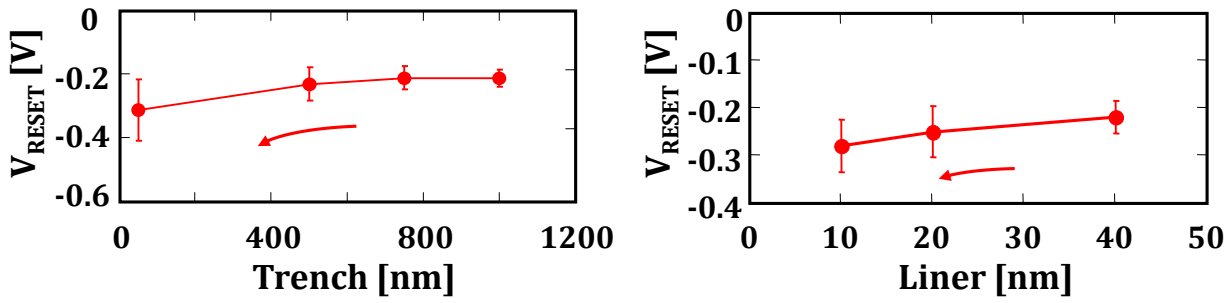

Figure 8. Size dependency of the SET Voltages for both Trench and Liner scaling

facilitate the ions migration, which explains the switching voltage reduction between Forming. With this deteriorated path, the defect are not as essential as during the forming to help the switching, which induces a loss of effect of the defects probability on the SET operations. Then, only the increase of electric field (up to 20%) due to the size reduction of the electrode plays a role in the SET voltage reduction (Figure 6). The decrease of V_{SET} is much more noticeable on the liner scaling than on the trench due to the higher lightning rod effect at smaller liner dimensions. This effect is due to the Chemical Mechanical Planarization (CMP) used to obtain the liner surface and creating the round shape of the liner.

Concerning RESET operation (Figure 8), both liner and trench reduction induce a slight $|V_{RESET}|$ increase. A large number of factors are involved in the RESET process, but it was not possible to conclude regarding this behavior with the current data. V_{RESET} corresponds to the highest current point during RESET operations, it symbolizes the starting point of the filament dissolution and is related to the filament morphology and available energy to the system. More insight on the RESET mechanisms will be given further in this chapter but it is at this moment, the origin of V_{RESET} dependence with cell scaling is not clear.

Finally, strong impact of liner scaling can be seen on the dynamic SET characteristics Figure 9. Using PS programming the SET time variation in function of the pulse voltage height has been studied. A great reduction of SET time by 5 decades at 0.8 V can be seen between the 10 nm and 40 nm liner samples with 10nm devices yielding a SET time of ~70ns.

In conclusion, cell scaling strongly impacts the CBRAM characteristics due to electric field enhancement, defect probability, switching voltages and resistance levels. Is also indicates the great importance to compare devices of the same architecture and dimension to be able to study the physical mechanisms involved in the CBRAM operation and extract their impact on the devices

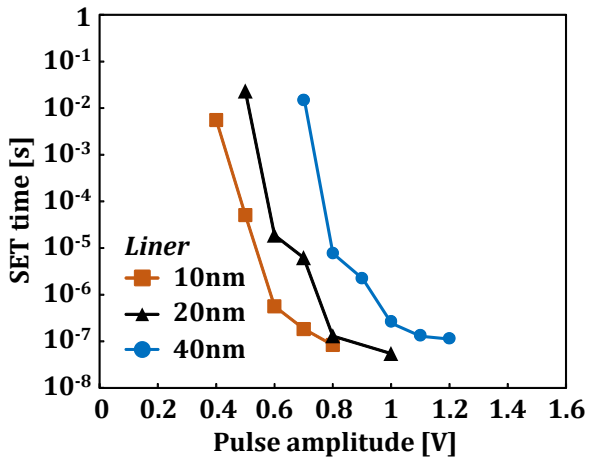

Figure 9. Dynamic SET time as a function of V_{Pulse} for various liner dimensions

characteristics. However, the results may vary depending on the studied architecture and the results obtained here on nano – Trench devices might not be identical for others architectures.

3. Physical understanding of the Forming and SET operations

The Forming and SET operations consist in the creation of a conductive path between the electrodes, their only difference being the initial state of the cell preceding the operation: pristine or erased cell for respectively Forming and SET. Both operations share mostly the same physical behavior and will be jointly treated in this chapter with highlights to their distinctive features.

Depending on the CBRAM material composition, it is possible to have Forming – free cells. It is the case of the chalcogenide based CBRAM which show no difference between the first cycle and the followings. Figure 10 Shows the difference of Forming and SET behavior for two different CBRAM technologies: chalcogenide and oxide based. The oxide based CBRAMs require in most cases a forming step before being cycled at lower voltages. However, some studies [Molas 1] not treated here have shown the possibility to greatly reduce the forming voltage toward forming – free cells using electrolyte doping.

This chapter section aims to propose a comprehensive understanding of the CBRAM Forming and SET operation including the impact of the material physical properties, filament morphology and temperature generation/conduction.

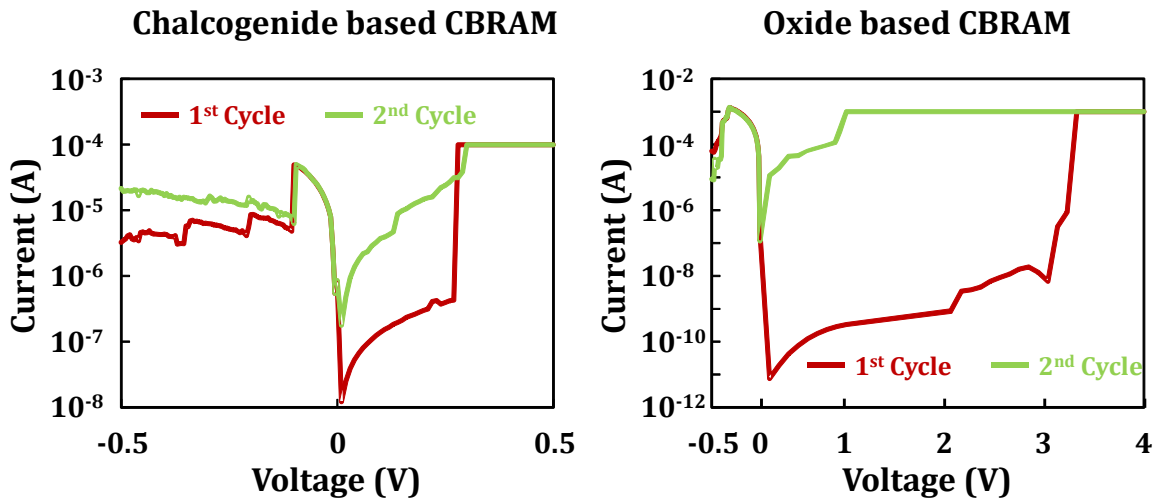

Figure 10. Experimental first and second cycle for chalcogenide and oxide based CBRAM, without and without forming

3.1 Impact of the CBRAM material stack on the Forming and SET operations

This section analyzes the role and impact of each layer of the CBRAM stack (Top Electrode: TE, Electrolyte or Resistive Layer: RL and Bottom Electrode: BE) on the Forming and SET operations. In regard to the KMC, this study is based on results using the contact electrical conduction model (Chapter III). The temperature generation/dissipation and oxygen vacancies generation are put aside for now and will be addressed later in this chapter. In this section, HRS is considered as a residual filament and is arbitrarily generated to model the SET operation, the height of the residual filament being tied to the initial HRS resistance value. A specific focus will be given to study the relation between the Forming/SET time and voltage. The $t_{Forming}(V_{Pulse})$ characteristics show an exponential dependence, meaning that increasing the programming pulse drastically reduces the required forming time. Moreover, the slope of these characteristics illustrates the time voltage dilemma of resistive RAMs; a sharp slope indicating that short programming times at high voltage and good disturb immunity at low voltage may be combined. Insights of the QS characteristic will also be given.

The study developed here have been carried on nano – Trench devices (see Chapter II) with various materials stacks summarized in Table 1.

Table 1. Studied samples to understand the Forming and SET mechanisms

Samples	S1	S2	S3	S4	S5	S6
Bottom Electrode BE	TiN	TiN	WSi	TiN	TiN	WSi
Resistive Layer RL	Al_2O_3 3.5nm	Al_2O_3 3.5nm	Al_2O_3 3.5nm	Al_2O_3 5nm	MO_x 5nm	Al_2O_3 5nm
Top Electrode TE	Cu	$CuTe_x$	$CuTe_x$	$CuTe_x$	$CuTe_x$	$CuTe_x$

3.1.1 Impact of the top electrode

To investigate the TE role in the CBRAM operation, pure Cu as well as $CuTe_x$ TE, both with the same TiN BE were jointly studied (Samples: S1 and S2). The restrained Tellurium concentration allows to consider a unique energy barrier height for the Cu redox reactions [Stefano 1] in both samples. The ionic hopping energy barrier height in the RL is also taken identical. The only variable considered by changing the TE is the metal work function (Φ_{TE}), which is respectively taken equal to 4.7 eV and 4.5 eV for Cu and $CuTe_x$ [Gartland 1, Jałochowski 1]. Figure 11 (a) shows the $t_{Forming}(V_{Pulse})$ simulated curves in good agreement with the experimental results. Increasing Φ_{TE} by 0.2 eV leads to a $t_{Forming}(V_{Pulse})$ shift of 0.25 V toward lower voltages and in term

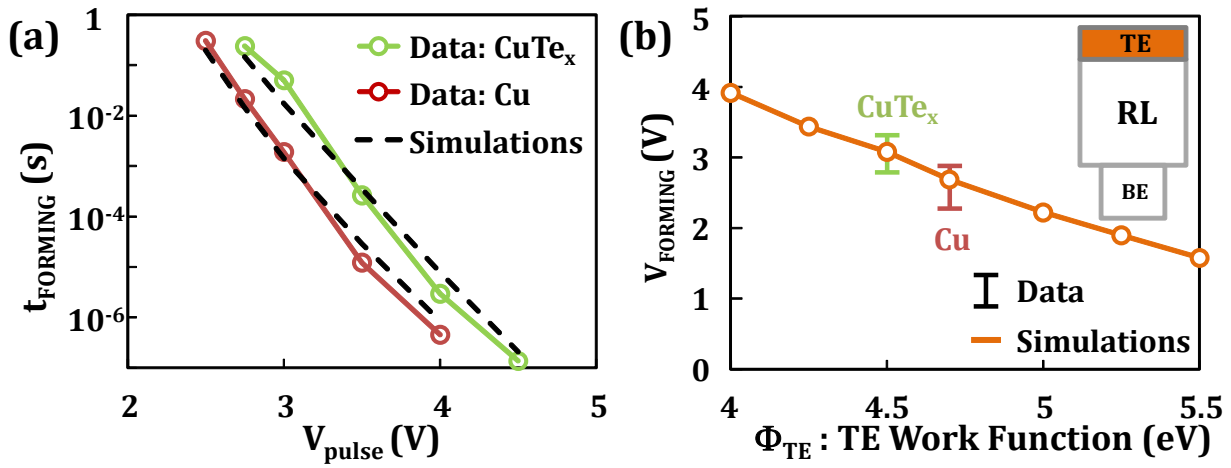

Figure 11. (a) Measured and simulated Forming time as a function of the applied voltage for CBRAM integrating Cu (S1) or CuTex (S2) as TE (ion supply layer). (b) Quasi static forming voltage dependence with TE work function.

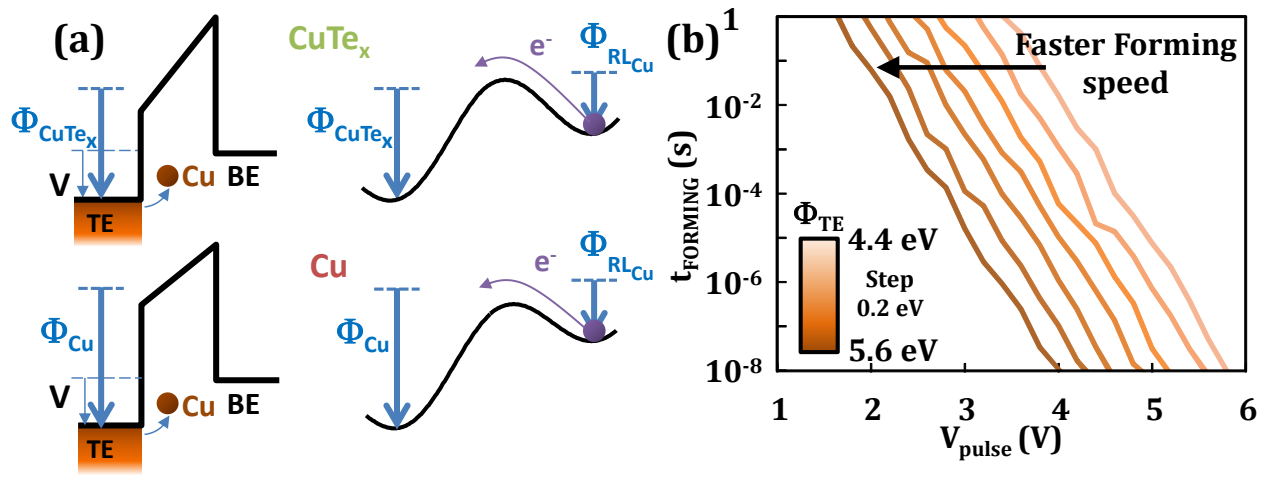

Figure 12. (a) Schematics illustrating the impact of the TE work function on the electric field in the RL, and on the oxidation-reduction reaction. (b) Simulated forming time as a function of the applied pulse voltage for various TE work functions.

of QS programming to a reduction of $V_{Forming}$ (Figure 11 (b)) shows the extrapolated impact of the TE work function on the $V_{Forming}$ for a wider range than the characterized one.

The TE work function has a double impact on the switching operation (Figure 12 (a)). Indeed, the difference of work function between TE and BE induces a flat band voltage V_{FB} which is reduced as Φ_{TE} increases:

$$V_{FB} = \Phi_{BE} - \Phi_{TE}$$

This flat band voltage adds up to the applied voltage and influences all the CBRAM physical mechanisms: oxidation and reduction reactions as well as ion migration. Its impact is modified by the RL thickness, the thicker the RL, the less visible its impact. Moreover, as stated in Chapter II, the Fermi level of the TE corresponds to the final state of the electrons during oxidation. A stronger Φ_{TE} leads to a lower Fermi level and the lower the Fermi level, the stronger the energy difference between the electrons starting and the finishing energy states. This is why, considering the Transition State Theory, a deeper Φ_{TE} leads to a faster oxidation reaction, thanks to the energy barrier height reduction in the transition rate referred in the chapter III as:

$$\vec{\Gamma} = \nu . \exp\left(- \frac{E_A - \frac{1}{2}(Q\, d\, (1 + L\, \chi)\, \vec{\varepsilon}_{Global}) - (\boldsymbol{\phi}_{\mathbf{final}} - \boldsymbol{\phi}_{\mathbf{initial}})}{k_B T} \right) (\vec{x}, \vec{y})$$

Where $\phi_{initial}$ and ϕ_{final} are respectively Φ_{RL} and Φ_{TE} (see Chapter III for more details). The two influences of TE previously described are antagonist. The reduction of $t_{Forming}$ with the increase of Φ_{TE} shows the dominant impact of the TE work function on the oxidation reaction speed in the studied samples. This behavior is extrapolated for a range of TE work function in Figure 12 (b). This figures reports simulated results and shows the shift of $t_{Forming}(V_{Pulse})$ towards lower faster switching speed with an increase of TE work function.

3.1.2 Impact of the bottom electrode

To understand the BE impact on the CBRAM characteristics, the study has been focused on two materials: TiN and Si doped W, both with the same $CuTe_X$ TE (samples S2 and S3). These materials have two different work functions respectively 4.8 eV and 4.4 eV [Fonseca 1, Davisson 1]. Figure 13 (a) shows that an increase of BE work function (Φ_{BE}) by 0.4 eV leads to a $t_{Forming}(V_{Pulse})$ shift of 0.5 V toward lower voltages and in term of QS programming to a reduction of $V_{Forming}$ (Figure 13 (b)). Similarly to the TE, the BE work function has two effects on the switching operation (Figure 14 (b)). First, a stronger Φ_{BE} leads to a lower Fermi level (initial electron energy during reduction reaction) and a slower reduction reaction of the ions reaching the BE following (1) where $\Phi_{Initial}$ and Φ_{Final} are respectively Φ_{BE} and Φ_{RL} this time. Thus, a higher Φ_{BE} increases V_{FB}, which accelerates the physical mechanisms including the oxidation reaction. The increase of BE work function is then responsible at the same time for faster oxidation speed

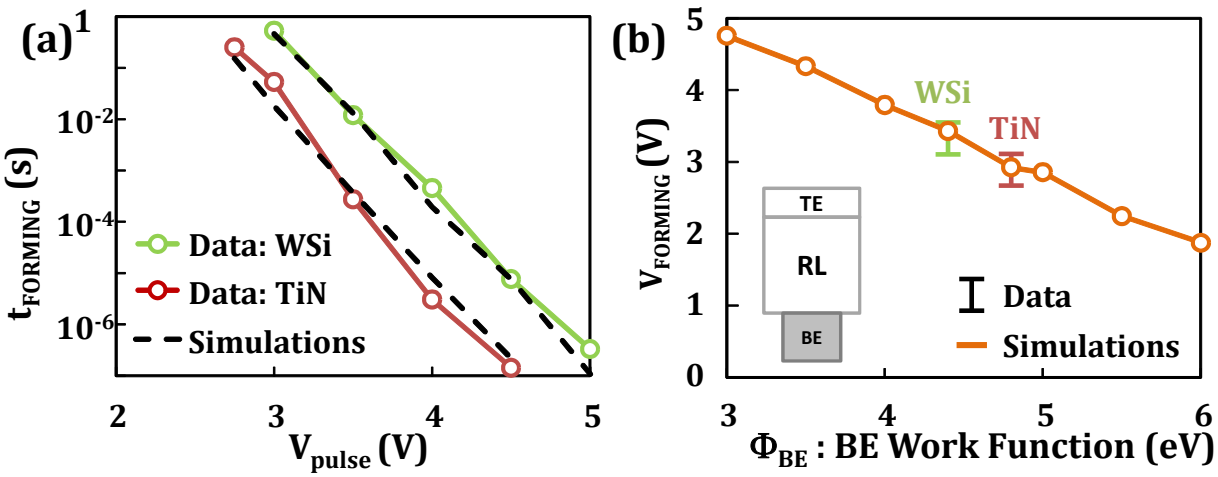

Figure 13. (a) Measured and simulated forming time as a function of the applied voltage for CBRAM integrating TiN (S2) or WSi (S3) as BE (inert electrode). (b) Quasi static forming voltage dependence with BE work function.

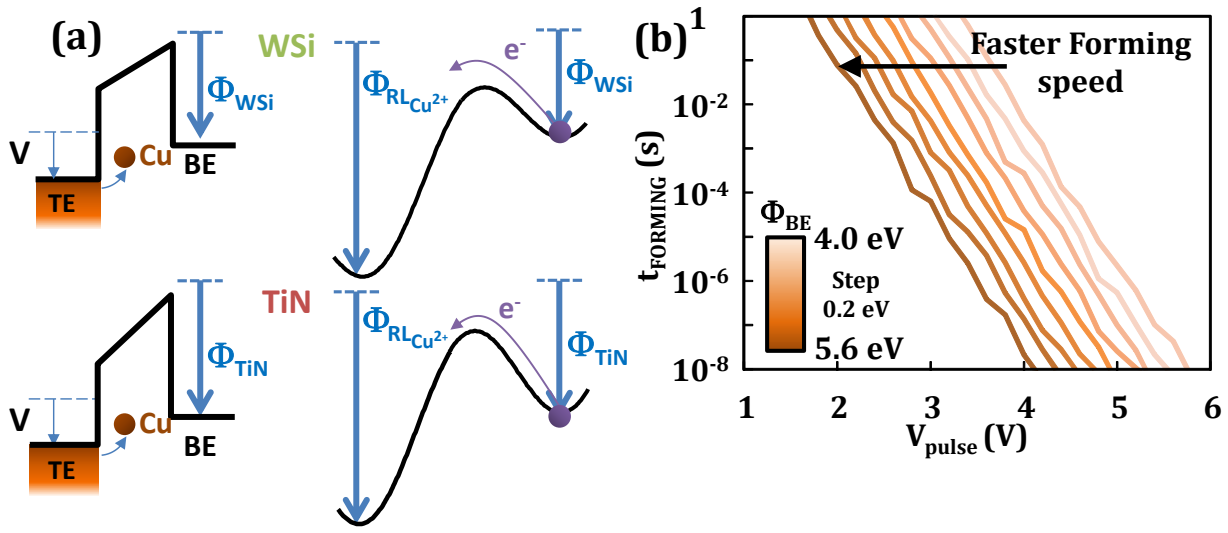

Figure 14. (a) Schematics illustrating the impact of the BE work function on the electric field in the RL, and on the oxidation-reduction reaction. (b) Simulated forming time as a function of the applied pulse voltage for various BE work functions.

and slower reduction speed. Figure 14 (b) shows that an increase of the BE work function reduces the $t_{Forming}$, and proves that the limiting mechanisms is the copper oxidation at the top electrode. The simulated results reported on this figure shows the shift of the $t_{Forming}(V_{Pulse})$ towards faster switching speed with an increase of BE work function.

3.1.3 Impact of the resistive layer

The RL has a much wider and complicated impact on the switching process as many mechanisms are involved. First, Figure 15 (a) shows an experimental shift and a change of slope of the $t_{Forming}(V_{Pulse})$ towards lower voltages by reducing the RL thickness, in agreement with our simulations. A RL thickness reduction of 1.5 nm turns into a reduction of Forming voltage between 1.25 V and 2 V in the studied area (for $t_{Forming} \approx 10^{-1}$ s, $V_{Forming} \approx 2.75$ V vs 4V and For $t_{Forming} \approx 10^{-7}$ s, $V_{Forming} \approx 4$ V vs 6 V). QS programming is also impacted by the reduced thickness with a decrease of forming around 0.3V (Figure 15 (b)). To understand the impact of the thickness on the slope of the $t_{Forming}(V_{Pulse})$, in opposition to all the others parameters shifting the curve, the relation between distance and electric field has to be analyzed:

$$\epsilon = \frac{V_{a-b}}{d_{a-b}}$$

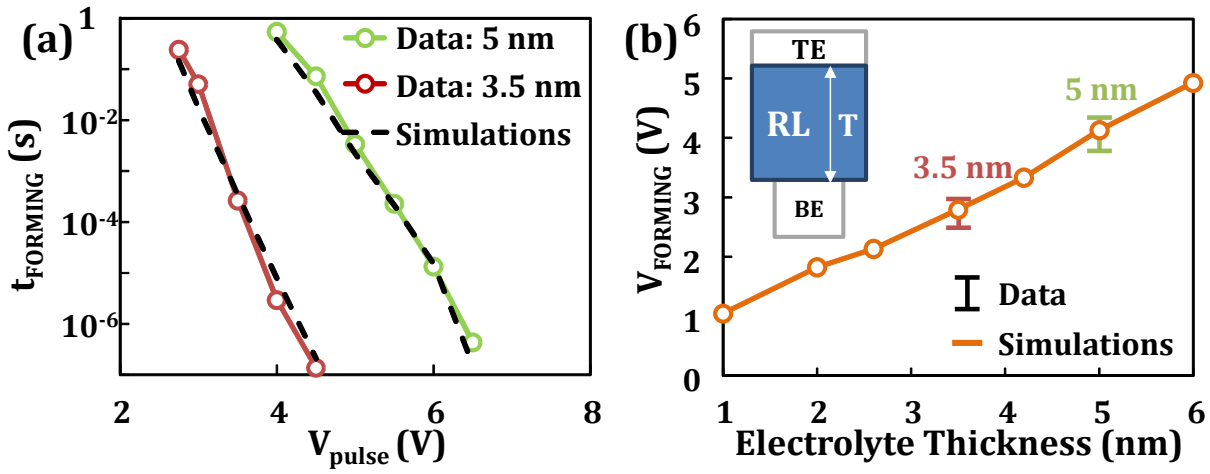

Figure 15. (a) Measured and simulated forming time as a function of the applied voltage for 3.5nm (S2) and 5nm (S4) Al_2O_3-based CBRAM. (b) Quasi-Static forming voltage dependence with RL thickness.

Where ϵ is the electric field, V the voltage drop between the points *a* and *b* and d the distance separating the points *a* and *b*. For the sake of simplification and to clarify this analyze, the distance *d* can be assimilated to the RL thickness. This means that the electric field increases faster with voltage for a thinner RL (Figure 16 (a)). The change of slope of the $t_{Forming}(V_{Pulse})$ can thus be explained by an enhancement of the voltage impact on the electric field for thin RL. Moreover, the reduction of the RL thickness translates into a shorter ionic migration path and a faster switching, partially responsible for the curve shift. The thickness impact is extrapolated for a larger range and reported in Figure 16 (b). Then, to go further into the understanding of the RL role in the CBRAM

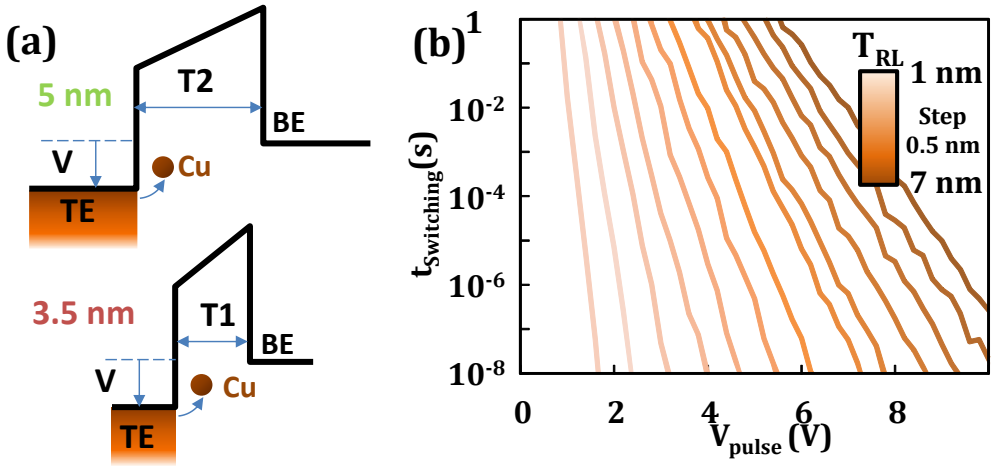

Figure 16. (a) Schematics illustrating the impact of RL thickness on the electric field. (b) Simulated $t_{Forming}$ as a function V_{pulse} for various RL thicknesses.

operations, the forming characteristics of Al_2O_3 and MO_x RL have been compared (samples S4 and S5). A steeper slope and a faster behavior are measured for MO_x as shown in Figure 17 (a). The QS V_{SET} evolution in function of the Cu energy level in RL has been extrapolated in Figure 17 (b) with fixed other parameters (electrical permittivity and hopping distance). The RL is the theater of redox reactions: the electrons initial state of the oxidation reaction through the Cu atoms traps and the electrons final state of the reduction reaction through the Cu ions traps. The depth of these traps directly influences the reactions speed, as the difference of energy levels between the starting and finishing point of the electrons accelerates the reaction. Thus, deep Cu atom traps (high energy) induce a low energy difference between the starting and finishing electrons states which leads to a slow oxidation reaction (Figure 18 (a)). In contrary, deep Cu ions traps increase the energy states difference and increase the reduction reaction speed. These trap depths can shift the $t_{Forming}(V_{Pulse})$ curve but cannot explain the change of slope shown in (Figure 17 (a)). To address the change of slope, parameters enhancing the electric field have to be analyzed. Once again, by referring to the transition rate, the local electric field is enhanced by the electric permittivity as well as by the distance between two transition states of the TST.

$$\vec{\Gamma} = \nu . \exp\left(- \frac{E_A - \frac{1}{2}(Q\, d\, (1 + L\, \chi)\, \vec{\varepsilon}_{Global}) - (\phi_{final} - \phi_{initial})}{k_B T} \right) (\vec{x}, \vec{y})$$

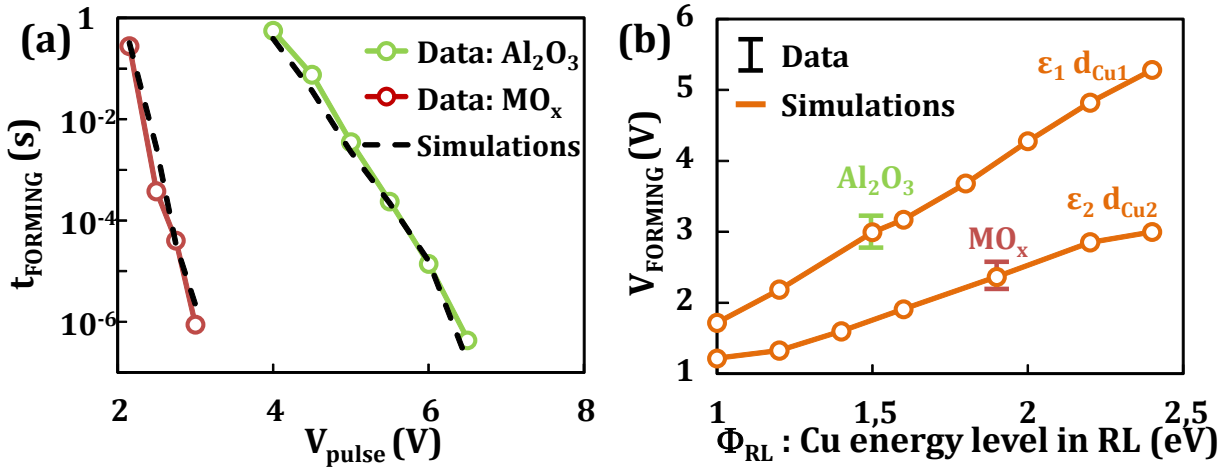

Figure 17. (a) Measured and simulated forming time as a function of the pulse voltage for Al_2O_3-based (S4) and MO_x-based (S5) CBRAM. (b) Quasi-Static forming voltage dependence with Cu energy depth (from vacuum) in the RL.

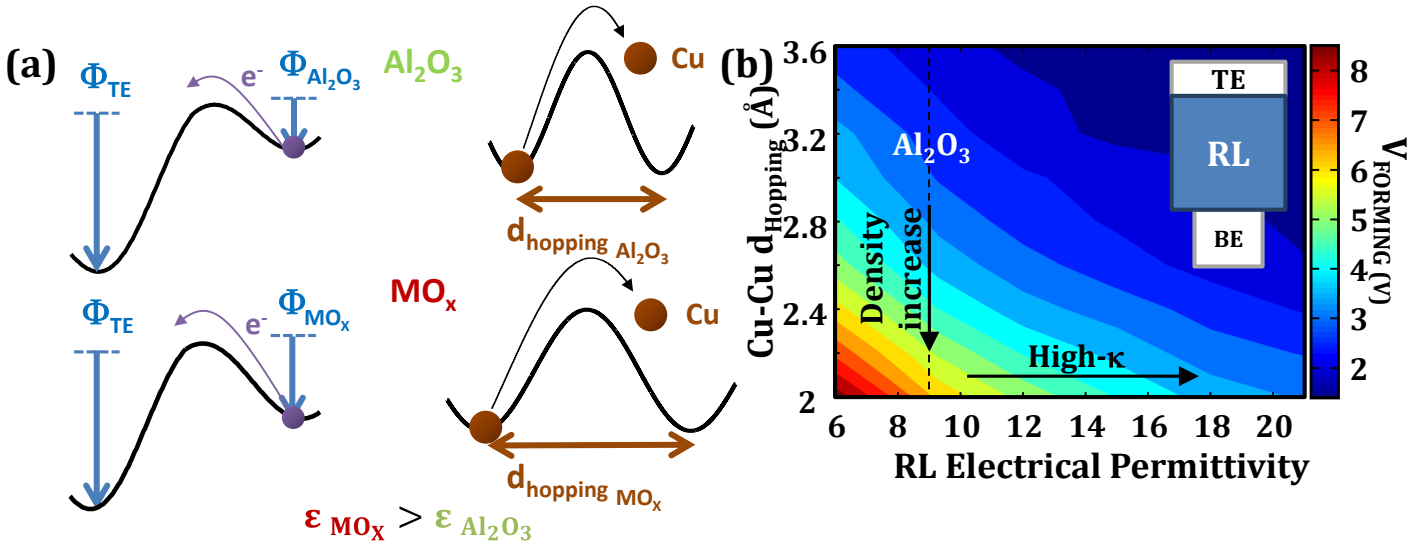

Figure 18. (a) Quasi-Static forming voltage dependence with Cu-Cu hopping distance in the RL, and RL permittivity. (b) Schematics illustrating the impact Φ_{RL} on the oxidation-reduction reaction obtain with the KMC simulation.

Where Q is the number of involved electric charges, d the distance between the two states L the Lorentz factor, χ the electric susceptibility tied to the electrical permittivity and $\vec{\varepsilon}_{Global}$ the electric field seen by the electrolyte. These parameters are different for the two RL and participate to the change of slope: the higher the permittivity and hopping distance, the bigger the slope. The distance between two states can be extracted by ab-initio calculation as previously stated and is affected by the RL density. It corresponds to the average value of the Cu-Cu distance in the RL for the ionic migration and in the interfacial region for the redox reactions. The impact of both electrical permittivity and hopping distance is represented in Figure 18 (b). Precisely tuning the RL physical parameters might be difficult as various parameters are tied together, however it is possible to foresee the behavior of a RL in function of its physical properties and density.

3.1.4 Material physical properties – Conclusion

It has been demonstrated that by tuning the material stack and properties it is possible to control the Forming and thus the SET operation in two ways as summarized on Figure 19. It is possible to shift the $t_{Forming}(V_{Pulse})$ characteristic by tuning the energy levels of the various layers (Φ_{RL}, Φ_{TE}, Φ_{BE}) but also to change the characteristics slope by altering the RL features enhancing the electric field (thickness, permittivity, hopping distance). Both the shift and slope changes of the $t_{Forming}(V_{Pulse})$ characteristics offer a way to increase the SET/Forming speed (or reduce the voltage) but in addition, the slope tuning brings on a way to improve the disturb immunity. This disturb

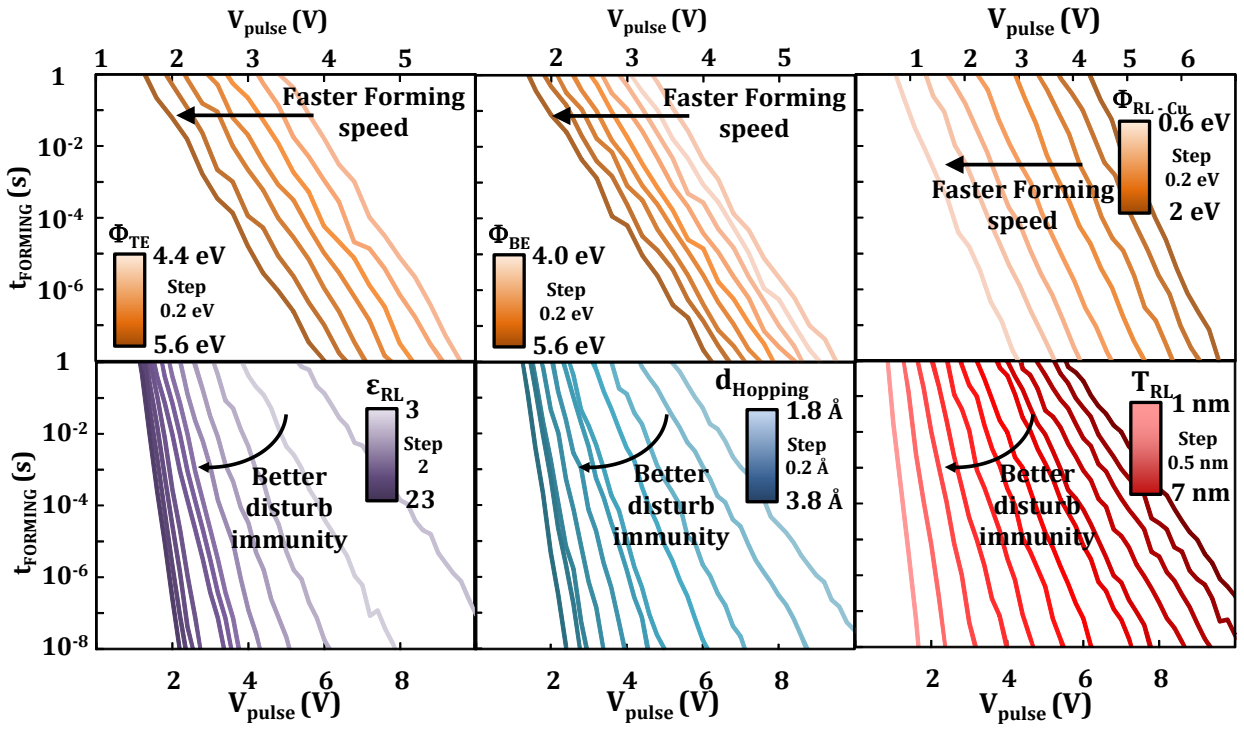

Figure 19. Summary of the impact of each physical parameter of the CBRAM stack on the time voltage Forming characteristics

immunity corresponds to the switching time at low voltages (typically V_{Read}) and can be tied to a better HRS retention. The disturb immunity is improved for high dielectric constant and thin RL. Finally, it is possible to extrapolate V_{SET} from different initial filament height corresponding to various initial HRS resistances as shown Figure 20 (a). It is possible to observe a transition from

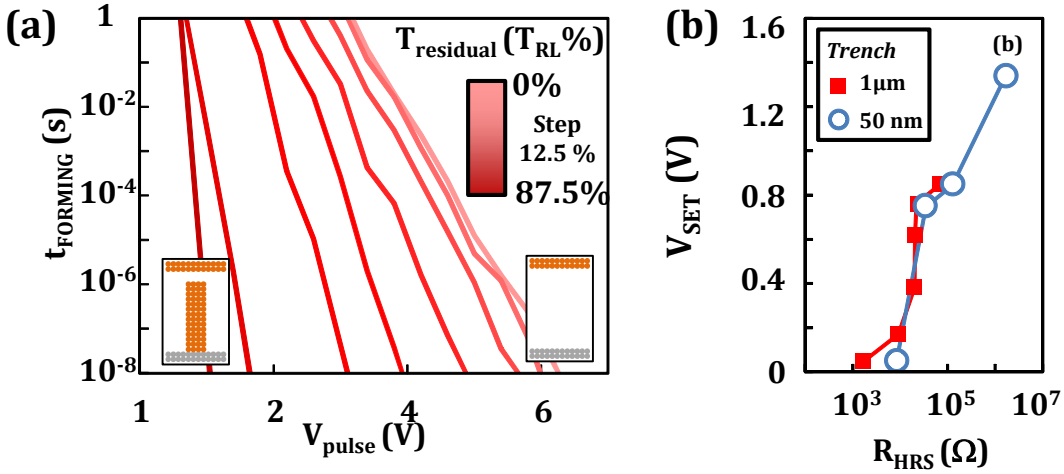

Figure 20. (a) Calculation of the SET time/voltage dependence for various residual filaments in the resistive layer, corresponding to various initial R_{OFF}. (b) Evolution of the SET voltage in function of R_{HRS}. Experimental results obtained on $CuTe_X/Al_2O_3$ (5 nm)/TiN for two different Trench dimensions.

high forming voltages to lower voltages proper to SET operations with the increase of residual filament in the resistive layer. This observation is in agreement with the increase of SET voltage with the increase of R_{HRS} reported in Figure 20 (b). This increase of R_{HRS} can be tied to the reduction of residual filament height as will be presented in the following.

A summary of the electrical performances difference between samples is presented at the end of the chapter in Table 2.

3.2 Temperature role in the Forming and SET operations

The thermal resolution, as stated in Chapter III, has been implemented in the KMC model to simulate the RESET operation which is known to be thermally activated [Tada 1]. However, to offer a complete cohesion between the SET and RESET understanding, the temperature impact also has to be verified during SET. The electrical characterizations used to study the temperature role have been completed on nano – Trench devices (Chapter II) with a copper based TE, Al_2O_3 RL and Silicon dopped Tungsten BE.

The temperature increase is considered as a result of joule heating in the conductive filament. The joule heating mechanisms can only occur with sufficient level of current flowing through the filament, a strong conductive path is thus required. This means that Joule Heating only occurs for a strongly restricted time in the course of SET operations and precisely during the fast current increase corresponding to the filament formation. For this reason joule heating has widely been neglected regarding Forming and SET. However, during the short duration of time corresponding to the SET spike, a strong increase of temperature briefly occurs. Under this high temperature, the thermal motions of the ions and electrons lead to a high increase of the transition rates between different locations or states (oxidized or reduced). Thus, the SET spike, which appears as an instantaneous process, seems in fact to be the succession of thermally accelerated mechanisms leading to the stabilization of the filament.

The stabilization of the filament consists in reducing the temperature by decreasing the current density and thus increasing the thickness of the filament. Figure 21 shows the different steps of the stabilization, from the creation of a thin conductive path to a stable filament. Another important factor of the heat reduction is the thermal dissipation induced by both the filament and the electrodes. By increasing the filament thickness, the contact surface between the filament and the electrodes becomes larger which increases the thermal exchange and helps the heat reduction and

filament stabilization. The thermal dissipation is regulated by the thermal conductivity of the CBRAM components, both electrodes being metallic, they generally offer the highest thermal conductivity of the system and serve to reduce the temperature of the cell. However a thermal conductivity modification of the BE could lead to a severe modification of the filament morphology. Indeed, changing the BE thermal conductivity in the KMC model, leads to different morphologies. As shown in Figure 22 a high thermal conductivity of the BE induces a thin filament, whereas a low thermal conductivity leads to a thick filament with a more conical shape. In order to exchange the same amount of heat with the bottom electrode, a larger contact surface is required with the lower thermally conductive BE, which explains the filament morphology difference. It is hard to experimentally confirm the statements concerning the filament shape as it is complicated to obtain precise observation of it. However, it is possible to support the previous statements with other behaviors that might be influenced by the filament morphology, such as data retention or RESET. Some insights regarding the change of filament morphology induced by the BE thermal conduction will be given during the RESET analyses.

To prove the real impact of the temperature during SET, unipolar cycling has been studied. Unipolar cycling consists in applying the same voltage to set and reset the cell (generally positive voltage on TE), the only difference being the limiting current during SET but not during RESET. In these conditions, the electric field keep the same direction during both SET and RESET and cannot explain the dissolution of the filament, thus this dissolution can only be thermally activated. Figure 23 shows the unipolar RESET characterized and simulated with the KMC model. The KMC

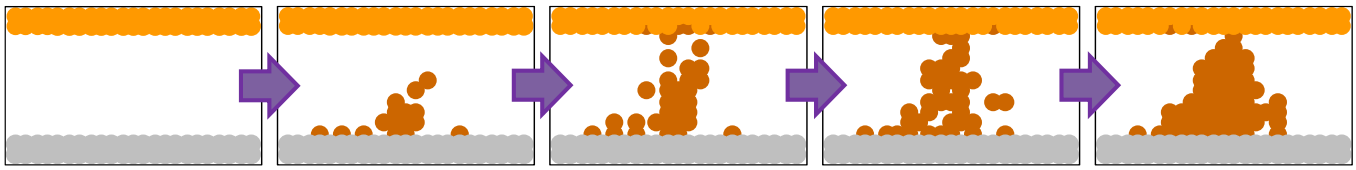

Figure 21. Filament formation and stabilization to reduce the current density and temperature.

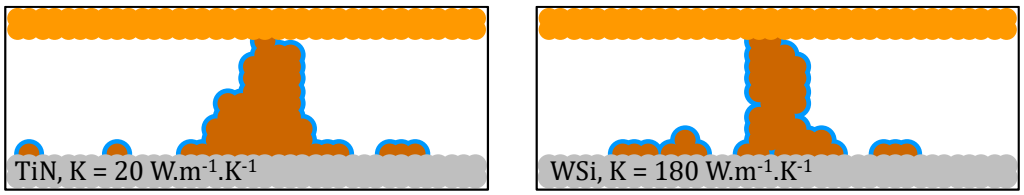

Figure 22. Simulated filament formation for two different BE, TiN with low thermal conductivity (left) and WSi with high thermal conductivity (right).

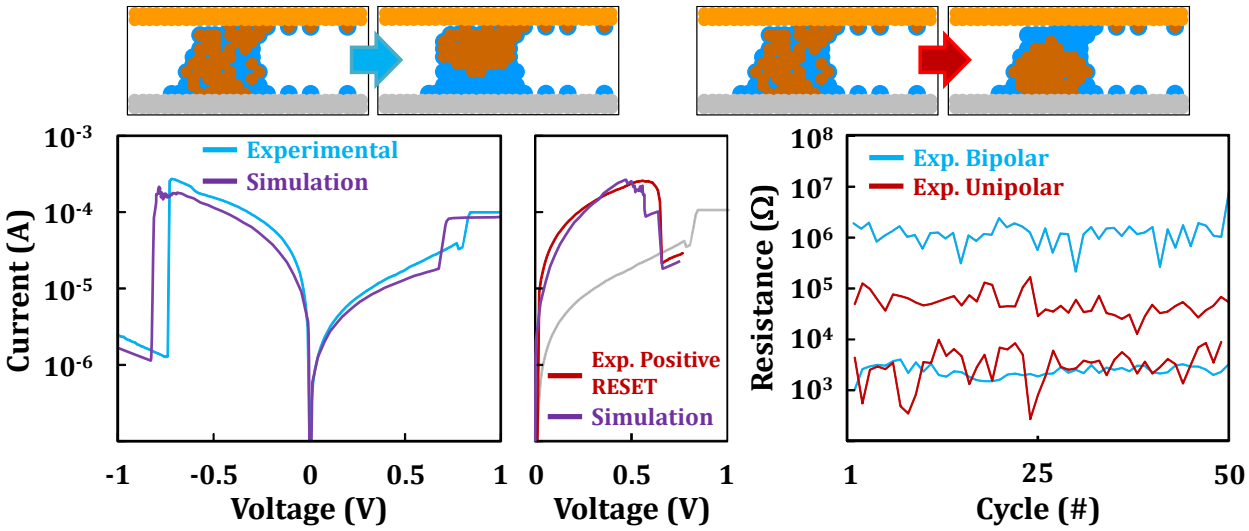

Figure 23. Measured and simulated IV characteristics for CBRAM operating in bipolar and unipolar modes. Typical measured endurance showing bad reliability for the unipolar case.

simulation shows an increase of temperature as soon as the filament is created. The model also shows that with the temperature increase, ion transitions of state and locations previously impossible at low temperature become possible and induce an instability of the filament. This phenomenon is especially noticeable at the thinnest point of the filament where the current density is the highest and the thermal dissipation the worst. The filament instability leads to a reorganization of the ions toward a stable arrangement with less heat and then less current. As long as the energy supplied to the TE is insufficient to inject Cu ions the unipolar RESET procedure continues. In order to proceed to a unipolar cycling, the RESET voltage has to be sufficiently high to trigger the filament instability but not too high (under V_{SET}) to avoid the Cu ions generation. Figure 23 also shows a short unipolar cycling compared to a standard cycling. Unipolar cycling offers way worst performances in terms of resistance variability and reduced memory window, and has only been studied to understand the thermal impact of joule heating during SET. Finally it is important to note that the unipolar RESET is only possible if the ionic hopping requires less energy than the oxidation reaction. This illustrates once again that the limiting factor of the studied CBRAM during SET is the oxidation reaction and not ions hopping. This statement was also confirmed by pushing the thermal impact study one step further. Using the filament self-heating during SET allowed to discriminate Cu^{i+} diffusion and injection. Figure 24 shows successive cycles (RESET operation done but not shown) with an increase of limiting current (I_C) for each SET step. Each SET operation shows the same behavior as the previous one: the current reaches the previous

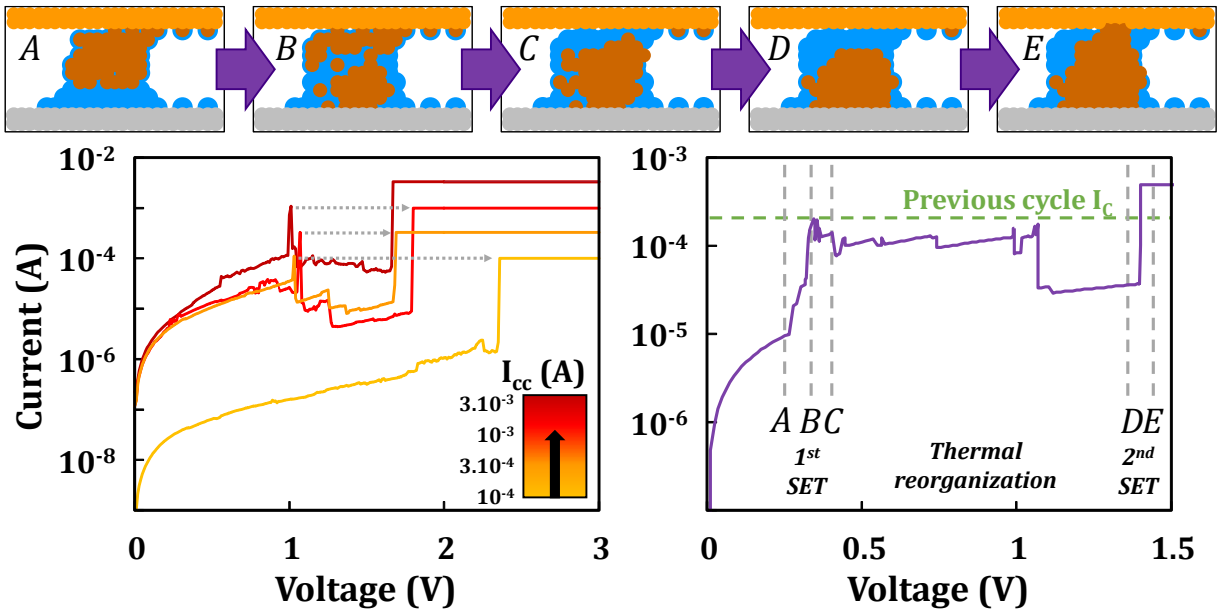

Figure 24. Measured (left) and simulated (right) IV SET characterics with increasing I_C for each subsequent SET cycles (RESET not shown). Current fluctuations are observed due to filament reorganization.

compliance current then falls back to a lower value before it reaches the new compliance current at much higher voltage. This behavior can be achieved and simulated using the KMC model. Considering the N^{th} cycle, the filament starts growing back to its $(N-1)^{th}$ written state from the available residual reset ions. Once the current slightly exceeds $I_C(N-1)$, a unipolar RESET occurs as stated previously and the current drops. The conductive path is then broken, leading to a deep resistance drop followed by a progressive decrease due to ionic reorganization. By further increasing the voltage, the energy becomes sufficient to generate ions from the TE and recreate a stable filament at $I_C(N)$. Therefore, filament formation during SET occurs in two successive steps: firstly the ionic migration of Cu ions available in RL and secondly the ionic generation and injection from the TE.

3.3 Modification of the filament morphology

This section will strongly relies on the KMC simulation and the information it offers on the filament shape. As stated during the previous section, it is complicated to precisely discern a filament position in an electrolyte, let alone the observation of its shape. The variability of the filament morphology will be used in the following of the manuscript and some insight proving its importance will be given. This is why this section will only describe the morphology variations that can be reached during the Forming/SET operations. As described during the temperature role

analysis, the thermal conductivity of the BE has a great impact in the filament morphology. A high thermal conductivity induces a thin filament, whereas a low thermal conductivity leads to a thick filament with a large basis as shown in Figure 22. During the thermal stabilization, the ion stability depends on the hopping activation energy, a high energy barrier induces a strong stability at high temperature.

Another great factor impacting the filament shape are the programming conditions. The filament formation consists in the vertical diffusion of ions from the TE toward BE pushed by the electric field. Once an ion arrives at the BE it increases the electric field in the insulating gap of electrolyte, creating a favorited path for the following ions. The more ions pile up on the BE and reduce the distance with the TE, the stronger is the favorited path until it reaches a critical point where all ions are pulled toward him. This critical point is tied to the electrical field between the top of the growing filament and the TE. Once the electric field is high enough the oxidation only occurs over the growing filament and the ions strictly diffuse in the path. However, the size of the growing filament required to reach this critical electric field strongly depends on the applied voltage. Indeed, as shown in Figure 25, the lower is the applied voltage, the taller is the required filament height to reach the critical electric field. Moreover, until the critical electric field is reached, ions tend to diffuse more or less randomly in the RL (still slightly pulled toward the growing filament). This observation has two consequences on the filament shape. Firstly, a reduction of the voltage applied during a PS programming, push the filament to grow thicker (with more atoms in the RL) before reaching its critical height. In the end, using PS programing and applying a long pulse at low

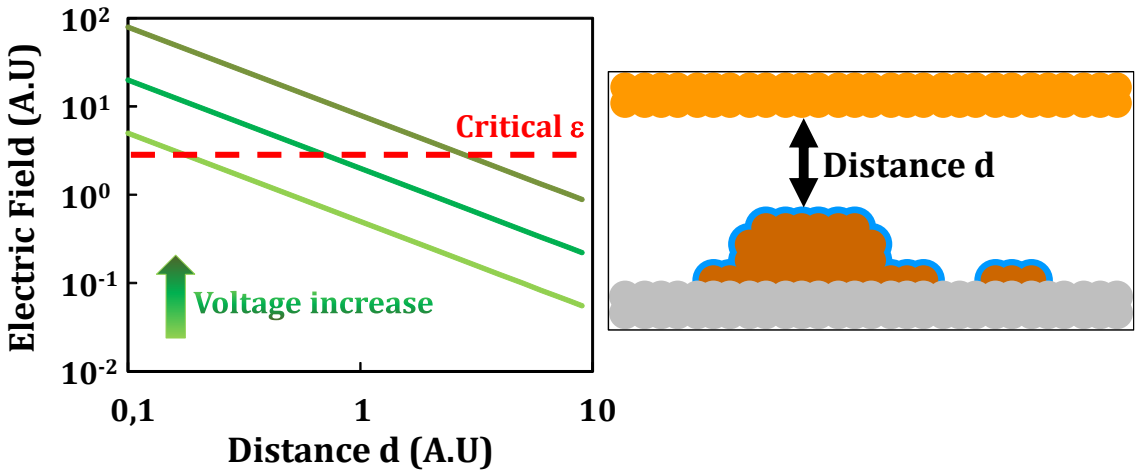

Figure 25. Schematic explanation of the required filament height to reach the critical electric field enhancing the fast and centralized filament completion

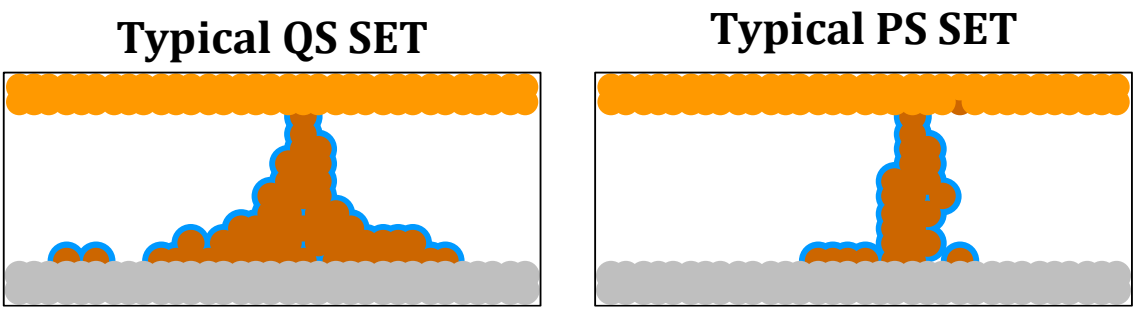

Figure 26. Filament morphology after two extreme conditions: QS programming and fast PS programming.

voltage will induce a thicker filament than using a short pulse at high voltage. Similarly QS programming, which is a very slow operating condition, shows filament thickness comparable to the one of obtained with low voltage PS programming. Figure 26 shows the comparison between QS and PS operating conditions. The second consequence of the critical electric field relies on the morphology variability. Due to the stochastic ion motion and redox reaction, the total number of atoms that have to be introduced in the RL in order to create a filament reaching the critical distance d (Figure 25), is variable. The smaller the distance d, the greater and more variable the number of required atoms. This distance d, as previously mentioned is tied to the voltage applied, which means that the lower the voltage, the more variable the number of atoms in the RL. A great part of these atoms serves to form the filament, thus the filament shape variability increases with the reduction of the applied voltage. In the end, QS or low voltage PS programming will globally lead to thicker filament than high voltage PS programming but with a larger dispersion of morphology.

The physical parameters involved in the morphology modification are the activation energies of the oxidation reaction and the ion hopping. They both modify the critical electric field required to create the strong favorited path pulling the ions and forcing the oxidation in the region over the growing filament.

3.4 Forming and SET behavior synthesis

It has been shown in this section the impact of the material properties on the CBRAM Forming and SET behavior. The focus was mainly put on the time dynamic behavior of the cell as it corresponds to the common industrial applications. It has been shown the possibility to improve the switching time versus applied voltage in two ways. Firstly, tuning the energy levels of ions involved in the redox reactions, such as the electrodes work functions or RL traps, leads to a shift

of the switching time characteristics and allows a combination of fast speed and low power consumption. The time voltage dilemma, which corresponds to the slope of the switching time versus applied voltage, has also been addressed. The capacity to modulate the slope by modifying the RL properties enhancing the electric field has been demonstrated. These parameters include the RL electrical permittivity, hopping distance tied to the RL density and the RL thickness. The impact and great importance of temperature and heating process during the Forming/SET operation has been revealed. The difference between ionic diffusion and generation has been demonstrated, as well as the CBRAM unipolar RESET capability (with degraded endurance).

Finally, this section not only describes the SET operation but also offers a physical understanding of the mechanisms impacting the global CBRAM operation which are the redox reactions and the ion migration. These mechanisms also operate during RESET, cycling and retention. It is then important to note that the previous conclusions regarding the mechanisms speed enhancements are still valid during the other operation of the CBRAM.

4. Physical understanding of the RESET operations

The RESET operation study has been focused on the temperature impact as it is known to be the main driving force of this operation and on the programing conditions This study has been conducted in two steps, firstly following a theoretical approach using COMSOL Multiphysics to model the temperature inside the filament during the RESET and then using the KMC model to push the analyzes one step further. Nano – Trench devices were characterized and used as input.

4.1 Temperature, key role in the RESET operation

The temperature role during RESET operation was studied with QS programming which offers a better current and voltage monitoring than PS programming. The samples were then erased using QS programming by applying a negative bias on the TE to dissolve the Cu-based filament. As stated during the Forming/SET study, electrode thermal conduction plays a great role in the heat dissipation. The study being focused on the temperature role during RESET, two samples with different BE were studied: one made of Silicon doped Tungsten (WSi) and one made of Titanium Nitride (TiN). The two BE exhibit a RESET voltage (V_{RESET}) difference of about 0.3 V. Indeed, as shown Figure 27, using TiN instead of WSi leads to a V_{RESET} reduction from about -0.2 to -0.5 V, with a wider dispersion in the latter. Thermal simulations using COMSOL Multiphysics were

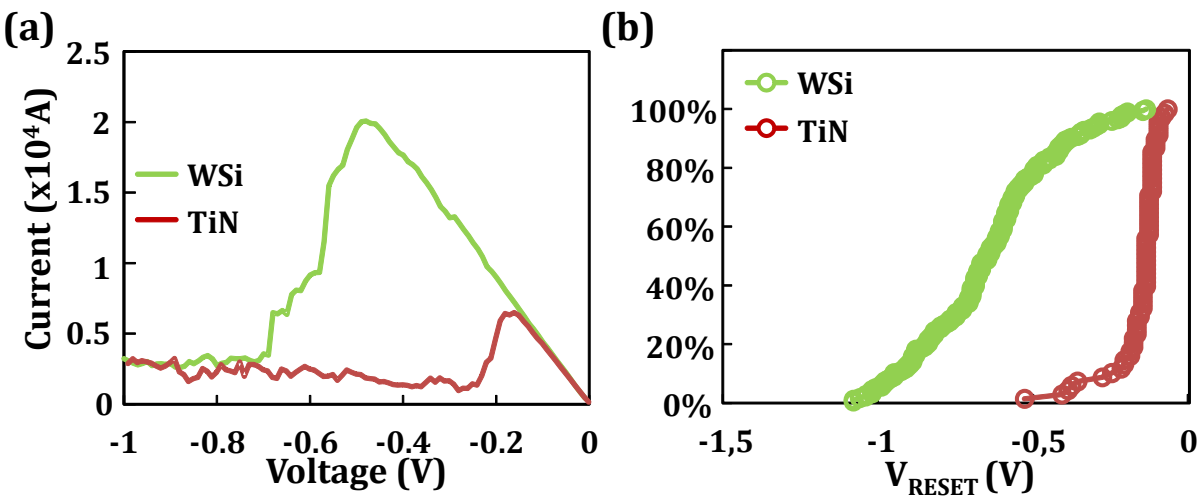

Figure 27. (a) Typical QS RESET behavior for two differente bottom electrodes. (b) Cumulative probabilities of V_{RESET} for the two samples.

performed to calculate the filament temperature elevation by Joule heating (T_{MAX}). A higher temperature for TiN BE is observed in the simulations due to the poor TiN thermal conductivity compared to WSi reducing the thermal dissipation (Figure 28 (a)), respectively κ_{TiN}=30 $W.m^{-1}.K^{-1}$; κ_{WSi}=170 $W.m^{-1}.K^{-1}$. This higher temperature observed in the TiN samples might explain the lower measured V_{RESET}. Indeed, the available energy under the form of voltage and temperature increases faster with the voltage ramp for the TiN sample compared to the WSi one. This means

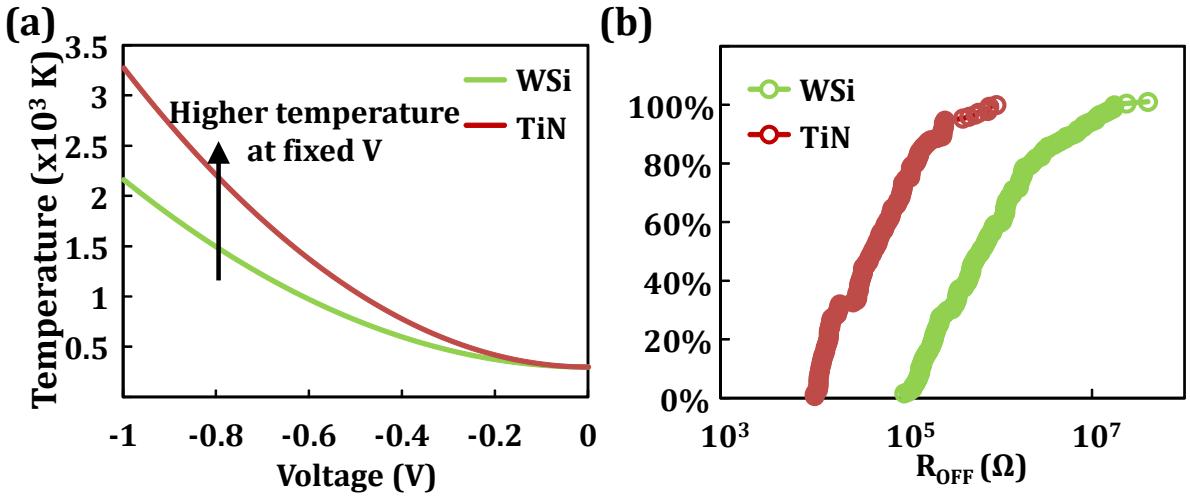

Figure 28. (a) Calculated maximum temperature in the CF as a function of the RESET voltage for WSi and TiN BE using COMSON Multiphysics. (b) Measured R_{OFF} distribution after RESET for WSi and TiN BE samples.

that the required energy to start the filament disruption is reached sooner (during the voltage ramp) for the TiN samples, leading to the lower V_{RESET}. However, WSi samples shows a R_{OFF} improvement (more than 1 decade) compared to TiN samples as seen in Figure 28 (b).

Using the same COMSOL simulations of Figure 29 but focusing on the temperature repartition, it is possible to see that the two BE do not only differ in term of temperature value but also regarding the temperature profile. While the highest temperature (T_{MAX}) is localized in the center of the filament for a WSi BE, it gets closer to the BE for TiN. The T_{MAX} location corresponds to the area offering the highest available energy. This area can consequently be assimilated to the starting point of the filament dissolution. Fig. 30 shows a schematized RESET process at the filament level. Once filament disruption starts, the filament is disconnected and the remaining part attached to the BE acts as a Cu source. Similarly to the TE during SET, the remaining filament tip is then progressively oxidized. This progressive dissolution of the remaining part could explain the progressive RESET behavior (Figure 27 (a)) and gradual R_{OFF} increase. Once the tip is completely dissolved, it becomes near impossible for the residual filament to be dissolved and the maximal R_{OFF} is reached. It is thus possible to modulate the R_{HRS} at the cost of a higher V_{RESET} by tuning the BE.

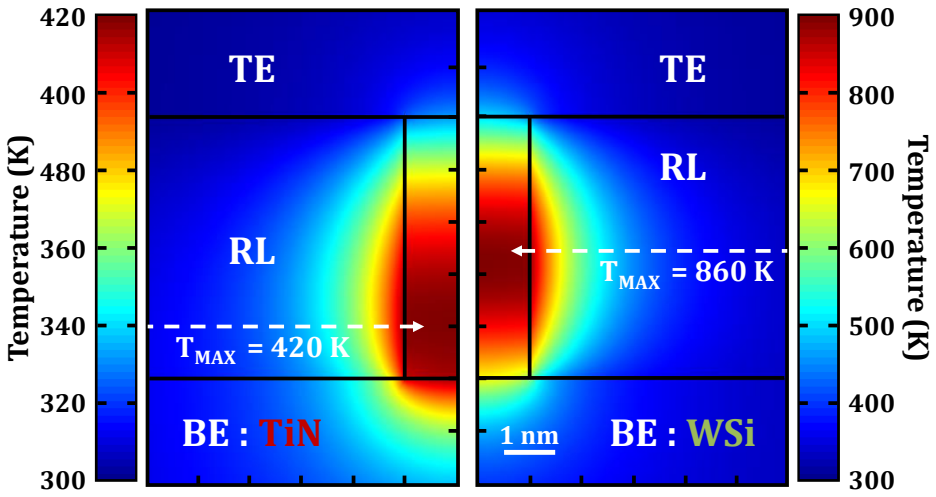

Figure 29. Thermal simulation of the two samples with different BE during RESET, using COMSOL Multiphysics

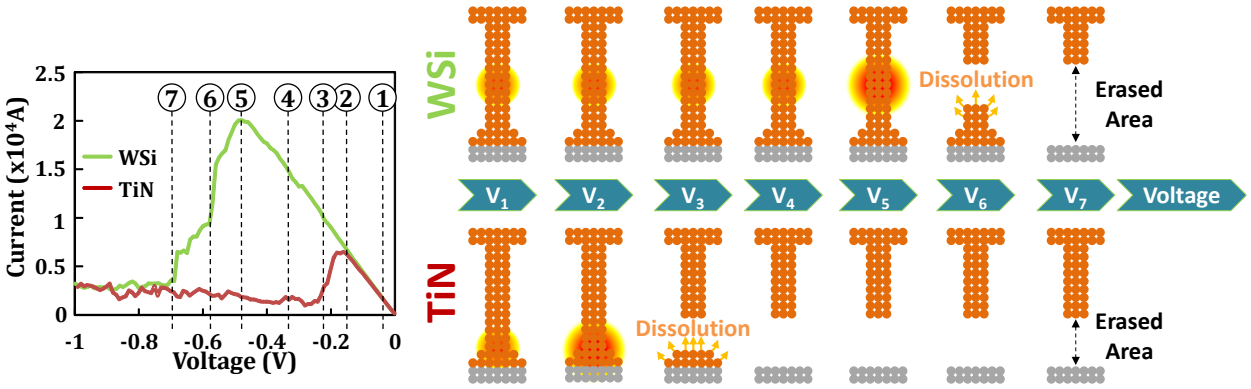

Figure 30. Schematic evolution of the RESET process for the two different BE and the corresponding states on the QS IV curves.

4.2 Impact of the programming conditions on the RESET operation

The programming conditions offer different ways to act on the RESET operation, directly and indirectly. It affects the RESET mechanisms during the operation but also modify the filament morphology during the previous SET which modify the RESET operation.

4.2.1 Direct impact of the programming condition on the RESET operation

As stated before, during the RESET operation, the filament disruption starts at the highest available energy location which generally corresponds to the highest temperature point. Considering a QS programming, the voltage ramp induces a progressive temperature increase of the filament. By increasing the temperature, the available energy (under the form of temperature and voltage) also increases. All the mechanisms involved require a proper amount of energy to occur: the higher the energy, the higher their probability to occur. By progressively increasing the energy brought to the system (voltage or temperature), the available energy level progressively reaches the requirement of the mechanisms one by one (or few by few). Considering the voltage ramp slow speed, (few volts/s) the filament disruption happening during QS RESET can be seen as a sequential behavior. Indeed, the temperature increases and reaches a critical level to push the less energy dependent transitions. Once these transitions done, the temperature is not sufficient enough to permit other transitions. The temperature has to reach the next sufficient level with the voltage ramp for the next most favorable transitions to occur. This progressive routine goes on until the temperature is high enough for the physical mechanisms to achieve the filament disruption. Once the filament is broken, the temperature greatly decreases due to the electrical current

reduction. As described before, the QS RESET ends with the dissolution of the residual filament tip on the bottom side of the cell. As the dissolution tip occurs, the gap increases and the required voltage to keep dissolving the filament tip increases. It is possible to slightly increase the R_{OFF} by increasing the final voltage of the QS RESET ramp. This behavior corresponds to the progressive RESET occurring once the current spike is achieved as seen previously Figure 27. The resistance increases with the stopping voltage until it reaches its maximum value and the cell starts degrading itself at higher voltage. Considering the sequential behavior of the QS RESET, the temperature reached is the lowest temperature possible to achieve the filament disruption. In term of physical mechanisms involved, only the most favorable one can occur during a QS RESET operation and the temperature does not reach a sufficient level for a global filament disruption. Using QS RESET ultimately leads to a HRS state with low R_{OFF}.

On the other hand, by using PS RESET, the voltage being fixed, the system directly reaches a high temperature. The temperature directly depends on the applied voltage which has to be higher than the QS V_{RESET}, in order to achieve a fast RESET. The high temperature induced by the high voltage greatly reduces the activation energies of all the mechanisms, leading to a large population of favorable reactions and migrations. The highest temperature location still plays a great role in the filament disruption and still offers the highest transition probability of the physical mechanisms. However, due to the much higher temperature the highest temperature area becomes much wider. In the same time, the high temperature greatly reduces the activation energies in this area which should narrow the difference between mechanisms probability. Consequently, the filament disruption should not occurs sequentially but in a generalized way at various locations of the filament, creating a global disruption of the filament. Once the filament is broken, the residual tip on the bot side is dissolved in the same manners than during QS RESET. In conclusion, the PS RESET offers a great way to improve the HRS resistance in comparison to the QS RESET. However, it will be shown later that applying RESET voltages too high during PS programming may also lead to a degradation of the cell and bad cycling endurance.

4.2.2 Filament morphology and indirect impact of the programming conditions

The filament morphology (tied to the programming conditions as previously stated) has been related to the RESET performances. As shown in Figure 31, forming the cell with a low voltage and long pulse leads to a higher $|V_{RESET}|$. The filament shape can be divided in two parts, the thinnest part acts as the main heat generator as it deals with the highest current density whereas the rest of the filament mostly acts as a heat dissipater, even though it still generates a small amount of heat. Then, depending on the size repartition of these two parts, the global temperature of the filament is modified. The highest temperature is for the device with the biggest heat generating part. Simulations have shown that Forming at high or low voltages creates two distinct CF morphologies. A low applied voltage during PS programing enlarges the CF bottom radius, leading to a smaller heating part and a larger and taller dissipating area, whereas high voltage SET leads to a thin filament acting mostly as heat generator. Regarding the low voltage/thick filament, a high current (i.e. higher V_{RESET}) is required to reach a sufficient temperature so that the filament disruption occurs. In contrary, concerning the high voltage/thin filament, the required current to reach the reset temperature is lowered and the voltage to initiate the filament dissolution reduced.

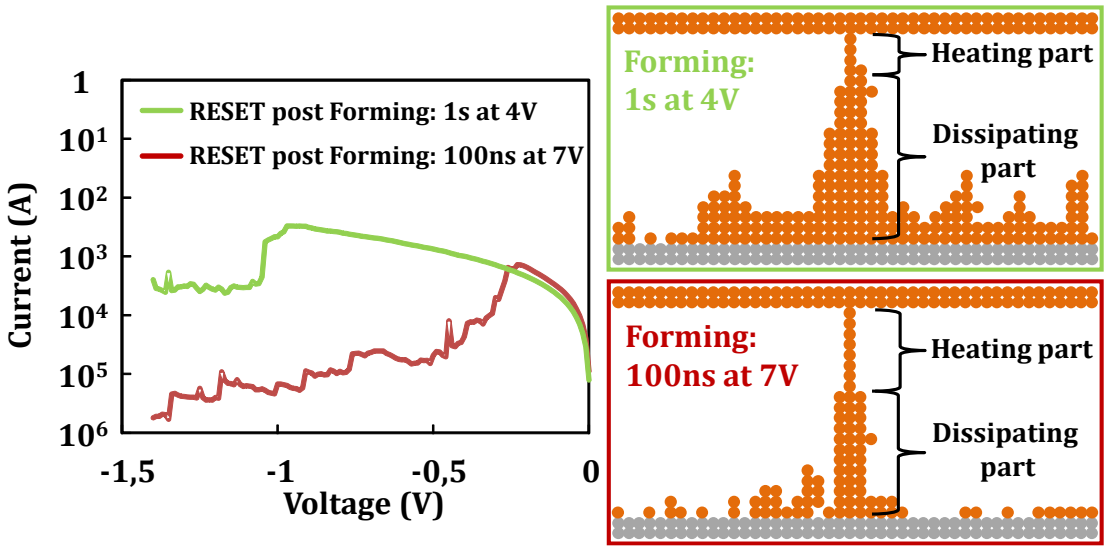

Figure 31. Measured IV RESET characteristics for TiN BE with Al_2O_3 RL and simulated filament morphologies after two extreme forming conditions: Cond.1: 1s at 4V, Cond.2: 100ns at 7V.

4.3 Technological optimization of the RESET operation

Based on the previous observations, optimization ways have been proposed, however only one have been verified due to time restrictions. As previously explained the temperature plays a great role in the RESET operation in term of voltage and achievable HRS resistance. By tuning the thermal behavior of the cell it is possible to modify those critical CBRAM parameters [Banno 1, Tada 1, Tada 2, Tada 3].

The disruption area corresponds to the highest temperature zone in the RL, the farther it is from the BE the higher the HRS resistance. The position of this zone is due to the non-equilibrium of thermal conduction of both electrodes, if an electrode has a higher thermal conductivity than the other, the disruption zone is located farther from this electrode. Figure 32 shows the impact of electrodes thermal conductivity difference on the disruption area position obtained using COMSOL Multiphysics. Then, by smartly tuning the thermal conductivity equilibrium it is theoretically possible to increase the HRS resistance. Modifying TE might induce a deep modification of the CBRAM electrical behavior too, it is not recommended to tweak the TE to modify the thermal conduction equilibrium, however, tuning the BE which has little impact on the electrical behavior as state before is a great opportunity to improve the resistance window. Using a highly conductive BE increases the distance between BE and the disruption area leading to a better R_{OFF} As shown with the use of WSi compared to TiN BE in Figure 28.

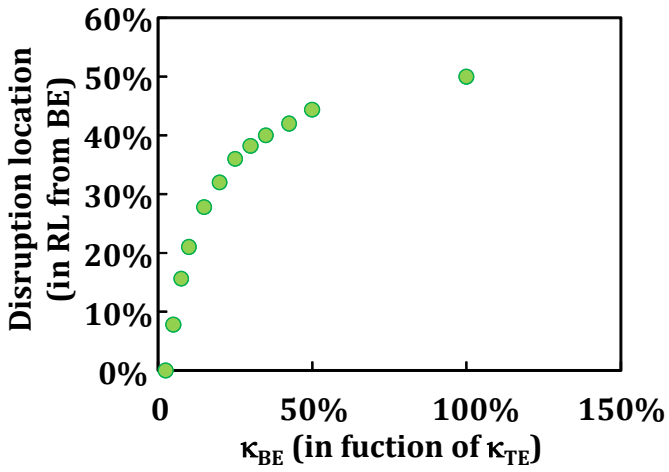

Figure 32. Highest location (or disruption point) distance from the BE in the RL in function of the thermal conductivity of the electrodes. Results obtained with COMSOL Multiphysics simulation

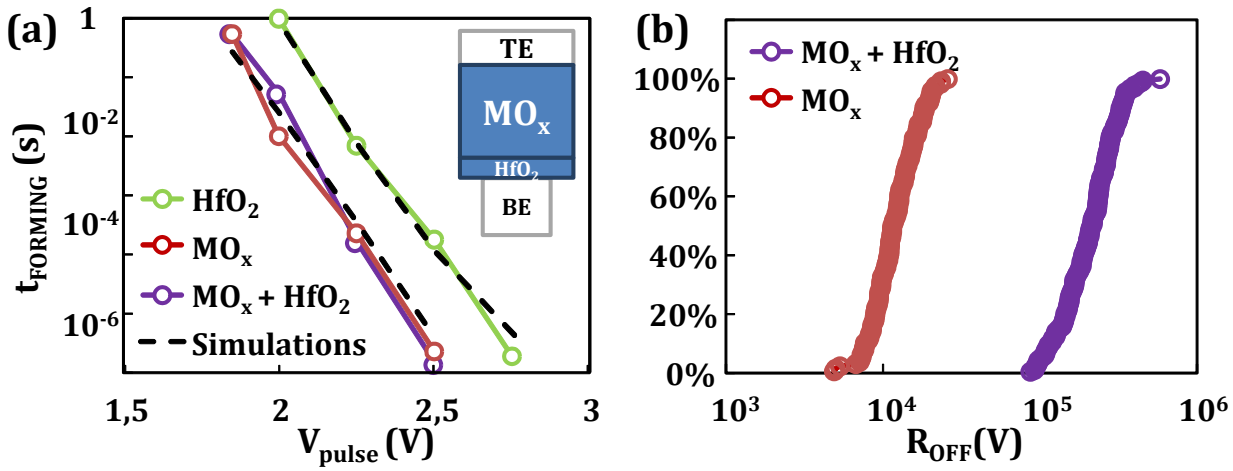

Figure 33. (a) Measured and simulated forming time as a function of the applied voltage for three different RL (b) Measured R_{OFF} after RESET for the two RL

Moreover, the RL also plays a noticeable role in the thermal aspect of the RESET operation. The RL can serve as a good thermal dissipater if offering good thermal conduction. RL plays a great role if not the greatest role of the CBRAM components in the CBRAM characteristics and modifying it might change more than just a thermal conduction equilibrium [Lee 1]. However, by introducing a thin secondary RL under the primary one it is possible to modify the thermal equilibrium without modifying the other characteristics of the cell. Indeed, as shown Figure 33 by adding an HfO_2 layer under a MO_X layer it is possible to increase the HRS resistance with no impact on the Forming characteristics. Figure 34 shows the thermal profile modification due to the higher thermal conductivity of the HfO_2 compared to the MO_X. The higher position of the

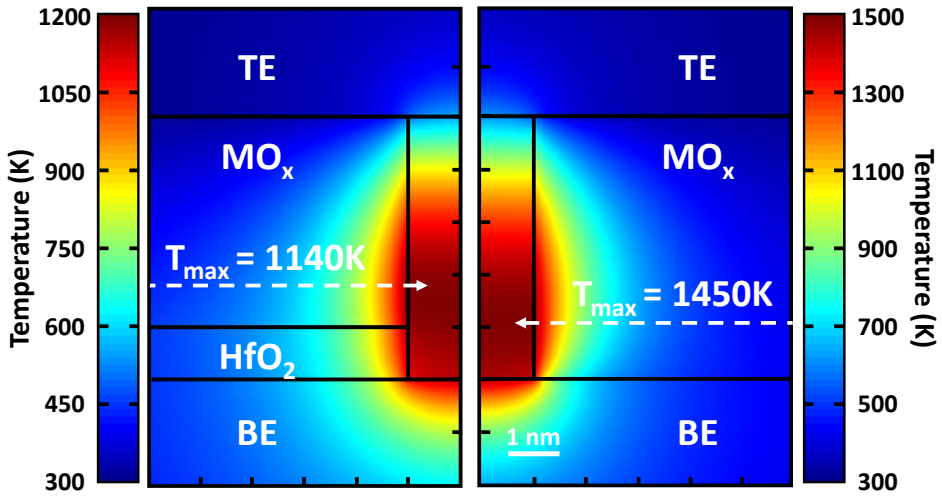

Figure 34. Thermal simulation of the two samples with different BE during RESET, using COMSOL Multiphysics

disruption area might explain the increased HRS resistance, other factor might also influence the HRS [Barci 1, Palma 1, Palma 2]. The thickness of the added layer greatly modify the impact on the thermal profile with a variation of the disruption area shown. It is important to note that these observations strongly depends on the materials stack and cannot be taken as universal.

The role of the secondary RL is only to modify the thermal profile, thus it is of great importance to keep this RL small enough so that the disruption area stays in the primary RL. Otherwise, the global behavior of the cell might be impacted.

Still with the goal to tweak the temperature profile, other theoretical assumptions have been made. However, as stated before the following hypothesis remains theoretical. The following cell, schematized in Figure 35, composed by a double BE have been studied to simulate the use of a bottom metal line. This study aims to understand the thermal behavior of a CBRAM composed by distinct BE and metal lines. Depending on the thermal conductivity of both electrodes, the disruption location varies inside the RL [Gopalan 1].

Considering a process requiring a specific metal line with poor thermal conductivity, it is important to know if it is possible to overcome this lack of thermal conductivity with a proper BE thickness. Figure 36 (a) shows that using a BE – 1 with a high thermal conduction and a sufficient thickness (greater than 4 nm), it is possible to greatly modify the thermal profile which should in theory increase the HRS resistance in agreement with previous statements. However, for a layer too thin (under 2 nm), the BE – 1 seem to have no effect on the thermal profile. This observation is of great interest, indeed, it seems possible to use a BE thin enough that it does not modify the thermal profile of the CBRAM. Figure 36 (b) confirms this hypothesis, as using a thin layer of BE – 1 with poor thermal conductivity doesn't impact the disruption location in the RL. In other words, if a

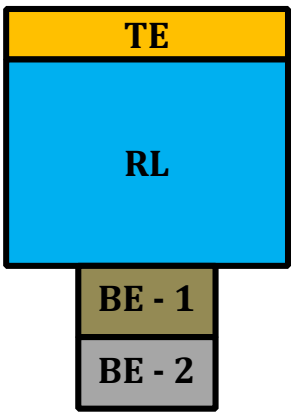

Figure 35. Dual BE cell

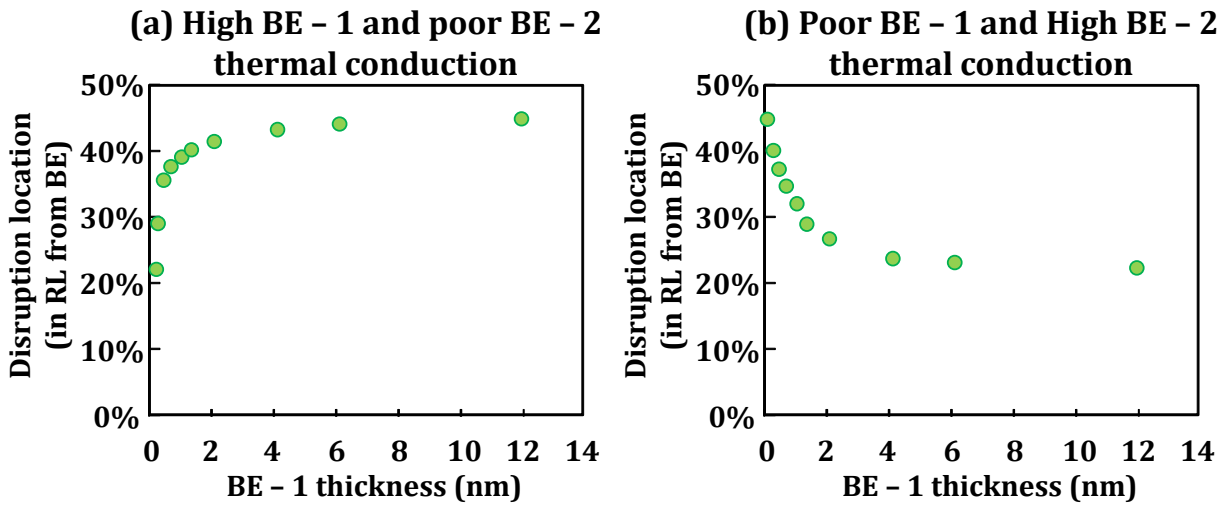

Figure 36. Disruption location in the RL in function of the double BE therman conduction showing the ability to negate the thermal impact of a BE if the thickness is low enough.

specific BE with low thermal conduction is required to optimize the CBRAM electrical behavior, it seems to be possible to overcome this lack of thermal conduction by using a sufficiently thin layer and a second BE with higher thermal conduction. In the end, the system would have two BE, the thinner one in contact with the RL would act as an electrical BE whereas the thicker one, under the first one, would act as a thermal BE.

4.4 RESET behavior synthesis

In this section the great impact and key role of the temperature on the RESET behavior has been discussed. The focus was firstly put on QS programming to understand the basis of the RESET mechanisms and then the study has been extended to PS programming. It has been demonstrated that not only the temperature value but also its distribution in the RL modify the RESET operation. The temperature brings energy to the system and changes the V_{RESET} whereas its distribution influences the R_{OFF} by changing the disruption location of the filament. The temperature value and distribution can be modified directly and indirectly by changing the programming conditions during RESET or during the previous SET which induces a change of filament morphology. Optimization ways have also been proposed taking advantage of the thermal conduction of the CBRAM components. By modifying the thermal conduction equilibrium it is possible to change the HRS resistance value and RESET voltages. Some optimizations (BE modifications, dual RL)

Table 2. Electrical characteristics of a sample selection. R_{HRS} Max corresponds to the highest achievable R_{RHS} using QS RESET with a $V_{RESET\ Stop}$ Max applied.

Memory stack (TE/RL/BE)	RL Thickness	QS $V_{Forming}$	PS $V_{forming}$ (t_{Pulse} = 10 µs)	Forming Time Voltage slope	R_{HRS} Max	$V_{RESET\ Stop}$ Max
Cu/Al_2O_3/WSi	3.5 nm (ALD)	3.1 V	4.5 V	3.5 Decades / V	$10^6\ \Omega$	-1.5 V
	5 nm (ALD)	4.4 V	6.5 V	2.0 Decades / V	$10^6\ \Omega$	-1.5 V
$CuTe_X$/Al_2O_3/WSi	3.5 nm (ALD)	3 V	4.75 V	3.5 Decades / V	$10^6\ \Omega$	-1.5 V
	5 nm (ALD)	4.5 V	7 V	2.0 Decades / V	$10^6\ \Omega$	-1.5 V
Cu/Al_2O_3/TiN	3.5 nm (ALD)	2.6 V	3.75 V	3.5 Decades / V	$5x10^4\ \Omega$	-1 V
	5 nm (ALD)	3.8 V	4.75 V	2.0 Decades / V	$5x10^4\ \Omega$	-1 V
$CuTe_X$/Al_2O_3/TiN	3.5 nm (ALD)	2.8 V	4 V	3.5 Decades / V	$5x10^4\ \Omega$	-1 V
	5 nm (ALD)	4.3 V	6.25 V	2.0 Decades / V	$5x10^4\ \Omega$	-1 V
$CuTe_X$/HfO_2/Ta	5.5 nm (ALD)	2.2 V	2.75 V	8.0 Decades / V	$5x10^5\ \Omega$	-1 V
$CuTe_X$/MO_x/Ta	5 nm (PVD)	2 V	2.4 V	8.0 Decades / V	$10^4\ \Omega$	-1 V
$CuTe_X$/HfO_2 + MO_x/Ta	5.5 + 1 nm	2 V	2.4 V	8.0 Decades / V	$5x10^5\ \Omega$	-1 V

were experimentally confirmed but others could not be verified and stayed as theoretical hypothesis.

5. Performances synthesis

Throughout the switching study, several samples have been characterized and analyzed. This section aims to offer a quick highlight of the electrical performances obtained on a selection of studied samples. This selection is summarized Table 2 and presents various materials combinations and electrical performances. In order to offer comparable performances, all the electrical characteristics reported here are based on a R_{LRS} between 10^3 and $10^4\ \Omega$. This is particularly important especially regarding the RESET operation.

6. Chapter IV synthesis

This chapter presented the physical mechanisms involved during Forming, SET and RESET operations. The impact of the cell scaling on the main CBRAM parameters have been exposed on nano – Trench devices. The increase of Forming voltage with the dimension reduction due to diminution of defect probabilities in the RL has then be shown. The amplified electric field in our structures during SET has also been exposed and induces a reduction of SET voltage with the size reduction. This translates regarding PS programming into a great enhancement of the

switching speed with the cell scaling. This preliminary study concerning the scaling also indicates the great importance to compare devices of the same size and architecture to study the physical parameters involved in the CBRAM functioning.

Both Forming/SET and RESET operations are based on the same physical mechanisms which are the redox reactions at the TE and BE interface and the ion migration in the RL. The Forming study has been of great help to understand these mechanisms with a restricted impact of exterior factors, as the CBRAM cells are in pristine state before this operation. It has then been demonstrated the possibility to modify the redox reactions speed, the switching limiting factor, by tuning the energy level involved in the reaction in accordance with the Transition State Theory. These energy levels correspond to the electrodes work functions and to the energy levels of the Cu traps in the RL. Regarding ions migration, this mechanism relies on the migrating entities (coming from TE) and the migration medium (the RL). In all the studied cases, the migration is not the limiting factor during Forming which makes it difficult to analyze the impact the migration speed could have on the switching characteristics. Moreover, in order to alter the migration mechanism a RL modification or a complete TE change (change of metal base of TE) would be required, what would also deeply modify the reactions speed. However, an insight of the ions migration role can be seen during SET, as it has been demonstrated that it regulates the SET voltage for standard cycling (fixed compliance current).

The great importance of the temperature on the physical mechanisms involved in the switching process has been demonstrated. During Forming and SET, the crucial impact of the Joule Heating on the filament stabilization and its final morphology has been verified. This Joule Heating is tied to the programming conditions and the action of the SET conditions on the filament morphology has been demonstrated. This filament shape then changes on the RESET characteristics, leading to an indirect impact of the SET conditions on the HRS characteristics. The RESET conditions also play a great role in the HRS characteristics, through the modification of the cell temperature. Depending on the programming conditions, a progressive and sequential filament disruption for QS RESET or a more global filament dissolution for PS RESET can be achieved, leading to different resistance levels for the erased state.

With the knowledge of the physical mechanisms involved in the CBRAM operation and the temperature importance, SET and RESET optimizations have been proposed.

Regarding SET operation, the crucial electrical characteristic is the time versus voltage switching curve. Two ways of tweaking this characteristics have been exposed: a shift of the curve, leading to faster switching times or a change of its slope, inducing an improved time voltage dilemma and a better disturb immunity. The curve shifting can be achieved by modifying the parameters impacting the energy level of the redox reactions or the flat band voltage, such as the electrodes work function or the energy level of the copper traps in the RL. The time voltage dilemma can be addressed by modifying the slope of the time versus voltage curve which is tied to the electric field efficiency. It can be modified by RL parameters only, including the RL thickness, RL electrical permittivity and hopping distance between two copper positions in the RL.

Concerning RESET, it has been shown the possibility to modulated both RESET voltage and HRS resistance by changing the CBRAM components and especially the BE. Adding a secondary RL also showed a successful increase of HRS resistance without modifying the rest of the electrical characteristics.

Chapter IV references

[Banno 1] Naoki Banno, Toshitsugu Sakamoto, Munehiro Tada, Makoto Miyamura,Koichiro Okamoto, Hiromitsu Hada, and Masakazu Aono, “ON-State Reliability of Solid-Electrolyte Switch under Pulsed Alternating Current Stress for Programmable Logic Device”, Jap. Journ. Appl . Phys., 50 (2011), 74201.

[Barci 1] Barci, M.; Molas, G.; Toffoli, A.; Bernard, M.; Roule, A.; Cagli, C.; Cluzel, J.; Vianello, E.; De Salvo, B.; Perniola, L., "Bilayer Metal-Oxide CBRAM Technology for Improved Window Margin and Reliability," in Memory Workshop (IMW), 2015 IEEE International , vol., no., pp.1-4, 17-20 May 2015

[Celano 1] Celano, U.; Goux, L.; Belmonte, A.; Schulze, A.; Opsomer, K.; Detavernier, C.; Richard, O.; Bender, H.; Jurczak, M.; Vandervorst, W., "Conductive-AFM tomography for 3D filament observation in resistive switching devices," in Electron Devices Meeting (IEDM), 2013 IEEE International , vol., no., pp.21.6.1-21.6.4, 9-11 Dec. 2013

[Davisson 1] C. Davisson and L. H. Germer; “The Thermionic Work Function of Tungsten”, Phys. Rev. 20, 300 – 1 October 1922

[Fonseca 1] L. R. C. Fonseca and A. A. Knizhnik, “First-principles calculation of the TiN effective work function on SiO2 and on HfO2”, Phys. Rev. B 74, 195304 – 3 November 2006

[Gartland 1] P. O. Gartland, S. Berge, and B. J. Slagsvold, “Photoelectric Work Function of a Copper Single Crystal for the (100), (110), (111), and (112) Faces”, Phys. Rev. Lett. 28, 738 – Published 20 March 1972

[Gopalan 1] Chakravarthy Gopalan, Wei Ti Lee, Yi Ma, Jeffrey Allan SHIELDS, “SOLID ELECTROLYTE MEMORY ELEMENTS WITH ELECTRODE INTERFACE FOR IMPROVED PERFORMANCE”, US Patent 2013/033934. Oct. 3, 2013.

[Jałochowski 1]Jałochowski, M., Mikołajczak, P., Subotowicz, M., “Measurements of the work function and the fermi level in thin tellurium films”, Physica status solidi”, Feb. 16 2006.

[Lee 1] Feng-Ming Lee, Yu-Yu Lin, “PROGRAMMABLE METALLIZATION CELL WITH TWO DIELECTRIC LAYERS”, US Patent 2013/0182487 Jul. 18, 2013.

[Molas 1] Molas, G.; Vianello, E.; Dahmani, F.; Barci, M.; Blaise, P.; Guy, J.; Toffoli, A.; Bernard, M.; Roule, A.; Pierre, F.; Licitra, C.; De Salvo, B.; Perniola, L., "Controlling oxygen vacancies in doped oxide based CBRAM for improved memory performances," in Electron Devices Meeting (IEDM), 2014 IEEE International , vol., no., pp.6.1.1-6.1.4, 15-17 Dec. 2014

[Palma 1] Giorgio Palma, Elisa Vianello, Gabriel Molas, Carlo Cagli, Florian Longnos, Jérémy Guy, Marina Reyboz, Catherine Carabasse, Mathieu Bernard, Faiz Dahmani, Damien Bretegnier, Jacques Liebault, and Barbara De Salvo, “Effect of the Active Layer Thickness and Temperature on the Switching Kinetics of GeS2 - Based Conductive Bridge Memories”, Japanese Journal of Applied Physics 52, 04CD02, 2013

[Palma 2] Palma, G.; Vianello, E.; Thomas, O.; Suri, M.; Onkaraiah, S.; Toffoli, A.; Carabasse, C.; Bernard, M.; Roule, A.; Pirrotta, O.; Molas, G.; De Salvo, B., "Interface Engineering of Ag-GeS2-Based Conductive Bridge RAM for Reconfigurable Logic Applications," in Electron Devices, IEEE Transactions on , vol.61, no.3, pp.793-800, March 2014

[Sakamoto2009] T. Sakamoto, M. Tada, N. Banno, Y. Tsuji, Y. Saitoh, Y. Yabe, H. Hada, N. Iguchi, and M. Aono, “Nonvolatile solid-electrolyte switch embedded into Cu interconnect”, proc. of VLSI Tech. Symp. 2009, pp.130-131.

[Stefano 1] F. De Stefano, V.V. Afanas’ev, M. Houssa, L. Goux, K. Opsomerb, M. Jurczak and A. Stesmans, “Influence of metal electrode stoichiometry on the electron barrier height at CuxTe1-x/Al2O3 interfaces for CBRAM applications”, Microelectronic Engineering, vol.120, pp.9-12, May 2014.

[Tada 1] M. Tada, T. Sakamoto, Y. Tsuji, N. Banno, Y. Saito, Y. Yabe, S. Ishida, M. Terai, S. Kotsuji, N. Iguchi, M. Aono*, H. Hada, and N. Kasai, “Highly Scalable Nonvolatile TiOx/TaSiOy Solid-electrolyte Crossbar Switch Integrated in Local Interconnect for Low Power Reconfigurable Logic”, IEEE IEDM Tech. Dig. 2009, pp.943-946.

[Tada 2] Munehiro Tada, Toshitsugu Sakamoto, Naoki Banno, Masakazu Aono, Hiromitsu Hada, and Naoki Kasai, « Nonvolatile Crossbar Switch Using TiOx/TaSiOy Solid Electrolyte », IEEE Trans. on Elec. Dev., 57, 8 (2010), pp.1987-1995.

[Tada 3] Tada, M.; Sakamoto, T.; Banno, N.; Okamoto, K.; Miyamura, M.; Iguchi, N.; Hada, H., "Improved reliability and switching performance of atom switch by using ternary Cu-alloy and RuTa electrodes," in Electron Devices Meeting (IEDM), 2012 IEEE International , vol., no., pp.29.8.1-29.8.4, 10-13 Dec. 2012

Chapter V. Cycling and reliability

1. Objectives

Following the understanding of SET and RESET operations, this chapter will be focus on the repeatability of these operations and the cell reliability during cycling. Similarly to the previous chapter, references will be made to chapters II and III regarding the description of the characterization protocols, studied samples and KMC simulations. This chapter relies on the stochasticity offered by the KMC simulation close to the CBRAM behavior. The model offers indeed great correlation with the experimental resistances distribution of both HRS and LRS as seen in Figure 1.

Experimentally, this study has been conducted on MESA devices (See Chapter II) with the following material stack: $CuTe_X/Al_2O_3/TaN$. These structures, combined with 64 devices matrix correspond to the closest samples to industrial devices among the studied ones. These samples offered the opportunity to study one of the last remnant limitation of the CBRAM: the variability and device reliability. Accordingly, the intrinsic behaviors and the impact of the previous state variability on the following ones will be exposed through electrical characterization and KMC simulation for both LRS and HRS. The cycle to cycle and cell to cell variability will be addressed and the operation conditions impact on cycling capabilities discussed.

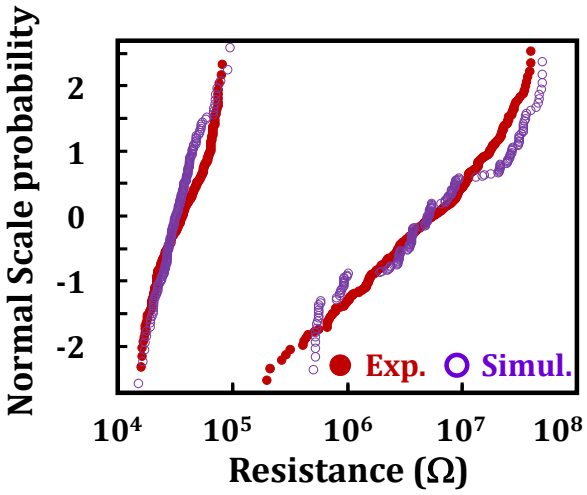

Figure 1. Typical experimental and simulated resistance dispersion of both LRS and HRS

The chapter will be focused alternatively on LRS and HRS to understand to mechanisms involved in the resistance variability. Then, the cycling failure mechanisms will be addressed and studied in function of the operating conditions.

2. Low Resistive State variability

Using the stochasticity proper to KMC, SET reliability has been analyzed to understand the role of the intrinsic and cycle to cycle variability on the R_{LRS} distributions.

First, the experimental results obtained on three 64 devices matrixes during 100 cycles have been compared. The LRS distributions have been divided in two groups as can be seen in Figure 2. Either the complete cell population in red, showing a strong HRS variability or a restrained HRS distribution in blue. The goal of this study is to understand the role of the previous state variability on the following one. The restrained initial HRS have been chosen to offer at the same time a limited resistance range and a large data sample to avoid affecting the statistics. Figure 2 shows that the LRS distributions after SET are quiet similar and the great reduction of HRS distribution doesn't show noticeable impact on the LRS distribution. Only a slight reduction on the LRS tails can be seen which shows no direct impact of the HRS variability on the LRS. The LRS seems to only suffer from intrinsic variability.

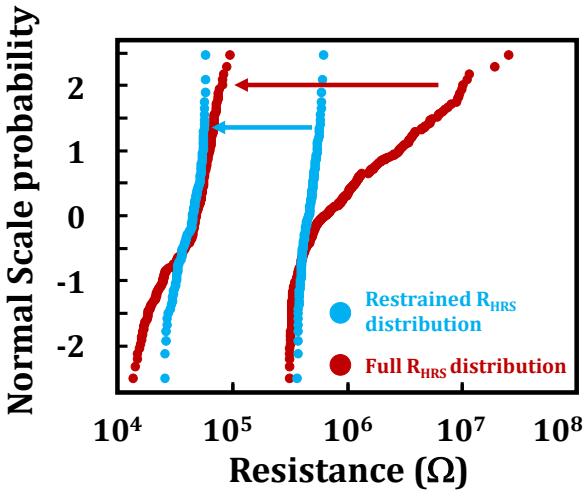

Figure 2. Experimental R_{LRS} distributions starting from a spread R_{HRS} distributions (Red) and a restrained R_{HRS} distribution (Blue).

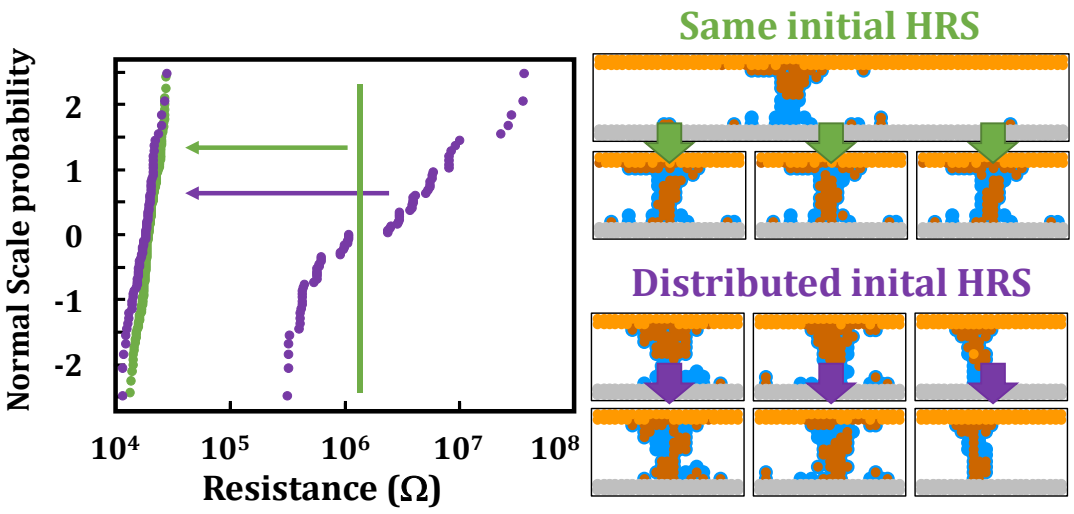

Figure 3. Simulated R_{LRS} distributions starting from the same initial HRS (green) or spread R_{HRS} distributions (purple).

This study has then been extended using the KMC simulation. The SET operations simulations were performed starting from the same HRS to obtain a perfectly restrained initial HRS and from distributed R_{HRS} values following experimental data. It is possible to achieve the same R_{HRS} with different filament morphologies. However, in order to avoid any impact of the filament morphology on the intrinsic variability study, the SET operation simulations were all performed starting from the same residual filament and HRS resistance. Figure 3 summarizes this study with a unique initial HRS in green and a distributed initial HRS in purple. As can be seen in both cases, R_{LRS} shows similar distributions after SET. This confirm the previous observation stating that R_{LRS} does not depend on the previous state, and that there is no cycle to cycle variability concerning the LRS. The resistance value of this state only depends on the compliance current and intrinsic mechanisms which will be discussed in the following.

The intrinsic mechanisms responsible for the LRS variability depends on the current level limiting the SET operation. In function of the applied compliance current, the R_{LRS} distribution varies. As seen in Figure 4, the lower the compliance current the stronger the resistance variability. The intrinsic variability of the SET operation is much more noticeable at low current and high resistance. R_{LRS} distribution can also be simulated in function of the limiting current during SET, in good agreement with the experimental data. The resistance dispersion is tied to a variation of filament morphology and can be explained by studying the stabilization of the filament during SET.

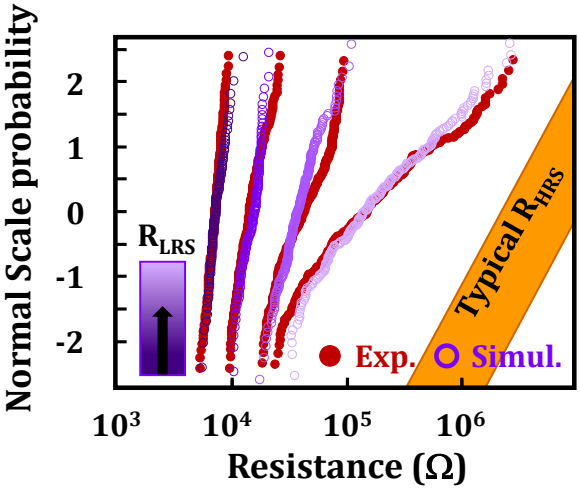

Figure 4. Measured and simulated R_{LRS} distributions for various SET currents I_C.

Figure 5 schematizes the filament stabilization in function of the available energy in the system. As briefly stated during the SET operation analyses, this operation can be divided in two phases: the filament initial formation and stabilization. During the first phase, the current is too low to induce joule heating, the main source of energy provided to the system is the applied voltage and the principal driving force is the electric field. Once the filament is created and the compliance current reached, the temperature rapidly increases due to joule heating. The temperature and energy brought to the system strongly depends on the resistance level: low resistance means high temperature. At the transition point, the energy brought to the system under the form of temperature and voltage is maximum.

The filament shape evolves to dissipate enough energy and stabilize itself. During the filament stabilization more atoms are brought from the top electrode, leading to a decrease of resistance.

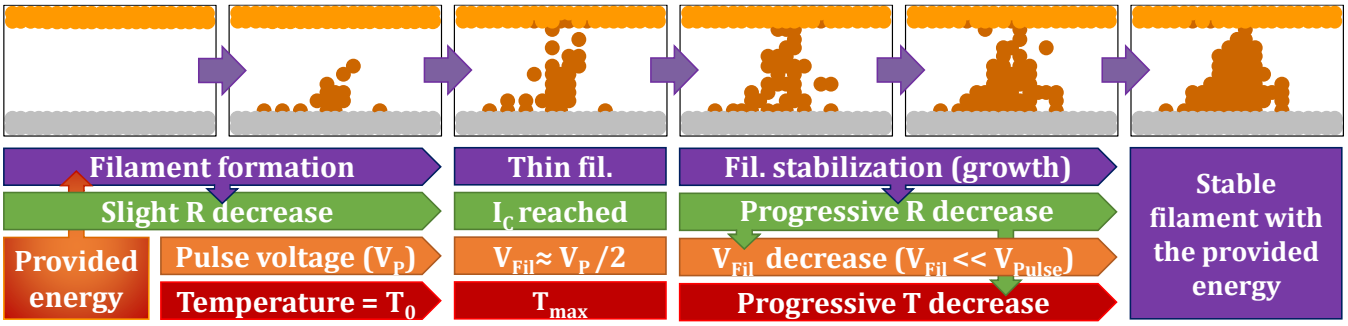

Figure 5. Sequences of filament formation and stabilization during SET operation

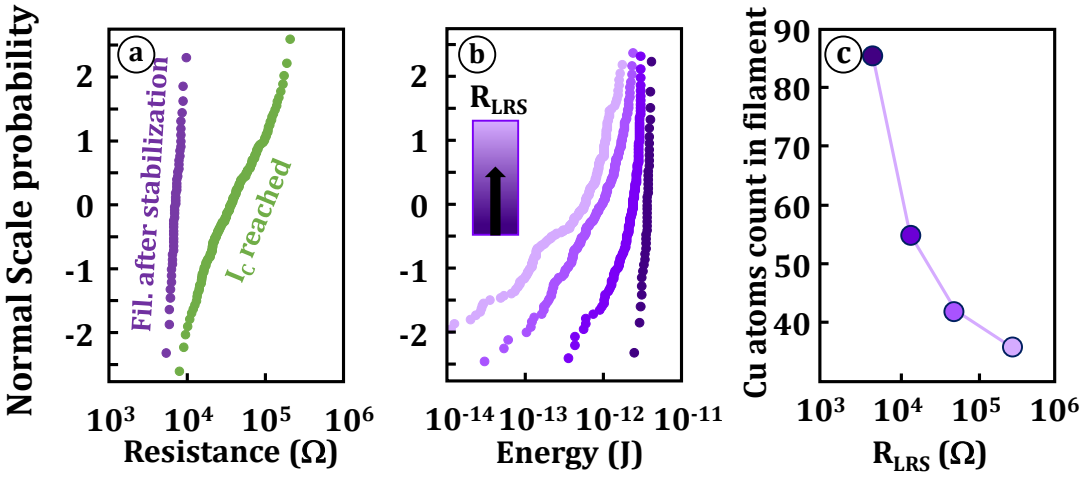

Figure 6. (a) Simulated R_{LRS} stabilization during SET. (b) Simulated energy provided to the system during SET. (c) Simulated number of Cu atoms in the filament after SET for various R_{LRS}

Induced by this resistance decrease, the energy available to the system also decreases due to the reduction of heat dissipation and voltage seen by the cell. The heat dissipation reduction is due to the decrease of thermal energy brought to the system as the current is fixed by the compliance, the resistance decrease and the thermal energy follows the equation: $P = R.I^2$. The voltage seen by the cell also decreases thanks to the voltage divider created by the current control and the decreasing cell resistance. Once the available energy is low enough the filament is stabilized and the filament morphology and resistance are fixed. The key parameters of the filament stabilization and morphology is then the available energy of the system. Figure 6 (a) shows the resistance distribution for two simulated state during the SET operation. These two states are taken at the end of the first phase of SET (once the filament is created) and at the end of the second phase (when the filament is stable). This figure shows that the stabilization of the filament not only leads to a reduction of the resistance mean value but also to a distribution narrowing. The available energy is responsible for the stabilization and the more available energy there is, the closer to the stabilized state the CBRAM is. The available energy comes in part from the heat generation induced by the current flowing through the filament. Accordingly, the energy depends on the current evolution during SET and especially on the compliance current. Figure 6 (b) shows the total available energy of the system during the SET in function of the compliance current and extracted by the KMC simulation. As expected, the mean value of the energy decreases with the current decrease. However, the energy distribution also becomes wider as the compliance current decreases. This can be explained by the number of atoms involved in the attainment of the compliance current.

Figure 6 (c) shows that this number decreases with the resistance value increase. Induced by this atom number reduction, the migration of one or few atoms during the filament stabilization has much more impact on the current level. A few atoms displacement can have a big impact on the morphology of a thin filament compared to a thicker one and thus on the current it allows to flow. This low but highly distributed available energy involved during a SET at low compliance current may explain the distributed stabilization observed at low programming current.

To sum up, by reducing the compliance current, the available energy to the system is reduced and more distributed. This energy being responsible for the stabilization of the resistance once the compliance current is attained, the stabilization is less important and more stochastic with the reduction of compliance current. Accordingly, the resistance distribution gets wider and wider as the compliance current decreases.

3. High Resistive State variability

Taking advantage of the KMC, the HRS variability has been studied similarly to the LRS one. In order to the discriminate intrinsic and cycle to cycle variability, the RESET operation have been simulated following different criteria. First, using a LRS distribution in following experimental data to observe the good agreement between simulation and samples behavior. Figure 1 confirms the KMC ability to simulate the HRS variability, and shows the experimental HRS distribution that will be detailed through intrinsic and extrinsic variability.

LRS variability includes a resistance dispersion but also a variability of the filament morphology. By centering the filament of each cells after simulated SET it is possible to map the global location of all atoms during the SET operations. The average filament shape is then extracted from the atoms locations occupied more than 50% of the time. Figure 7 summarizes the acquisition of this average filament shape. HRS variability is then simulated using this single filament shape for numerous RESET operations. R_{LRS} is thus centered on the experimental LRS distribution and the HRS distribution is shown in Figure 8. The mean HRS resistance value is similar to the one obtained previously from the dispersed LRS. However, the width of the distribution is reduced, particularly around its center. This means that, even by starting from a unique filament shape a variability of the HRS occurring during the RESET operation is observable. As stated during the RESET operation analyses, the filament disruption starts from one of the highest energy locations in the RL. However, thanks to the high energy brought to the system under the form of voltage and

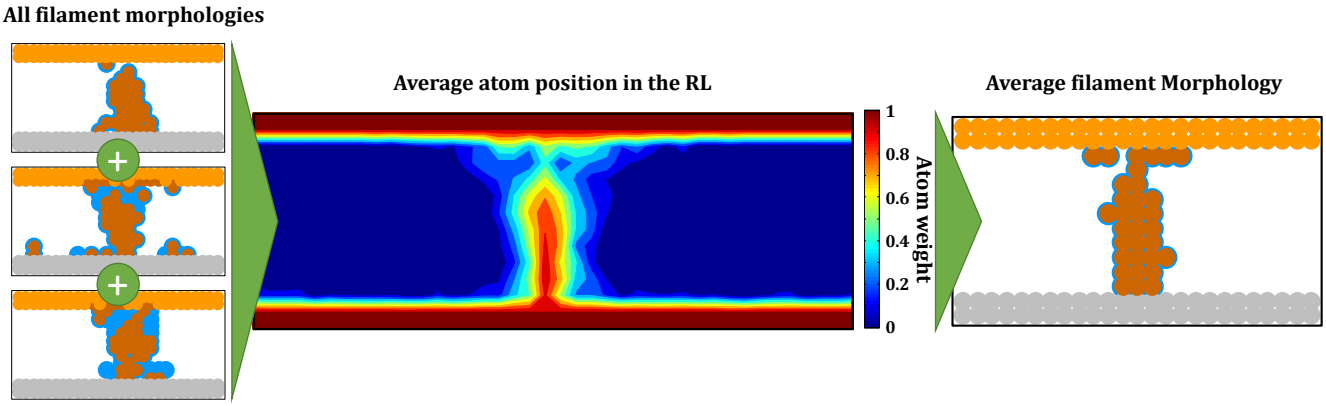

Figure 7. Acquisition of the average filament morphology from all the filament shapes

thermal dissipation, the area of favorable transitions is much expanded. This means that the initial disruption point of the filament can randomly occur from several locations and similarly to the butterfly effect or chaos theory changes the complete dissolution evolution and final resistance level. The intrinsic behavior of the HRS variability plays a great role in the dispersion. However this dispersion is not identical to the one obtained from a dispersed initial LRS, meaning that the HRS dispersion cannot only be attributed to intrinsic variability.

The RESET operation has then been simulated starting from two different R_{LRS} distributions, chosen on both side of the initially studied LRS distribution. The distributions obtained after RESET can be seen on Figure 9 (a). This time it is possible to observe the shift of the distribution. Indeed, the distributions remains similar but the mean values are slightly moved with the initial

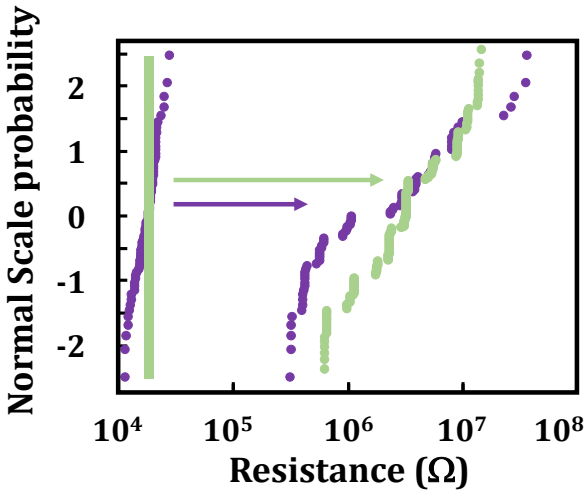

Figure 8. Simulated R_{HRS} distributions starting from a fixed LRS corresponding to the average filament morphology (green) or spread R_{LRS} distributions (purple).

R_{LRS}: the lower the R_{LRS} the lower the R_{HRS}. The dependency of R_{HRS} with R_{LRS} is summarized Figure 9 (b). However, due to the LRS range studied there, the R_{HRS} windows does not show a large spread. The main difference impacting various R_{LRS} is the filament morphology. The lower the R_{LRS} the more current flow through the filament, thus requiring a thicker filament. The thicker the filament, the harder it is to dissolve as stated in the previous chapter. This means that the lower the R_{LRS} the lower the R_{HRS}, explaining the mean value shift previously observed in the R_{HRS} distributions.

The mean value of the HRS distribution is thus correlated to the filament morphology. Moreover, as stated before, different filament morphologies can be obtained for the same R_{LRS} as the constriction is mainly controlling the resistance level. Various filament shapes can share the same resistance as long as the constriction size remains similar. To extract the filament morphology impact from the resistance level, RESET simulations have been performed on two distinct filament shapes. These filaments corresponds to the extreme morphologies of the studied LRS – HRS dependency: a thin and a thick filament but both sharing the same R_{LRS}, mean value of the LRS distribution. Figure 10 shows the filaments morphologies and the resistance distributions depending on the initial states. As observed previously in Figure 8, starting from a fixed filament morphology reduced the HRS distribution after RESET. This is still the case in the current study with a reduction of the resistance spread for both extreme morphology. Moreover, it is also possible

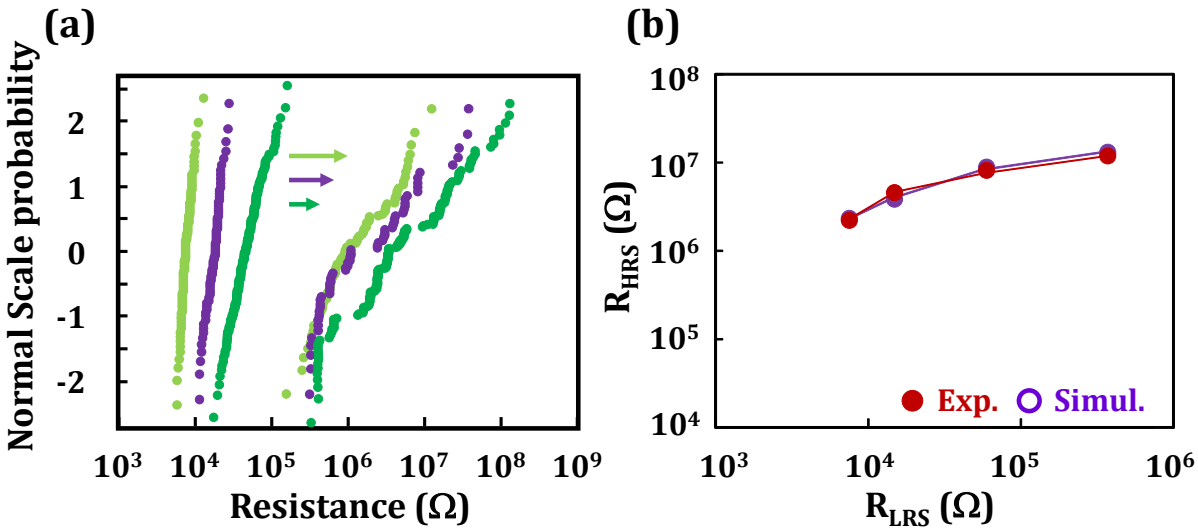

Figure 9. (a) Initially studied HRS variability from a distributed LRS (purple) surrounded by two LRS distribution and corresponding HRS distribution. (b) Evolution of the mean R_{HRS} in function of the mean R_{LRS} controlled by the compliance current.

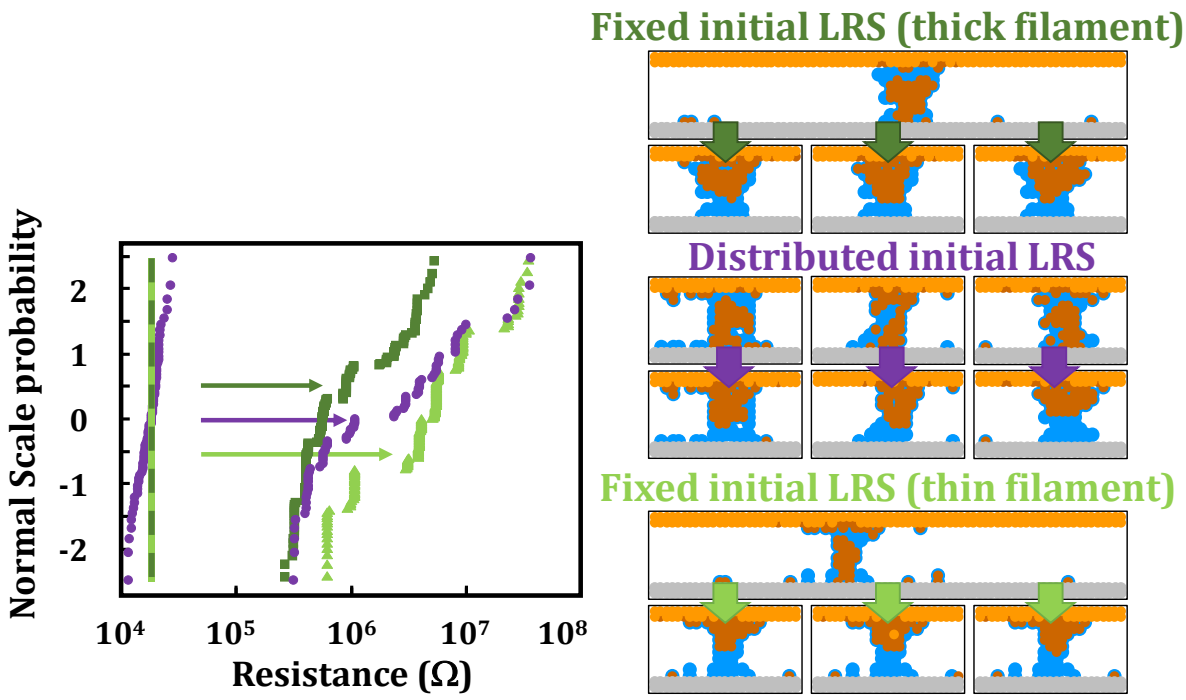

Figure 10. Simulated R_{HRS} distributions starting from two initial fixed LRS (green: same R_{LRS} but different filament shapes) or spread R_{LRS} distributions (purple).

this time to see a shift in the mean resistance value. The thicker filament leads to a low R_{HRS} whereas the thinner one offers a better RESET and higher R_{HRS}. This figure shows in the same time a change of the resistance distribution width and mean value. The global HRS distribution is bordered by the two extreme shapes and can thus be explained by the shape variability between these two extrema. The HRS cycle to cycle variability is thus mainly due to the filament shape variability evolving with the SET operation. This shape variability is present at fixed R_{LRS} but is also increased by the R_{LRS} variability. Indeed, depending on the R_{LRS} the population of thick filaments versus thin filaments varies which explains the HRS dependency with LRS.

To summarize, the intrinsic behaviour of the HRS state responsible in part for the HRS variability has been shown and is tied to the stochastic transitions occurring during the RESET (migration and redox reactions). However, in opposition with the LRS behaviour, a strong cycle to cycle dependency has also been observed. Indeed, R_{HRS} mean value depends on the R_{LRS} and especially to the filament morphology as a large filament is harder to erase and will most likely lead to a thick residual filament and reduced R_{HRS}.

4. Endurance reliability and failure mechanisms

As mentioned in the first chapter, the CBRAM devices can be prone to failure mechanisms during cycling depending on the technology and the targeted memory window. The failure mechanisms are difficult to observe, and only the effects on the endurance reliability are hinting about the degradation of the CBRAM cell. The endurance degradation occurs in different ways: LRS fails, HRS drift or fails and oxide breakdown. This section will be focused on LRS fails and HRS drift as HRS fails and oxide breakdown are mainly due to unsuited and extreme operating conditions coupled to sensitive technology. In this section, the arrays of CBRAM devices have been characterized to obtain an extensive overview of the endurance behavior. From these observations and the use of the KMC model, the mechanisms involved in the endurance failure are addressed and correlated to the operating conditions.

Depending on the operating conditions, it is possible to obtain various endurance behaviors. Using soft SET conditions might induce a loss of LRS but using strong SET and RESET conditions might lead to a loss of HRS. Figure 11 shows the LRS and HRS degradation behaviors for two 64 bits matrix. Regarding the resistance mean value of the 128 devices, both LRS and HRS show the same degradation behavior: a progressive loss of their state. However, a first hint of the difference between these two failure mechanisms can be seen with the resistance dispersion. Indeed, the degraded LRS dispersion is much higher than the degraded HRS one. To analyze this observation,

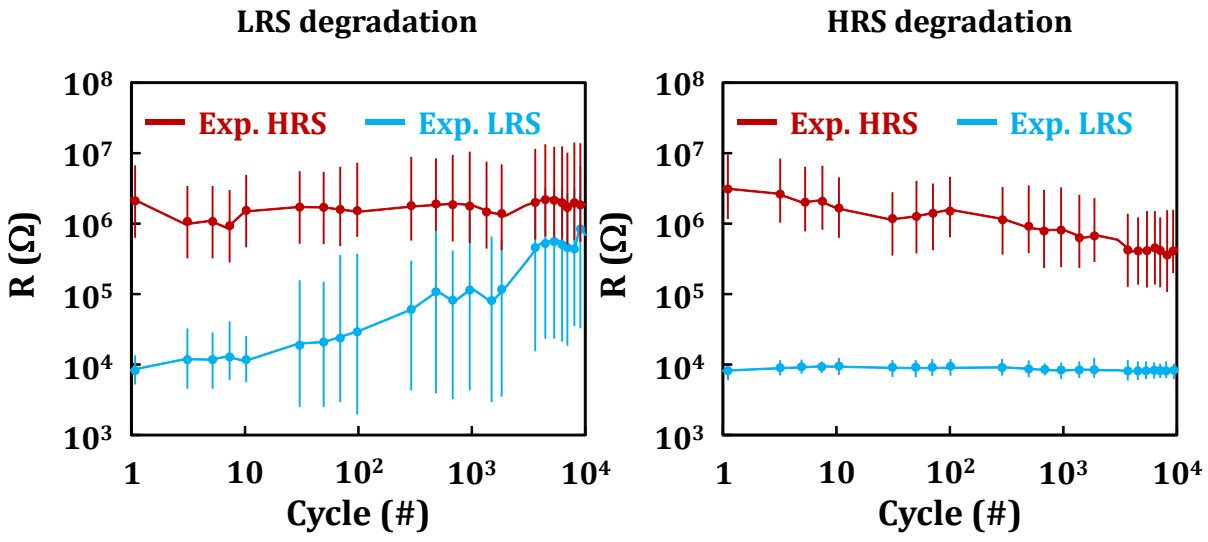

Figure 11. Resistance dispersion and mean value of two 64 bit matrix showing either a LRS (left) or HRS (right) degradation.

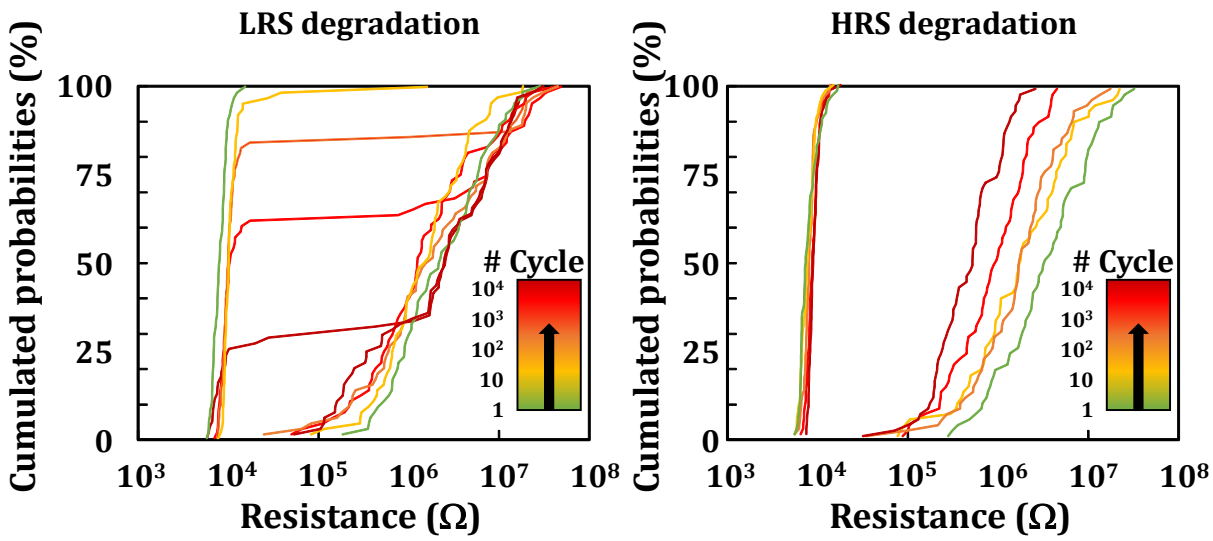

Figure 12. LRS and HRS distribution for both degradation mechanisms

the resistance distributions have been plotted on Figure 12. This figure reports the cumulated probabilities of the resistance from 1 to 10^4 cycles using a logarithmic scale. The difference between LRS and HRS degradation is much more noticeable. The HRS degradation clearly shows a progressive decrease of resistance whereas LRS degradation results in an increasing number of non-written cells. To understand the physical mechanisms hidden behind those observations, endurance cycles were simulated on several independent devices.

Regarding the LRS degradation when the SET condition are too soft (pulse time or voltage), the LRS does not progressively shift toward HRS but abruptly from one cycle to the following and stays at HRS after a failed SET. This means that the higher the number of cycles endured by the cell, the lower the chance for the cell to SET. This behavior can be seen Figure 13 with the corresponding simulation. The cell cycles normally until it starts to become impossible to be written with the current operating conditions. In term of physical mechanisms, it means that there comes a cycles when the gap between the residual filament and the BE becomes too wide for the applied field to drive the ions migration.

Figure 13 also represents the filament shape after the first cycle and once the cell hits its erratic behavior. Throughout the cycling operation and especially during the RESET, the residual filament tends to become wider and wider due to the dissolution of the bottom of the filament. As stated during the SET analyses, during cycles at the same compliance current the ions are reorganized to recreate the filament and only a few or none are generated from the TE. The progressive thickness

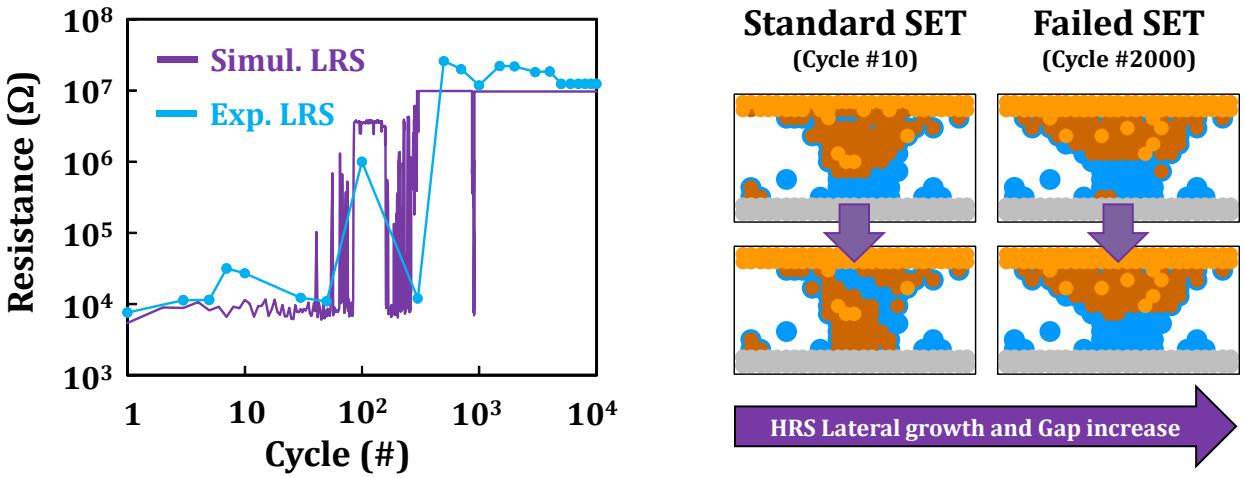

Figure 13. Experimental and simulated stochastic degradation of the LRS state. Filament and RL situation corresponding to the inability to SET the cell after degradation.

increase of the residual filament with a constant number of ions in RL leads to an increase of gap between the residual filament and the BE. Throughout the cycling operation, the gap becomes wider and wider until the electric field and voltage pulse is not sufficient enough to allow the ions to migrate and recreate the filament. Due to the stochastic behavior of the LRS fails, it is hard to notice the gap increase on the R_{HRS} evolution and only a slight increase of the mean R_{HRS} is visible. However, the stochastic increase of R_{HRS} can be seen on the resistance dispersion whose highest point increase with the number of cycle (Figure 12). This gap increase can also be seen in Figure 13 with the increase of the resistance level of the failed LRS until the state is completely blocked. Once the cell is blocked on HRS it is possible to apply slightly stronger SET conditions to regain the switching behavior. Regarding the physical parameters influencing this behavior, the model shows that the residual filament enlarging is correlated to the migration activation energy in pristine RL. A high activation energy leads to a high number of cycles required to sufficiently increase the residual filament width and degrade the LRS. On the contrary, if the migration activation energy is much lower once oxygen vacancies are introduced in the degraded RL, LRS degradation is delayed.

Considering the HRS degradation when SET and RESET conditions are too strong, the HRS progressively shifts toward the LRS. This behavior can be seen in Figure 14 with the corresponding simulation. The cell cycles normally and starts with a higher initial R_{HRS} thanks to the stronger RESET conditions. However, as the cycles number increases, R_{HRS} progressively decreases. In term of physical mechanisms, the gap between the residual filament and the BE becomes smaller

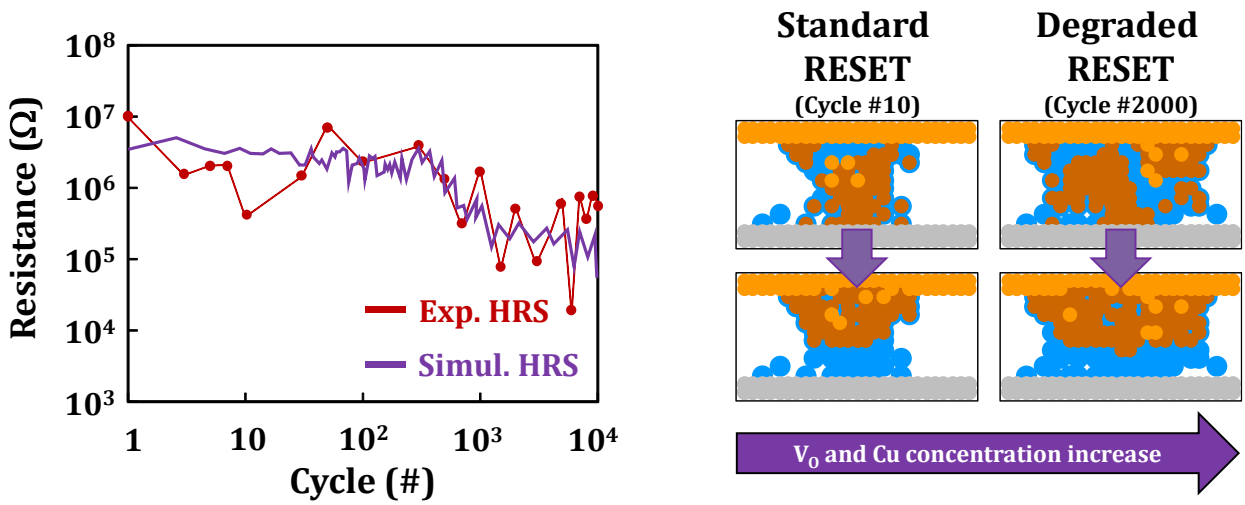

Figure 14. Experimental and simulated progressive degradation of the HRS state. Filament and RL situation corresponding to the HRS loss the cell after degradation.

and smaller explaining the resistance reduction. This figure also represents the filament shape after the first cycle and once the cell hits its degraded behavior. The gap reduction after RESET is caused, as expected, by the strong SET but also by the strong RESET. The strong RESET initially causes a bigger gap but also a wider residual filament. To recreate the filament, a stronger SET is required thanks to the bigger gap. However, due to the wide aspect ratio of the residual filament it becomes energetically easier to ionize atoms from the TE than to reuse the ions too far aside in the RL. These ions are outside of the favorited growing area mentioned in the SET analyses chapter IV and the electric field is not strong enough to pull them toward the growing filament. The TE atoms oxidation leads to a progressive increase of the ions number involved in the RL. The ions left aside make it difficult to dissolve the filament and push the ions previously oxidized, what ultimately leads to the reduction of the gap responsible for the resistance loss. Moreover, the energy increase seen by the cell and ions movement leads to a higher concentration in oxygen vacancies also reducing the resistivity of the RL. In opposition to the LRS degradation, it is impossible to improve the memory window by applying a stronger SET or RESET as these operations are already too strong. Using an oven at high temperature might partially solve the problem but cannot be applied to industrial devices. Regarding the physical parameters influencing this behavior, the degradation of the HRS being originally due to the residual filament enlarging, the model shows the same conclusion as for the LRS degradation study. Indeed, the residual filament enlarging is correlated to the migration activation energy in pristine RL. Stronger programming conditions can

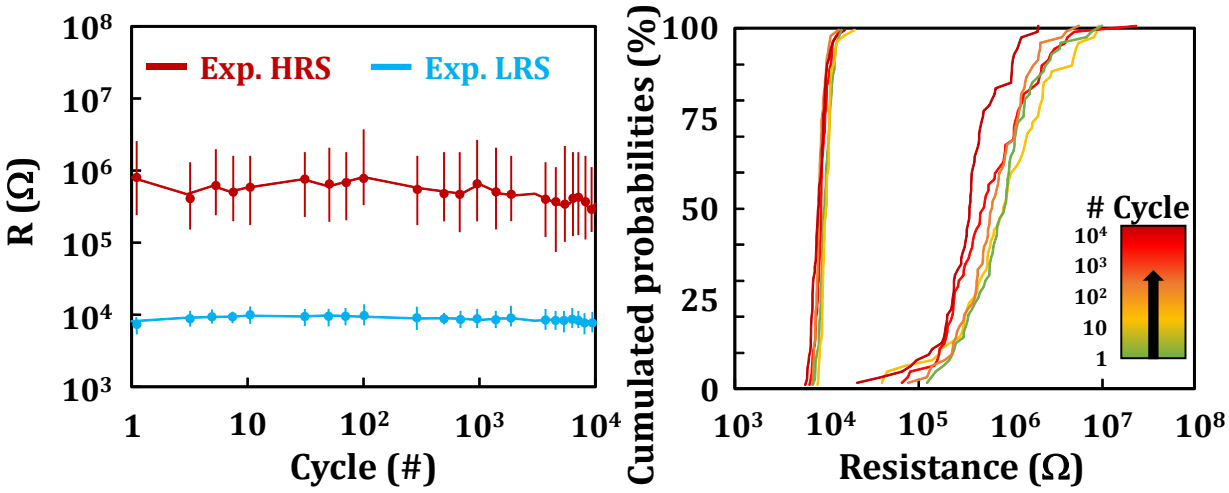

Figure 15. Stable endurance characteristic offering good memory windows without degradation of neither LRS nor HRS

be endured avoiding HRS degradation with higher ion migration activation energy in the pristine RL.

It is then very important to smartly choose the operating conditions to obtain the best endurance possible. The SET conditions must be strong enough but not too strong to the point of requiring strong RESET degrading the RL. Figure 15 shows the awaited endurance characteristics using optimized conditions. In order to obtain the best endurance behavior, a smart programming routine can also be used. This routine aims to write the cell with the lowest possible energy. To achieve such goal, SET operations are performed with an increase of pulse time and/or voltage until the cell is written. This programming routine takes longer to write the cell due to several SET and Read operation required but offer the best way to achieve good endurance. Figure 16 schematizes two different routines used to improve the endurance, either pulse height or time increase. A combination of the two is also possible if the voltage sustainable by the cell is limited for example.

5. Chapter V synthesis

In this chapter the variability of both states and the degradation mechanisms occurring during cycling have been presented. LRS is prone to a strong intrinsic variability whereas HRS is subject to both cycle to cycle and intrinsic variability. The intrinsic variability of LRS comes from the available energy in the system to stabilize the filament. With high energy come strongly stabilized filaments and low variability, which is the case at high compliance current. In contrary,

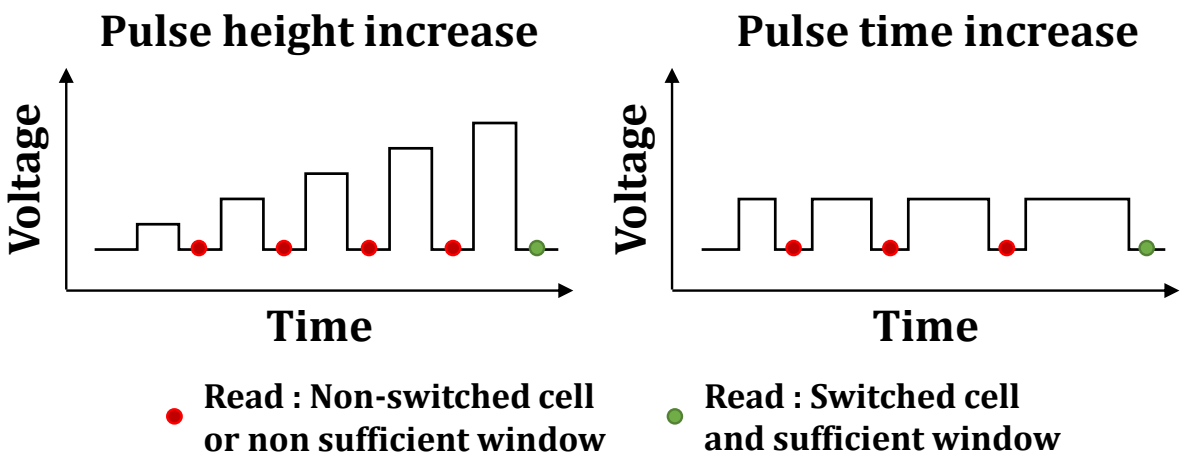

Figure 16. Smart programming routine to improve the cell endurance without degrading the memory window

low compliance current brings low and highly distributed available energy, explaining the high variability of filament stabilizations and final resistances. Another factor of the intrinsic variability is the randomness of the transitions (ions migration, reaction…) occurring, especially at high temperature and high electric field. This randomness of transitions is particularly visible on the filament stabilization during SET and filament dissolution during RESET, as these two phenomena both occur with high temperature.

The stochastic behavior of the occurring transitions can also be observed in the LRS failure during cycling. Before definitively losing the LRS, there are cycles where the cell can randomly be written and other where it cannot. A particular succession of transition can lead to a favorable situation to write the cell whereas some other cannot. The achievement of these particular succession of transitions are highly tied to randomness. In fact, the global degradation of the LRS state can be understood with this randomness factor in mind. Indeed, the SET operation can be divided in two steps: the creation of a favorable zone for the filament formation (high electric field and temperature) and the proper filament formation. The probability to achieve such a favorable zone is very high at first (close to 100% in normal conditions) but decreases with the cycles until it becomes so low that the cell seems blocked in the HRS. However, as can be seen in Figure 13 the cell is not endlessly blocked and can still be written even after thousands of cycles blocked in HRS. The filament morphology plays a great role in the HRS variability. Indeed, the cycle to cycle variability observable on the HRS is tied to the filament shape variability during SET. This variability comes from the stochastic filament formation previously described but is also in some extent bond to the resistance level: the higher the compliance current and the lower the resistance

level, the thicker the filament and the worst the HRS. The HRS degradation described in this chapter is actually caused by the progressive increase of the filament thickness. This change of shape, caused by too strong operating conditions and RL degradation, leads to a progressive reduction of the gap dimension and diminution of R_{HRS}. The loss of HRS is also worsened by the insertion of oxygen vacancies degrading the RL and its resistivity. The SET conditions have a great impact on the filament shape and thus on the HRS endurance too. It is of great importance to use smart programming conditions to obtain the best endurance possible as it is impossible to recover from a lost HRS state in opposition to a lost LRS. To find the best programming conditions, routines can be used and rely on a progressive increase of the energy brought (voltage and time) to the system during SET or RESET until the desired state is obtained.

Chapter VI. Data retention and high temperature behavior

1. Objectives

Once the data stored in the CBRAM devices, thanks to the Forming, SET and RESET operation, it is important to understand how it will last through time. Pursuing the clarification of the CBRAM global behavior, this chapter will focus on the data retention and the behavior of the CBRAM at high temperature. In the same manner as the previous chapter, references will be made to chapters II and III regarding the description of the characterization protocols, studied samples and KMC simulations. Considering the previous observations regarding the impact of the scaling on the CBRAM electrical characteristics, only samples with identical dimensions and architectures will be compared in this chapter.

The data retention is a key factor for every memory technology and corresponds to the ability to store the information as long as possible. Regarding CBRAM devices, the loss of data can occur for both resistance state, LRS as well as HRS. The loss of LRS is due to the progressive dissolution of the conductive filament whereas the loss of HRS is more complicated but initially due to the recreation of a conductive path between the electrodes followed by a strong resistance increase. This resistance increase can lead to the requirement of a strong writing process comparable to the Forming step in order to obtain the LRS back. As stated in Chapter I and II, the targeted application may require several years of data retention capability, leading to an impossible way to verify these specifications in standard conditions. This is why the data retention is thermally accelerated and the behavior at high temperature has to be studied. Studies have been published proposing the acceleration of data retention by applying a low voltage at the electrodes which leads to the resistance disturbance [Longnos 1, Vianello 1, Hsieh 1].

This chapter will be organized around the description and understanding of the physical events leading to the loss of the high and low resistance states. Then optimization trends, in term of technological solutions and operating conditions will be proposed and supported by experimental and theoretical results using the KMC simulation.

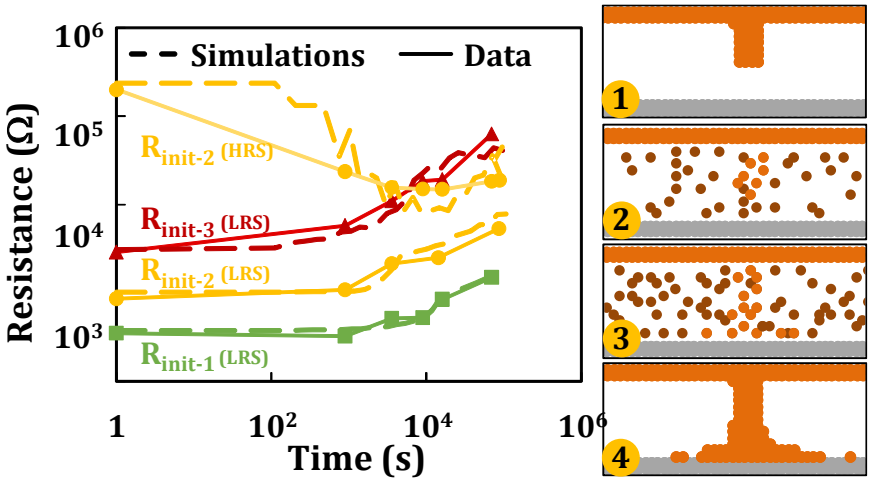

Figure 1. LRS and one HRS Data Retention experimental results and KMC simulations at 100°C and the filament dissolution. The yellow curves share the same LRS resistance. 1: Initial HRS, 2: Final HRS, 3: Final LRS, 4: Initial LRS, all corresponding to the Data: R_{init-2}.

2. Physical understanding of the data retention behavior.

Depending on the technological choice, the CBRAM cell can offer two different failure mechanisms at high temperature. Chapter I related the technological evolution of CBRAM devices and especially the transition from chalcogenide based to oxide based resistive layer. This transition showed improved data retention capabilities in term of LRS. However, the chalcogenide based CBRAM were known for offering a stable HRS retention which is not the case anymore for the oxide based ones. This section will be focused alternatively on the LRS retention and then HRS retention and relies on experimental results and KMC simulation able to compute LRS and HRS retention behavior as shown in Figure 1.

2.1 Low Resistive State retention and degradation mechanisms.

As briefly exposed in this chapter introduction, the loss of LRS state is due to the progressive dissolution of the conductive filament. However, this dissolution follows a specific pattern from a stable conductive filament to dissolved filament and non-conductive RL. Figure 2 shows the standard LRS retention behavior experimentally obtained on oxide based CBRAM and nano – Trench architecture. Using the traditional logarithmic scale representation for data retention, an exponential increase of the resistance value can be seen. This traditional representation is of great interest to observe at the same time the early and late behavior of the cell

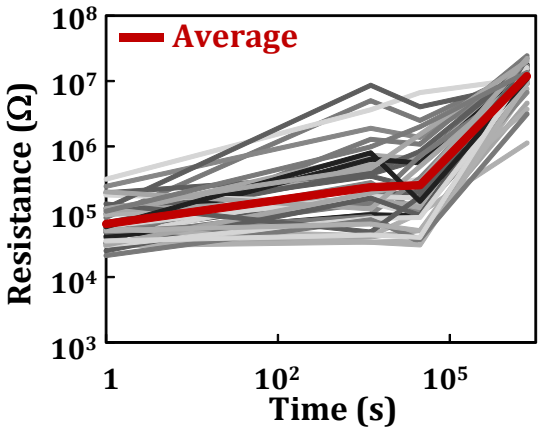

Figure 2. Typical retention LRS behavior at high temperature (200°C here) for low programming curent

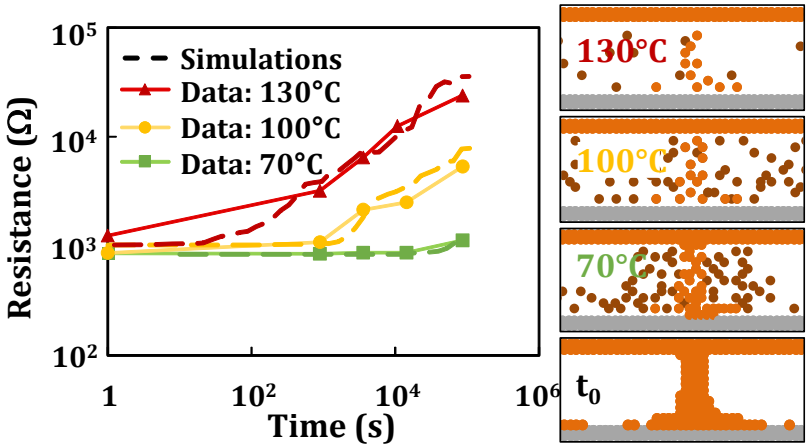

Figure 3. Temperature impact on the LRS retention behavior. The higher the temperature, the faster the LRS loss

at high temperature. This resistance increase corresponds to the filament dissolution in the RL. Depending on the temperature at which the retention is accelerated the resistance increase is faster or slower. Figure 3 shows that the higher the temperature, the faster is the resistance loss. By using a semi-log scale Figure 4 it is possible to divide the retention behavior in two parts in function of the slope. The first part of the curve has a much higher slope and corresponds to the dissolution of the filament, whereas the second corresponds to the homogenization of the conductive atoms in the RL. As long as the filament stands and shows a continuous conductive path, the electrical conduction follows the Ohm law, using quantum conductance (see Chapter III). During the first part of the retention curve, the filament get progressively dissolved leading to a shrinkage of the filament dimensions. The resistance increase is then due to the loss of conductive area. To simplify, considering a filament cut made of *n* parallel atoms and resistances (constant and tied to the quantum conductance), the global resistance of the cut can be expressed as:

$$R_{Cut} = \frac{R_{Quantum}}{n}$$

Where $R_{Quantum}$ is the Quantum of resistance (12.9 kΩ) induced by the presence of an atom and *n* the number of atoms in the cut. During the shrinkage of the filament the number of atoms in the cut decreases leading to a global increase of resistance following an inverse law (1/*n*) of the atom removing from the filament. The first slope is then due to this inverse law of resistance evolution and to the atom removing speed.

During the second part of the retention curve, the filament is completely dissolved, meanings that the conduction no longer follows the Ohm law but instead traps assisted behavior (assuming conduction only between Cu atoms in the resistive layer). During the second phase of retention, the distance between atoms tends to increase in order to occupy the entirety of the RL, in agreement with Fick's Laws. However, the distance between atoms directly modify the electrical resistance between them thanks to the trap assisted tunneling. The equation used to describe the resistance between two atoms is reminded here (See Chapter III):

$$R_{Cu-Cu} = R_{Quantum}\, exp\left(2\frac{\sqrt{2m^{*}E_C}}{\hbar}\,(d-a)\right)$$

Where $R_{Quantum}$ is the Quantum of resistance (12.9 kΩ), m^* the effective mass of electron for a specific electrolyte, E_C the energy barrier for electron tunneling, d the distance between two atoms, a the contact distance between two atoms and $\hbar$ the Planck constant. As can be seen, the resistance exponentially increases with the distance between atoms.

The difference of slope between the two dissolution phases depends on joint effect of the electrical conduction law and the speed of the mechanisms involved during the phase. Depending on the energy level of Cu inside the RL, its state might vary between pure Cu and ionized Cu^{i+}. Based on this state, an oxidation reaction might be required to initiate the filament dissolution as pure Cu migration cost too much energy to be considered as a viable solution. Thus, the two physical mechanisms involved during the first step are the oxidation reaction and the desorption from the

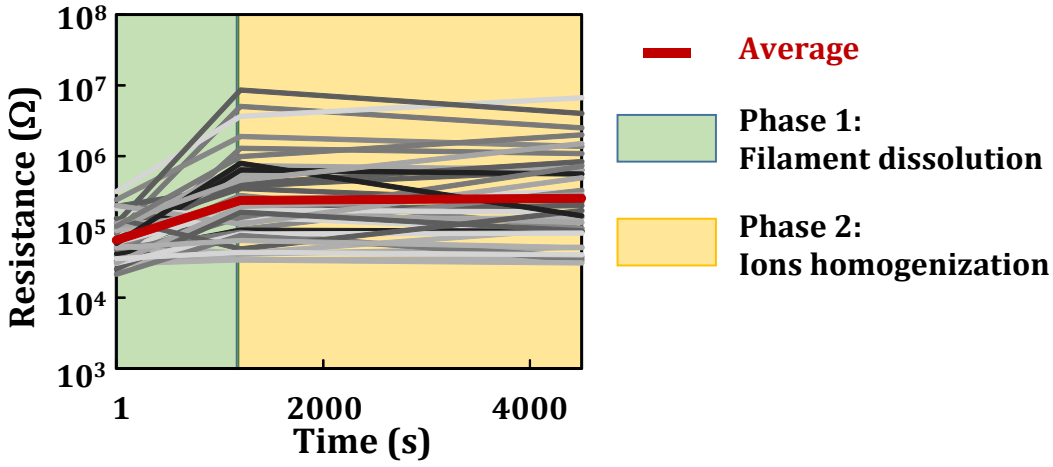

Figure 4. Semi-log representation of the retention behavior (Figure 1) showing the two degradation phases.

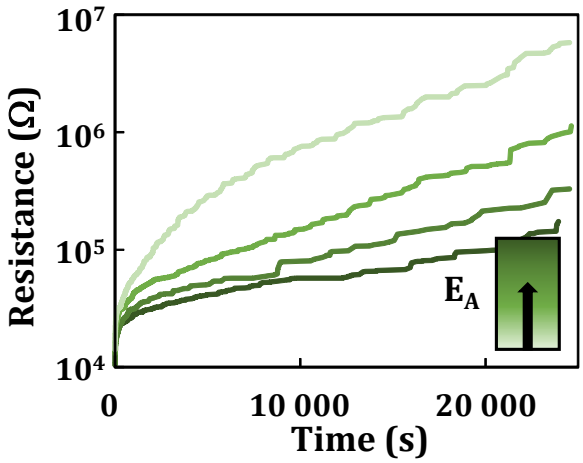

Figure 5. Simulated retention behavior at 200°C with different activation energy for the Cu desoption from the aggregate. A slope modification can be seen in function of the activation energy.

Cu ions aggregates. The activation energies of these two mechanisms greatly influence the slope of the first part of the curve as shown in Figure 5. The increase of activation energy stabilizes the filament and reduce the dissolution speed. Regarding the second phase of the retention, corresponding to the Cu concentration homogenization in the RL, only volume migration of the ions is involved. Thus the slope of the second part of the curve is modified by the activation energy of the ion volume diffusion.

In the end, under the joint action of the Cu atoms oxidation, aggregate disruption and volume diffusion, the LRS state is degraded toward higher resistance values.

2.2 High Resistive State retention and degradation mechanisms.

As briefly exposed in this chapter introduction, the loss of HRS is initially due to the recreation of a conductive path between the electrodes. However, the HRS loss pattern is more complicated than the LRS one as can be seen in Figure 6. This figure shows the typical retention behavior experimentally obtained on oxide based CBRAM, corresponding to a progressive loss of HRS. However, Figure 6 also shows the extended HRS retention behavior with a double trend occurring if the retention temperature is high enough or time sufficient. The difference of sample in term of resistive layer with pure Al_2O_3 (left) and Al dopped Al_2O_3 (right) allows the observation of the two behaviors with the same retention conditions. This double trend (right) is composed by a decrease of resistance followed by an increase toward higher resistance values. Depending on the temperature at which the retention is accelerated the resistance variation is modified and the second

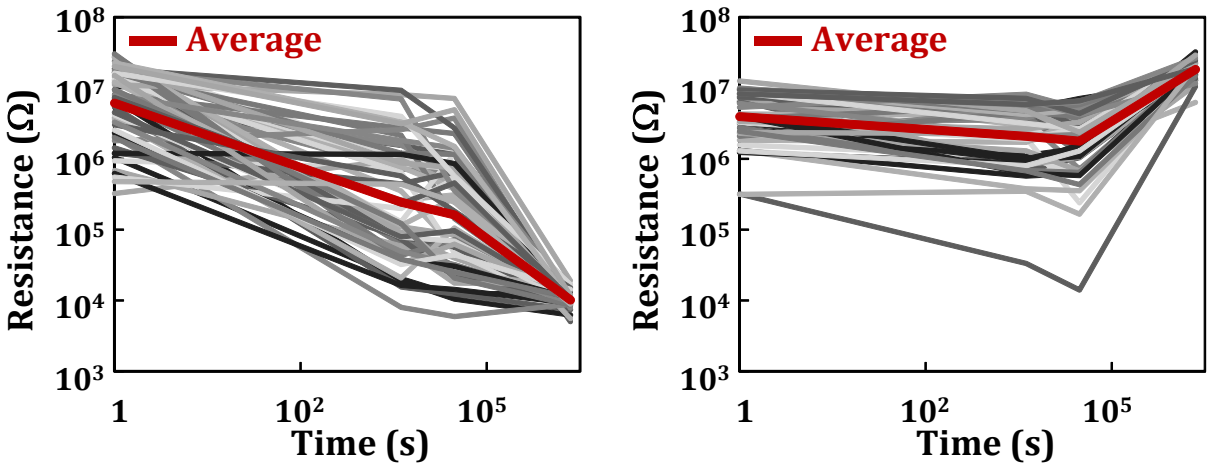

Figure 6. Typical HRS retention behavior (left) and extended HRS retention behavior with sufficient time or temperature to observe the double trend. Both obtained at 200°C on different samples.

trend might or might not be visible as shown Figure 6. Similarly to LRS retention, the higher the temperature, the faster the resistance evolution.

The recreation of a conductive path mentioned previously corresponds to the first phase of HRS degradation. As stated during the SET and RESET study, oxide based CBRAM show a residual filament after RESET. The residual filament acts as a source of ions, which with sufficient time or energy (temperature) are migrating toward area less concentrated in conductive atoms. The gap between the residual filament and the BE is one of these areas and the increase of conductive atoms concentration in this gap leads to the progressive resistance reduction seen in Figure 6 during the first phase. At the beginning of this phase, the electrical conduction is based on trap assisted tunneling. However, as the concentration increases, a continuous conductive path can appear leading to a percolation electrical conduction and a great reduction of resistance. The HRS is thus degraded and the resistance keep decreasing until it reaches a minimal value (no lower than the previous LRS resistance) signing the end of the first phase. Figure 7 (a) shows another occurrence of this behavior using Nano-Trench architecture, still with oxide based CBRAM. On these samples with dimension variations, this behavior has been observed multiple times in multiple temperature and programming conditions. It is possible to correlate the resistance value at the lowest point recorded to R_{LRS} preceding the RESET operation as shown Figure 7 (b). However, the stochastic characteristic of this behavior makes it difficult to monitor especially considering the logarithmic time scale involved in the study. The resistance value obtained at the drop might not exactly correspond to the lowest point reached at high temperature and this could explain the relative

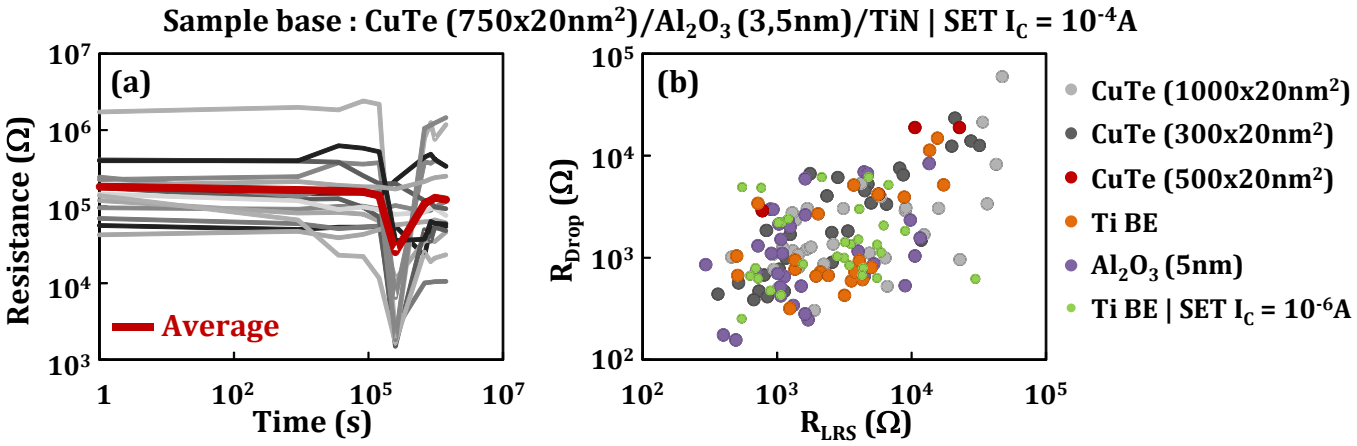

Figure 7. (a) Stochastic resistance drop due to the reformation of a conductive path during data retention (100°C here). (b) Correlation between the resistance level during the drop and the resistance of the previous LRS observed on various samples and conditions

dispersion of measurements. This correlation shows that during HRS retention, the residual filament tends to recreate a conductive path similar to the LRS filament. The resistance drop is tied to the filament reformation and ions migrations induced by the temperature. The higher the temperature the faster is the filament recreation and the sooner occurs the resistance drop appearance.

At the end of the first phase a conductive path is recreated and the cell is in a state comparable to LRS. This means that the second phase of HRS retention might be similar to the LRS degradation with a progressive dissolution of the conductive path and a homogenization of the conductive atoms in the RL. Thus, the resistance increases with time and the filament ends up being completely dissolved in the RL.

The HRS retention can be seen as the competition of two antagonist mechanisms: the one responsible for the HRS loss toward lower resistance value being the recreation of the conductive path and the one responsible for an increase of resistance value being the lateral dissolution of the residual filament. The dominant behavior of one over the other will determine the global behavior of HRS retention and will be discussed further in the HRS retention optimization section. Figure 8 schematizes the dual trend of HRS retention and the competition between lateral and vertical diffusion.

It is important to note that if a conducive path is recreated, the secondary phase of HRS retention is superfluous in terms of pure retention capability as the HRS is already degraded after the first

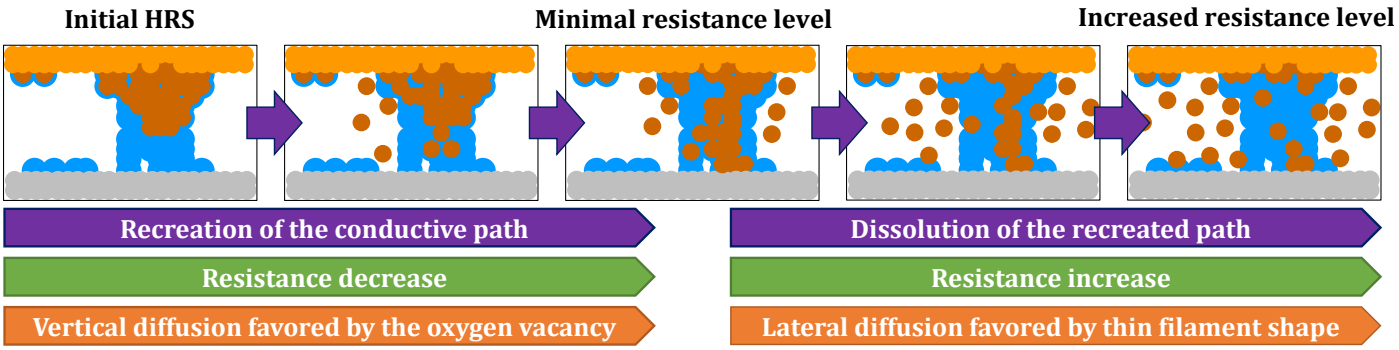

Figure 8. Schematic representation of the HRS retention dual trend and competition between vertical and lateral diffusion

phase. However, it is imperative to acknowledge the global behavior of HRS degradation as a poorly timed retention study might neglect or miss this erratic behavior and only focus on the starting and finishing resistance levels. This erratic behavior can indeed occur quickly in time considering the logarithmic scale followed to study retention. The retention study in Figure 7 (a) shows this erratic behavior and illustrates how important it is to acknowledge this comportment in order to avoid considering the erratic points as measurement artefacts as it have been the case during early retention analyses. HRS degradation requires a residual filament whose presence is tied to a reduced R_{OFF} compared to the pristine resistance. Chalcogenides based CBRAM in regular operating conditions (low compliance current) have HRS resistance at the level of the pristine state meaning that there should be no residual filament in the RL. This observation might be the reason that chalcogenide HRS is stable (still in regular operating conditions) at high temperature.

Both phase of the HRS degradation relies on the dissolution of a filament, residual or recreated and to the homogenization of the conductive atoms in the RL. Thus, the mechanisms involved are the desorption from the aggregate of the Cu ions and then the volume diffusion for both phases. The oxygen vacancies considered for the first time during the variability might also be involved in the HRS retention. Indeed, the erased filament print in the RL leaves oxygen vacancies that offers a favorited area for the conductive path reconstruction. The vertical diffusion of the residual atoms is then faster than the lateral one which facilitates the recreation of a conductive path and the degradation of the HRS.

3. Data retention optimization

The physical mechanisms hidden behind the resistance state degradation being exposed, it is possible to optimize the retention capabilities of both LRS and HRS. The retention studies have

mainly been focused on the retention optimization through smart programming condition. However, technological solution have also been studied experimentally and theoretically. This section will be organized around the programming condition optimization of LRS then HRS and then the technological improvements.

3.1 Programming conditions and data retention.

Both LRS and HRS retention capabilities are greatly impacted by the programming conditions, this part will combine experimental data obtained on oxide based nano – Trench CBRAM and KMC simulation results. The main part of the reasoning developed here was initially born using the first version of the KMC model but confirmed with the most advanced one.

3.1.1 Low Resistive Sate retention

The LRS retention as exposed before is tied to the filament dissolution. The experimental results Figure 9 (a) shows the retention behavior in function of the initial resistance value obtained on CuTeGe/Al_2O_3/TiN nano-Trench devices. It can be seen that the LRS degradation occurs much faster for a high initial R_{LRS}. As shown during the SET analyses, the resistance of LRS is controlled by the compliance current applied during the SET operation. Increasing this current leads to a lower R_{LRS} and then a better LRS retention over time. This experiment results is in great agreement with the KMC simulations as show Figure 9 (b). This figure shows the resistance increase per year at

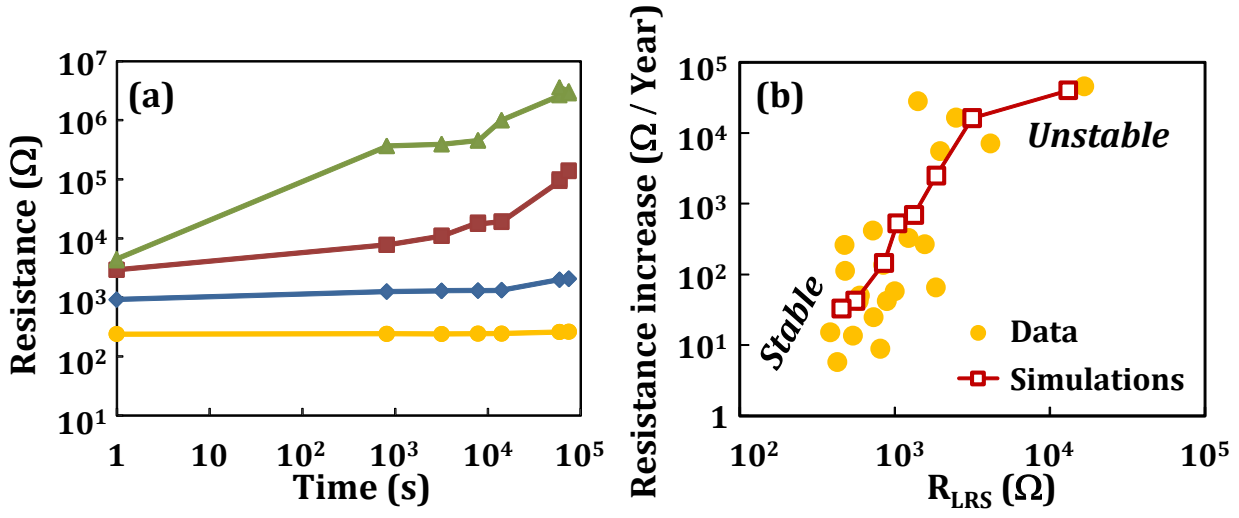

Figure 9. (a) LRS degradation over time in function of the initial resistance level at 100°C (b) Simulated and experimental resistance level increase of LRS per year in function of the initial R_{LRS}.

100°C as a function of the intial R_{LRS} for the studied samples. These data were extracted from the slope of the curves obtained experimentally and through the KMC simulation. By reducing the initial resistance level of LRS it is possible to improve the thermal stability and reduce the resistance degradation over time. It shows that a LRS under 10^3 Ω, the cells seems perfectly stable at high temperature. The instability starts occurring between 10^3 Ω and 10^4 Ω with a strong increase of resistance loss. This figure validates that a low initial resistance leads to strong LRS retention capabilities. In term of filament morphology, R_{LRS} is tied to the filament thickness: a thick filament allows more current to flow and induces a lower resistance. A thick filament means more atoms involved in the conduction mechanisms. The disruption of the filament requires consequently more atoms to be removed from the filament to cut the percolation conduction. The core of the filament then remains intact longer and the first phase of the retention (filament disruption) takes longer to occur. Then considering the increased number of atoms in the RL the average distance between atoms responsible for the resistance increase in the second phase (conductive atom homogenization in RL) stays lower, inducing a better second phase of retention too.

In order to achieve good LRS retention capabilities it is then important to use a compliance current sufficiently high. The LRS programming is then a tradeoff between required retention capabilities and tolerable power consumption. [Barci 1]

3.1.2 High Resistive State retention

The HRS retention is more complicated and cannot only be correlated to the initial resistance value of the HRS. Indeed, as can be seen Figure 10 (a) there is no direct correlation between the initial resistance and the retention behavior. Two trends can be seen on the experimental data obtain at 100°C on CuTeGe/Al_2O_3/TiN nano-Trench devices: some cells experience a strong HRS degradation and some other show good thermal stability. However, by taking a look into the resistance value of the LRS state preceding the studied HRS, a correlation can be seen. Indeed, depending on this LRS resistance value the HRS retention behavior is different: for a strong SET the HRS gets degraded at high temperature whereas for a weaker SET the HRS stays stable. This HRS retention trend in function of the resistance value of the anterior LRS can be quantified by the decrease of resistance per year shown Figure 10 (b). Similarly to the LRS retention study, this results were extracted from the slope of the experimental results and the simulations. For this study, only the cells with a HRS resistance around 10^5 Ω have been

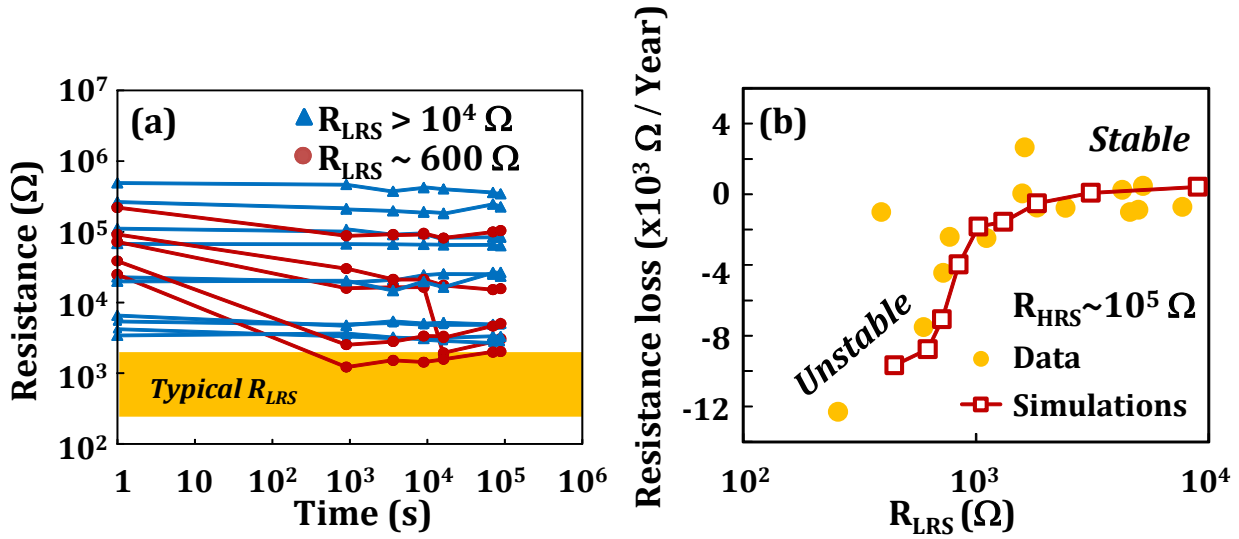

Figure 10. (a) Experimental HRS retention behavior showing two different trends in function of the anterior R_{LRS}. (b) Simulated and experimental resistance loss of HRS per year in function of the anterior R_{LRS}.

considerated in order to avoid any possible effect of the HRS state on its own retention. This study clearly shows the increase of slope (in absolute value) with the decrease of LRS resistance. In other words, it shows that the stronger the SET the worst is the following HRS retention. To understand this observation, it is necessary to take a look into the filament morphology after SET and RESET. As previously stated, a low LRS resistance or a strong SET is obtained with a high compliance current and leads to a thick filament and a high concentration of Cu atoms. To RESET the cell a portion of the filament has to be dissolved, as exposed in the SET and RESET analyzes (Chapter IV). Depending on the final resistance, a residual filament remains in the RL and acts as an ion supplier during the HRS retention. The morphology of this residual filament is directly tied to the morphology of the filament before RESET. This means that a thick filament due to a strong SET leads to a thick residual filament inducing a high quantity of residual Cu atoms in the RL. The loss of HRS retention being due to the recreation of a conductive path in the RL from the residual atoms, the bigger is the residual filament the easier it is to recreate the conductive path and the worst is the HRS retention. As reported in Figure 10 (b) by increasing the resistance value of the LRS preceding the studied HRS, the thickness of the filament and residual filament are reduced and the HRS retention behavior is improved. The filament thickness mainly impacts the LRS resistance value but has only a limited influence on the HRS resistance for which the gap between the electrode and the residual filament is the main factor.

Now that the impact of the SET conditions on HRS retention behavior are known, it is possible to focus the study on the impact of the RESET conditions. To do so, the HRS retention behavior of two different SET conditions have been studied in function of the RESET conditions and reported Figure 11. As demonstrated during the RESET analyzes, it is possible to modulate the HRS resistance by modifying the voltage slope and especially the stopping voltage. The RESET conditions modify the gap in the RL which is the main factor of the HRS resistance. By increasing the gap, the resistance increase. Figure 11 shows that, while the HRS resistance increase has no impact on HRS behavior of softly SET cells and already stable, it offers a way to greatly improve the retention behavior and even achieve a stable HRS retention for a sufficiently strong RESET of strongly SET cells. Going back to the cause of HRS degradation, which is the recreation of a conductive path: the bigger is the gap to fill between the residual filament and the electrode, the harder it is to recreate a conductive path and the better is the retention.

Knowing the impact of the residual filament shape, in term of both thickness and height, it is now possible to discuss the dominant behavior of the antagonist mechanisms acting during HRS retention which are the vertical diffusion (recreation of the conductive path) and the lateral diffusion (complete dissolution of the filament). This dominant behavior is directly tied to the filament morphology: a thin and short residual filament facilitates the lateral diffusion whereas a thick and tall residual filament facilitates the vertical diffusion. By acting on the filament morphology thanks to the SET and RESET conditions, it is then possible to optimize the HRS

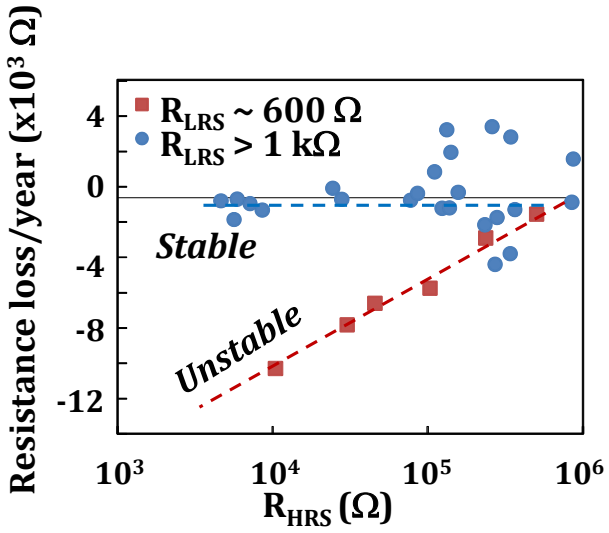

Figure 11. Measured HRS degradation as a function of the initial R_{HRS}, following two SET conditions. For strong SET condition, stable HRS can be recovered for high initial R_{HRS}.

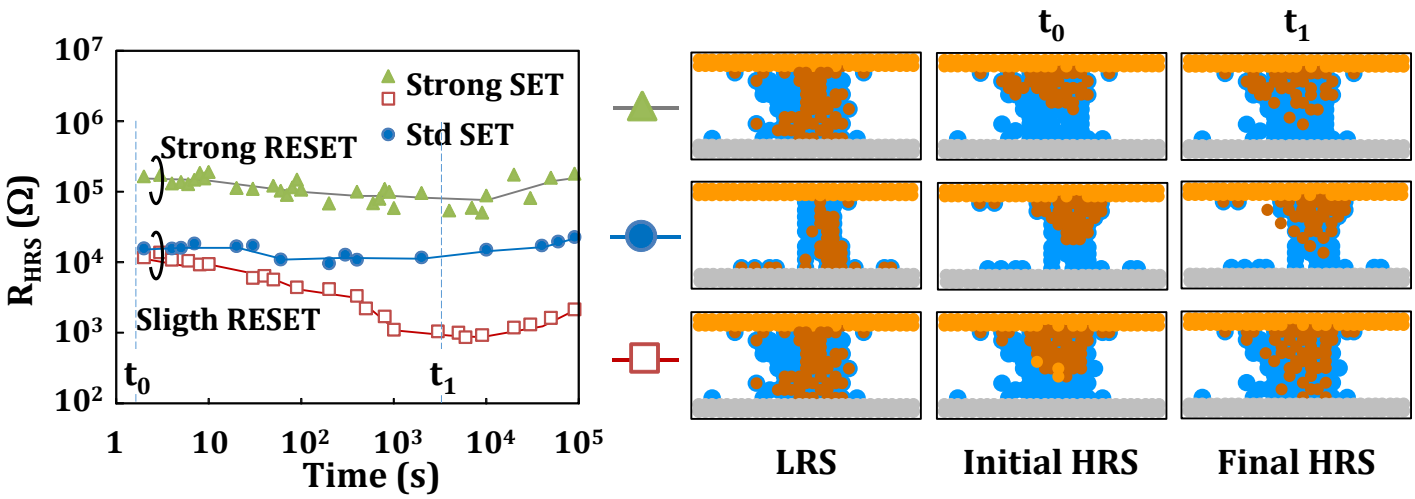

Figure 12. Simulated 100°C HRS retention for various initial filament morphologies. Filament thickness (resp. height) is governed by SET (resp. RESET). The filament shape governs the HRS stability.

retention, either by applying a strong SET and strong RESET or a soft SET and soft RESET, and then reduce the degradation of the retention. Figure 12 reports the simulated filament shape and experimental results obtained on the same nano-Trench samples before and after RESET condition optimization.

Taking advantage of the CBRAM 64 bit matrix with MESA architecture and $CuTe_X/Al_2O_3/TaN$ stack, the resistance distribution after HRS retention has also been addressed. First, the effect of the compliance current during SET on the R_{HRS} post retention dispersion have been studied. Figure 13 shows the R_{HRS} distributions after 24 hours at high temperature (200°C) for the two

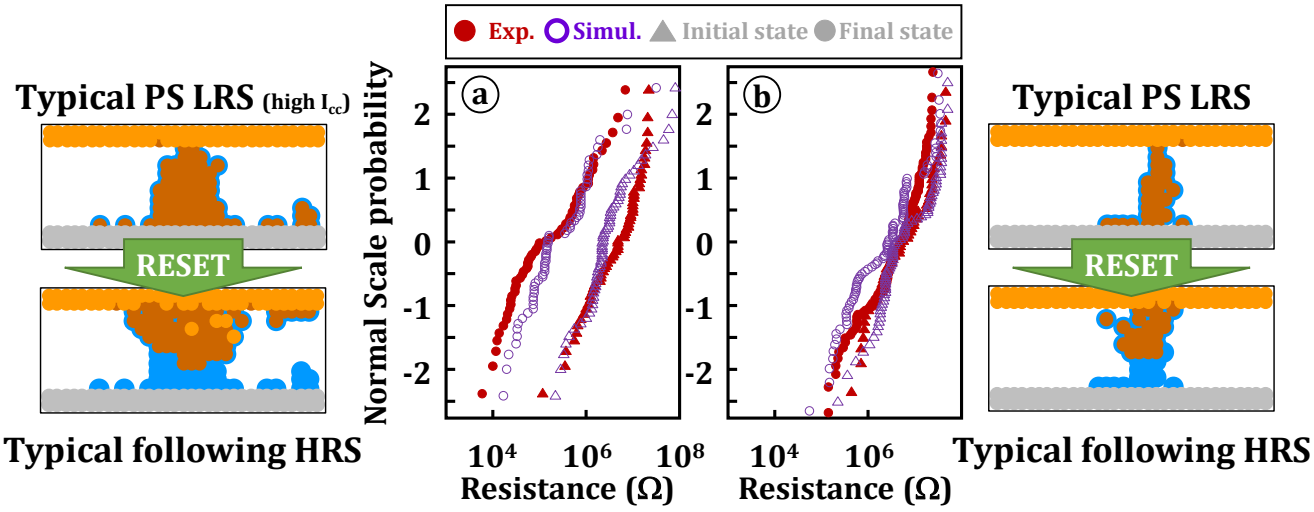

Figure 13. Measured and simulated R_{HRS} distributions before and after bake at 200°C for two previous R_{LRS}: (a) ~9.10^3 Ohms (thick filament) and (b) ~2.10^4 Ohms (thin filament).

programming conditions. The RESET operations are kept identical to neglect the RESET impact on the HRS retention. This figure shows a complete shift of the resistance distribution with a diminution of the mean R_{HRS} post bake at high compliance currents. This observation is in agreement with the previous statement.

Moreover, as stated in the SET analyses chapter IV, the programming conditions also modify the filament morphology which is responsible for the HRS retention capabilities. Consequently, the filament morphology has also been studied in function of the operation mode: QS and PS. PS programming creates a thinner filament than QS programming, which should in theory offer better HRS retention behavior after RESET. To verify this statement, cells have been set using PS and QS programming but with the same LRS resistance target and then reset with the same PS protocol to ensure identical RESET operations. A retention study has then be conducted and the results are shown Figure 14. This figure shows the resistance distributions after 24 hours at high temperature (200°C) for the two programming conditions. As can be seen, the resistance loss induced by a QS programming is much more important than the one induced by the PS programming. The same initial HRS resistance has been taken for both SET programming conditions in order to avoid any influence of the initial resistance value. The difference of retention behavior can then be attributed to the filament morphology and especially to the increase of filament and residual filament thickness induced by the QS programming. In opposition to the behavior pictured in Figure 13, QS programming not only modifies the mean value of the resistance distribution but also its dispersion.

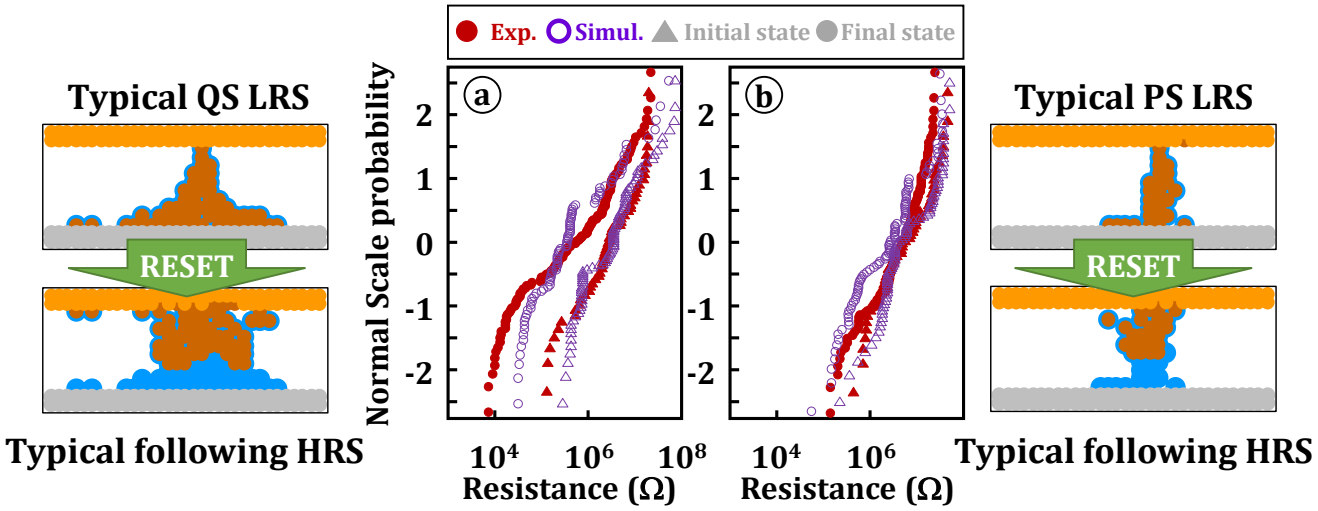

Figure 14. Measured and simulated R_{HRS} distributions for two programming conditions: (a) Quasi-Static forming and SET (thick filament and high V_O concentration) and (b) Pulsed forming and SET (thin filament and low V_O concentration)

Using QS programming induces a strong resistance degradation of the distribution tail as can be seen in Figure 14. The slower filament formation with QS programming induces a stronger filament morphology variability, as exposed in chapter IV. The filament shape variability after QS programming spreads from thin to thick filament which could explain the distribution expansion after retention. Indeed, the few cells showing thin filament after QS programming have good retention capabilities similarly to the one PS programmed. However, with the statistical increase of filament thickness, the retention behavior is degraded and the bad tail behavior appears.

3.1.3 Programming conditions, LRS and HRS synthesis

As exposed in the two previous sections, the CBRAM cells require specific programing conditions in order to offer the best retention capability for both LRS and HRS retentions. The delicate part regarding the programming is that the SET conditions not only affect the LRS retention but also the HRS retention. The main cause of this double impact of the SET operation relies on the filament morphology that remains after RESET through the residual filament. Thus, as stated before, in order to optimize the LRS retention it is important to increase the programming current and reduce the LRS resistance. However, increasing the programming current leads to a thicker filament degrading the HRS retention after RESET. The HRS retention can however be optimized with smart RESET condition but at the cost of higher power consumption and possible cell degradation as seen in the previous chapter. The retention optimization of a cell through smart programming conditions can be seen as a tradeoff between LRS/HRS retention capabilities and power consumption. Thus, strong SET and RESET operations lead to a large window margin and good retention capabilities whereas soft SET and moderate RESET allow a stable retention behavior with lower memory window but lower power consumption. Figure 15 summarizes the possible retention cases in function of the operating conditions experimentally observed and simulated for CuTeGe/Al_2O_3/TiN nano-Trench technology at 100°C.

The HRS retention can also be improved by switching from QS to PS SET. Indeed, the filament being thinner (see Chapter IV) with a PS programming, the recreation of a conductive path is less likely to occur. The QS programming can lead to bad HRS retention as exposed during this section. However, it is possible to recover the CBRAM retention capabilities after a QS Forming by applying a few PS cycle (3 cycles on Figure 16.). This means that the filament morphology does not seem to modify the RL irretrievably. This can be correlated to the resistance drop observed

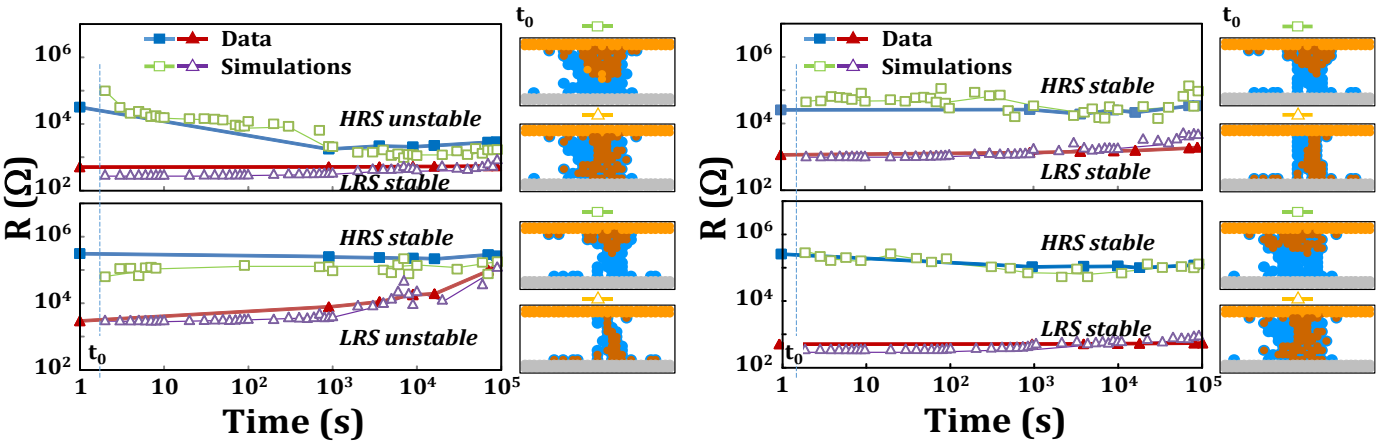

Figure 15. Measured and simulated 100°C LRS and HRS retention curves for non-optimized (left) and optimized (right) SET and RESET conditions. The initial filament shapes before bake are represented in each case. Optimized condition: $V_{RESET} \approx$ - 0.5 V; $V_{SET} \approx$ 0.5 V; $E_{SET} \approx$ 5 pJ (top); $V_{RESET} \approx$ -1 V; $V_{SET} \approx$ 0.9 V; $E_{SET} \approx$ 50 pJ (bottom).

during HRS retention being tied to the R_{LRS} of the preceding cycle but not of the one before, which is also in good agreement with the lack of cycle to cycle variability of LRS.

The KMC simulation coupled with experimental inputs can be used to find optimized operating conditions offering the best retention possible for the targeted applications. A patent [Guy 1] has been proposed based on the comprehensive understanding of the CBRAM data retention and offering easy optimization ways from few experimental inputs. The flowchart followed to optimize the retention behavior taken from the patent is reported in Figure 17. This patent relies on the KMC simulation ability to rapidly simulate all the filament morphology combinations for LRS and HRS

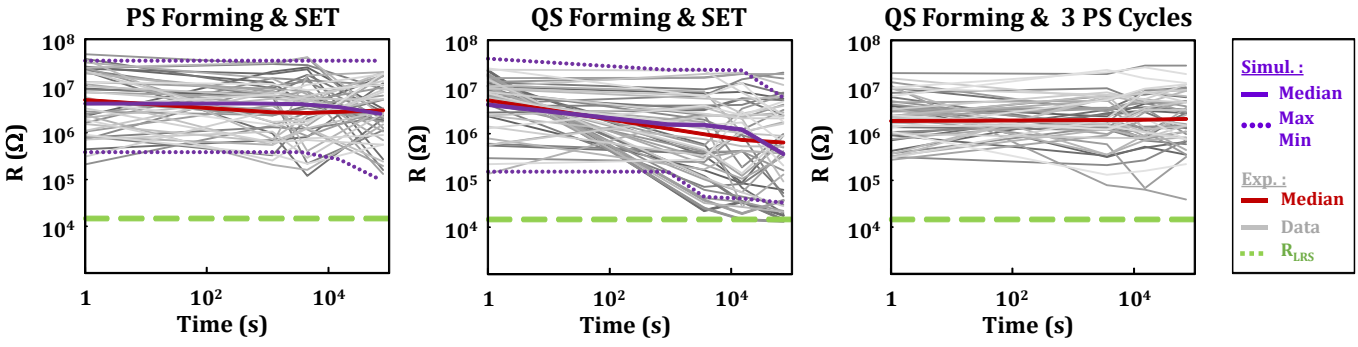

Figure 16. Measured and simulated 200°C retention characteristics for three programming conditions: Pulsed Forming and SET, Quasi-Static Forming and SET and Quasi-Static Forming followed by 3 Pulsed SET/RESET cycles. Results on 64 cells are represented as well as the median trends (thick lines). Pulsed programming improves retention reliability (mean behavior and tails).

retention. Only a few set of experimental SET, RESET and retention characteristics are required to initialize the KMC simulation and more precisely obtain the activation energies ruling the ionic reactions and migrations. After the initial fitting of SET/RESET and retention of the CBRAM cell, it is possible to extract the expected retention behavior in function of the temperature and operating conditions. Similarly to Figure 9 (b), R_{LRS} values after 10^5 second at 200 °C can be simulated in function of the programming current. These data, coupled to the simulated R_{HRS} values after 10^5 second at 200 °C reported in Figure 18, offer the possibility to obtain the window margin after data retention reported in Figure 19. Then, depending on the targeted margin, operating conditions can be chosen according to the requirements.

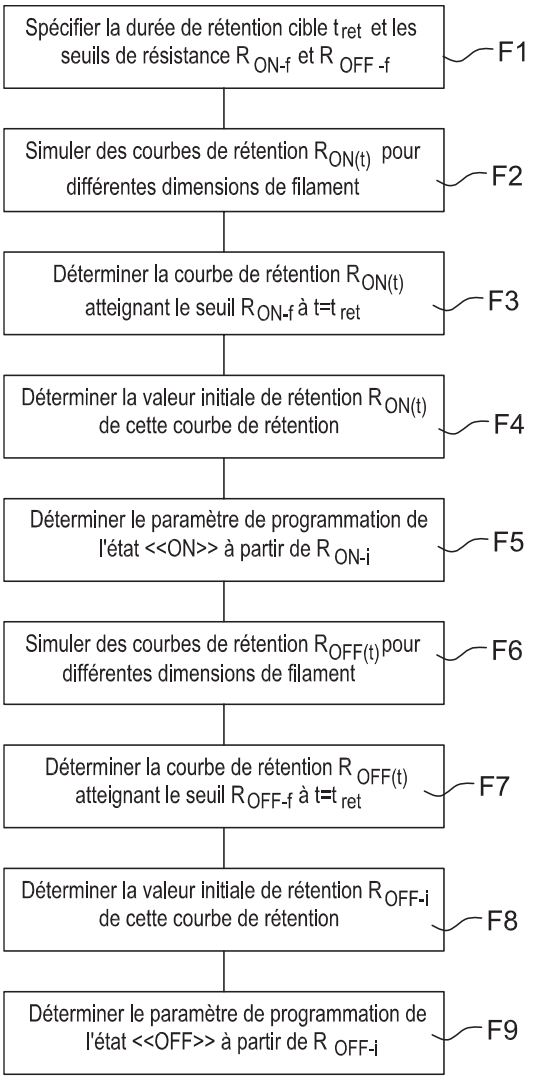

Figure 17. Flowchart of the optimization steps (extracted from the French patent)

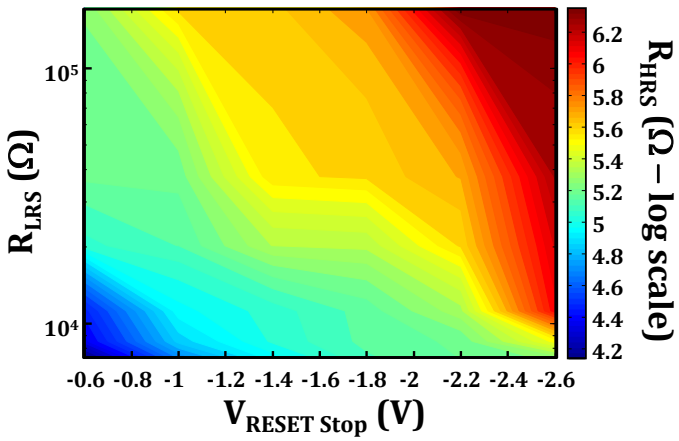

Figure 18. Simulated R_{HRS} after 24h at 200°C depending on both SET and RESET conditions

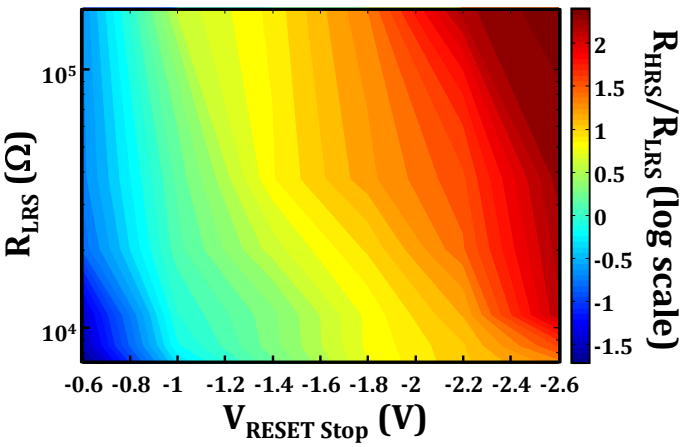

Figure 19. Simulated memory margin after 24h at 200°C depending on both SET and RESET conditions

3.2 Resistive layer material optimization

As exposed previously in this chapter, the LRS and RHS degradation is due to the dissolution of the filament or residual filament inside the RL. This dissolution occurs in one or two steps depending on the conductive atoms state (ionized or not) in the RL. The atoms have to be ionized to migrate and the migration has to be easy enough to occur at the studied temperature. A way to improve the retention stability is then to focus on stabilizing the conductive atom coming from the top electrode inside the resistive layer, either by favoring their reduced state or by increasing the migration activation energy. This optimization can be directly addressed by smartly choosing the TE and RL materials, but it is also possible to improve the retention behavior of a given TE/RL couple. The following results are based on VIA devices (Chapter II) with Ag/GeS_2 – Sb dopped/TiN stack. As stated before this technology based on chalcogenide is immune to HRS degradation, this study has then been focused on the LRS retention behavior. However, the HRS degradation relying on the same physical mechanisms as the LRS, these results might be extrapolated to HRS degradation in the case of a residual filament in the RL.

For this study, the GeS_2 RL has been doped with various concentration of Sb (10 – 20%) whose role is to stabilize the conductive filament. The first sign of the stronger filament stability can be seen during the SET and RESET operation. Using the same RESET QS conditions, the cells have been SET with a progressive increase in compliance current leading, as expected, to a decrease of R_{LRS}. An optimized window can be seen Figure 20 (a) and corresponds to the current margin in

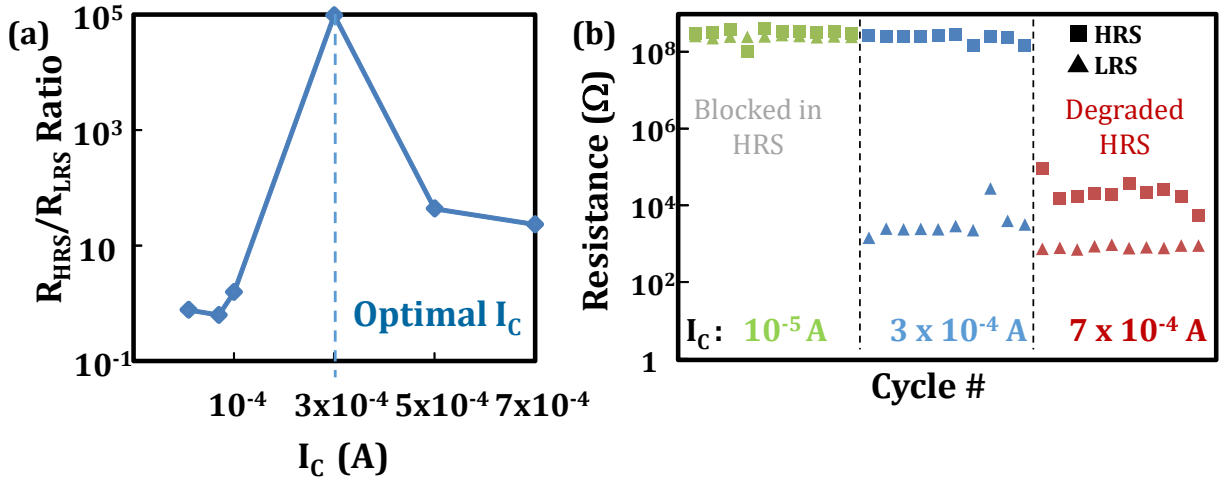

Figure 20. (a) Evolution of the memory windows in function of the compliance current. (b) Switching behavior around the optimal compliance current of $3x10^{-4}$ A. Both results have been obtained on the reference sample (0% Sb)

which the cell can be correctly SET and RESET. For programming current lower than the optimal I_C the cell is blocked in HRS and the filament is not stable after SET, thus the cell does not store the data. For programming current higher than the optimal I_C the filament is too stable to be dissolved and the HRS is degraded (Figure 20 (b)). Figure 21 shows that the optimized programming current window is modified towards lower current for high Sb concentration. This means that the higher the Sb concentration, the harder it is to RESET the cell for the same R_{LRS}. This behavior can be tied to an increased stability of the conductive atoms (Ag) with Sb doping. Indeed, referring to Chapter IV, the RESET operation is tied to the filament stability under the influence of heat generation and applied voltage. From Figure 21 it is possible to extract an optimal compliance current at which the CBRAM performs the best and offers the best memory window for each Sb composition.

As stated before the LRS retention is strongly tied to the initial resistance value of the state. In order to avoid the effect of the initial resistance, the retention capabilities of all samples were firstly tested with a fixed initial resistance around 40 kΩ. Figure 22 (a) gives the result of this experimental study showing a great improvement in data retention study with an increase of almost two decades after 24 hours at 130°C between 10% Sb – doping and 20 %. This clearly illustrates an increase of thermal stability of the filament with an augmentation of Sb doping. Another interesting aspect of the retention behavior can be seen while comparing the samples retention at their respective optimal LRS state. This time the initial resistance is not the same anymore, the

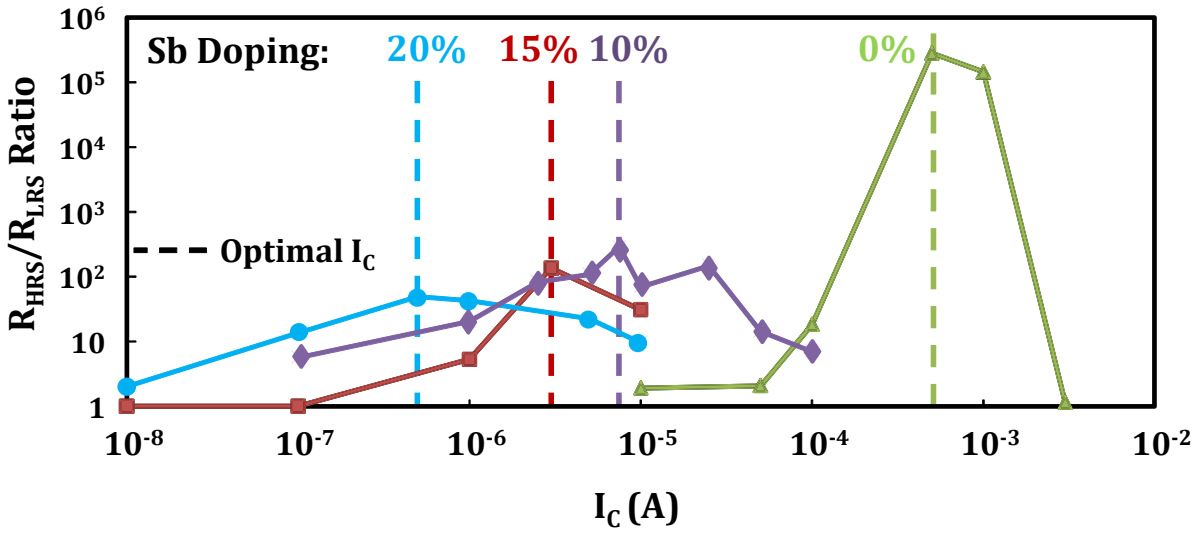

Figure 21. R_{HRS}/R_{LRS} ratio versus compliance current for the three Sb doping showing a shift of the optimal current with the doping concentration.

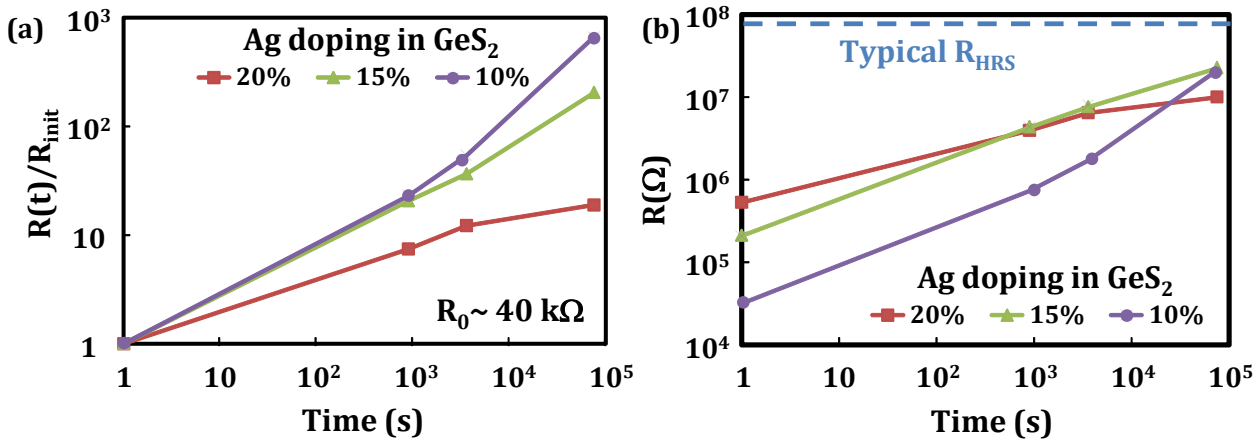

Figure 22. (a) LRS retention behavior at 130 °C for the three Sb concentrations in GeS_2 RL starting from the same initial R_{LRS}. (b) LRS retention behavior at 130 °C for the three Sb concentrations starting this time from the optimal compliance current.

lower the Sb content, the lower the initial resistance in agreement with the increase of optimal compliance current. This means that the filament morphology is also greatly modified with thin filament for high Sb content and thin filament for low Sb content. However, despite the great impact of filament morphology on the retention capability, the high Sb content samples still shows the best retention capabilities (Figure 22 (b)). The increase of stability induced by the Sb doping allows to overcome the retention loss that should induce a thin filament. This means that the Sb doping not only improves the stability at same LRS but also offers a way to reduce the required current to stabilize the LRS retention leading the lower power consumption.

To understand this statement, ab – initio calculations were performed, using the Density Functional Theory with SIESTA code by the CEA simulation lab and E. Vianello [Vianello 1]. A silver filament has been simulated by inserting 2 mono-layers of Ag atoms in a Sb-doped GeS_2 matrix. The time evolution of the filament dissolution was simulated by high temperature molecular dynamics: the spread of the silver distribution in GeS_2 over time has been calculated with and without Sb in the GeS_2 electrolyte. In particular, from the Ag distribution the standard deviation σ which quantifies the Ag spread in GeS_2 is computed in Figure 23. Figure 23 shows the extracted σ value as a function of the baking time. It can be seen that with Sb-doped GeS_2, the Ag diffusion is slower which can be correlated to the improved thermal stability of GeS_2 (Sb) CBRAM. The diffusion of Ag is due to the formation of Ag_2S complexes that migrate through the matrix. S preferentially bonds with Sb over Ag, therefore doping the GeS_2 with Sb reduces the formation of

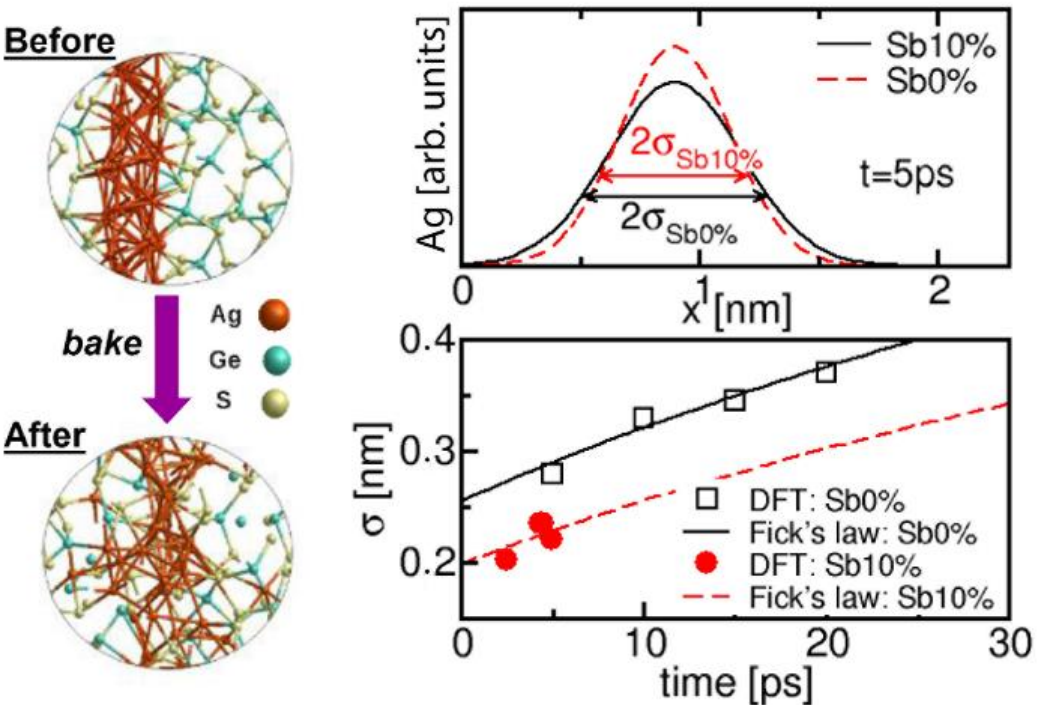

Figure 23. Ab initio calculation of a silver based filament dissolution in the GeS_2 (Sb doped) matrix and calculation of Ag distribution after 1000 °C bake 5 ps [Vianello 1].

Ag_2S complexes responsible for the filament dissolution and ultimately improves the data retention.

3.2.1 Optimization synthesis

Throughout the data retention study, several samples have been characterized and analyzed. Among these samples two technological paths have been studied: chalcogenide and oxide based resistive layer. The first study has been focus on chalcogenide (GeS_2) RL before transitioning to oxide RL in order to improve the data retention capabilities. The memory stack Ag/GeS_2/W showed limited retention behavior with the complete loss of LRS at 130°C for 24 hours. However, by doping the RL with Sb it has been possible to greatly improve the retention capabilities with a memory margin higher than one decade after 24 hours at 130°C. Moreover, the strength of this device is the very low power consumption with programming current of 5 µA leading to a R_{LRS} around $10^6\,\Omega$ which also reduces the power consumption during RESET (Figure 20). To improve the retention behavior, oxide based RL have been introduced, starting with Al_2O_3. The initial memory stack build around this oxide is CuTeGe/Al_2O_3/TiN. After optimizing the operating conditions, it have been possible to obtain two stable behaviors: either a reduced power

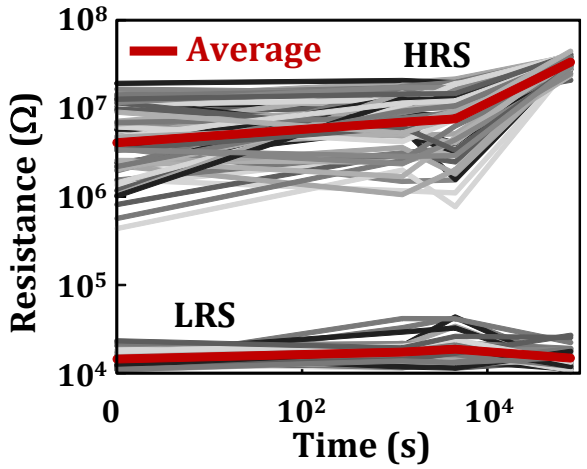

Figure 24. Data retention behavior of $CuTe_X/Al_2O_3/TaN$ devices after 24 hours at 200°C

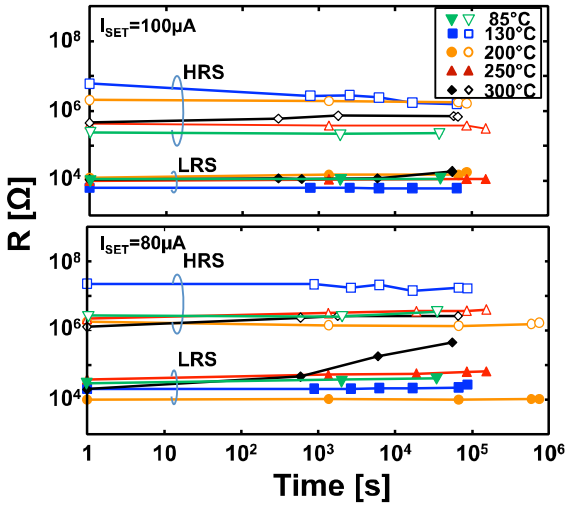

Figure 25. Data retention behavior obtained on oxide based CBRAM devices at various temperature and operating conditions [Barci 1].

consumption programming leading to more than one decade of memory margin after 24 hours at 100°C or strong operating conditions offering almost three decades of memory margin after 24 hours at 100°C (Figure 15). However, both programming conditions show higher power consumption than the $Ag/GeS_2/W$ devices with respectively R_{LRS} around $10^3\ \Omega$ and $3x10^2\ \Omega$. In order to enhance the stability at higher temperature, a $CuTe_X/Al_2O_3/TaN$ stack have been developed and studied. These samples, only show a slight improvement over the previous one with the loss of the LRS for 50% of the cells after 24 hours at 200°C. However, similarly to the improvement obtained on Sb doped chalcogenide RL, it has been possible to greatly increase the thermal stability by doping the Al_2O_3 RL with an overconcentration of Al. This technological optimization coupled with smart programming conditions allowed to obtain more than three decades after 24 hours at 200°C (Figure 24). These samples correspond to the most stable samples characterized during this research work. Nevertheless, following the same operating conditions optimization offered by the KMC simulation, a joint study has been carried out with M. Barci to find the best memory margin possible for a metal-oxide (confidential composition) based CBRAM. With adapted operating conditions and especially smart RESET targeting precise R_{HRS} values, these devices offered more than 2 decades of memory margin after 24 hours at 300°C as shown in Figure 25. Table 1 compiles the operating conditions and the retention capabilities of the previous devices. It can be seen that pure Al_2O_3 based CBRAM does not offer great retention capability. However, the intensive study

Table 1. Performance synthesis of the studied devices.

Memory stack (TE/RL/BE)	Programming Current (LRS control)	RESET voltage (HRS control)	R_{LRS}	R_{HRS}	Retention capabilities
$Ag/GeS_2/W$	100 µA – 1 mA	- 1 V	$10^2 – 10^3\Omega$	$\approx 10^8\,\Omega$	Fail at 130°C for 24h
Ag/GeS_2-Sb/W	5 µA	- 1 V	$10^5 – 10^6\Omega$	$\approx 10^8\,\Omega$	≈ 2 decades at 130°C for 24h
$CuTeGe/Al_2O_3/TiN$	100 µA	- 0.5 V	$10^3\,\Omega$	$>10^4\,\Omega$	> 1 decades at 100°C for 24h
	1 mA	- 1 V	$3x10^2\,\Omega$	$>10^5\,\Omega$	≈ 3 decades at 100°C 24h
$CuTe_X/Al_2O_3/TaN$	50 µA	- 2 V	$10^4 – 10^5\Omega$	$10^6 – 10^8\Omega$	50% fails at 200°C for 24h
$CuTe_X/Al_2O_3$-Al /TaN	50 µA	- 2 V	$\approx 10^4\,\Omega$	$10^6 – 10^7\Omega$	> 3 decades at 200°C for 24h
Metal oxide based	80 µA	Smart RESET	$\approx 10^4\,\Omega$	$\approx 10^6\Omega$	≈ 2 decades at 300°C for 24h

of devices build around this oxide allowed a deep understanding of the retention mechanisms and the development of optimization ways applicable to other oxides resistive layers.

4. Chapter VI synthesis

This chapter presented the physical mechanisms involved during LRS and HRS retention fail. Depending on the CBRAM technology the cell might be subject to LRS retention failure only or both HRS and LRS retention failure. Both states degradation with time are due to the dissolution of the conductive filament for LRS, or residual filament resulting of RESET operation for HRS. This dissolution leads to a resistance variation depending on the state.

During LRS retention, the dissolution of the filament occurs in two steps: first the dissolution of the core of the filament and then the homogenization of the conductive atoms in the RL. The dissolution of the filament induces a transition from an electrical conduction close to bulk conduction to a Trap Assisted Tunneling which results in an increase of resistance and loss of LRS. The state degradation speed is tied to the filament morphology and migration energy barrier height of the conductive atoms: the higher the energy the best the retention. Regarding the HRS retention, the state degradation is also tied to the dissolution of the residual filament. However, this dissolution can influence the resistance level in two ways. The vertical diffusion of the atoms composing the filament tends to recreate a conductive path whereas the lateral diffusion leads to the complete dissolution of the filament. These diffusions occur in the same time but the dominant one will be responsible for the retention behavior. The vertical diffusion will then lead to the loss of HRS but the lateral diffusion to an increase of the resistance level. The dominant behavior of

one or the other diffusion mechanism is tied to the filament morphology and RL degradation: a thick or tall residual filament will lead to a dominant vertical diffusion whereas a thin or short one will lead to a dominant lateral diffusion. Moreover, the oxygen vacancies location in the RL might also enhance one of these diffusion. Similarly to the LRS retention, the degradation speed of the state is tied to the activation energy of the conductive atoms migration mechanisms.

From the knowledge of the mechanisms responsible for the retention failure, optimization ways have been proposed in term of operating conditions and integrated materials. The filament morphology being a crucial parameter of the retention capabilities, it is important to optimize the programming conditions to offer the best tradeoff between at thick filament for LRS retention but not too thick and sufficiently erased for HRS retention. Using programming conditions optimization actually consist in finding the best tradeoff between both state retention and power consumption. However, by tuning the material properties and especially the migration energy barrier height, it is possible to greatly improve LRS and HRS retention. It has accordingly been demonstrated that doping the RL with Sb or Al induces a better filament stability and improves the retention behavior. Finally, a patent relying on the KMC simulation has been proposed to offer optimized operating conditions based on the targeted memory margin.

Chapter VI references

[Barci 1] Barci, M.; Guy, J.; Molas, G.; Vianello, E.; Toffoli, A.; Cluzel, J.; Roule, A.; Bernard, M.; Sabbione, C.; Perniola, L.; De Salvo, B., "Impact of SET and RESET conditions on CBRAM high temperature data retention," in Reliability Physics Symposium, 2014 IEEE International , vol., no., pp.5E.3.1-5E.3.4, 1-5 June 2014

[Guy 1] Guy. J, G. Molas, “METHOD FOR DETERMINING ELECTRICAL PARAMETERS USED TO PROGRAMME A RESISTIVE RANDOM ACCESS MEMORY,” US Patent 20150162081, Jun. 11, 2015.

[Hsieh 1] Min-Che Hsieh, Yung-Wen Chin, Yu-Cheng Lin, Yu-Der Chih, Kan-Hsueh Tsai, Ming-Jinn Tsai,Ya-Chin King and Chrong Jung Lin, “A new laterally conductive bridge random access memory by fully CMOS logic compatible process,” Japanese Journal of Applied Physics, Vol. 53, Num. 4S, Mar. 2014.

[Longnos 1] Longnos, F.; Vianello, E.; Molas, G.; Palma, G.; Souchier, E.; Carabasse, C.; Bernard, M.; De Salvo, B.; Bretegnier, D.; Liebault, J., "On disturb immunity and P/E kinetics of Sb-doped GeS2/Ag conductive bridge memories," in Memory Workshop (IMW), 2013 5th IEEE International , vol., no., pp.96-99, 26-29 May 2013

[Vianello 1] Vianello, E.; Molas, G.; Longnos, F.; Blaise, P.; Souchier, E.; Cagli, C.; Palma, G.; Guy, J.; Bernard, M.; Reyboz, M.; Rodriguez, G.; Roule, A.; Carabasse, C.; Delaye, V.; Jousseaume, V.; Maitrejean, S.; Reimbold, G.; De Salvo, B.; Dahmani, F.; Verrier, P.; Bretegnier, D.; Liebault, J., "Sb-doped GeS2 as performance and reliability booster in Conductive Bridge RAM," in Electron Devices Meeting (IEDM), 2012 IEEE International, pp.31.5.1-31.5.4, 10-13 Dec. 2012

Chapter VII. Synthesis and perspective

1. Objectives

Throughout this research work, the joint study of the KMC model and physical characterization has offered a great way to understand the physical mechanisms involved in the CBRAM operation. The technical understanding of the CBRAM keeps improving, leading to very high density integration [Zahurak 1]. However, a global physical understanding of the mechanisms hidden behind the devices operation is still lacking. This research work aims to offer a first approach to this global understanding by creating a bridge between the physical parameters of the materials composing the device and its electrical characteristics. Crucial physical mechanisms to the CBRAM understanding have been exposed and allowed to address endurance as well as data retention limitations. From the understanding of the CBRAM operations, optimizations have been proposed to improve the CBRAM global performances.

This last chapter will be organized around a synthesis of the mechanisms involved in the global CBRAM operation. The CBRAM optimization will be discuss in term of programming conditions and technological trade off. Finally, to conclude this work, the limitation of the current understanding will be discussed and improvements proposed.

2. Technological and operating conditions optimizations

Throughout the CBRAM global behavior study optimizations has been proposed to address precise characteristics of the CBRAM. These optimizations, in term of technological improvements or operating conditions adaptations were developed to address specific aspects of the CBRAM behavior. However, the perfect CBRAM device has not been developed yet and tradeoff have to be found depending on the targeted application.

Starting from the Forming operation, optimizations have been proposed to enhance the speed and energy efficiency of this step by modifying the material stack. Indeed, by changing the bottom electrode of a reference sample Cu/Al_2O_3 (5 nm)/WSi by TiN, it has been possible to reduce the forming voltage by almost 2V from 6.5 V to 4.75 V. This sample still showing high required energy, has been optimized one step further with the introduction of MO_X used as resistive layer. With this material, the Forming voltages have been reduced to 2.4 V. Thanks to its high electrical

permittivity and low density deposition, this resistive layer offers a great time versus voltage characteristic with a forming time reduction of 8 decades per volt, compared to the 2 decades per volt of Al_2O_3 samples. SET voltages have been tied to the HRS and the residual filament height. The taller the residual filament and higher the R_{HRS} and the V_{SET}. A range of SET voltage from 0.2 V to 1.4 V have been obtained for R_{HRS} varying from 10^4 Ω to 10^6 Ω on $CuTe_X/Al_2O_3/TiN$ samples. However, these two optimizations of Forming and SET operations also induced a degradation of the HRS with low R_{HRS} (around $3x10^4$ Ω) for TiN or MO_X based cells. The RESET operation shows a strong dependence with the temperature repartition in the CBRAM cell. By changing the thermal conduction equilibrium between electrodes and resistive layer, it is possible to modify R_{HRS} and V_{RESET}. Changing the bottom electrode from WSi to TiN in order to improve the Forming behavior also changed the thermal conduction equilibrium. Due to the lower thermal conduction of TiN, V_{RESET} decreased from -0.5 V to -0.2 V but R_{HRS} also decreased from 10^6 Ω to $3x10^4$ Ω. This observation illustrates the tradeoff impacting the CBRAM technologies. However, with advanced optimizations it is possible to overcome this tradeoff. Regarding RESET operation and HRS, it has been possible to combine both the low Forming voltage of MO_X samples with high resistance level after RESET. By introducing a thin (1 nm) second resistive layer made of HfO_2, R_{HRS} increased up to $3x10^5$ Ω from $3x10^4$ Ω without modifying the Forming improvements induced by MO_X.

The majority of oxide based CBRAM studied here showed their best behavior with programming current around 10^{-4}A and R_{LRS} between 10^3 and 10^4 Ω. Nonetheless, using a chalcogenide (GeS_2) resistive layer coupled with silver top electrode offers great memory margin with R_{LRS} and R_{HRS} respectively at 10^3 Ω and 10^8 Ω for a writing current of 10^{-4}A. Doping GeS_2 resistive layer with Sb allows to greatly reduce the power consumption at the cost of a smaller memory margin. Indeed, R_{LRS} and R_{HRS} are respectively at 10^6 Ω and 10^8 Ω for a writing current of 10^{-6}A with 20% Sb doping, showing another sign of tradeoff.

Finally both SET and RESET operation are impacted by the active zone confinement. The nano - Trench architecture scaling showed great results with a reduction of SET time by 5 decades at 0.8 V between the 10 nm and 40 nm liner on $CuTe_X/Al_2O_3/TiN$ samples. 10nm devices yields a SET time of ~70ns.

The Data retention study has shown a strong correlation between LRS and HRS behavior. LRS retention is tied to the initial R_{LRS} whereas HRS retention is tied to the initial R_{HRS} but also to the anterior R_{LRS}. Regarding the LRS retention, the lower the R_{LRS} the better the LRS retention but a

R_{LRS} too low can also degrade the HRS retention. To overcome the HRS retention degradation induced by a R_{LRS} too low, a strong RESET operation is required. The retention of both states has to be considered as a tradeoff and programming conditions have been proposed to offer either low power consumption with limited memory margin after retention or higher power consumption and higher memory margin. Based on $CuTe_X/Al_2O_3/TiN$ samples, it was possible to obtain either 1 decade or 3 decades at 100°C for 24 hours for respectively a programming current of 100 µA or 1m A and RESET voltages of -0.5 V or -1 V. Using material optimization such as resistive layer doping combined with smart programming conditions, it was also possible to enhance the retention behavior in both oxide and chalcogenide based CBRAM. GeS_2 Sb doped resistive layer showed 2 decades of memory margin after 24 hours at 130°C whereas Al_2O_3 Al doped showed more than 3 decades after 24 hours at 200°C, in agreement with the better thermal stability of the oxides.
Another great concern regarding the CBRAM technology is the endurance and reliability of the devices. To offer high density storage, the variability has to be restrained as much as possible. The LRS and HRS variability have been studied. The LRS only shows intrinsic variability tied to the programming current whereas HRS shows intrinsic variability coupled to cycle to cycle variability. Using 64 bits matrix, it has been demonstrated that the lower the programming current the wider the LRS resistance dispersion. In order to offer the best endurance possible it is essential to limit the energy brought to the cell as much as possible during SET and RESET. Using smart programming routines based on successive programming pulses with incrementing energy offers the best way to improve the endurance.

3. Physical interpretations, discussion and perspectives

Throughout this manuscript, the physical mechanisms involved in the CBRAM operation have been exposed. This section will take advantage of the complete analysis of the CBRAM operations to propose extended hypotheses on the CBRAM behavior. The comprehensive impact of all the mechanisms on the CBRAM operation as well as the materials physical properties involved in these mechanisms will be discussed.

3.1 Filament morphology, the heart of the CBRAM operating

The filament morphology can be seen as the missing link between the CBRAM macroscopic behavior and the physical mechanisms involved at atomic level. The KMC model,

coupled to specific electrical characterizations offered some insight regarding the filament shape and its great impact on the global CBRAM behavior.

The filament shape depends on many parameters and operating conditions. The migration speed of the conductive ions in the RL has an impact on the filament shape: an easy and fast migration speed leading to a thick filament basis. The migration speed joint to the aggregation mechanism are part of the filament thermal stabilization during SET. Indeed, joule heating leads to the generation of a high energy quantity that has to be dissipated to stabilize the filament. The thermal dissipation depends of the global heat conduction of the system and especially of the two electrodes which are the CBRAM parts the most thermally conductive. The filament shape is then directly correlated to the thermal conduction of the electrodes: the filament thickness increases as the electrodes thermal conduction decreases in order to extend the thermal exchange surfaces. The shape of the residual filament after RESET also depends on the thermal conduction of the system. The thermal equilibrium between both electrodes controls the location of the highest temperature point which corresponds to the filament disruption point. Modifying the location of this point changes the finale residual height and thickness of the filament. The filament morphology is also modified by the oxygen vacancies that acts as favored migration path for the conductive ions.

In term of electrical characteristics, the filament and residual filament morphologies control the resistance level of both HRS and LRS. The resistance level of LRS decreases as the filament thickness increases, allowing more current to flow through the cell. Regarding the HRS, the resistance level depends on both the residual height and thickness: the taller and larger the residual filament, the lower the resistance level. The filament morphology is thus tied to the resistance level. However it is important to note that different morphologies can lead to the same resistance. The controlling factor of the resistance level is the constriction part of the filament, the rest of the filament having no strong impact on the current flow limitation. The global morphology of the filament can thus be modified by the programming conditions without modifying the resistance level. PS programming allows globally thinner filaments than QS programming: the higher the pulse voltage and shorter the time, the thinner the filament. This is one of the reason behind the complexity of the CBRAM electrical characterization as it is impossible to know the filament shape based on the sole resistance level. This is much more damaging as the filament shape is involved in several degradation mechanisms. Indeed, the filament morphology is responsible for the data retention degradation: a thick filament leads to a good LRS retention but a bad HRS retention

unless the residual filament is strongly dissolved. In opposition, a thin filament induces a strong HRS retention but degraded LRS one. The filament shape is also involved in the LRS and HRS variability, indeed, the intrinsic variability of both states are due to different ions reorganization during switching leading to different filament shapes and resistances. The LRS shape variability is also in part responsible for the HRS cycle to cycle variability by modifying the RESET effectiveness to dissolve the filament. The filament shape and ions reorganization is finally also responsible for the memory window degradation during cycling. A filament too thick degrades the RL and makes filament difficult to erase leading to progressive loss of HRS whereas a residual filament too short can lead to the impossibility to recreate a filament and the abrupt loss of LRS.

3.2 Conductive atoms stability in the resistive layer

The CBRAM operations revolve around the formation and dissolution of a conductive filament. The atoms composing this filament come from the oxidation of the TE making the redox reactions the basis of the CBRAM technology. The stability in the RL of the conductive atoms coming from the TE is of great concern and especially under which form (ionized or reduced) they stay stable. This information can be extracted from ab – initio calculation [Sakamoto 1, Todorova 1] as shown in Figure 1. Depending on the RL crystallinity and composition the conductive atoms can either be stable, ionized or reduced. In the γ - Al_2O_3 case, this figure shows the systematic ionized state of Cu with Cu^+ and Cu^{2+} much more energetically favorable.

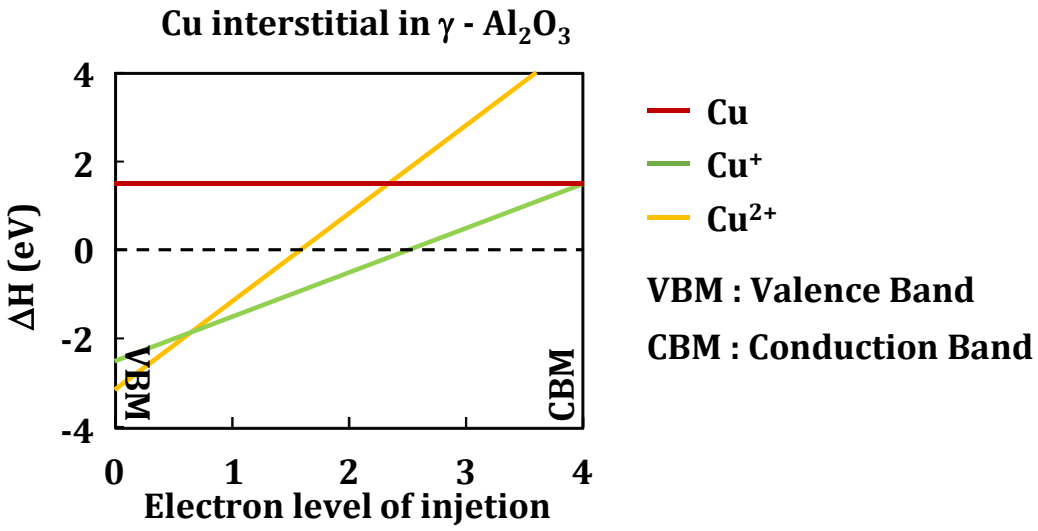

Figure 1. Formation enthalpies of the three Cu state in Al_2O_3 in γ state.

Depending on the energy level of the electrons injected the ionized state might vary especially around the Valence Band but globally the most favorable state is Cu^+. It is important to note that this representation is only correct for low Cu concentration in the Al_2O_3 matrix and other calculations are required depending on this concentration. Aggregations could greatly reduce the energy level of reduced Cu.

It is difficult to verify the ionized or reduced form of the atoms composing the filament, using microscopic observation. However, by taking advantage of the global understanding exposed in this manuscript, it is possible to propose a hypothesis concerning the ionized or reduced form of the conductive atoms. The first insight comes from the retention study. Indeed, the energy required to move reduced atoms instead of ionized one is generally too high. By making the hypothesis that the atoms are reduced during the programming operation, the dissolution of the filament over time is only possible if the atoms are ionized first. It is important to note that this hypothesis is made by considering that the physical mechanisms involved during the thermally accelerated retention study and the non-accelerated retention are the same. In other words, the accelerating temperature is low enough to not generate parasitic mechanisms, which is actually the basis of the thermally accelerated data retention study. This means that a self-ionization of the atoms has to occur over time and due to the negligible energy brought to the system during retention, which can only be explained by an unstable state of the reduced form. This discordance between the initial hypothesis being the stable reduced form after programming but the unstable reduced form required to the retention loss bring up inquiries regarding the stable atom form after programming. To confirm the original hypothesis, the atoms have to be reduced and stable during programming condition but unstable at rest. Translated in term of electrical and thermal conditions, this means that the reduced form must be stable and favored at high energy (high current, voltage and temperature during programming) but unstable at rest and low energy. Theoretically this situation might be envisaged and with enough energy in the system, reduced Cu can exist in Al_2O_3 matrix. However, this seems unlikely considering the SET and RESET behavior. Both these operations involve a high level energy, which should stabilize the reduced atoms form to confirm the initial hypothesis. This stabilization of the reduced form is in complete opposition to the RESET requirement which is to dissolve the filament. It seems then impossible to have a stable reduced form for the atom composing the filament at high temperature and voltage as it would make the filament dissolution impossible. The possibility to achieve a unipolar cycling using positive voltage finally confirm that

a high level of energy cannot in the same time stabilize and unstablize the reduced form of the filament atoms. Consequently the atoms composing the filament should generally remain ionized in the RL.

The atom stability can be improved by the formation of aggregate favoring the conductive atoms reduction at high concentration. The conductive atoms surrounded by their peers could create an aggregate and limit the migration impact. The stability of the filament during RESET and retention might come from this aggregation. The atom aggregates might also facilitate the temperature diffusion and reduction during SET to stabilize the filament. The aggregates dissolution during RESET or retention induces a loss of stability of reduced atoms in agreement with the previous statements.

The atoms and filament stability has a great impact on the global functioning of the CBRAM. It is responsible for the Forming speed and voltage as the oxidation reaction is the limiting factor but is also involved in the SET, RESET and retention capabilities through the aggregation dissolution. This atoms stability greatly depends on the materials composing the CBRAM stack. A change of TE composition even while keeping the same atom base can lead to a stability modification. For example Figure 2 shows the Forming voltage difference for two different TE: pure Cu versus $CuTe_X$. The resistive layer material also plays a great role in the filament stability with the great example of the transition from chalcogenide to oxide base resistive layer to improve the thermal stability. Finally, the stability might also be indirectly modified by the BE or other materials capping the cell due to some constituents migrating into the RL and modifying its composition.

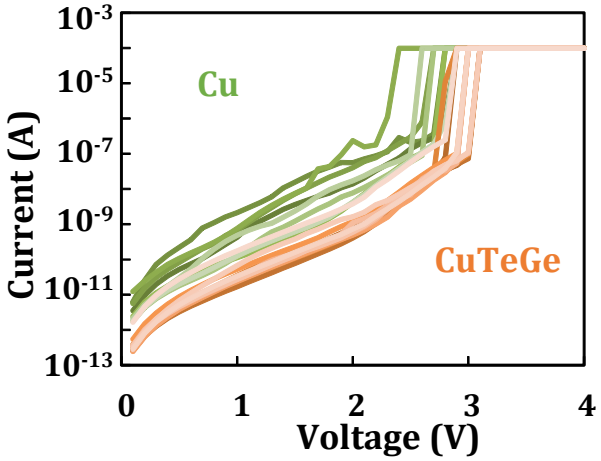

Figure 2.Forming characteristics for two different top electrode compositions.

Regarding the material physical parameters implemented in the KMC model the redox reactions relies on the reaction activation energy but also the energy level of the atom and ions in the RL. The aggregation is also controlled by an activation energy regulating the atom extraction from the aggregates.

3.3 Conductive ions migration in the resistive layer

Once the ions are generated from the top electrode, thanks to the oxidation reaction, they have to migrate through the electrolyte to create the filament. The ions migration can be seen as a behavior in complete opposition to the atom and filament stability including the aggregates formation. The ions migration directly modifies the state of the cell and is taken advantage of during SET and RESET. However, the ion migration also bring one of the CBRAM limitation: the data retention degradation and the CBRAM behavior at high temperature.

The migration is not the limiting factor when ion generation is required. Indeed, it has been shown that the migration speed is much higher than the redox reaction speed. This means that during Forming, only the generation is ruling the system dynamics, whereas during SET and RESET the migration is the limiting factor as the generation of new ions is generally not required.

A high migration speed is responsible for a fast SET but also plays a role during the RESET operation. Fast migration allows a better and more homogenous dissolution of the filament, leading to a higher resistance level. As expected this is a great advantage for the memory window but this can deteriorate the data retention capabilities. Indeed, the ions migration is responsible for the homogenization of conductive atom in the RL during retention. The impact of the migration in the RESET and retention has been shown using Sb doping to reduce the migration speed, inducing a degradation of resistance level after RESET but also an increased retention behavior.

The migration speed is one of the many tradeoff impacting the CBRAM and affect in opposite way the cycling characteristic and the retention ability.

In the KMC model the migration is controlled by an activation energy following as the others physical mechanisms the transition state theory. This migration can be impacted by preferential sites such as aggregates or oxygen vacancies. The model also shows that a modification of the migration energy could results in variation of the filament morphology.

3.4 Oxygen vacancies in the resistive layer.

Oxygen vacancies were the last improvement added to the KMC simulation after a study showed their crucial impact on the CBRAM operations [Molas 1].They are considered as essential to describe the ions migration. The oxygen vacancies generally come from the electrodes and migrate similarly to the ions inside the RL. It is energetically more favorable to firstly insert and displace vacancies and then ions than just ions. Once inserted inside the resistive layer they act as favored migration path for the ions. These vacancies can be electrically observed by applying a reverse forming with negative bias on the TE. This reverse forming [Molas 1] slightly reduces the resistance level by creating a vacancies path between the electrodes. Then, by applying a positive bias on the TE, the first true forming appears at much lower voltage, afterward the cell shows the same global behavior. This proves that oxygen vacancies create a favored migration path for the ions but also reduces the RL resistance.

The vacancies play a great role in every operations of the CBRAM. During SET and RESET they facilitate the ions migration in a given path but also restrain the ions homogenization in a confined area around the filament. This has been observed during the endurance study: the filament confinement facilitates the ions reorganization during SET and reduces the need for new ions oxidation which ultimately leads to an endurance improvement. However, as several aspect of the CBRAM, this comes as a trade off with the retention behavior and especially the HRS retention. Indeed, the HRS degradation during retention is tied to the recreation of a conductive path between the residual filament and the electrode. The filament confinement inside the oxygen vacancies and the favored migration path under the filament (see Figure 3.) facilitate the recreation of the conductive path.

Figure 3. Schematic representation of the erased filament and the oxygen vacancies.

In the KMC model, the generation of oxygen vacancies is not simulated as a proper mechanisms following the transition state theory. To simulate the vacancies the migration activation energy is increased when ions migrate outside of favored path but. This is one of the current model limitation and it might be interesting to consider the oxygen vacancies as moving entities conducting the electrical current, similarly to the ions and following the transition state theory for their

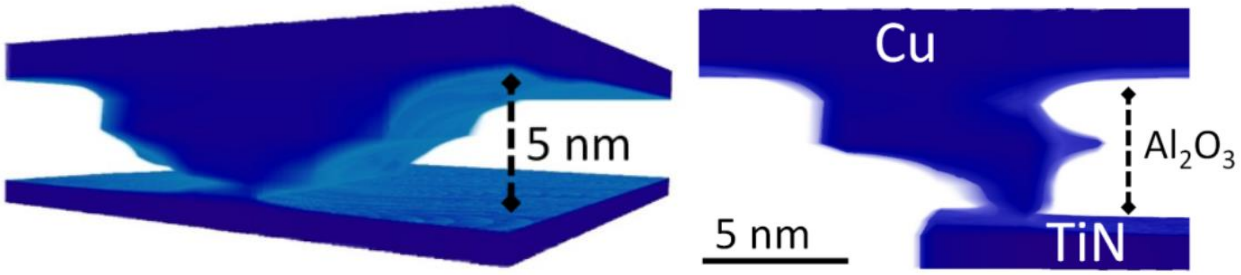

Figure 4. Observed filament morpholgy by U. Celano et al. [Celano 1], showing an inverted shape

generation and migration. In the present state, oxygen vacancies are generated and follow the ions while they migrate through the RL.

The consideration of the vacancies in the KMC model modifies the way the filament reformed itself after RESET and the morphology it adopts. Works have been published [Celano 1], showing the filament morphology by using Tomographic Atomic Force Microscopy (T-AFM). These works showed an inverted filament shape compared to the filament initially obtained with the model not considering the oxygen vacancies. Figure 4 shows this morphology with the filament thinnest location at the bottom of the cell (near the inert electrode). They attributed this filament morphology to the slow ion migration speed compared to the fast redox reaction. In these conditions, a continuous ion flow is migrating from the top electrode until it tip contacts the bottom one. The experimental results presented during the SET analyze to discern the ions migration from the generation are not in concordance with this statement. However, it is possible to explain this kind of filament morphology after SET using the fast migration and slow generation exposed in this work and the introduction of oxygen vacancies. Figure 5 shows the programming steps seen by the KMC to obtain such morphology. At the end of the Forming operation, the first oxygen vacancies are generated and positioned at the filament location. During the first RESET, the bottom of the filament is dissolved and the top part of the residual filament becomes wider. The following

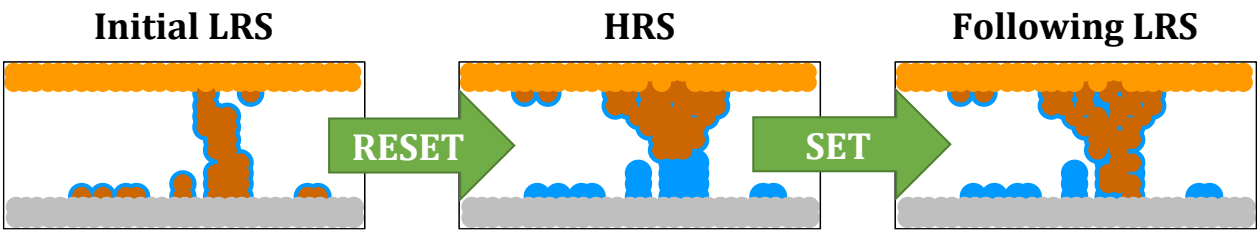

Figure 5. Cycle steps allowing the recreation of the inverted filament shape through the KMC simulation

SET tends to fill the favored area left by the dissolved filament which ends up creating the filament morphology observed by T - AFM.

3.5 Temperature impact on the CBRAM

The role of the temperature in the RESET operation is well known and is the primary reason behind its integration in the KMC model. However, to assure the complete model consistency between every CBRAM operation it is important to compute the temperature evolution during the SET operation. The temperature simulation allows a good RESET operation with low RESET voltage and expected R_{HRS} as shown Figure 6. The thermal generation enhances the filament dissolution greatly decreasing the RESET voltage. The temperature, in the same manner as the electric field, drives the physical mechanisms (redox reaction and migration) responsible for the CBRAM states changes. However, in opposition to the electric field, the temperature does not prioritize one direction which greatly help to the dissolution of the filament during RESET.

The temperature implication during SET was not considered impactful due to the lack of current before SET and the current limitation after it. However, the temperature implication during the SET has been correlated to the filament stabilization, greatly modifying the filament shape as can be seen Figure 7. During the RESET operation, the temperature modifies both the final resistance level and the RESET voltage or time.

The temperature dissipation is also tied to the intrinsic and extrinsic variability of the SET and RESET operations. During SET operations the filament has to dissipate the temperature, the filament width increases to conduct enough temperature towards the electrodes. The quantity of

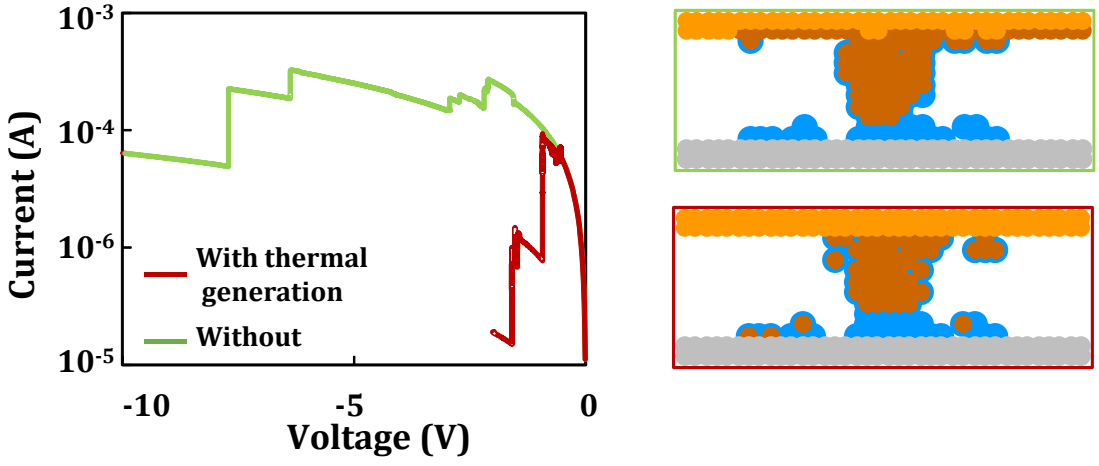

Figure 6. Comparison of the RESET behavior with and without thermal generation.

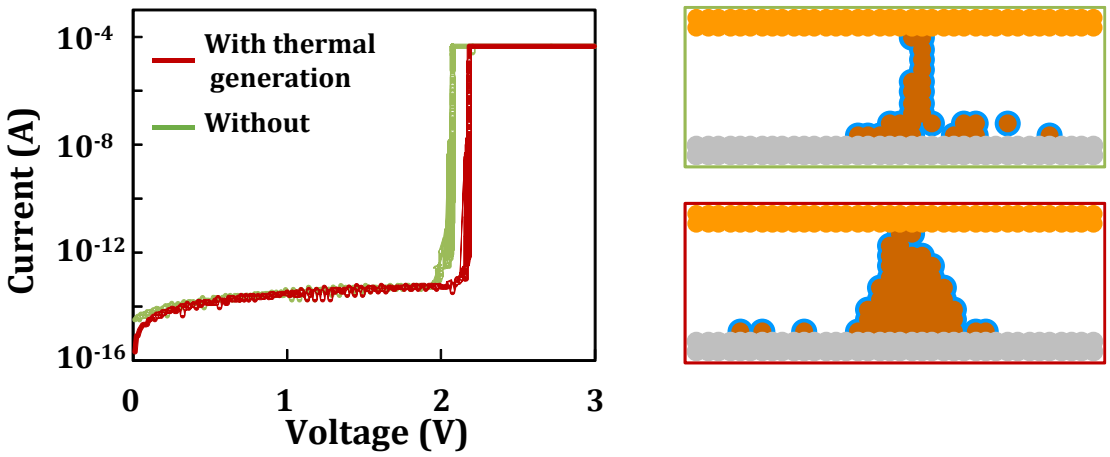

Figure 7. Comparison of the Forming behavior with and without thermal generation. The Forming voltage difference is only due to the stochastic behavior.

energy (heat and electric field) brought to the system controls the stabilization process, the final state of the filament and its variability. During RESET the current is not limited which induces a strong heat dissipation and temperature increase. Due to the high temperature and the thermal conduction in the filament and the RL, an area at high temperature appears. The high temperature reduces the difference of probability for the mechanisms to happen in this area. The filament disruption can then statistically start from every point of this area and drastically change the dissolution evolution and final R_{HRS}.

The thermal dissipation is then not only crucial to the RESET but also to the SET operations and allows to understand the variability concerns impacting the CBRAM devices.

4. Conclusion

The physical understanding of the CBRAM keeps improving but is still late compared to the great devices and circuits developed lately. The research work presented in this manuscript proposes a first approach of a global understanding of the CBRAM operations. This understanding aims to create a bridge between the physical characteristics of the materials composing the CBRAM and the devices behavior during each and every operation. The crucial role of the filament shape has been exposed and ways to control it proposed. Based on the comprehension of the CBRAM behavior, optimizations have been developed in term of electrical conditions or technological improvements. These optimizations, initially coming from theoretical assumptions, have shown great impact on experimental devices to improve both LRS and HRS retention, and endurance capabilities that are the main limiting factors to the industrialization of the technology.

The variability has also been addressed and simulated to discriminate the intrinsic variability proper to the technology and the cycle to cycle variability. The CBRAM optimization appears as a constant tradeoff between retention, endurance, easy cycling… However, the versatility of the CBRAM is a great strength of this technology and offers vast application possibilities by focusing the optimization on precise requirements.

The CBRAM technology still offers a several axis of improvement, not only in term of scaling but also in term of material and conditions optimizations and deeper understanding of the physics involved. Great technological improvements seems around the corner and smart logic circuits might offer interesting solutions to the intrinsic limitation of this technology. Great product integration have already been presented in the past years such as Micron 16 Gb devices [Zahurak 1] and seems to announce interesting evolutions of the technology in the near future.

Chapter VII references

[Celano 1] Celano, U.; Goux, L.; Belmonte, A.; Schulze, A.; Opsomer, K.; Detavernier, C.; Richard, O.; Bender, H.; Jurczak, M.; Vandervorst, W., "Conductive-AFM tomography for 3D filament observation in resistive switching devices," in Electron Devices Meeting (IEDM), 2013 IEEE International , vol., no., pp.21.6.1-21.6.4, 9-11 Dec. 2013

[Molas 1] Molas, G.; Vianello, E.; Dahmani, F.; Barci, M.; Blaise, P.; Guy, J.; Toffoli, A.; Bernard, M.; Roule, A.; Pierre, F.; Licitra, C.; De Salvo, B.; Perniola, L., "Controlling oxygen vacancies in doped oxide based CBRAM for improved memory performances," in Electron Devices Meeting (IEDM), 2014 IEEE International , vol., no., pp.6.1.1-6.1.4, 15-17 Dec. 2014

[Sakamoto 1] Sakamoto, T., Lister, K., Banno, N., Hasegawa, T., Terabe, K. and Aono, M., “Electronic transport in Ta2O5 resistive switch”, Appl. Phys. Lett., 91(9), p.092110.

[Todorova 1] Todorova, T.Z.; Blaise, P.; Vianello, E.; Fonseca, L.R.C., "Understanding the conduction mechanism of the chalcogenide Ag2S silver-doped through ab initio simulation," in Solid-State Device Research Conference (ESSDERC), 2013 Proceedings of the European , vol., no., pp.342-345, 16-20 Sept. 2013

[Zahurak 1] Zahurak, J.; Miyata, K.; Fischer, M.; Balakrishnan, M.; Chhajed, S.; Wells, D.; Hong Li; Torsi, A.; Lim, J.; Korber, M.; Nakazawa, K.; Mayuzumi, S.; Honda, M.; Sills, S.; Yasuda, S.; Calderoni, A.; Cook, B.; Damarla, G.; Tran, H.; Bei Wang; Cardon, C.; Karda, K.; Okuno, J.; Johnson, A.; Kunihiro, T.; Sumino, J.; Tsukamoto, M.; Aratani, K.; Ramaswamy, N.; Otsuka, W.; Prall, K., "Process integration of a 27nm, 16Gb Cu ReRAM," in Electron Devices Meeting (IEDM), 2014 IEEE International , vol., no., pp.6.2.1-6.2.4, 15-17 Dec. 2014.

Author bibliography

International Patent:

- **J. Guy** and G. Molas, "METHOD FOR DETERMINING ELECTRICAL PARAMETERS USED TO PROGRAMME A RESISTIVE RANDOM ACCESS MEMORY", PATENT 20150162081.

Publications:

- **J. Guy**, G. Molas, P. Blaise, et al., "Investigation of Forming, SET, and Data Retention of Conductive-Bridge Random-Access Memory for Stack Optimization," Transactions on in Electron Devices, IEEE, no.99, pp.1-1.
- **J. Guy**, G. Molas, P. Blaise, et al., "Experimental and theoretical understanding of Forming, SET and RESET operations in Conductive Bridge RAM (CBRAM) for memory stack optimization," International Electron Devices Meeting 2014, IEEE, pp.6.5.1-6.5.4, 15-17 Dec. 2014.
- **J. Guy,** G. Molas, E. Vianello, et al., "Investigation of the physical mechanisms governing data-retention in down to 10nm nano-trench Al_2O_3/CuTeGe conductive bridge RAM (CBRAM)," International Electron Devices Meeting 2013, IEEE, pp.30.2.1-30.2.4, 9-11 Dec. 2013.
- **J. Guy,** G. Molas, E. Vianello, et al., "Impact of Sb doping on power consumption and retention reliability of GeS2 based conductive bridge random access memory," Thin Solid Films, Volume 563, 31 July 2014, pp. 15-19.

Co-author in the following publications:

- G. Molas, E. Vianello, F. Dahmani, M. Barci, P. Blaise, **J. Guy**, et al. "Controlling oxygen vacancies in doped oxide based CBRAM for improved memory performances," International Electron Devices Meeting 2014, IEEE, pp.6.1.1-6.1.4, 15-17 Dec. 2014.
- M. Barci, **J. Guy**, G.Molas, E. Vianello, et al. "Impact of SET and RESET conditions on CBRAM high temperature data retention," International Reliability Physics Symposium 2014, IEEE, pp.5E.3.1-5E.3.4, 1-5 June 2014.
- G. Palma, E. Vianello, G. Molas, C. Cagli, F. Longnos, **J. Guy** et al., "Effect of the active layer thickness and temperature on the switching kinetics of GeS2-Based Conductive Bridge Memories," Japanese Journal of Applied Physics, Vol. 52, Num. 4S, February 2013.
- E. Vianello, G. Molas, F. Longnos, P. Blaise, E. Souchier, C. Cagli, G. Palma, **J. Guy** et al., "Sb-doped GeS2 as performance and reliability booster in Conductive Bridge RAM," International Reliability Physics Symposium 2012, IEEE, pp.31.5.1-31.5.4, 10-13 Dec. 2012.

Conferences:

- **J.Guy**, G. Molas, L. Perniola, "Unified Kinetic Monte Carlo simulation of Forming, SET, RESET and data retention for Conductive Bridge RAM, a bond between material properties and device behaviour," poster to be presented at SISC 2015.
- **J. Guy**, "Conductive Bridge RAM (CBRAM) Forming, SET and RESET operations understanding, for memory stack optimization," CEA Memory WorkShop 2014.
- **J. Guy**, "Correlation between retention capabilities and filament morphologies in Conductive Bridge RAM (CBRAM) technology", CEA Memory WorkShop 2013.
- **J. Guy**, G. Molas, E. Vianello, et al., "Impact of Sb doping on power consumption and retention reliability of GeS_2 based CBRAM", e-MRS 2013.
- **J. Guy**, "Numerical modelling of Conductive Bridge Memory (CBRAM) retention", IWSMM – 2012.